Sub-Kelvin Cryogenics for Experimental Cosmology

A thesis submitted to the University of Manchester
for the degree of Doctor of Philosophy
in the Faculty of Science and Engineering

2019

By
Andrew James May
School of Physics and Astronomy

Contents

Word count: $\sim$48000

List of Tables

List of Figures

List of Abbreviations

BET: Brunauer-Emmett-Teller

CAD: Computer-aided Design

CMB: Cosmic Microwave Background

CP: Cryopump

CRC: Chase Research Cryogenics

DR: Dilution Refrigerator

FEA: Finite Element Analysis

GM: Gifford-McMahon

HEX: Heat Exchanger

HS: Heat Switch

HWP: Half-wave Plate

IC: Intercooler

LATR: Large Aperture Telescope Receiver

MC: Mixing Chamber

MDR: Miniature Dilution Refrigerator

MLI: Multi-layer Insulation

PTC: Pulse Tube Cryocooler

QUBIC: QU Bolometric Interferometer for Cosmology

RTD: Resistance Temperature Detector

SQUID: Superconducting Quantum Interference Device

TES: Transition Edge Sensor

UC: Ultracooler

The University of Manchester

ABSTRACT OF THESIS submitted by Andrew James May
for the Degree of Doctor of Philosophy and entitled
“Sub-Kelvin Cryogenics for Experimental Cosmology”
April 2019

Polarization anisotropies in the Cosmic Microwave Background contain a wealth of cosmological information. The forthcoming generation of observatories will make measurements across a range of frequencies and angular scales. These data will support a large number of science goals, including the search for direct evidence of cosmic inflation, measurements of neutrino properties, and the placing of further constraints on cosmological parameters.

These observatories will be based around cryogenic receivers housing multiple cold optics stages at progressively lower temperatures. In order to reach the sensitivities required by their science goals, the receivers will have to support large optical throughput to arrays of transition edge sensor bolometers at sub-Kelvin operating temperatures.

This thesis describes the development of a number of key subsystems for several of these forthcoming experiments: QUBIC, the Simons Array, and the Simons Observatory.

QUBIC, the Q&U Bolometric Interferometer for Cosmology, is a European-led experiment which will deploy a Fizeau interferometer to directly target B-mode polarization anisotropies at degree angular scales. The beam combiner will be operated at 1 K and the resulting interference fringe patterns measured by two arrays of transition edge sensor bolometers at 350 mK. A high-capacity 1 K ^{4}He sorption cooler has been developed, along with a novel superfluid film breaker to maximise the hold time of the system. Novel convective heat switches have been developed to precool the 1 K stage and provide isolation during the cooler recycling. A dual ^{3}He/^{4}He cooler has been provided to operate the detector stage at 350 mK.

The Simons Array is a US- and Japanese-led continuation and extension of the successful POLARBEAR experimental program. It will consist of three POLARBEAR-type telescopes with upgraded cryogenic receivers, POLARBEAR -2A, -2B, and -2C,which will directly image the microwave sky. Each receiver will house the cold optics, focal plane detector array, and cold readout components. The focal plane in each case will be cooled to 270 mK by a multi-stage sorption cooler. Extensive efforts have been devoted to the development of a code, based

on the calculation of Allan deviations, to characterise the stability and identify noise components in the focal plane temperature.

The Simons Observatory is a US-led experiment that will field both a 6 m large aperture telescope and an array of 42 cm small aperture telescopes to probe a wide range of angular scales with very high sensitivity. The large aperture telescope will be coupled to a 2.4 m diameter receiver cryostat which will house thirteen optics tubes. The 1 K and 100 mK stages of the cryostat will be necessarily well-isolated from the higher temperature stages; in order to minimise the total cooling time of these stages, a precooling heat switch scheme has been devised, based on experimental measurements, and simulated. Furthermore, as both the large and small aperture telescopes will operate focal planes at 100 mK, a novel miniature dilution refrigerator has been developed for fast-turnaround operation of a detector wafer test cryostat.

Declaration

No portion of the work referred to in this thesis has been submitted in support of an application for another degree or qualification of this or any other university or other institution of learning.

Copyright

The author of this thesis (including any appendices and/or schedules to this thesis) owns certain copyright or related rights in it (the “Copyright”) and he has given The University of Manchester certain rights to use such Copyright, including for administrative purposes.

Copies of this thesis, either in full or in extracts and whether in hard or electronic copy, may be made **only** in accordance with the Copyright, Designs and Patents Act 1988 (as amended) and regulations issued under it or, where appropriate, in accordance with licensing agreements which the University has from time to time. This page must form part of any such copies made.

The ownership of certain Copyright, patents, designs, trade marks and other intellectual property (the “Intellectual Property”) and any reproductions of copyright works in the thesis, for example graphs and tables (“Reproductions”), which may be described in this thesis, may not be owned by the author and may be owned by third parties. Such Intellectual Property and Reproductions cannot and must not be made available for use without the prior written permission of the owner(s) of the relevant Intellectual Property and/or Reproductions.

Further information on the conditions under which disclosure, publication and commercialisation of this thesis, the Copyright and any Intellectual Property and/or Reproductions described in it may take place is available in the University IP Policy (see http://documents.manchester.ac.uk/DocuInfo.aspx?DocID=24420), in any relevant Thesis restriction declarations deposited in the University Library, The University Library’s regulations (see http://www.library.manchester.ac

.uk/about/regulations/) and in The University's policy on Presentation of Theses.

Acknowledgements

First of all, I would like to thank Prof Lucio Piccirillo, Dr Simon Melhuish, and Dr Paolo Calisse for the opportunity to undertake my postgraduate research and for their extraordinary support over the last three years. I'd also like to thank Dr Mark McCulloch, Dr Gabriele Coppi, Vic Haynes and Graham Bird for their guidance and advice during our various projects.

I am very grateful for the receipt of an STFC studentship which has supported me during my PhD.

I'd like to thank Dr Logan Howe, Dr Nick Galitzki and Prof Brian Keating for hosting me during my visits to UC San Diego. Je voudrais remercier aussi les professeurs Michel Piat et Jean-Christophe Hamilton pour m'avoir accueilli au laboratoire d'Astroparticules et Cosmologie.

Huge thanks are due as well to Nialh, Joel, Dan, Dom, Chessi, Eunseong, Luke, and Josh for being so much fun to share an office with for the last 3 years.

I can't begin to thank my family enough for supporting me in my scientific career so far. My Mum especially ignited my passion for physics, my Dad and my Grandpa always encouraged me to work hard and do myself justice, and my brother always kept me grounded.

Finally, my greatest thanks go to Emma. The completion of this thesis wouldn't have been possible without her love, support and encouragement.

The Author

Andrew James May graduated MEng (Hons) Aerospace Engineering from the University of Manchester in 2015. This included a 12-month internship spent at the STFC Daresbury Laboratory Accelerator Science and Technology Centre under Shrikant Pattalwar, primarily on the development of cryogenic systems for the Hi-Lumi LHC project at CERN. He then spent the summer studying at TU Dresden, Politechnika Wrocławska and NTNU Trondheim after being accepted to the European Course of Cryogenics.

Following completion of his MEng, he moved to the Jodrell Bank Centre for Astrophysics to work on millikelvin cryogenics under Lucio Piccirillo in the Cosmology Group, where he was awarded his MSc by Research in 2016. He was then awarded an STFC studentship to undertake a PhD, of which this thesis is the result.

Supporting Publications

Miniature Sorption Coolers: Theory and Applications
L. Piccirillo, G. Coppi, **A. May**. (2018); CRC Press, UK

Thermal architecture for the QUBIC cryogenic receiver
A. May, et al. (2018); Proceedings of SPIE Astronomical Telescopes + Instrumentation 2018, Austin, TX, USA

Performance of NbSi Transition Edge Sensors read out with a 128 MUX factor for the QUBIC experiment
M. Salatino, **A. May**, et al. (2018); Proceedings of SPIE Astronomical Telescopes + Instrumentation 2018, Austin, TX, USA

QUBIC: The Q & U Bolometric Interferometer for Cosmology
C. O'Sullivan, **A. May**, et al. (2018); Proceedings of SPIE Astronomical Telescopes + Instrumentation 2018, Austin, TX, USA

Simulations and performance of the QUBIC optical beam combiner
C. O'Sullivan, **A. May**, et al. (2018); Proceedings of SPIE Astronomical Telescopes + Instrumentation 2018, Austin, TX, USA

Cooldown strategies and simulations for the Simons Observatory
G. Coppi, **A. May**, et al. (2018); Proceedings of SPIE Astronomical Telescopes + Instrumentation 2018, Austin, TX, USA

Simons Observatory large aperture receiver simulation overview
J. Orlowski-Scherer, **A. May**, et al. (2018); Proceedings of SPIE Astronomical Telescopes + Instrumentation 2018, Austin, TX, USA

The Simons Observatory cryogenic cameras
N. Galitzki, **A. May**, et al. (2018); Proceedings of SPIE Astronomical Telescopes + Instrumentation 2018, Austin, TX, USA

Simons Observatory large aperture telescope receiver design overview
N. Zhu, **A. May**, et al. (2018); Proceedings of SPIE Astronomical Telescopes + Instrumentation 2018, Austin, TX, USA

Performance of the POLARBEAR-2b and POLARBEAR-2c cosmic microwave background cryogenic receivers
L. Howe, **A. May**, et al. (2018); Proceedings of SPIE Astronomical Telescopes + Instrumentation 2018, Austin, TX, USA

POLARBEAR-2: a new CMB polarization receiver system for the Simons Array
M. Hasegawa, **A. May**, et al. (2018); Proceedings of SPIE Astronomical Telescopes + Instrumentation 2018, Austin, TX, USA

Electrical characterization and tuning of the integrated POLARBEAR-2a focal plane and readout
D. Barron, **A. May**, et al. (2018); Proceedings of SPIE Astronomical Telescopes + Instrumentation 2018, Austin, TX, USA

Fabrication process and techniques to realize high yield detector arrays for the POLARBEAR-2/Simons Array CMB experiment
C. Raum, **A. May**, et al. (2018); Proceedings of SPIE Astronomical Telescopes + Instrumentation 2018, Austin, TX, USA

Optical modelling and analysis of the Q and U Bolometric Interferometer for Cosmology
D. Burke **A. May**, et al. (2018); Proceedings of SPIE OPTO, San Francisco, CA, USA

The POLARBEAR-2 and Simons Array Focal Plane Fabrication Status
B. Westbrook, **A. May**, et al. (2017); Journal of Low Temperature Physics, LTD17 Special Issue

QUBIC - The Q&U Bolometric Interferometer for Cosmology - A novel way to look at the polarized Cosmic Microwave Background
A. Mennella, **A. May**, et al. (July 5-12, 2017); Proceedings of Science, The European Physical Society Conference on High Energy Physics, Venice, Italy

QUBIC Technical Design Report
J. Aumont, **A. May**, et al. (September 15, 2016); arXiv:1609.04372

Sorption-cooled continuous miniature dilution refrigeration for astrophysical applications
A. May, et al. (2016); Proceedings of SPIE Astronomical Telescopes + Instrumentation 2016, Edinburgh, UK

Developing a long duration ^{3}He fridge for the LSPE-SWIPE instrument
G. Coppi, **A. May**, et al. (2016); Proceedings of SPIE Astronomical Telescopes + Instrumentation 2016, Edinburgh, UK

Chapter 1

Introduction

Cosmology today enjoys an era of unprecedented precision [1]. Highly sensitive measurements of the Cosmic Microwave Background (CMB) radiation from the early Universe [2, 3], along with the observed expansion of space demonstrated by the recession of distant galaxies in accordance with the Hubble law [4, 5] and the abundance of light elements consistent with Big Bang Nucleosynthesis [6, 7], underpin the concordance model of cosmology.

The incredibly precise CMB data currently available would not have been possible without the exceptionally sensitive instrumentation that has been developed over the last several decades [1]. This thesis reports the development of a number of cryogenic systems which will form part of the next generation of CMB observatories; the first chapter will detail the observational motivation and receiver requirements that have driven the development of said systems.

1.1 The Cosmic Microwave Background

Figure 1.1 shows the history of the Universe according to the concordance model of cosmology, from the Big Bang (shown on the left of the figure) to the present epoch (on the right).

Prior to the Epoch of Recombination (∼380,000 years), the Universe would

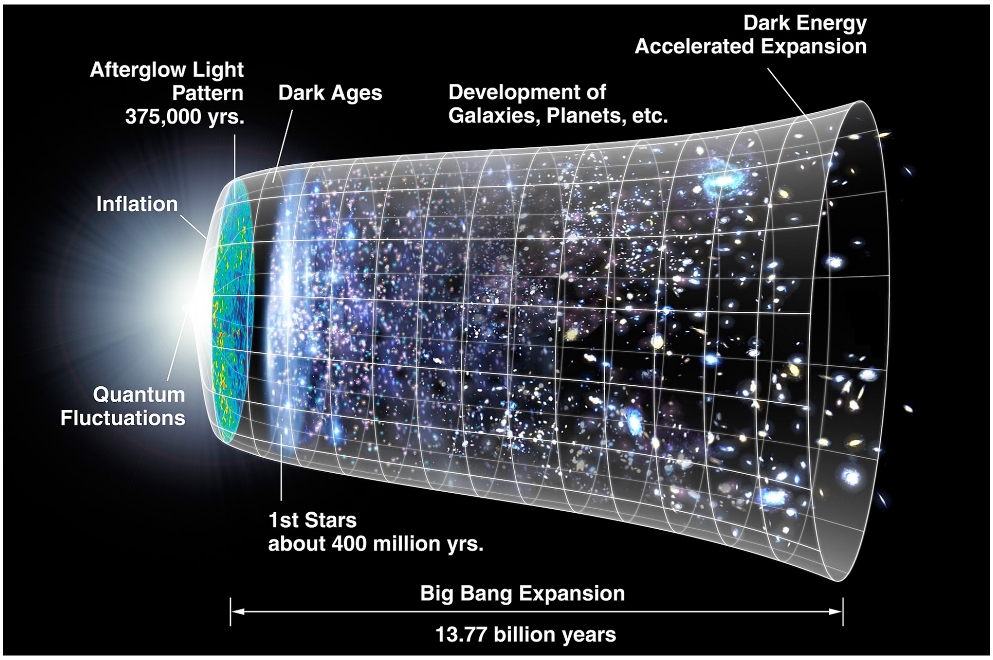

Figure 1.1: Timeline of the Universe from the Big Bang to the present epoch; the size of the Universe is represented by the vertical extent of the grid [8]

have been at a sufficiently high temperature so as to be fully ionized and hence opaque to photons [1]. At Recombination, the energy density reached a sufficiently low level as the Universe expanded to allow matter to recombine. The photons scattered here were then able to free stream through the Universe. This so-called Last Scattering Surface may be observed today as a near-isotropic signal across the entire sky at redshift $z \sim 1100$ [3].

1.1.1 CMB Temperature

Due to Thomson scattering prior to Recombination, the primordial plasma would have been incredibly close to thermal equilibrium at temperature T [1]. As such, the signal generated at Last Scattering was a near-perfect blackbody spectrum of the form

$$I_\nu = \frac{4\pi\hbar\nu^3/c^2}{e^{(2\pi\hbar\nu/k_BT)} - 1} \tag{1.1}$$

where I_ν is the specific intensity, $\hbar$ is the reduced Planck constant, ν is the frequency, c is the speed of light and k_B is the Boltzmann constant [9]. As the Universe continued to expand from Recombination to the present epoch, the frequencies of the CMB photons have been redshifted to the microwave regime, whilst conserving the blackbody profile [10].

The CMB was first measured by accident in 1964 in New Jersey. Two astronomers, Arno Penzias and Robert Wilson, whilst working on the Holmdel Horn Antenna at Bell Labs, measured an excess antenna temperature of ~3.5 K that was "within the limits of our observations . . . isotropic, unpolarized, and free from seasonal variations" [2]. In a companion paper published in the same issue of the Astrophysical Journal [11], Dicke et al. proposed that the signal that had been measured was in fact the relic radiation from a hot big bang. In the years since, observational cosmology has dedicated significant efforts to measuring the CMB with increasing sensitivity and angular resolution [12].

In the early 1990s, NASA's COBE (Cosmic Background Explorer) satellite [13] made then-unprecedented full-sky measurements of the CMB. The FIRAS (Far Infrared Absolute Spectrophotometer) instrument onboard COBE observed the spectrum with incredible precision [14, 15]; the data presented in Figure 1.2 have had the error bars magnified by a factor of 400 for clarity and excellent agreement can be seen with the spectrum of a 2.725 K blackbody.

The second instrument carried by COBE was the DMR (Differential Microwave Radiometers). DMR provided the first clear evidence of temperature anisotropies (once the dipole due to the motion of the Earth relative to the CMB rest frame had been subtracted) [16]. Further satellites, namely NASA's WMAP (launched in 2001) [17] and ESA's Planck (launched in 2009) [18], have provided further full-sky measurements at increasingly higher resolution and sensitivity. These anisotropies arise from density perturbations, Doppler shifting and gravitational redshift at Last Scattering (primary anisotropies), as well as interaction with gravitational wells and high-energy electrons along the line of

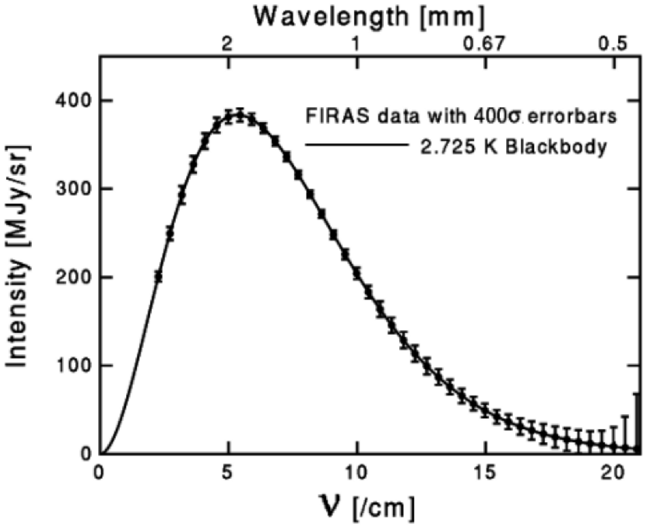

Figure 1.2: Spectrum of the CMB measured by the FIRAS instrument on the COBE satellite plotted with that of a 2.725 K blackbody [15]. Note that the error bars have been magnified by a factor of 400 for clarity.

sight (secondary anisotropies). The measured deviations from the mean CMB temperature are on the order of only 1 part in 10^5.

The full-sky temperature map produced by a joint baseline analysis of Planck, WMAP and 408 MHz observations [19] is given in Figure 1.3 [18]; here, foreground emission[1], the CMB monopole (i.e., average temperature) and dipole have been removed.

The specific positions on the sky of individual temperature maxima or minima are not predicted by theoretical descriptions of Recombination a priori. Instead, the models predict the amplitude of the fluctuations as a function of scale, given a set of cosmological parameters [1, 21, 22]. More specifically, if the anisotropies $\delta T\left(\theta, \phi\right)/T$ are considered in terms of spherical harmonics $Y_m^\ell\left(\theta, \phi\right)$ as

$$\frac{\delta T\left(\theta, \phi\right)}{T} = \sum_{\ell=1}^{\infty} \sum_{m=-\ell}^{\ell} a_{\ell,m} Y_m^\ell\left(\theta, \phi\right) \tag{1.2}$$

---

[1] A number of processes, principally thermal dust, synchrotron and free-free emissions, contribute to the microwave sky and must therefore be accounted for in CMB map-making. This is a complex endeavour and, as with much of the work to which reference is made in this thesis, a significant area of research in its own right [20].

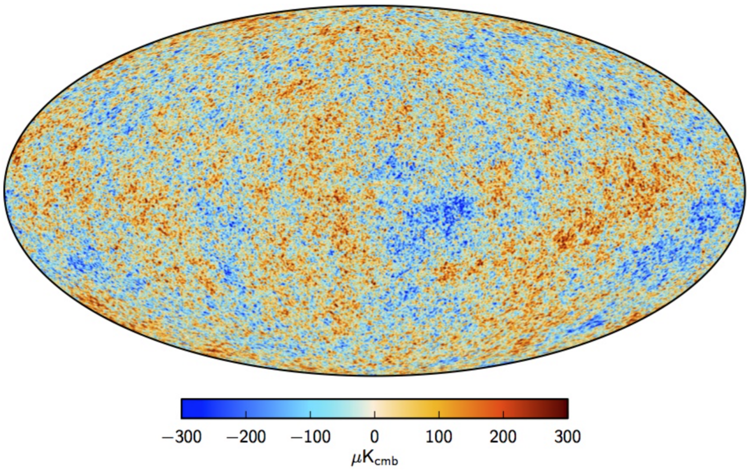

Figure 1.3: Maximum posterior CMB intensity map at 5’ resolution derived from the joint baseline analysis of Planck, WMAP, and 408 MHz observations [18]

with coefficients $a_{\ell,m}$, it can be seen that the temperature autocorrelation (TT) power spectrum may be computed as a function of multipole [3] and characterized completely[2] by defining an average

$$C_\ell \equiv \left\langle |a_{\ell m}|^2 \right\rangle \tag{1.3}$$

The shape of the TT power spectrum, specifically the position and amplitude of the acoustic peaks, is strongly dependent on the cosmological parameters [3]. Measurements of the first peak were initally reported in 2000 by the balloon-borne BOOMERanG [23] and MAXIMA [24] experiments. Further measurements by WMAP [17] and Planck [18] showed the presence of further peaks at higher multipoles; the full power spectrum determined from the 2015 data release from Planck is given in Figure 1.4.

Excellent agreement with these data is given by the standard spatially-flat six-parameter ΛCDM (Λ Cold Dark Matter) model [25]; that is, the standard cosmological model with only six parameters: the Hubble constant H_0, the physical baryon density $\Omega_b h^2$, the physical CDM density $\Omega_c h^2$, the primordial amplitude and spectral index of scalar perturbations A_s and n_s, and the optical depth to

---

[2] Each $a_{\ell m}$ has an average that depends only on ℓ as the distribution is taken to be Gaussian

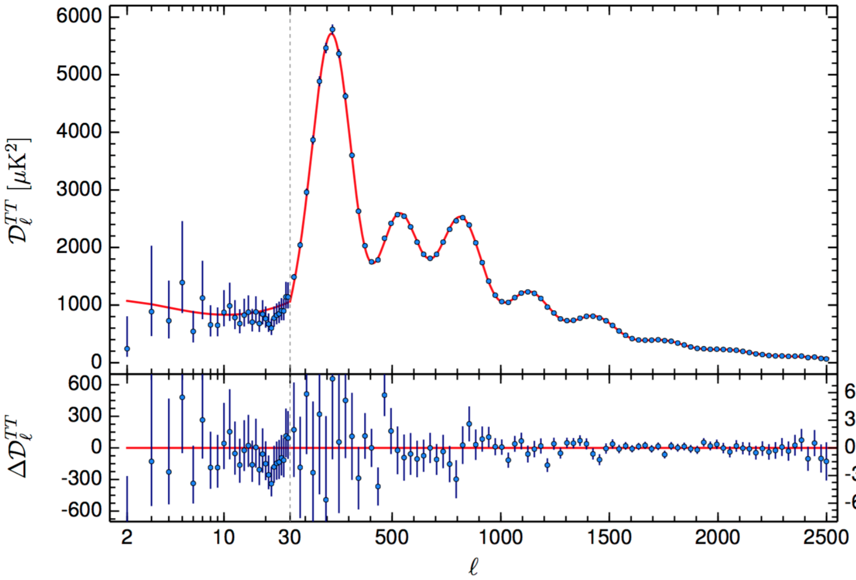

Figure 1.4: The Planck 2015 temperature power spectrum, with the best-fit ΛCDM model (in red) [18]

reionization τ [26]. The parameters determined from the best-fit model to the data in Figure 1.4, in combination with polarization and lensing data (see Section 1.1.2), are given in Table 1.1. This precision in the temperature data is such that the cosmological parameters have been broadly constrained to the percent-level and Planck can be considered the definitive mission on scales $\geq$ 5' [27, 28].

Parameter	Value
H_0	67.81 ± 0.92
$\Omega_b h^2$	0.02226 ± 0.00023
$\Omega_c h^2$	0.1186 ± 0.0020
$\ln(10^{10} A_s)$	3.062 ± 0.029
n_s	0.9677 ± 0.0060
τ	0.066 ± 0.016

Table 1.1: Cosmological parameters from base ΛCDM from Planck 2015 power spectra in combination with polarization and lensing data [25]. Note: the Hubble constant is given in the conventional units of km s^{-1} Mpc^{-1}.

1.1.2 CMB Polarization

Whilst the observed Universe is well-described by the concordance cosmology, there are several observations which remain unresolved.

The first issue, known as the Horizon Problem, is that the CMB temperature is correlated on scales greater than the causal horizon at Recombination (seen today under an angle of $\sim 1^\circ$ on the LSS) [1]. Another problem with the standard theory is the absence of observation of magnetic monopoles and other stable relics; models from particle physics predict that an early hot Universe would have resulted in their copious production, yet these are not observed in the Universe in the present epoch [1]. A further problem is that of flatness. The measured mass density is consistent with that of a flat Universe (as first determined by BOOMERanG [23]); that is, that Euclidean geometry is valid on the scale of the Universe, which raises a fine-tuning problem regarding initial conditions.

The theory of cosmic inflation [29, 30] solves these problems by postulating that the very early Universe underwent a period of exponential expansion. This expansion is shown in Figure 1.5 (note that, owing to the variation of inflationary theories, the numbers are largely illustrative) [31]. The evolving radius of the Universe described by the standard non-inflationary theory is related by the purple line. The inflationary theory, however, describes a Universe evolving as shown by the red line, where the period of exponential expansion is highlighted in blue.

The Horizon Problem is solved by this theory as the regions which appear to have been outside of causal contact at Last Scattering would have been inside each other's causal horizons before inflation. The relic problem is also solved, as a period of inflation after their production would have diluted their density below an observable level in the present epoch. Furthermore, the initial source of structure in the CMB is explained: quantum fluctuations in the very early Universe stretched to cosmological scale by inflation would manifest as regions of

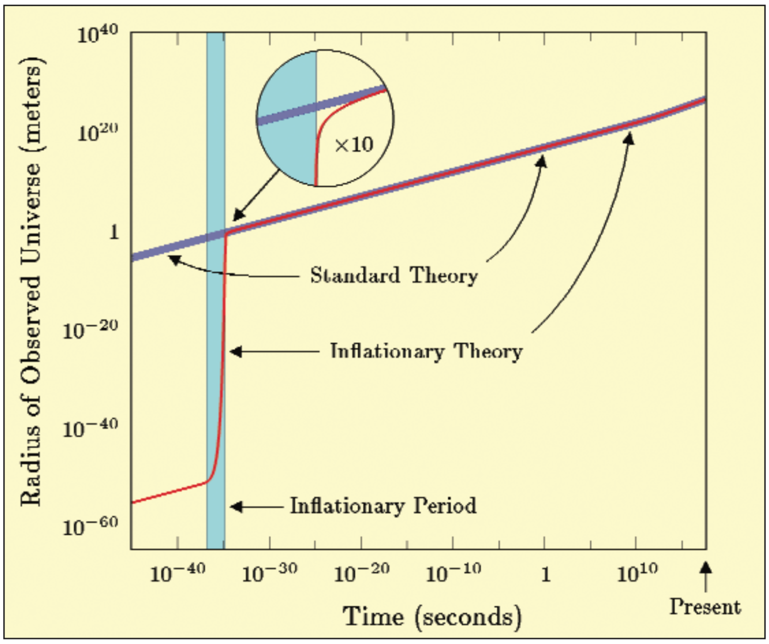

Figure 1.5: Size evolution of the Universe described by inflation [31]

over- and under-density at Recombination [32], seeding the formation of structure in the Universe [1].

Whilst a number of different theories of inflation have been proposed, a fundamental and consistent prediction is the generation of a stochastic Gravitational Wave Background (GWB) [33]. The long wavelength GWB would have been propagating through the Universe at the Epoch of Recombination and hence would have affected the conditions at Last Scattering [34]. Specifically, such tensor perturbations would give rise to a polarization of the last-scattered photons, giving the possibility of an observational test for inflation in measurements of the CMB. Figure 1.6 shows how this (linear) polarization is generated by Thomson scattering where the incoming radiation field has a quadrupole anisotropy; the thick lines (blue) represent radiation from a hot (overdense) region and the thin lines (red) represent that from cold (underdense) regions.

Polarized signals from point sources or across a small patch of sky are typically characterised by the Stokes parameters I, Q, U and V [36], defined with respect to a fixed coordinate system on the sky. However, whilst Stokes Q and U may

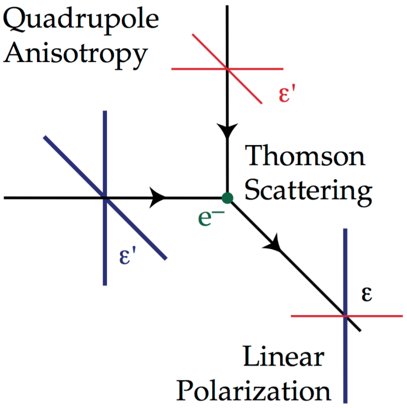

Figure 1.6: Generation of linear polarization by quadrupole anisotropy [35]

be well defined over a small patch, they become ambiguous once the entire sky is considered, as a rotationally invariant orthogonal basis cannot be defined on a sphere [37]. For a larger patch, or indeed for the full sky, the polarization field may instead be analysed by decomposing into divergence-containing and curl-containing components; these are referred to as E- and B-modes respectively[3].

At Recombination, quadrupole anisotropy may be generated by both scalar and tensor perturbations. As shown in the upper left panel of Figure 1.7, density waves (scalar perturbations, seen in the CMB temperature maps described in Section 1.1.1) naturally give rise to E-mode polarization; this is shown for the crossing of three plane waves in the upper right panel. Measurements of E-modes were first reported by the ground-based interferometer DASI in 2002 [38], and later measured further by a number of experiments including WMAP and Planck, with polarization amplitude on the order of a few μK. The E-mode autocorrelation (EE) and temperature cross-correlation (TE) spectra can be computed as for the TT power spectrum as described in Section 1.1.1; these data were used by in the analysis reported by the Planck Collaboration [25], contributing to the constraints on the cosmological parameters given in Table 1.1.

Gravitational lensing (GL) of E-modes by large-scale structure in the Universe

---

[3] Named in analogy to electric and magnetic fields

gives rise to a B-mode anisotropy signal at small angular scales [39]. Direct measurements of this were first reported by the ground-based telescope POLARBEAR in 2014 [40]. Following this initial detection, the GL signal is now beginning to be explored in detail to study this structure as well as to constrain the sum of neutrino masses [41, 42].

As shown in the lower left panel of Figure 1.7, quadrupole anisotropy can also be generated at Last Scattering by x-polarized gravitational waves (tensor perturbations) travelling across the Last Scattering Surface. This would then result in the B-mode polarization pattern shown in the lower right panel[4], which would peak at degree-angular scales. Measurement of B-modes at this scale would therefore constitute direct evidence for inflation [43, 44].

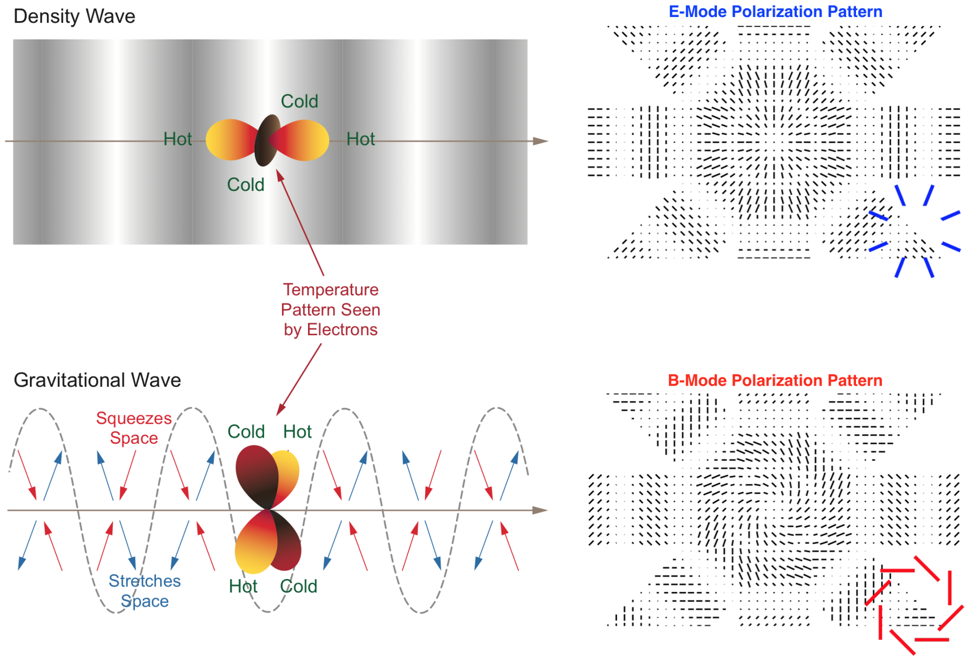

Figure 1.7: Illustration of mechanisms for polarization generation in the CMB. Upper left: density wave at Last Scattering with peaks in dark gray and troughs in white generating quadrupole anisotropy. Upper right: E-mode polarization pattern generated by three crossing plane waves. Lower left: quadrupole anisotropy generated by a x-polarized gravitational wave. Lower right: resulting B-mode pattern [45]

The amplitude of the B-mode signal is poorly constrained theoretically and

---

[4] Note also that +-polarized GWs would generate E-mode polarization [37]

depends on the assumed potential of the inflaton field. This amplitude is commonly parameterised by the tensor-to-scalar ratio r. Measurement of r would allow constraints to be placed on the energy scale of inflation, as well as discrimination between different inflationary models [46].

In 2014, the BICEP2 collaboration reported $>5\sigma$ detection of a degree-scale B-mode signal [47]. However, subsequent joint analysis of BICEP2/Keck Array and high-frequency data from Planck found strong evidence that the signal was the result of polarized Galactic dust emission and found no statistically significant evidence for tensor modes [48, 49].

Currently, the tensor-to-scalar ratio[5] is constrained at the level of $r_{0.002} < 0.07$ by combining CMB data from Planck and BICEP2/Keck Array with measurements of baryon acoustic oscillations [50].

Figure 1.8 shows a comparison of the temperature, E-mode, lensing B-mode, and (theoretical) primordial B-mode power spectra. The latter is shown for two illustrative values of r. Overlaid are B-mode measurements from BICEP2/Keck Array, POLARBEAR, and SPTPol.

Observationally, a tensor-to-scalar ratio of 0.01 would correspond to B-mode polarization fluctuations on the order of several nK [52]. As a result, the forthcoming observatories aiming to measure r will require very high sensitivity, as well as unprecedented control of instrumental systematic effects and astrophysical foregrounds.

1.2 Detector Technologies for CMB Observations

Historically, both coherent and incoherent technologies have been used in CMB telescopes. Coherent receivers, such as the Planck Low Frequency Instrument (LFI), preserve the phase information of the signal. LFI, which observed in three frequency bands centred at at 30, 44, and 70 GHz, was based around high electron

---

[5] The Planck analysis defines r at $k \sim 0.002$ Mpc^{-1}

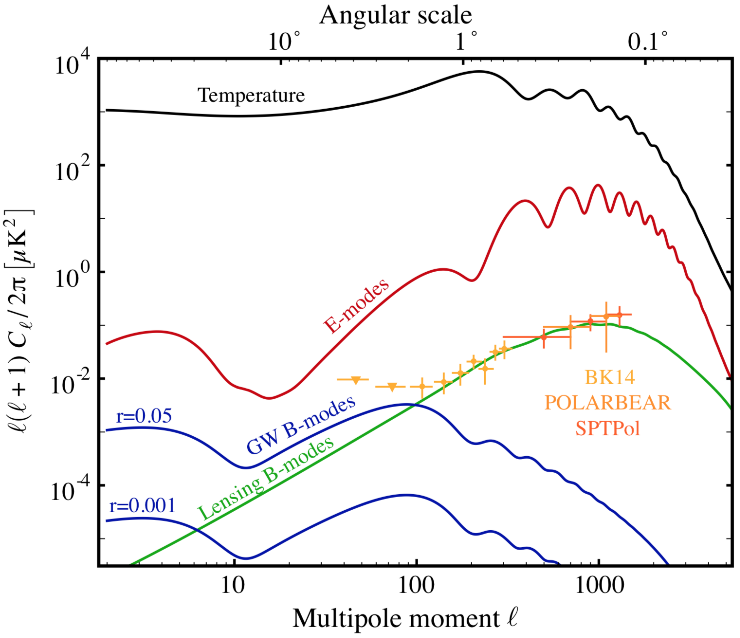

Figure 1.8: Comparison of the temperature (black), E-mode (red), lensing B-mode (green), and theoretical primordial B-mode (blue) power spectra. Overlaid are B-mode measurements from BICEP2/Keck Array (light orange), POLARBEAR (orange), and SPTPol (dark orange). [51]

mobility transistors [53]. On the other hand, as it is only the total power of the CMB that needs to be be measured, it is also possible to use incoherent detectors (which do not preserve phase information); this was done in the Planck High Frequency Instrument (HFI), which used bolometers to observe six bands at 100, 143, 217, 353, 545, and 857 GHz [54].

Detector technology development since Planck is such that, for the ground- and balloon-based CMB polarization observatories that are either currently observing or due to be fielded in the next ∼5 years, transition edge sensor (TES) bolometers are nearly universally used [52, 55]. It is possible that future CMB experiments may use kinetic inductance detectors (KIDs), although currently the technological maturity is not sufficient for their large-scale implementation [56].

Bolometers are comprised of an absorber that transforms incident radiation into heat, a thermometer coupled to the absorber, and a weak thermal link between the absorber and a temperature sink [57, 58], as shown in Figure 1.9.

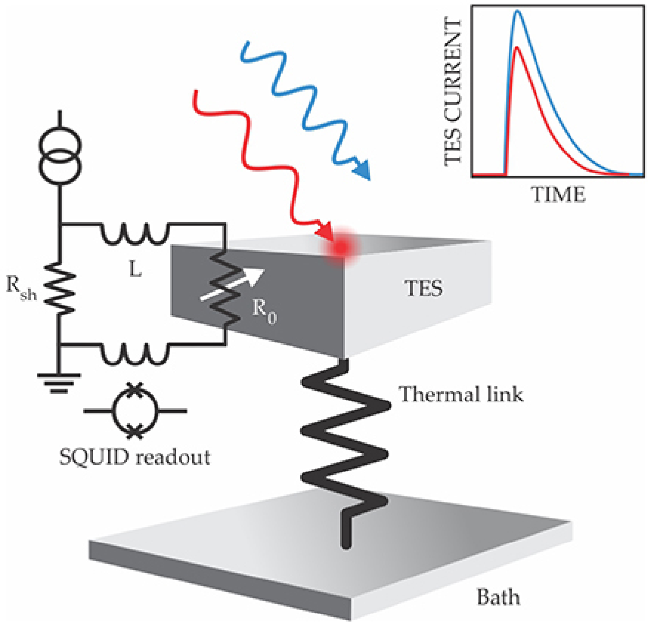

Figure 1.9: TES architecture [59]. The operation and circuit diagram are described in the text.

In the steady state, temperature of the absorber T is due to the background radiative power absorbed Q and the electrical bias power P as

$$G\,(T - T_0) = Q + P \tag{1.4}$$

where G is the conductance of the weak link and T_0 is the sink temperature [60, 61]. In response to the presence of an additional signal from the sky $\Delta Q e^{j\omega t}$,

$$C\frac{d\,(\Delta T)}{dt} + G_{eff}\,(\Delta T) = \Delta Q \tag{1.5}$$

where C is the heat capacity of the absorber. It may be seen that there is a tradeoff between having fast response (the time constant of the bolometer $\tau = C/G$) and high sensitivity

$$\left|\frac{dT}{dQ}\right| = \frac{1}{G_{eff}\sqrt{1+\tau^2\omega^2}} \tag{1.6}$$

To optimize both, C should be minimized; hence a small absorber at low temperature is used. For a thermometer with bias current I_{bias}, the responsivity $\Re$ (i.e., the change in voltage V with respect to Q) is

$$\Re = \frac{dV}{dQ} = I_{bias}\alpha R\frac{dT}{dQ} = \frac{I_{bias}\alpha R}{G_{eff}\sqrt{1+\tau^2\omega^2}} \tag{1.7}$$

where R is the resistance of the thermometer and

$$\alpha = \frac{1}{R\left(T\right)}\frac{dR\left(T\right)}{dT} \tag{1.8}$$

To achieve a high α, superconducting transition edge sensors are used, which can have α ~1000 K^{-1} around their critical temperature [62]. Furthermore, the TES can be voltage biased so as to be maintained at this point, indicated by the red dot in Figure 1.10, via Joule heating $P = V_{bias}^2/R$.

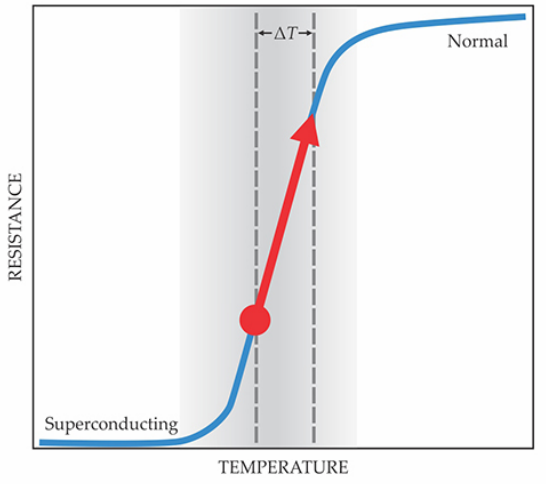

Figure 1.10: Resistance of a superconducting TES with temperature, showing the bias point and increase in resistance associated with the absorption of incident power [59]

Representation of a typical TES circuit is shown in Figure 1.9. Here, a constant bias current I_{bias} is applied to a shunt resistor R_{sh} in parallel with a series combination of a parasitic resistance R_{par} (not shown), a TES, and an inductance L. The circuit can be represented by a Thévenin-equivalent circuit where a bias voltage $V_{bias} = I_{bias}R_{sh}$ is applied to a series combination of a load resistor $R_l = R_{sh} + R_{par}$, the inductance L, and the TES. When the sensor is warmed by an amount ΔT (see Figure 1.10), its resistance will increase proportionally to the amount of energy deposited (indicated by the red arrow). The accompanying reduction in Joule power acts as a restoring force, providing a negative electrothermal feedback, stabilizing operation.

The current state of the art readout method for TESs is to measure the inductance of the input coil coupled to a superconducting quantum interference device (SQUID) to determine the current, as shown in Figure 1.9. Furthermore, it has been possible to develop multiplexing techniques which allow multiple pixels to be read out by a single transmission line [63]; this reduces significantly the number of wires and hence the mechanical complexity of the readout for multipixel arrays, as well as the thermal loading which is essential for low temperature operation [64]. Such arrays may be produced using techniques such as thin film deposition and optical lithography [65].

A measure of the sensitivity of a TES is the Noise Equivalent Power (NEP) per root bandwidth, which is the incident signal power required to match the internal noise of the detector to give a signal-to-noise ratio of one. As the noise contribution terms are independent, the total NEP is given by the quadrature sum of contributions from the instrument and the contribution from the signal itself (which is intrinsic) as

$$NEP^2 = \underbrace{NEP^2_{Johnson} + NEP^2_{Phonon}}_{Detector} + \underbrace{NEP^2_{Photon}}_{Background} \tag{1.9}$$

The Johnson noise component results from the random motion of electrons in the sensor and is

$$NEP^2_{Johnson} = \frac{4k_BTR}{\Re^2} \tag{1.10}$$

where k_B is the Boltzmann constant. The contribution from phonon noise is due to the quantised vibrations in the material structure [66] and is

$$NEP^2_{Phonon} = \frac{4k_B T^2 G_{eff}}{G^2_{eff} + (2\pi f C)^2} \tag{1.11}$$

Whilst the photon noise is intrinsic, both the Johnson and phonon noise scale with temperature and can therefore be reduced by cooling the sensor. The ultimate aim for a bolometer therefore is to operate so as to be background limited [67], i.e., the NEP is dominated by the photon noise. In practice, this requires operating the TES below 300 mK.

Background limited performance of TES technology has been well demonstrated across a range of bands and platforms [64]. In order to increase the sensitivity for future CMB polarization observatories, the trend is towards increasingly larger format arrays with higher optical throughputs [68]. This is driving the development of increasingly complex cryogenic receivers [69].

1.3 Forthcoming CMB Observatories

To measure the polarization anisotropy of the CMB, a number of experiments are currently in various stages of proposal, development, deployment, and observation, and target a range of different frequencies and angular scales. A non-exhaustive list of experiments is given in Table 1.2. In order to minimise microwave atmospheric absorption by precipitable water vapour [70], the observatories are located either in the Atacama Desert in Chile or one of the polar regions.

These observatories are broadly based around large throughput cryogenic receivers housing multiple cold optics stages at progressively lower temperatures down to focal plane arrays with $100 < T < 300$ mK. This gives rise to exceptionally challenging cryogenic requirements [69] and has driven the development of a number of systems which are the subject of this thesis. The work reported here has been carried out as part of the QUBIC, POLARBEAR-2/Simons Array, and

Project	Country	Location	Status	Frequencies (GHz)	ℓ range	Ref.
Advanced ACTPol	USA	Atacama	Starting	28, 41, 90, 150, 230	60-3000	[71]
BICEP3/Keck	USA	Antarctica	Running	95, 150, 220	50-250	[72]
CLASS	USA	Atacama	Starting	38, 93, 148, 217	2-100	[73]
LSPE	Italy	Arctic	$\geq$2019	43, 90, 140, 220, 240	3-150	[74]
QUBIC	France	Argentina	$\geq$ 2019	150, 220	30-200	[75]
Simons Array	USA, Japan	Atacama	Starting	90, 150, 220	30-3000	[76]
Simons Observatory	USA	Atacama	$\geq$ 2021	27, 39, 93, 145, 225, 280	30-5000	[77]
SPIDER	USA	Antarctica	Running	90, 150	20-500	[78]
SPT–3G	USA	Antarctica	Running	95, 148, 223	50-3000	[79]

Table 1.2: Summary of forthcoming CMB polarization observatories

Simons Observatory collaborations.

1.4 About This Thesis

Chapter 1 of this thesis has given an overview of the observational motivation, detector technologies, and receiver requirements for the forthcoming generation of CMB polarization observatories.

Chapter 2 gives a background in the relevant properties of matter and techniques at low temperatures, supporting the work reported in the subsequent chapters.

Chapter 3 details the instrument QUBIC (QU Bolometric Interferometer for Cosmology), with a focus on the thermal architecture. A novel high power ^{4}He sorption cooler has been developed for cooling the large 1 K optics box and is reported. Also reported is the development of a double stage ^{3}He/^{4}He cooler to cool the focal plane arrays to 300 mK, novel precooling and isolation heat switches, modelling and thermal analysis, and laboratory cryogenic testing of the receiver.

Chapter 4 describes the POLARBEAR-2 cryogenic receivers for the Simons Array and reports the development of a code, based on the calculation of Allan deviations, to characterise the stability and identify noise components in the temperature of the focal plane, which is cooled to 250 mK by a multi-stage sorption cooler.

Finally, Chapter 5 reports experimental study of a number of heat switch technologies for precooling the 1 K and 100 mK stages of the Simons Observatory Large Aperture Telescope Receiver (LATR), along with simulation of their implementation. Furthermore, as both the LATR and Small Aperture Camera will operate focal planes at 100 mK, development is reported of a detector wafer test cryostat based around a novel miniature dilution refrigerator for fast-turnaround operation.

Chapter 2

Low Temperature Techniques

The development of large and complex cryogenic receivers necessarily requires a broad understanding of the behaviour of cryogens and materials at low temperatures, cryogenic heat transfer, thermal modelling, and a variety of low temperature techniques. The following chapter provides an overview of these in the context of the systems described in Chapters 3, 4, and 5. Given the depth of these subjects, the interested reader is encouraged to refer to Refs [80, 81, 82, 83, 84].

2.1 Properties of Helium at Low Temperatures

Table 2.1 gives the boiling temperature under atmospheric pressure and the latent heat of evaporation for some cryogenic liquids.

Substance	O_2	Ar	N_2	Ne	H_2	^{4}He	^{3}He
T_b (K)	90.1	87.2	77.2	27.1	20.3	4.21	3.19
L (kJ·l^{-1})	243	224	161	103	31.8	2.56	0.48

Table 2.1: Boiling point at $P = 1$ bar, T_b, and latent heat of evaporation, L, at T_b for some cryogenic liquids. Data taken from [80].

Due to various issues of safety, availability and expense, O_2, Ar, and Ne are not commonly used as cryogens in laboratory systems. Typically, liquid N_2

(LN_2) may used to provide a 77 K stage[1] and to precool lower temperature stages. Liquid ^{4}He (LHe) is then used to provide a 4 K stage. However, as this thesis will focus on systems developed for use in dry dewars (i.e., those operating nominally without liquid cryogens and instead using mechanical cryocoolers down to 4 K, see Section 2.5), only the two stable isotopes of helium (^{4}He and the much rarer ^{3}He) will be discussed further.

The nucleus of ^{4}He contains two protons and two neutrons, each with anti-parallel spin orientation. The total nuclear spin $I = 0$ and ^{4}He is hence a boson (the superfluid obeying Bose-Einstein statistics, see below). The nucleus of ^{3}He by comparison contains only one neutron, therefore having $I = 1/2$ and is a fermion (the liquid obeying Fermi-Dirac statistics). Whilst the different statistics give rise to the different properties discussed below, both isotopes similarly exhibit a number of remarkable properties. Both have notably low boiling points and critical temperatures, as given in Table 2.2. Furthermore, both isotopes, unlike any other liquids, do not solidify under their own vapour pressures, even at $T = 0$ K. As a consequence, neither exhibit triple points where the gas, liquid and solid phases can coexist. These properties arise firstly due to their weak van der Waals forces (owing to the closed electronic s-shell of helium [80]) and secondly due to the small atomic mass m and hence large quantum mechanical zero-point energy E_0 given by

$$E_0 = \frac{h^2}{8ma^2} \tag{2.1}$$

where $a = (V_m/N_0)^{1/3}$ is the radius of the sphere to which the atoms are confined and N_0 is Avogadros number [80]. The weak van der Waals forces lead to exceptionally low boiling temperatures, and the large zero-point energy is responsible for the persistence of the liquid state down to absolute zero.

Superfluid behaviour is also present in both isotopes; however, this state is

---

[1] As is the convention for cryogenic systems design, this thesis will reference temperature stages by their *nominal* operating temperatures

reached at a much lower temperature in ^{3}He. Some properties are given for the liquid phases of both isotopes in Table 2.2 and their P-T phase diagrams are given in Figures 2.1 and 2.2 (note the difference in temperature scales).

	^{3}He	^{4}He
Boiling point, T_b (K)	3.19	4.21
Critical temperature, T_c (K)	3.32	5.20
Maximum superfluid transition temperature, T_c (K)	0.0025	2.1768
Density^a, ρ (g·cm^{-3})	0.082	0.1451
Classical molar volume^a, V_m (cm^3·mol^{-1})	12	12
Actual molar volume^a, V_m (cm^3·mol^{-1})	36.84	27.58
Melting pressure^b, P_m (bar)	34.39	25.36
Minimum melting pressure, P_m (bar)	29.31	25.32
Gas-to-liquid volume ratio^c	662	866

Table 2.2: Properties of liquid helium. ^{a}At saturated vapour pressure and $T = 0$ K. ^{b}At $T = 0$ K. ^{c}Liquid at 1 K, NTP gas (300 K, 1 bar). Data taken from [80].

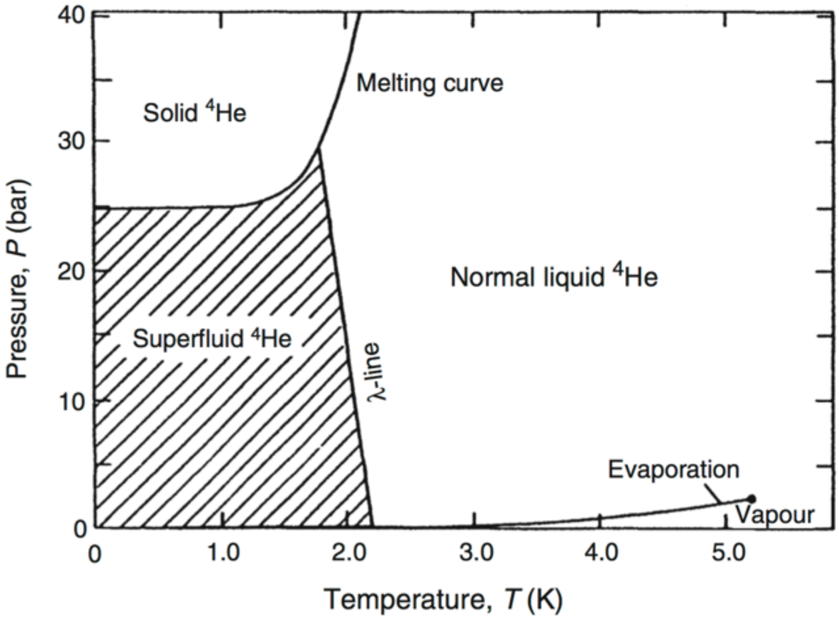

Figure 2.1: ^{4}He phase diagram [80]

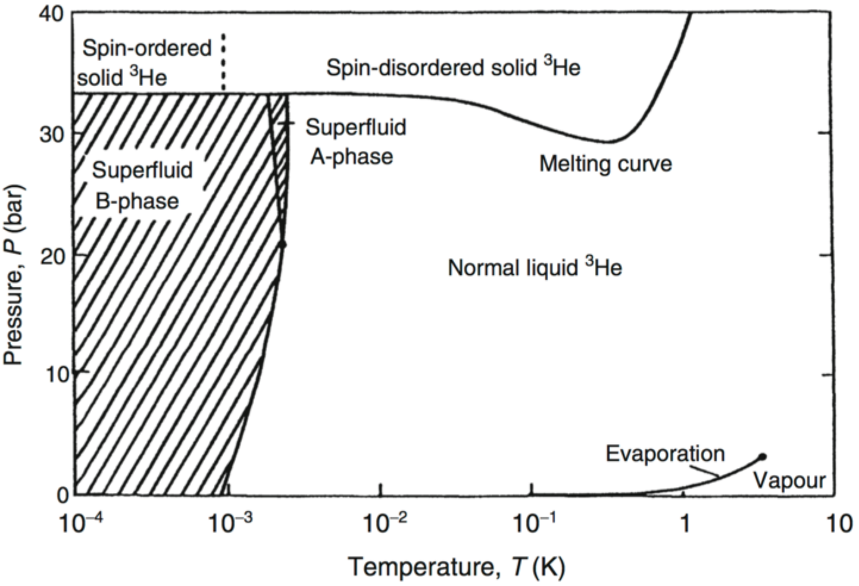

Figure 2.2: ^{3}He phase diagram [80]

2.1.1 Superfluidity

Below the λ-line shown in Figure 2.1, Bose-Einstein condensation of ^{4}He results in the superfluid phase change[2]. In this regime, helium (sometimes denoted He-II to distinguish it from the normal fluid He-I) behaves as a perfect fluid with zero viscosity [87]. Behaviour in its superfluid state is well described by the two-fluid model of Landau and Tisza [88, 89], which considers He-II to be comprised itself of a normal-fluid component and a superfluid component, each with their own independent densities, ρ_n and ρ_s, and velocities, $\boldsymbol{v_n}$ and $\boldsymbol{v_s}$. The total density of the liquid is the sum of the densities of the two components $\rho = \rho_n + \rho_s$. In this model, the acceleration of the superfluid component $\partial \boldsymbol{v}_s / \partial t$ may be written as

$$\frac{\partial \boldsymbol{v}_s}{\partial t} = -\frac{1}{\rho}\nabla P + s\nabla T \tag{2.2}$$

It may be seen therefore that, firstly, the superfluid flows under the influence of

---

[2] As an example of a macroscopic quantum phenomenon analogous to superconductivity, the study of superfluidity is expansive and is only treated here in the context of systems developed as part of this thesis. For a more detailed treatment, the interested reader is directed to References [85, 86].

pressure gradients ∇P and, secondly, it also responds to gradients in temperature. It may be understood from the so-called “fountain” term $s\nabla T$ (where s is the specific entropy of the normal component) that the superfluid will accelerate towards warmer regions giving rise to the thermomechanical or “fountain pump” effect.

2.1.2 Latent Heat

The λ-point also represents a discontinuity in other physical properties of helium, including the latent heat of evaporation L[3]. L as a function of temperature is given in 2.3 for both ^{4}He and ^{3}He.

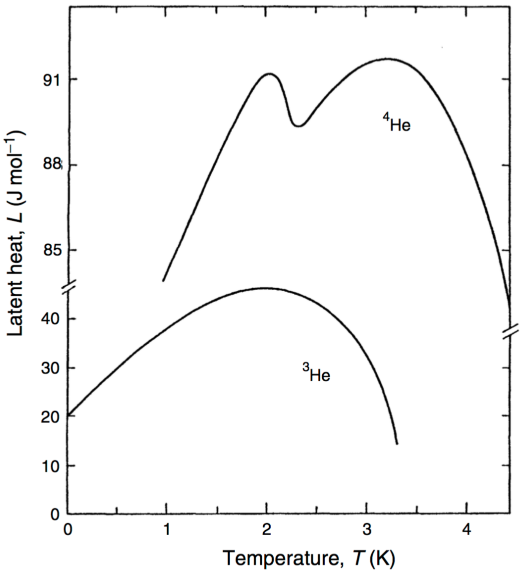

Figure 2.3: Latent heat curves for ^{3}He and ^{4}He (note the discontinuity of scale) [80]

In the case that a bath of liquid helium is used to produce cooling by accepting some external heat load, it may be considered that the cooling power given by the resulting boil-off is

$$\dot{Q} = \Delta H \dot{n} = L \dot{n} \tag{2.3}$$

---

[3] It should be noted here that this can make modelling transitions with these properties challenging

where ΔH is the difference in enthalpy between the liquid and vapour phase (i.e. the latent heat of evaporation) and $\dot{n}$ is the molar flow rate.

2.1.3 Specific Heat Capacity

In the temperature regime below the λ-point, the specific heat capacity (at constant volume) c_v is given in Figure 2.4, along with that of ^{3}He and copper by way of comparison. It should be noted here that as c_v of liquid ^{4}He is up to several orders of magnitude higher than that of copper, the thermal behaviour of a system in many cases is dominated by the amount and thermal behaviour of the liquid helium it contains.

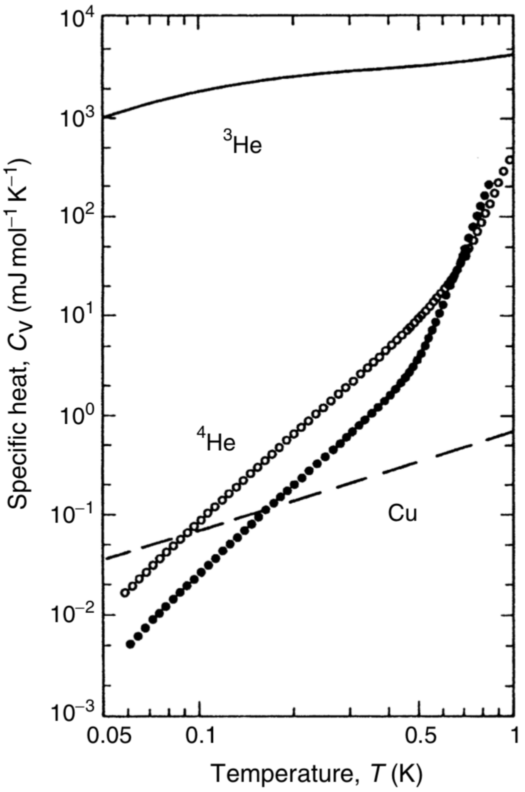

Figure 2.4: Specific heats of liquid helium and copper as a function of temperature below 1 K [80]. The solid line is for ^{3}He. The open dots are for ^{4}He under its own vapour pressure and the solid dots are under an applied pressure of 22 bar. The dashed line is for solid copper.

2.1.4 Vapour Pressure

The vapour pressure P_{vap} is that exerted by a vapour in thermodynamic equilibrium with its condensed phase. This varies as a function of temperature; an approximation is given by the Clausius-Clapeyron equation [80] as

$$\left[\frac{dP}{dT}\right]_{vap} = \frac{s_{gas} - s_{liquid}}{V_{m,gas} - V_{m,liquid}} \tag{2.4}$$

Taking the difference in entropies of the liquid and gaseous phases as L/T, the observation that $V_{m,liquid} \ll V_{m,gas}$ and, from the ideal gas equation, that $V_{m,gas} \approx RT/P$, it may be seen that integrating Equation 2.4 gives

$$P_{vap} \propto e^{-L/RT} \tag{2.5}$$

This agrees well with experimental data, as shown in Figure 2.5.

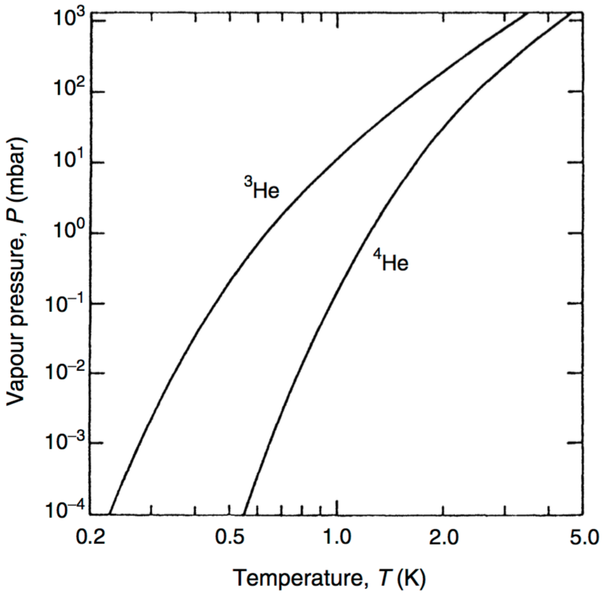

Figure 2.5: Vapour pressure curves for ^{3}He and ^{4}He [80]

2.2 Physical Adsorption

As is revisited in later chapters, adsorbent materials may be used to trap gases such as helium at cryogenic temperatures; this may be done either to improve the level of vacuum attainable in a cryostat (see Section 2.5) or, more importantly in the case of this thesis, to control the vapour pressure (and hence temperature) over a liquid bath and act as a pump.

The amount of adsorption at a given pressure is temperature dependent, and it is therefore possible to provide a pressure increase (gas release) or decrease (gas trapping) by simply controlling the temperature of the material [90].

Charcoals and zeolites are typically used sorbents due to their high specific surface areas (~1000 m^2/g) which result from their internal networks of pores. Data for a selection of charcoal samples is given in Table 2.3.

Type	Source	Mesh (mm)	Supplier	Surface area ($m^2 \cdot g^{-1}$)
PCB	Coconut	1.7-0.6	Calgon	1150-1250
BPL	Coal	1.7-0.6	Calgon	1050-1150
GAC 1240	Coal	1.7-0.4	Ceca, Inc.	1000-1100
Nuchar WV-B	Hardwood	2.0-1.7	Westvaco	1500-1700

Table 2.3: Surface area data for a range of charcoal samples. Data taken from [91]

The binding of helium gas to charcoal at low temperatures occurs due to physical adsorption. This is distinct from chemical adsorption, for which the binding energies are much higher. In physical adsorption, also known as physisorption, the forces involved are intermolecular (van der Waals' forces). The van der Waals' forces are the sum of the attractive and repulsive forces between molecules; the presence of these forces gives the van der Waals' equation of state which in turn gives rise to the Lennard-Jones (L-J) potential $U(r)$ [92] described by

$$U(r) = -\left(\frac{c_1}{r}\right)^6 + \left(\frac{c_2}{r}\right)^{12} \tag{2.6}$$

where c_1 and c_2 are constants and r is the intermolecular distance. It may be seen from this equation that the L-J potential contains an attractive component proportional to r^{-6} (relatively long range) and a repulsive component proportional to r^{-12} (relatively short range). The combination of these effects gives a potential well in which gas particles of a sufficiently low kinetic energy may become trapped. It may therefore be seen how gas molecules may be physisorbed onto the surface of a suitable sorbent, as well as how heating the sorbent may provide sufficient excitation to trapped particles to desorb them. The BET theory of Brunauer, Emmett, and Teller considers the L-J potential extended to a multilayer kinetic theory [93] and is specific to the gas species adsorbed[4]. This is then described as

$$\frac{P}{v\left[P_0 - P\right]} = \frac{c-1}{v_{\mathrm{m}}c}\left(\frac{p}{p_0}\right) + \frac{1}{v_m c} \tag{2.7}$$

where v is the volume of gas adsorbed at equilibrium pressure P, v_m is the volume of the monolayer adsorbed gas, P_0 is the saturation pressure (hence a function of T) and c is the BET constant (specific to the given combination of adsorbant and gas species). Equation 2.7 is hence an isotherm, which agrees well with the data given by Reference [80] for specific adsorption as a function of pressure at different temperatures (presented in Figure 2.6). It is clear from the figure that there are several orders of magnitide in difference between the amount of helium adsorbed by charcoal above 28 K and the amount adsorbed below 4 K.

It should also be noted here that whilst there is an observed correlation between the BET surface area and helium accumulation at a given temperature and pressure, there are deviations from this. As reported by Sedgeley et al. [91], other variables in the manufacturing and treatment can have some influence in terms of both helium accumulation capacity and pumping speed.

---

[4] A detailed treatment is given in Reference [94].

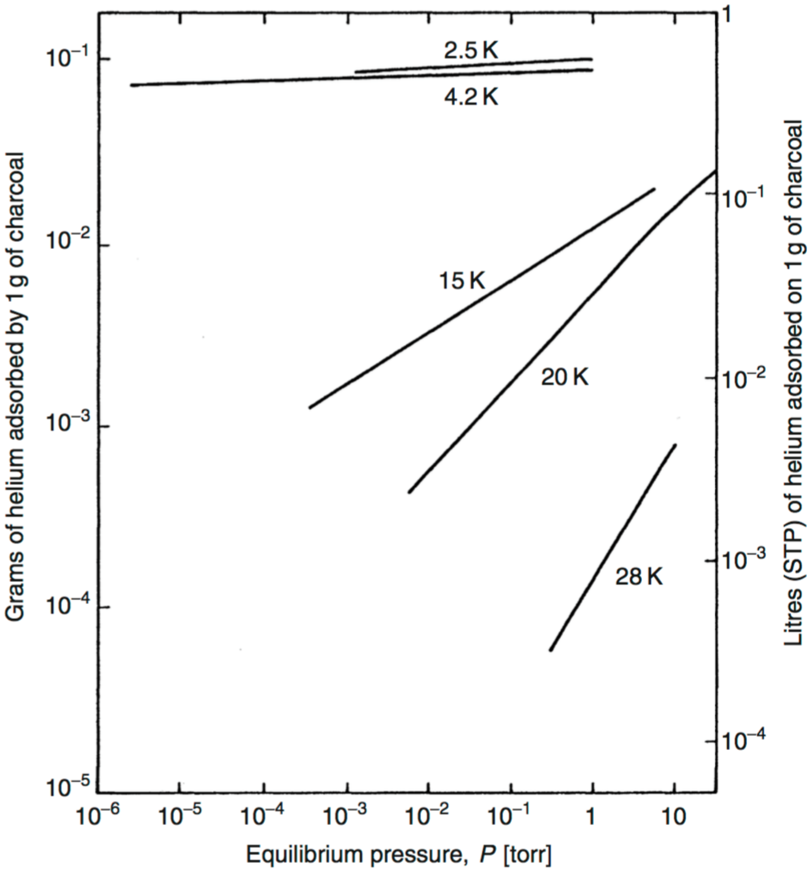

Figure 2.6: Adsorption isotherms for helium by charcoal for a range of temperatures [80]

2.3 Cryogenic Heat Transfer

The three mechanisms of heat transfer; conduction, convection and radiation; must be well understood for the design of low temperature systems.

2.3.1 Thermal Conduction

Conductive heat transfer is that which occurs, primarily within solids, although also within liquids and gases, without mass transport. It is given by Fourier's law, which may be written in the one-dimensional case as

$$\dot{q} = -k\left(T\right)\frac{dT}{dx} \tag{2.8}$$

where $\dot{q}$ is the conductive heat flux and $k\left(T\right)$ is the conductivity of the material, which is a function of temperature T and is generally non-linear, implying that numerical integration over T is necessary in most practical cases[5]. It may be considered that in the case that the cross sectional area A of the domain is constant, then the total rate of heat transfer $\dot{Q}_{cond}$ for a domain of length L is

$$\dot{Q}_{cond} = \frac{A}{L}\int_{T_{cold}}^{T_{hot}} k\left(T\right) dT \tag{2.9}$$

as shown in Figure 2.7.

Figure 2.7: Conductive heat transfer in the one-dimensional case for a medium of constant cross-section A and length L [95]

It is common in the literature to find data for the thermal conductivity integral $\int_{T_{cold}}^{T_{hot}} k\left(T\right) dT$. These values may then be used in calculating the heat load and thermal interception from room temperature to the cold stages of a given system as described in Section 2.4.

Heat transfer via conduction may also occur in liquids and gases. In the case of liquids, k may be defined as for solids; data for liquid ^{3}He and ^{4}He (above the λ-point) are given in Figure 2.8.

Below the λ-transition, the conductivity of ^{4}He is theoretically infinite under idealised conditions ($\dot{Q} \to 0$). Practically, k is finite but very large, with the exact value depending on the experimental conditions [80]. k of He-II under a range of conditions is given in Figure 2.9.

Conductive heat transfer in gases may also occur. In order to analyse this,

---

[5] See Section 2.4 for data for a range of materials

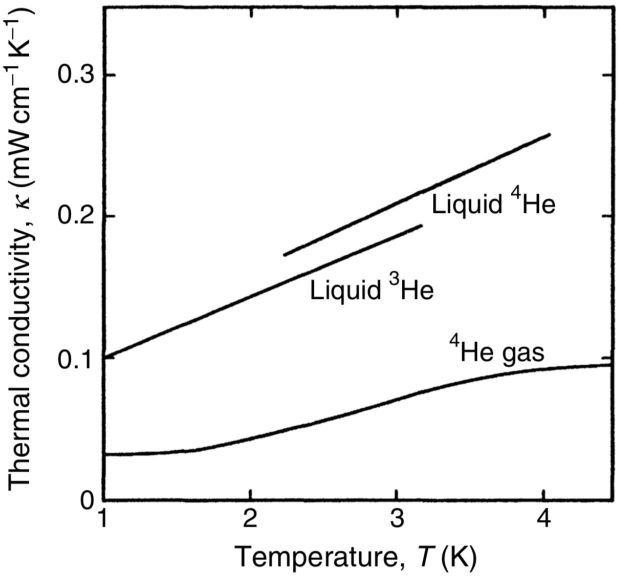

Figure 2.8: Thermal conductivities of gaseous and liquid helium [80]

it is first necessary to identify the regime of behaviour so as to consider the appropriate gas dynamics. Two distinct regimes exist, separated by a transition regime. The mean free path of the gas molecules λ may be given by

$$\lambda = \frac{RT}{\sqrt{2}\pi d^2 N_0 P} \tag{2.10}$$

where R is the universal gas constant ($= 8.31$ J·mol^{-1}·K^{-1}), and d is the molecule diameter. In the case that $\lambda \gg L$, where L is the distance between the two surfaces involved in the heat transfer, free molecular gas dynamics are applicable. Where $\lambda \ll L$, continuum flow dynamics are instead applicable [96].

The rate of heat transfer in the free molecular regime $\dot{Q}_{cond,free}$ is given by Kennard's law [96, 97] as

$$\dot{Q}_{cond,free} = A\alpha \left(\frac{\gamma+1}{\gamma-1}\right) \sqrt{\frac{R}{8\pi M}} \frac{\Delta T}{\sqrt{T}} P \tag{2.11}$$

where α is an accommodation coefficient, γ is the ratio of specific heat capacities and M is the molar mass of the gas. Typical values for α are given in Table 2.4.

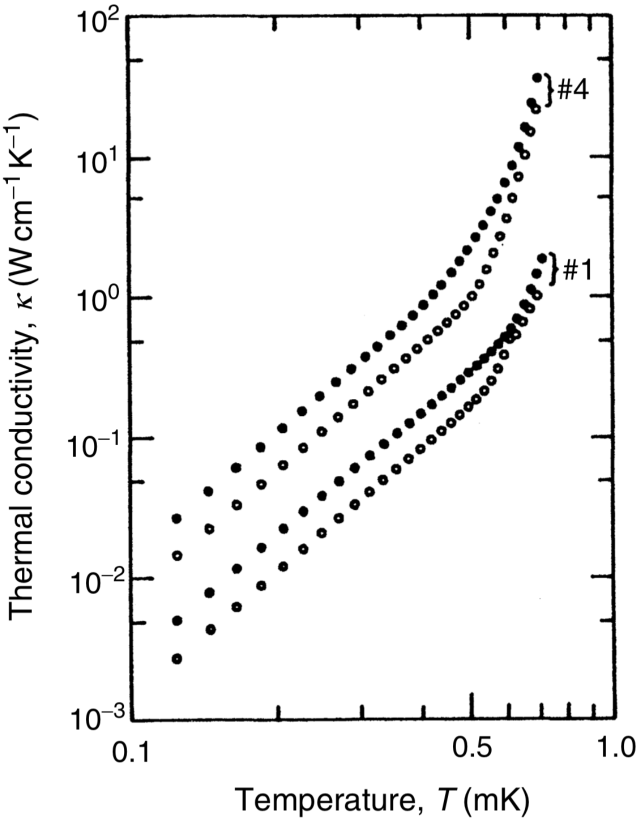

Figure 2.9: Thermal conductivity of superfluid helium under a range of experimental conditions [80]. The solid dots denote liquid at 2 bar and the open dots liquid at 20 bar. #1 denotes liquid in tubes of 1.38 mm diamater and #4 denotes liquid in tubes of 7.97 mm diameter.

Species	α
He	<0.5
Ar	~0.78
N_2	~0.78

Table 2.4: Accommodation coefficients for free molecular convective heat transfer. Data taken from [97].

Heat transfer of this type in the continuum regime is instead described by a Fourier law. Whilst not relevant to the systems described in Chapters 3, 4, and 5, the interested reader may find a detailed treatment in Reference [97].

2.3.2 Thermal Convection

In many wet cryostats, both forced and free convection of both liquids and gases provides useful heat transfer. However, this is not used in any of the dry cryostats described in Chapters 3, 4, and 5 (save for the case of the convective heat switches described in Chapter 3, where the specific theory of convection developed is discussed). Furthermore, the vacuum spaces of the cryostats described operate at sufficiently high vacuum so as to render any convective heat transfer negligible; convective heat transfer in the general sense is therefore not discussed further here. The interested reader is directed to Reference [82].

2.3.3 Thermal Radiation

A surface at a given (finite) temperature absorbs, reflects, and emits electromagnetic radiation. The spectrum of the emitted power for a blackbody is described by Planck's law, as discussed already in Section 1.1.1 in the context of the CMB. Integrating Planck's law with respect to frequency gives the Stefan-Boltzmann law

$$\dot{q}_{rad,bb} = \sigma T^4 \tag{2.12}$$

which gives the total hemispherical blackbody emissive power per unit area $\dot{q}_{rad,bb}$ at T, where σ is the Stefan-Boltzmann constant ($= 5.670 \times 10^{-8}$ W·m^{-2}·K^{-4}). The ratio of the power emitted by a real surface $\dot{q}_{rad}$ to $\dot{q}_{rad,bb}$ is the emissivity ε, hence

$$\dot{q}_{rad} = \varepsilon \sigma T^4 \tag{2.13}$$

Emissivities for a range of commonly used cryogenic materials are given in Figure 2.10.

Two real surfaces of areas A_1 and A_2 at temperatures T_1 and T_2 with emissivities ε_1 and ε_2 with a given relative orientation exchanging heat radiatively are

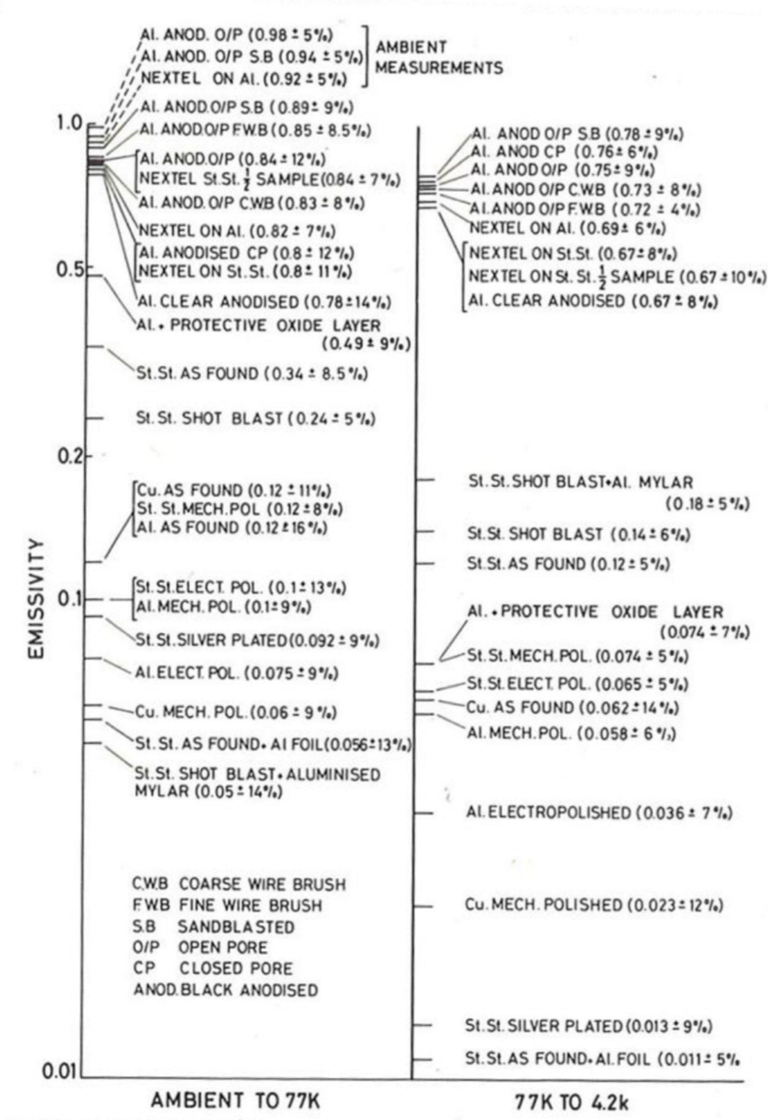

Figure 2.10: Emissivities for a range of commonly used materials [98]

shown in Figure 2.11.

It may be seen that the rate of heat exchange between the surfaces is simply the difference between the heat emitted from the first surface and absorbed by the second, and that emitted by the second surface and absorbed by the first. The general form is given by

$$\dot{q}_{rad,1-2} = \sigma \left(T_1^4 - T_2^4\right) / \left(\frac{1-\varepsilon_1}{\varepsilon_1 A_1} + \frac{1}{A_1 F_{12}} + \frac{1-\varepsilon_2}{\varepsilon_2 A_2} \right) \tag{2.14}$$

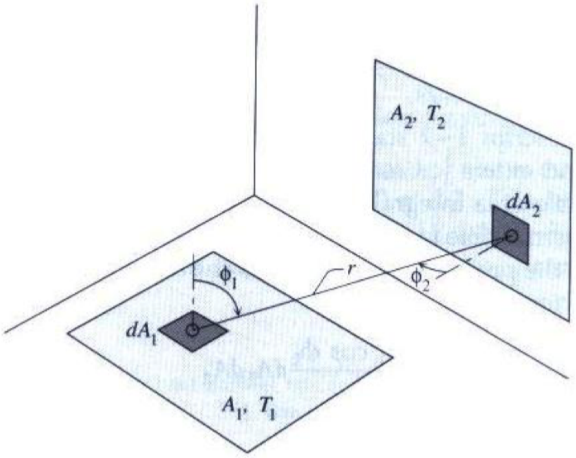

Figure 2.11: Radiative heat exchange between two surfaces [95]

where F_{12} is the "view factor", which is simply the fraction of the heat leaving the first surface that is intercepted by the second. Note the reciprocity relation

$$A_i F_{ij} = A_j F_{ji} \tag{2.15}$$

View factors may be calculated for a given geometry; in practice, view factors for many common geometries are available in the literature, see for instance Reference [99].

2.4 Material Properties at Low Temperatures

Table 2.5 gives a list of commonly used materials for cryogenic applications on the basis of their various material properties.

In cryostat design, it is vital to understand both the mechanical and thermal properties of any materials used. Furthermore, these properties can change significantly with temperature; this must of course be allowed for in the design.

Material	Typical uses
Austenitic stainless steels, e.g., 304/L, 316, 321	Low k components
Aluminum alloys e.g. 6061/3, 1100	High k components
Brass	Various, interface pieces
Copper e.g. OFHC, ETP	Very high k components
Fiber reinforced plastics, e.g., G-10 and G-11	Very low k components
Niobium and Titanium	Superconducting RF
Invar (Ni/Fe alloy)	Low α components
Indium	O-rings
Kapton and Mylar	Electrical insulation
Quartz	Vacuum windows

Table 2.5: Commonly used cryogenic materials

2.4.1 Thermal Properties

In order to calculate the thermal conduction through some medium as in Equation 2.9, the thermal conductivity k must be known. This is given as a function of temperature for many commonly used materials in Figure 2.12.

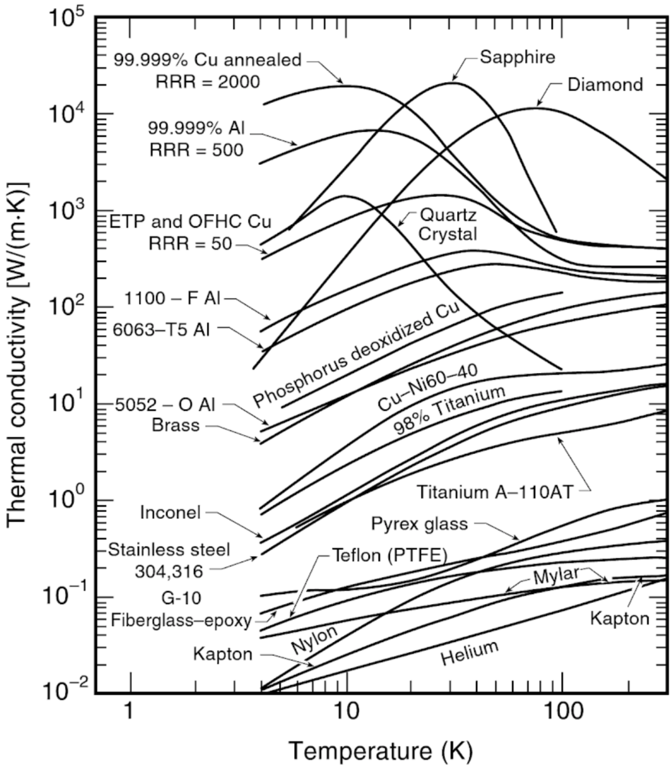

Figure 2.12: Thermal conductivities for a selection of materials [97]

In practice, it is useful to know the thermal conductivity integral $\int_{T_{cold}}^{T_{hot}} k\left(T\right) dT$. For convenience, these are given for some common materials in Table 2.6.

	20 K	80 K	290 K
OFHC copper	11000	60600	152000
DHP copper	395	5890	46100
Aluminium 1100	2740	23300	72100
Aluminium 2024	160	2420	22900
Stainless steel AISI 304	16.3	349	3060
G-10	2	18	153

Table 2.6: Thermal conductivity integrals (W/m) for selected materials between indicated temperatures and 4.2 K. Data from [70].

When calculating cooldown times, as described in Section 2.5, it is important to know the specific heat capacity of the various materials used which is a strong function of temperature, particularly <200 K. This data is shown for some common materials in Figure 2.13.

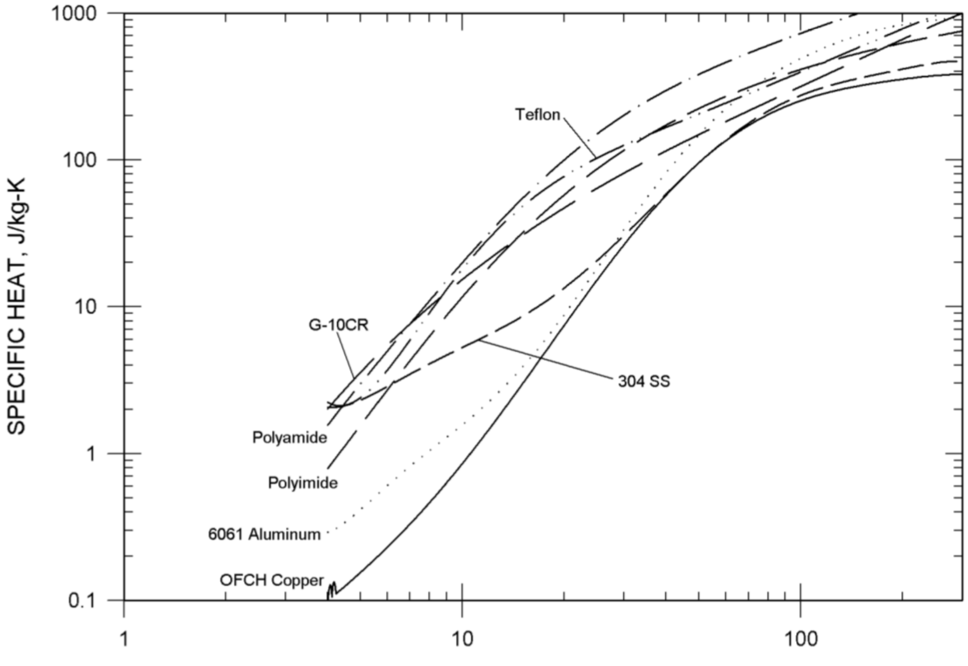

Figure 2.13: Specific heat capacities for a selection of materials [100]

Furthermore, Reference [100] gives a general equation for both thermal conductivity and specific heat capacity of the form

$$\log(k), \log(c_p) = a + b\log(T) + c\log(T)^2 + d\log(T)^3 + e\log(T)^4 + f\log(T)^5 + g\log(T)^6 + h\log(T)^7 + i\log(T)^8 \tag{2.16}$$

where the coefficients *a*-*i* are provided for a wide range of materials.

2.4.2 Mechanical Properties

The mechanical properties of materials also change with temperature, which must be considered during cryostat design.

The coefficient of linear thermal expansion α is defined as

$$\alpha = \frac{1}{L}\frac{dL}{dT} \tag{2.17}$$

where L is a given length measurement. The integral form (which, as for thermal conductivity, is the form most commonly seen in the literature) is then

$$\int_{T_{ref}}^{T} \alpha(T)\, dT = \frac{\Delta L}{L} \tag{2.18}$$

Figure 2.14 gives $\Delta L/L$ data as a function of temperature for a selection of materials ($T_{ref} = 300$ K). Note that the majority of the contraction occurs above 77 K.

In the elastic domain of deformation, the uniaxial stress σ ($= F/A$) is proportional to the strain ϵ ($= \Delta L/L$); the yield strength gives the limit to elastic deformation and generally increases with reducing temperature as shown in Figure 2.15.

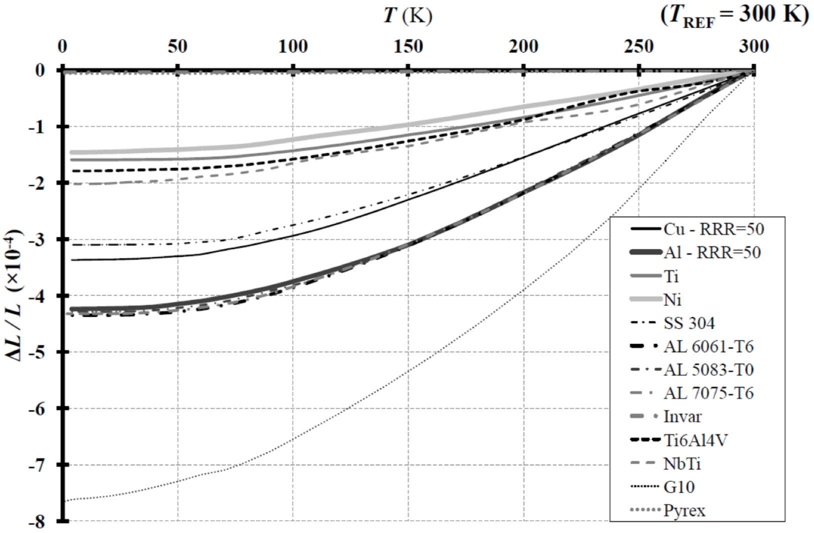

Figure 2.14: Thermal contraction as a function of temperature for a selection of materials [101]

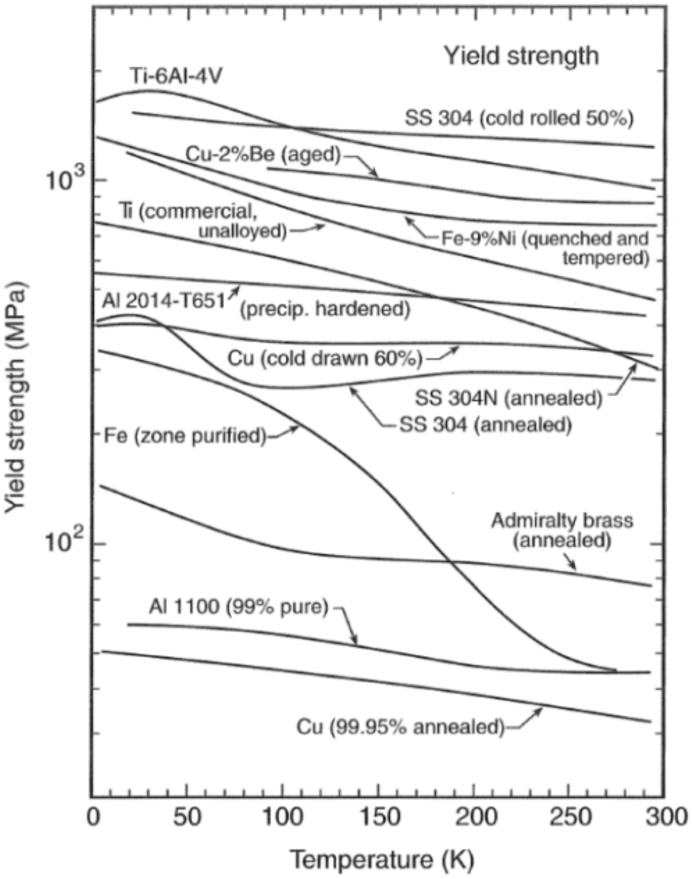

Figure 2.15: Yield strength of a selection of materials as a function of temperature [101]

2.4.3 Boundary and Kapitza Resistance

In any real case, the boundary between two media will not be in perfect thermal contact. Figure 2.16 illustrates this in the case of a solid-solid boundary, where imperfections in the two surfaces result in the constriction of flux lines and hence a thermal impedance R_c ($= \Delta T/\dot{Q}$).

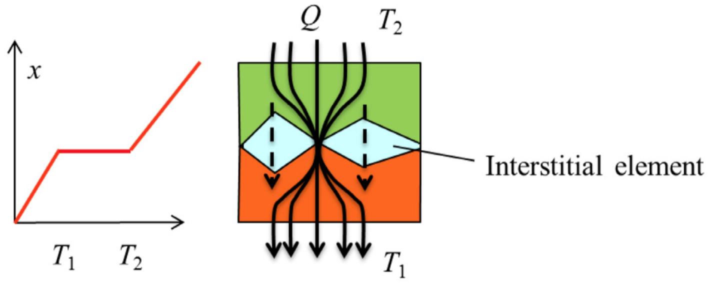

Figure 2.16: Thermal resistance for a solid-solid boundary [95]

Furthermore, scattering of phonons at the boundary (so-called Kapitza resistance R_K, see below) also contributes to the thermal impedence. R_c is strongly dependent on material combinations, surface cleanliness, compression force, and the presence (or lack thereof) of interstitial materials. Figure 2.17 gives thermal conductance ($= 1/R_c$) data for a range of solid-solid joints. The use of interstitial materials such as charged grease and indium, as well as various surface treatments, are commonly used to minimise R_c, especially for the lowest temperature applications.

R_K (i.e. that arising specifically from the boundary scattering of phonons) is of great importance in low temperature liquid helium applications. The temperature step that arises across a solid-superfluid helium boundary is shown in Figure 2.18.

This specific type of temperature discontinuity is well documented [102] and was first described by Kapitza in 1941 [103]. In order to most effectively communicate the helium temperature to the solid, this step must of course be reduced as far as possible. Due to the absence of free electrons in helium, heat transfer across the boundary occurs only via phonon transmission [80]. Acoustic mis-

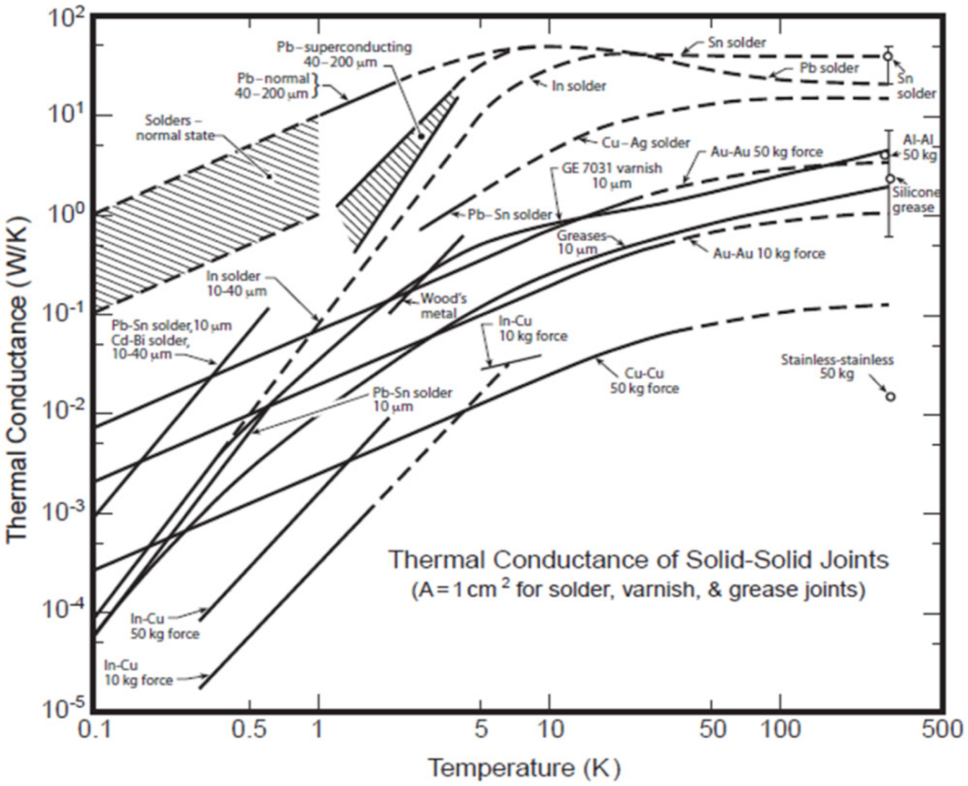

Figure 2.17: Thermal conductance data for solid-solid joints as a function of temperature [97]

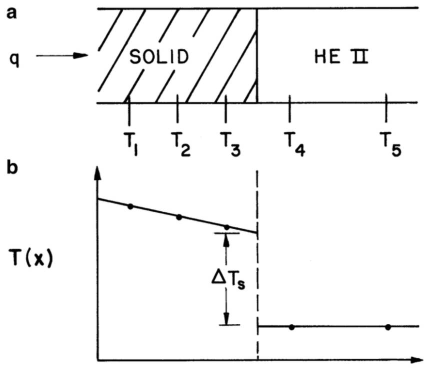

Figure 2.18: Schematic of Kapitza conductance experiment: (a) shows temperature sensors located in the vicinity of a solid-He interface and (b) shows the temperature profile [83]

match theory, developed primarily by Khalatnikov [104] and independently by Mazo and Onsager [105] describes the scattering by way of analogy to optics [80]. Hence, Snell's law may applied to the passage of transverse phonons in the helium towards the boundary

$$\frac{\sin \alpha_{He}}{\sin \alpha_s} = \frac{v_{He}}{v_s} \tag{2.19}$$

where α_{He}, α_s, v_{He} and v_s are the normal angles and phonon velocities in liquid helium and the solid respectively. There exists a critical angle α_c, beyond which phonons are not transmitted across the boundary into the solid, which is

$$\alpha_c = \arcsin \frac{v_{He}}{v_s} \tag{2.20}$$

This then defines, in three dimensions, a cone of transmission in terms of phonon velocities. For the typical phonon velocities in helium and copper (200 and 5000 ms^{-1} respectively [80]), a value of 3° is found for α_c. The fraction of phonons that are transmitted is then

$$f = \frac{2sin^2\left(\alpha_c\right)}{2\pi} = \frac{1}{2}\left(\frac{v_{He}}{v_s}\right)^2 \tag{2.21}$$

Furthermore, because of the difference in acoustic impedance Z, only a fraction described by the energy transmission coefficient t are transmitted as

$$t = \frac{4Z_{He}Z_s}{\left(Z_{He} + Z_s\right)^2} \tag{2.22}$$

The total fraction of phonons that are transmitted is therefore

$$ft = \frac{8\rho_{He}v_{He}^3}{\rho_s v_s} < 10^{-5} \tag{2.23}$$

The heat transfer per unit contact area is then

$$\dot{q} = \frac{1}{2} ft \left(\frac{E}{V}\right) v_{He} \tag{2.24}$$

where the energy density E/V is calculated by integrating the phonon spectrum for the thermal energy in the helium, which, for He-II, is described by Bose-

Einstein statistics [83]. The heat flux is then

$$\dot{q} = \frac{16\pi^3 k^4 \rho_h \nu_h}{15 h^3 \rho_s \nu_s^3} T^3 \Delta T \tag{2.25}$$

and hence

$$\Delta T = R_k \dot{q} \tag{2.26}$$

where

$$R_k = \frac{const.}{AT^3} \tag{2.27}$$

For a liquid helium-copper boundary, it has been shown experimentally [80] that this resistance is

$$R_K \approx \frac{0.025}{AT^3} \tag{2.28}$$

The T^{-3} dependence highlights the importance of this effect at the lowest temperatures. Typically, copper or silver sinter is used to maximise the effective contact area and hence minimise the temperature step across the boundary.

2.5 Cryostat Design

Cooling down to ∼4 K may be done using either wet or dry cryostat architectures, as shown in Figure 2.19.

Wet cryostats use baths of liquid cryogens to provide the desired temperature stages where the cooling is provided by the boil-off as in Equation 2.3; very high cooling powers may therefore be provided, as the bath will provide a thermal reservoir as long as the vapour pressure is maintained. These types of cryostats have a hold time dependent on the thermal loading and the initial quantity of cryogens before they must be refilled, which is a key operational concern. Avail-

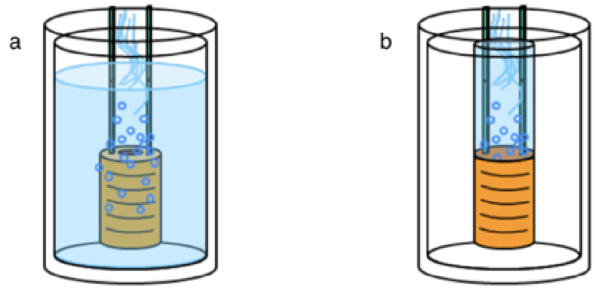

Direct cooling
Bath cooling

Indirect cooling
Bath cooling

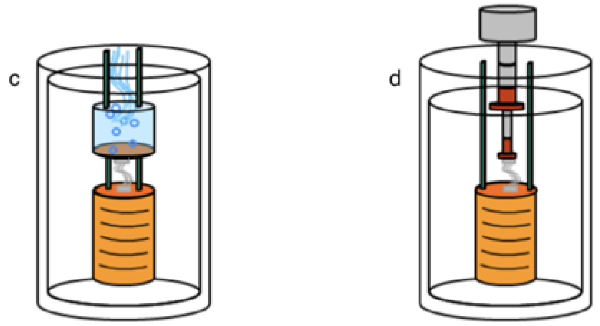

Indirect cooling
Bath as cold source

Indirect cooling
Cryocooler as cold source
Thermal link

Figure 2.19: Wet (a-c) and dry (d) cryostat architectures [95]

ability of cryogens is markedly different between a laboratory environment and a remote observing location. As such, all of the systems described in Chapters 3, 4, and 5 are instead based around dry architectures and hence wet systems are not discussed further here.

Dry (cryogen-free) cryostats provide cooling through the use of mechanical cryocoolers, most commonly two-stage Gifford-McMahon (GM) and Pulse-Tube (PTC) type coolers [106]. These types of coolers circulate helium gas in a closed cycle and therefore only require electrical power to produce refrigeration. Gas is compressed nearly isothermally at room temperature by the compressor (which may be water cooled) and supplied through a high pressure supply line to the cold head. Low pressure gas is returned from the cold head to the compressor through a return line. It may be seen in Figure 2.20 that a GM cold head is comprised of a cylindrical volume which may be alternately connected to the high- and low-pressure lines. Within the cylinder is a displacer containing a regenerator which may be actuated up and down by an inverter-controlled drive motor.

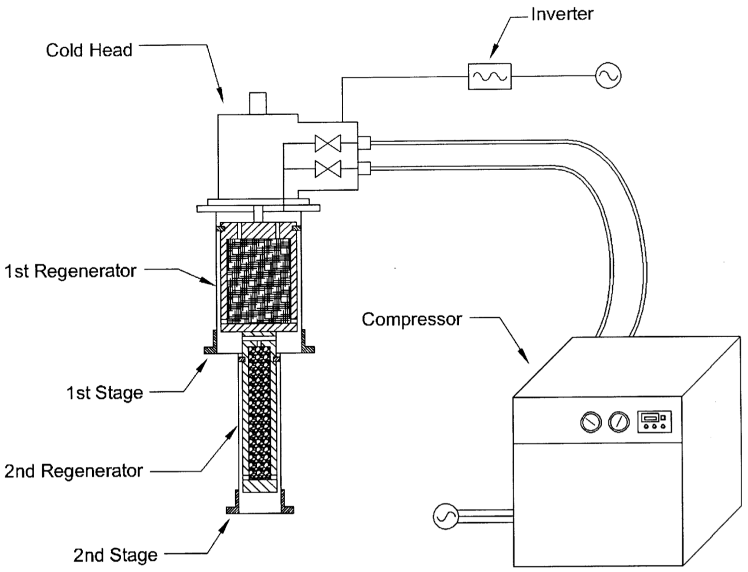

Figure 2.20: Gifford-McMahon cryocooler schematic [107]

GM coolers operate in an isobaric-isothermal Ericsson cycle [81]. This is achieved by synchronising the operation of the rotary valve with the regenerator as follows:

(i) With the displacer at the bottom of the cold head, the rotary valve is opened to the high-pressure side. High-pressure gas fills the space above the displacer and the regenerator at ambient temperature.

(ii) With the valve to the high-pressure side still open, the displacer is moved to the top of the cold head. The gas passes through the regenerator matrix where it exchanges heat and is cooled isobarically. The gas fills the space below the displacer at low temperature.

(iii) With the displacer in its upper position, the rotary valve is closed to the high-pressure side and opened to the low-pressure side. The gas within the coldhead (both in the regenerator and the cold space) expands, taking in heat from the environment surrounding the cold side (i.e., producing the useful heat lift).

(iv) With the rotary valve still open to the low-pressure side, the displacer is moved back to the bottom of the cold head. The gas passes back through the regenerator matrix where it is warmed isobarically and fills the space above the displacer at ambient temperature

It can be seen that by operating in this cycle continuously, cooling may be provided indefinitely. The cycle typically operates at ∼1 Hz. It may also be seen that this can be easily extended to a double-stage cooler as in Figure 2.20 where an intermediate cooling stage exists halfway down the coldhead and the displacer is a single component with two discrete regenerators.

PTCs operate with a similar cycle. Various architectures are used, all avoiding the use of cold moving parts. As shown in Figure 2.21, PTCs generally consist of three subsystems:

- A pressure-wave generating subsystem; this may be a compressor and a rotary valve to the cold head as in the case of a GM cooler
- A first tube containing a stationary regenerator with the warm end connected to the incoming gas and the cold end connected to the cold end of a second tube
- A second (hollow) tube, with its warm end connected via a flow impedance to a buffer volume

The pressure-wave generating system generates oscillations causing piston-like flow of the gas through the system. The impedance gives a phase difference between the pressure wave and the flow velocity, supporting cooling through an Ericsson cycle as described for a GM cooler. This has the advantage of reducing

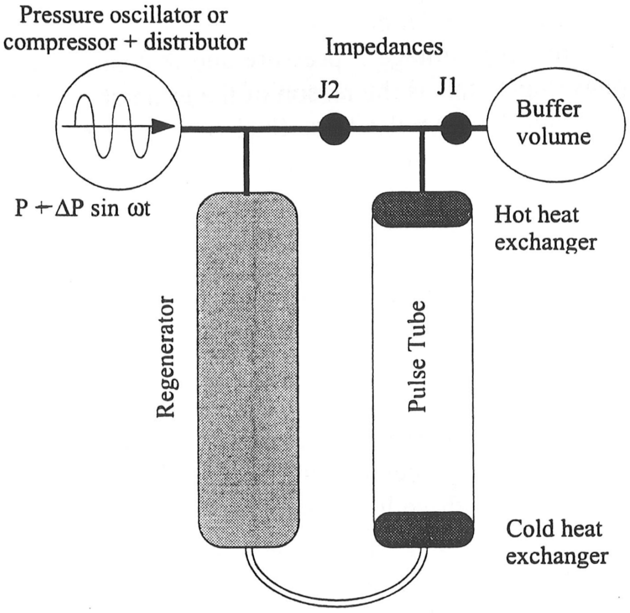

Figure 2.21: Pulse-tube cryocooler schematic [81]

vibration at the cold stages relative to a GM, at the expense of some cooling power. For a more detailed review of mechanical coolers, the interested reader is directed to Reference [108].

As cryocooler technology has developed and matured over the past several decades, increasingly lower base temperatures and cooling powers have been demonstrated, principally due to advances in regenerator material technologies [106]. Figure 2.22 gives the capacity map which shows the first and second stage cooling powers for a typical commercially available GM cooler[6].

A general cryostat design[7] based around either one or several mechanical coolers may therefore be comprised of an outer vacuum chamber at ambient temperature (~300 K) and concentric 40 K and 4 K stages cooled by the first and second cryocooler stages respectively.

The vacuum chamber is typically evacuated to $<10^{-4}$ mbar using rotary and then turbomolecular vacuum pumps, in order to prevent convective loading and minimise residual gas conduction (see Section 2.3). Note that when the cryostat is

---

[6] `http://www.shicryogenics.com`

[7] For a far more detailed review, see Reference [81]

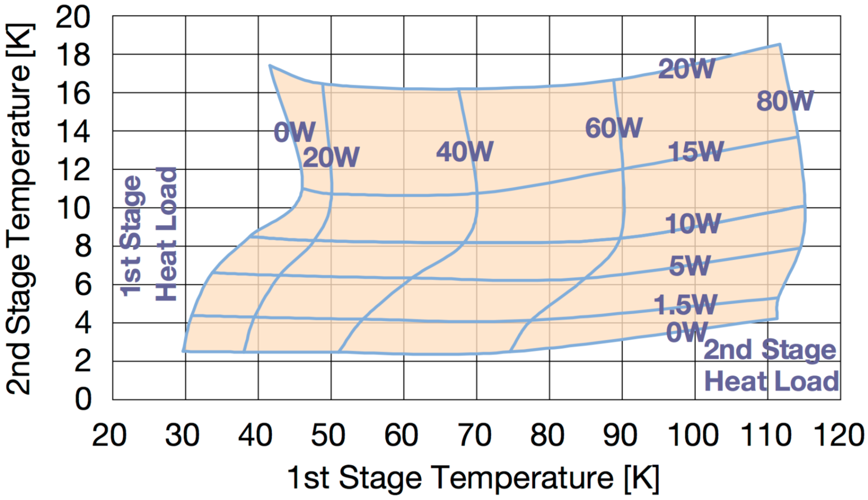

Figure 2.22: Capacity map for a Sumitomo RDK-415D GM cryocooler. Image courtesy: SHI Cryogenics Group.

cold, the vacuum pressure is frequently much better than this due to cryopumping by cold surfaces. The vacuum chamber must therefore be designed to deal with the pressure differential to atmosphere, as well as whatever mechanical loads arise from the cold stage supports, whilst maintaining the required alignments with an appropriate factor of safety. It must also allow for whatever feedthroughs are demanded by the experiment (thermometry, instrumentation, optical windows, etc.). Mechanical finite element analysis (FEA) should be used to study the behaviour of a given design, along with analytical calculations to verify.

The 40 K stage typically comprises a low-ε shield to intercept thermal radiation and provide a thermal sink for physical connections to the colder stages, as it is thermodynamically most efficient to intercept heat leaks at the warmest temperature practical. ε is typically minimised through the use of highly polished copper or aluminium (see Figure 2.10), or more commonly multilayer insulation (MLI).

MLI blankets consist of sheets of highly reflective layers, typically aluminized mylar, stacked alternately with insulating spacers. The mylar sheets then are floating temperature screens between T_1 and T_2. A simplified thermal model [99] considers contributions from radiation and residual solid conduction across the blanket thickness as

$$\dot{q}_{MLI} = \left[\frac{\beta}{N+1} \cdot \left(T_1^4 - T_2^4\right)\right] + \left[\frac{\alpha}{N+1} \cdot \frac{T_1 + T_2}{2} \cdot (T_1 - T_2)\right] \tag{2.29}$$

where α and β are coefficients that may be found experimentally. In the case of the MLI used for the LHC dipole cryostats, $\alpha = 1.401 \times 10^{-4}$ and $\beta = 3.741 \times 10^{-9}$. It may be considered from this model that there exists an optimal packing density for MLI; this has been found experimentally to be between 15 and 20 layers/cm [99].

As may be seen from Equation 2.9, the conductive thermal loading via the supports and other connections (e.g. instrumentation wiring) to the cold stage(s) may be minimised by maximising length and minimising cross sectional area of connections.

The 4 K stage is the coldest stage provided by the crycooler, where the main experimental apparatus may be located. If cooling to lower temperatures (see Section 2.8), it may be used as thermal bath, as well as supporting a second radiation shield and thermal sinking for connections to the colder stage(s).

2.6 Thermal Modelling

In order to better design cryogenic systems, thermal modelling can be a powerful tool. Lumped element modelling broadly is an approach which may be used to model a given spatially-distributed thermal, mechanical, or electrical system as a set of discrete elements that approximate the behaviour of the system. One example of this is thermal finite element analysis, for which there are several commercially-available packages including ANSYS[8], COMSOL Mul-

---

[8] `https://www.ansys.com/`

tiphysics[9], and ESATAN-TMS[10].

However, in modelling dry systems, it is presently very challenging to apply cooling powers which are a function of the temperature at multiple points in the system, such as in the case of a two-stage mechanical cryocooler. Therefore, a code has been written in Python to simulate the transient thermal behaviour of a typical PTC-cooled cryostat. The code is presented in full in Appendix A.1 and has been written so as to be easily extended to more complex cryostat designs by simply adding further coupled elements.

The model firstly defines the initial temperature for each of the lumped elements. It then defines the heat capacity as a function of temperature (see Section 2.4.1). The assumption for each element is that the rate of heat transfer inside the element is much greater than rate of heat transfer across the boundary to other elements. Heat transfer couplings (conductive and radiative) are then defined between each pair of elements, using the equations given in Section 2.3. For the crycooler, cooling powers to the first and second stage elements are defined as a function of the temperature of both elements, by interpolating from the capacity map (see Section 2.5).

The model has a defined timestep. It loops so as to calculate the heat transferred in each coupling during said timestep, finding the net heat transfer for each element, calculating the new temperature from the (temperature-dependent) heat capacity, updating all of the temperatures, and then moving on in the timestep. The loop terminates when the defined end time is reached, although it could just as easily be set to terminate when some other condition is met (for example, a steady state condition on one or more elements).

The simulated cooldown for the cryostat described above is given in Fig. 2.23 below and is in good agreement with experiment, showing a cooldown time from room temperature of ~4.5 hours.

---

[9] `https://www.comsol.com/`

[10] `https://esatan-tms.com/`

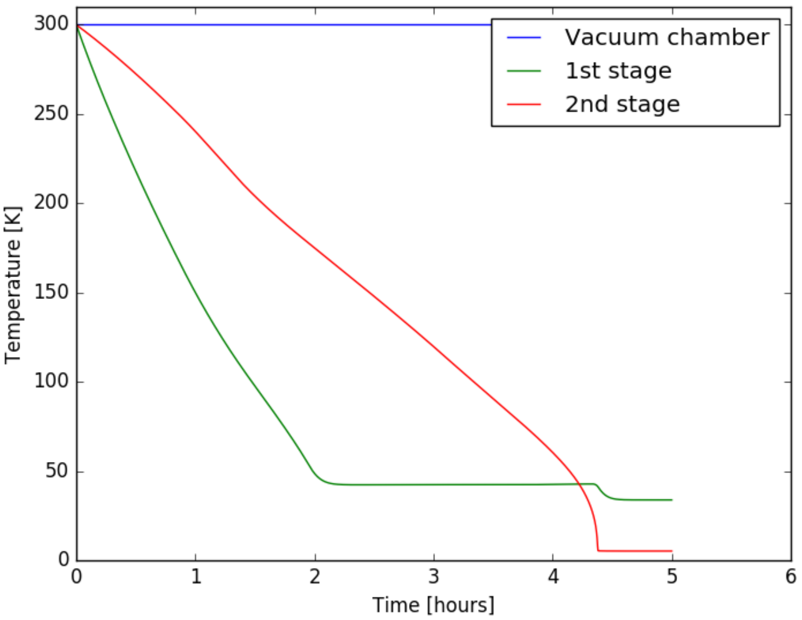

Figure 2.23: Simulated cooldown of a medium-sized pulse-tube cooled cryostat

There are, however, limitations to such a model. Firstly, the model approximates continuum behaviour by discretising in both time and space. The model should have a suitably small timestep and suitably fine geometric discretisation such that the solution given is suitably accurate. In practice, this may be done by reducing the timestep and increasing the number of elements until the solution does not change (relative to the level of precision required in the result). Furthermore, it has been the author's experience that the effects of thermal boundary resistance between components (e.g., that of a bolted joint, see Section 2.4.3) may be very difficult to capture. As such, great care must be taken when interpreting these types of results; any thermal model should always be validated with respect to experimental data and should be used as a guide in design only.

2.7 Low Temperature Thermometry

A range of thermometry technologies are used in low temperature work, and an appropriate selection must be made on the basis of the required resolution,

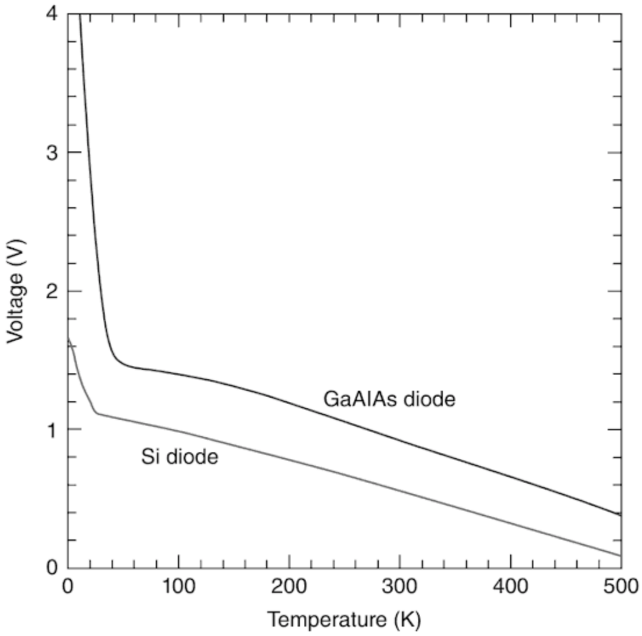

Figure 2.24: Typical forward voltages for diode thermometers under an excitation of 10μA [109]

temperature range, stability, and power dissipation. Most commonly used are commercially available (as well as home-made) diode and resistance temperature detectors (RTDs).

Si (and, less commonly, GaAIAs) diodes may be used as thermometers as, under a constant current excitation, the forward voltage varies with temperature as shown in Figure 2.24. Si diodes from manufacturers such as Lake Shore Cryotronics[11] can have sufficient repeatability so as to be accurate to within 0.25 K from a standard calibration curve. Diode thermometers are typically useful from room temperature down to 1.5 K.

RTDs work by simply measuring the resistance, which is a strong function of temperature for some suitable sensor. There is no reliable fundamental a priori physical law for $R(T)$ and hence sensors must be calibrated. However, generic forms are followed for a given sensor type. RTDs may use either positive coefficient metallic resistors (e.g., Platinum, Rhodium Iron), or negative coefficient

---

[11] `https://www.lakeshore.com/`

semi-conductor like resistors (e.g., Ruthenium Oxide, Cernox, Germanium), as shown in Figure 2.25.

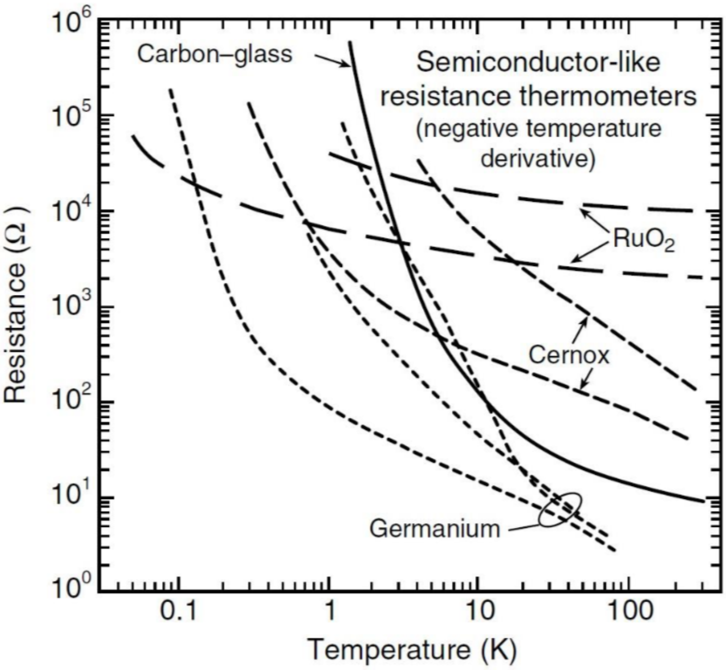

Figure 2.25: Resistance temperature curves for a range of RTDs [109]

RTDs are read out using AC resistance bridges for high-resolution, low-power measurements. Furthermore, selectable current excitation levels are used to minimise self-heating at lower temperatures (where R is high) and loss of resolution at higher temperatures (where R is low). Commercially available RTDs such as the Cernox range from Lake Shore may be used down to 100 mK with a calibrated accuracy of ±5 mK.

In addition to self-heating, the temperature of a sensor may be higher then the experiment due to heat leak through the wiring and poor thermal contact with the mounting position. In order to minimise this, the sensor packaging should be designed so as to provide excellent thermal contact and heat sinking of the wires. An example of a home-packaged Cernox thermometer is shown in Figure 2.26.

In order not to measure the resistance drop across the sensor leads, 4-wire measurements may be used where the excitation current is applied across one

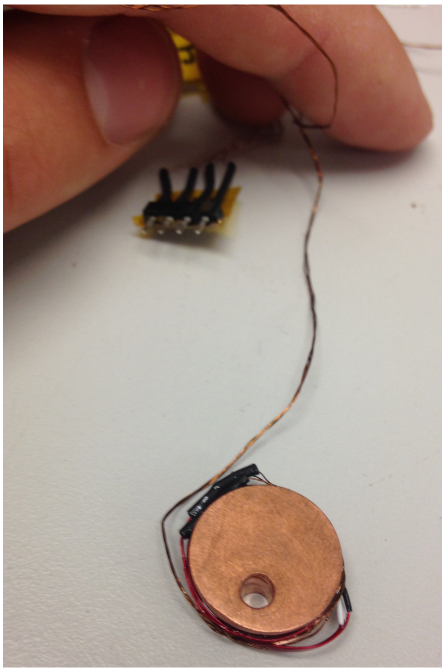

Figure 2.26: Cernox packaged in homemade copper bobbin with GE varnish for thermal sinking of wires

wire pair (I+, I-) and the voltage drop is measured across the second wire pair (V+, V-). Sensor leads are also typically arranged as twisted pairs; this aids in both cancelling microphony and shielding from magnetic interference.

2.8 Cooling Below 4 K

Through the use of mechanical cryocoolers, cooling experiments to 4 K has become routine for a variety of laboratory applications. Below this temperature, as is required for a number of forthcoming astronomical receivers including those discussed in Chapter 1, cooling becomes more far more challenging.

In order to reach temperatures <1 K, three techniques [80] are in principle available: adiabatic demagnetisation refrigeration (ADR), sorption cooling of ^{4}He or ^{3}He, and dilution refrigeration of ^{3}He in ^{4}He.

ADRs have been used successfully to reach 50 mK for a number of astrophysical applications. However, as fields of up to 5 T are typically required [110], this method presents significant challenges for integration with TES bolometer arrays due to their sensitivity to magnetic fields.

Sorption cooling of ^{4}He and ^{3}He may be used to reach temperatures of $\sim$800 and $\sim$320 mK respectively [80]. It has further been shown that the minimum temperature of a ^{3}He cooler may be improved upon through the use of a ^{4}He precooler [111]. However, systems developed for past receivers have typically not had a heat lift performance on the order of that needed for large arrays.

In order to reach temperatures $<$300 mK without the use of magnetic fields, dilution refrigeration may be used. 50 mK is routinely reached in laboratory environments [80]. However, conventional diluters require external gas handling systems and mechanical pumps; the external connections, high power consumption, mechanical reliability and vibrations make their use highly undesirable for operation with telescope focal planes. Furthermore, the use of conventional diluters may be prohibitively expensive, complex and slow-turnaround for rapid-feedback detector testing during receiver development.

Given the sub-Kelvin regime in which large sections of the forthcoming CMB polarization observatories will operate, a range of systems have been developed which are described in the following chapters.

Chapter 3

The QUBIC Cryogenic Receiver

QUBIC[1], the QU Bolometric Interferometer for Cosmology [75, 112, 113], is a forthcoming instrument which will directly target the CMB B-mode polarization anisotropy at intermediate angular scales ($30 < \ell < 200$). As opposed to direct imaging of the microwave sky (see Chapters 4 and 5), QUBIC exploits instead the technique of bolometric interferometry.

The receiver will operate a cold Fizeau interferometer, which requires complex optical stages at 40 K, 4 K, and 1 K, and a TES bolometer array at 350 mK. The cryostat uses two pulse tube coolers, a novel ^{4}He sorption cooler and a double-stage ^{3}He/^{4}He sorption cooler to provide cooling to these temperatures. Given the size and complexity of the receiver cryostat (detailed in the Section 3.1), extensive modelling and thermal analysis has been required to support the thermal and mechanical design, as well as laboratory cryogenic testing of various subsystems. Additionally, in view of the size of the 1 K box and level of thermal isolation, significant efforts have been devoted to developing a precooling strategy to support reasonable cooldown times for both laboratory testing and deployment of the receiver.

As well as contributing to the cryogenic design, experimental testing, and com-

---

[1] The full collaboration list and details of supporting funding agencies are available at `http://qubic.in2p3.fr/`

missioning of the receiver generally, the author has been responsible specifically for the development of the 1 K optics box cooler, testing and characterisation of the 350 mK detector stage cooler, heat switch design and development, and integration of these systems with the receiver cryostat.

3.1 Science Goals and Instrument Architecture

As discussed in Chapter 1, the primordial B-mode signal is exceptionally weak. As such, high sensitivity detectors are required, as well as strong control of instrumental systematic effects that could potentially induce polarization leakage from the relatively large E-signal into B, and high-confidence foreground disentanglement. QUBIC has been designed to address these challenges with a novel approach, namely bolometric interferometry [114] using a Fizeau interferometer as shown in Figure 3.1.

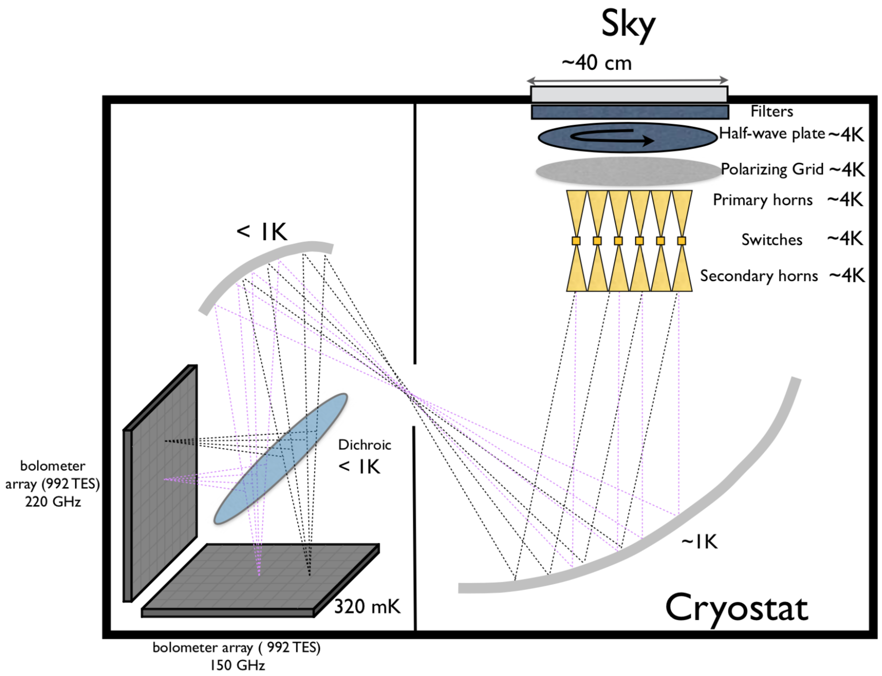

Figure 3.1: QUBIC instrument schematic [112]

The signal from the sky enters the cryostat vacuum through a 40 cm clear aperture window in front of a series of thermal filters. The polarization is then modulated by a cold stepped half-wave plate[2] (HWP) at 4 K. One polarization state is then selected by a polarizing grid, also at 4 K. An array of 400 back-to-back horns then collects and re-images the radiation [118]. The horn array is composed of two blocks of 400 horns each, placed back-to-back with interstitial switches that can open or close the optical path to the radiation; this allows for the self-calibration technique which is based on comparing redundant baselines produced by the outputs of equally spaced pairs of horns[3] [119]. The radiation is reimaged onto a dual-mirror optical combiner at 1 K [118] that sums all of the signals picked up by the sky-side horns onto the TES detector stage at 350 mK. QUBIC is therefore able to combine the background-limited sensitivity of TES with the control of systematics allowed by the observation of interference fringe patterns [112, 119].

The full instrument design, based on this architecture [112], is shown in section-view in Figure 3.2. The cryostat measures 1.4 m in diameter and 1.55 m in height; when the forebaffle cone is mounted around the window, the total height will be 1.9 m and the total instrument mass will be 800 kg.

Having been validated individually at several of the collaborating institutions, all of the subsystems were shipped to the Laboratoire Astroparticule et Cosmologie (APC) for integration and testing [113]. Receiver integration is planned in two stages: the first with a reduced number of TES operating at 150 GHz (referred to as the technological demonstrator, TD) and then an upgrade to the full focal plane of 2048 TES (the full instrument, FI), before deployment to the Alto Chorrillos site in 2020.

---

[2] HWPs are composed of a birefringent substrate which rotate the incident polarization signal [115, 116, 117]

[3] When operating in the self-calibration mode, QUBIC will successively shut pairs of horns whilst observing a polarized calibration source. The signals measured by each individual pair of horns can then be reconstructed and compared. Redundant baselines correspond to the same mode and therefore any difference in the measured signals can result only from instrumental systematic effects and photon noise. The method described in Reference [119] can then be used to reconstruct the synthesized beam and improve map-making, reducing polarization leakage.

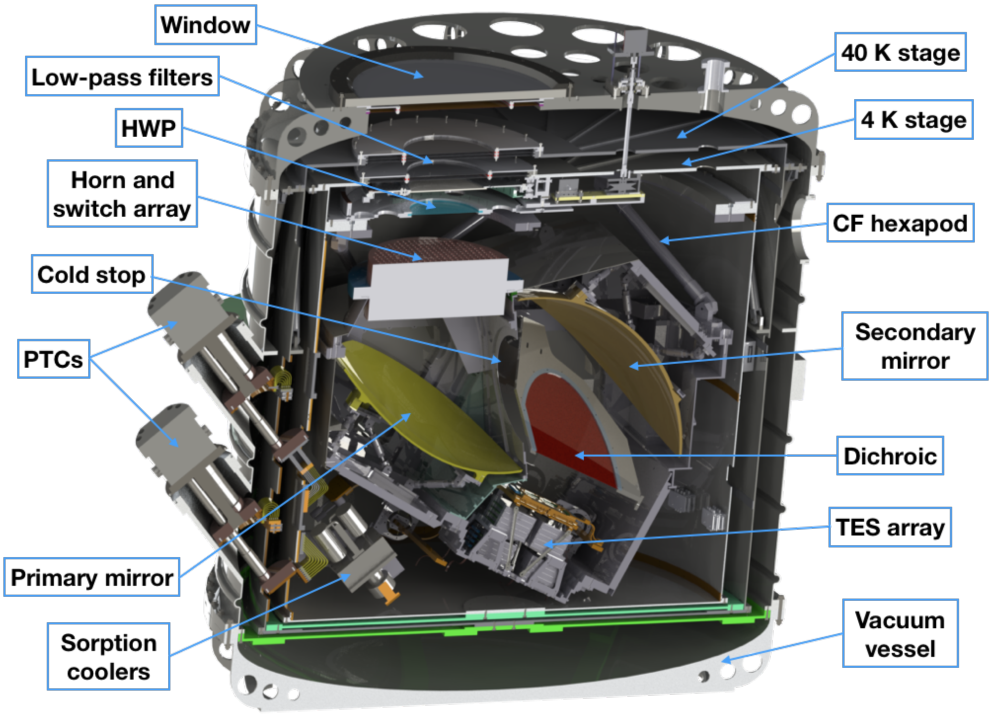

Figure 3.2: QUBIC receiver CAD model; the cryostat measures 1.4 m in diameter and 1.55 m in height. Image courtesy: G. D'Alessandro.

Instrument forecasting has shown that the first QUBIC module will be able to constrain the tensor-to-scalar ratio with a projected uncertainty of $\sigma(r) = 0.01$ after a two-year survey [112, 120]. Further modules could be added in the future to increase the sensitivity and frequency coverage of the instrument.

3.2 Vacuum Chamber, 40 K and 4 K Stages

Given the thermal requirements for the subsystems outlined in Section 3.1, the cryostat design is based on relatively low mass 40 K and 4 K stages with a large and complex 1 K stage and a subsequent very low mass 350 mK stage.

In order to house all of the optical elements described in Section 3.1 (see especially Figure 3.2), a large (order of 1 m^3) vacuum chamber is required.

The shape and structure of the jacket have been optimised for withstanding the stress of atmospheric pressure outside the cryostat. The structure is a vertical cylinder with top and bottom bulkheads, fabricated from aluminium alloy sheets, as shown in Figure 3.3. The cylinder is roll-bent and welded, with reinforcing ribs. The shell has diameter of 1.4 m and height of 1.55 m. Buna-N o-ring seals are used to hold the vacuum.

The clear aperture optical window on the top bulkhead (see Figure 3.2) is fabricated from ultra high molecular weight (UHMW) polyethylene (PE). A cylindrical slab (560 mm diameter and 20 mm thick) of PE has been used to meet the structural requirement whilst providing excellent mm-wave transmission [121].

The first cold stage is a 40 K shield which intercepts radiative loading from the vacuum chamber at 300 K. This stage also supports low-pass thermal filters as described in Section 3.1. The shield is fabricated from aluminium and is wrapped in MLI to reduce the effective emmissivity [122] (see Section 2.3.3). Copper strips are bolted to the aluminium to help improve the uniformity of the temperature distribution in the shields. Fibreglass tubes arranged in a hexapod configuration are used to mount the shield off the vacuum chamber. Figure 3.3 shows the 40 K shield being mounted by the group at Università di Roma La Sapienza.

The next temperature stage is a 4 K shield, which is of a similar construction and mounted concentrically inside the 40 K shield. A second hexapod is used to mount the 4 K shield off the 40 K stage to minimise parasitic conductive loading (see Section 2.3.1).

Behind the window, a series of single-layer metal-mesh element low-pass filters are stacked at 300 K, 40 K, and 4 K, to reduce the thermal radiative loading to the cold stages through the optical chain by sequentially rejecting short wavelength radiation.

Cooling of the 40 K and 4 K stages is provided by two Sumitomo RP-082B2S[4] pulse tube cryocoolers (PTCs) operating in parallel. Each cooler has a nominal capacity of 0.9 W at 4.2 K and 35 W at 45 K. Copper straps between the PTC

---

[4] `http://www.shicryogenics.com`

Figure 3.3: 40 K shield mounting in cryostat. Image courtesy: S. Masi.

heads and the shields allow for differential thermal contraction during cooldown.

Thermal models of the cryostat give an estimated loading of 0.1 W on the 4 K stage and 16 W on the 40 K stage; as such, operation with a single PTC is possible. However, two PTCs are used in order to both reduce the cooldown time (see below and Section 3.4) and to accept the large intermittent loading associated with recycling the 1 K and 350 mK coolers (see Sections 3.5 and 3.7).

As shown in Figures 3.2 and 3.4, the longitudinal axes of the two PTCs are tilted by 40° with respect to the vertical; this allows observations with elevations between 30° and 70° whilst maintaining the PTC heads within 20° of vertical where cooling performance is maximised.

Initial cooldown testing of the cryostat with the 40 K and 4 K shields mounted has been carried out in Roma. This testing was done to validate the integrity of the vacuum jacket and the performance of the PTCs; both have been successful. The measured cooldown time was ∼72 hours, with a final temperature of the 4 K

Figure 3.4: Closed cryostat under test. Image courtesy: S. Masi.

stage of 3.1±0.5 K, as shown in Figure 3.5.

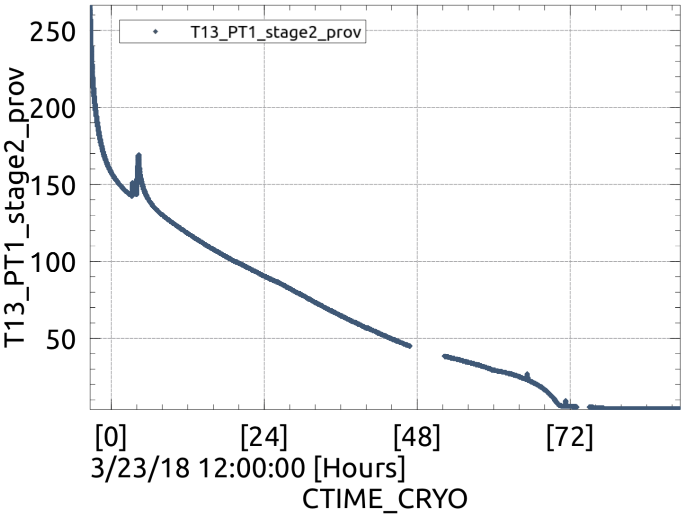

Figure 3.5: Cooldown of the 4 K stage during test in Roma; spikes are due to periods where the two PTCs have been switched off to switch from mains power to UPS. Figure courtesy: S. Masi.

As well as the radiation shield, the 4 K stage also supports further low-pass filters, the HWP, and horn array.

The HWP used is a broadband metal mesh design [123], 30 cm in diameter. In order to step the HWP, a cryogenic rotation mechanism is needed. The mechanism designed for QUBIC inherits several of the solutions developed for the PILOT balloon-borne instrument successfully flown by CNES in 2015 and 2017 [124]. The HWP is rotated by a stepper motor mounted outside the vacuum chamber (at 300 K). Rotation is transmitted through the jacket by means of a magnetic joint to a fibreglass axle. This axle then runs down to the 4 K stage and drives a Kevlar belt which is tensioned by a spring-loaded capstan pulley. The HWP is mounted inside a support ring which has a groove for the Kevlar belt. The mounting of the HWP uses a custom block in order to reduce the differential thermal contraction between the support ring and the HWP. An optical encoder records the position of the ring. The rotator is shown under test in the cryostat in Roma in Figure 3.6.

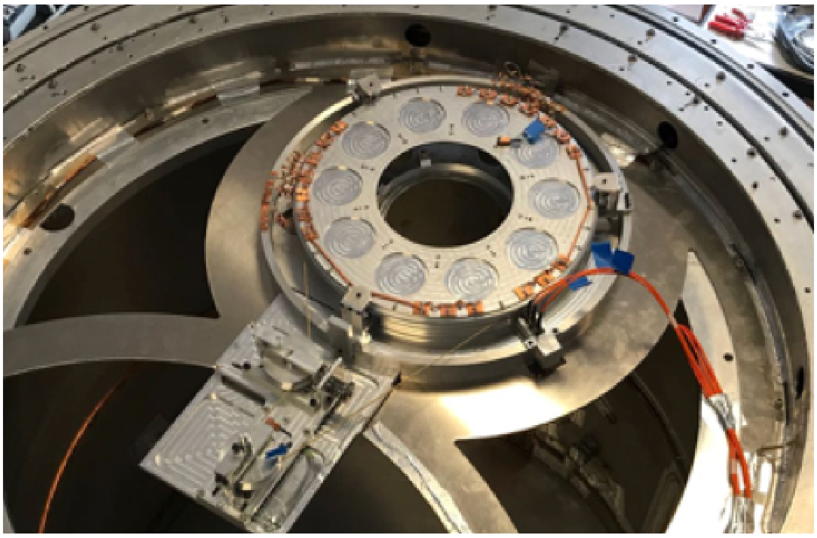

Figure 3.6: HWP rotator mounted in cryostat. Image courtesy: G. D'Alessandro.

Mounted below the HWP are a photolithographed polarizing grid and the array of 400 back-to-back corrugated horns. One block of the horn array is shown during assembly at the Università degli Studi di Milano-Bicocca in Figure 3.7.

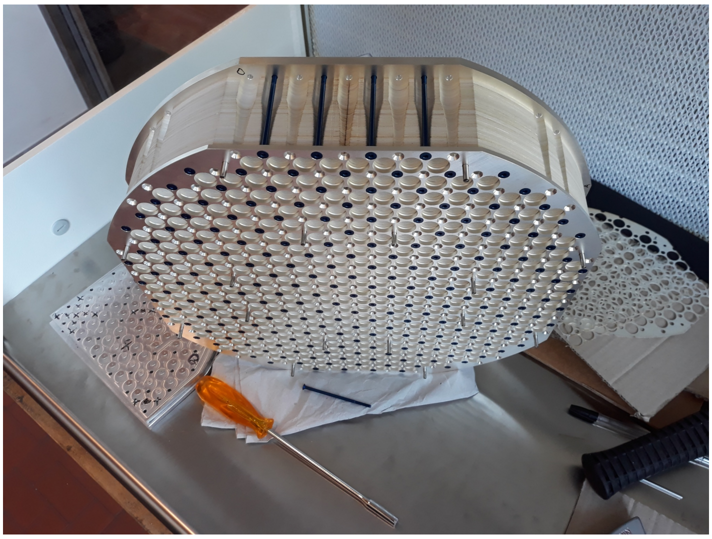

Figure 3.7: One block of 400 horn module. Image courtesy: M. Zannoni.

Having completed validation testing, both the cryostat and these subsystems were shipped to the Laboratoire Astroparticule et Cosmologie (APC) at Université Paris Diderot for integration and testing.

3.3 1 K Optics Box

Given the requirements for a number of optical elements to be operated at 1 K (see Section 3.1), a 1 K stage is mounted off the 4 K stage described above. This stage includes the 1 K optics box, as well as precooling heat switches for the box, a ^{4}He 1 K cooler and an isolation switch for the cooler; these subsystems are described in Sections 3.4, 3.5, and 3.6 respectively.

The 1 K optics box contains the primary and secondary mirrors (M1 and M2) for the optical combiner, the cold stop, dichroic and focal plane assembly. The CAD model is shown in Figures 3.8 and 3.9.

The mirrors are designed at their final temperature and machined in aluminium so as to reach their desired geometries after thermal contraction down

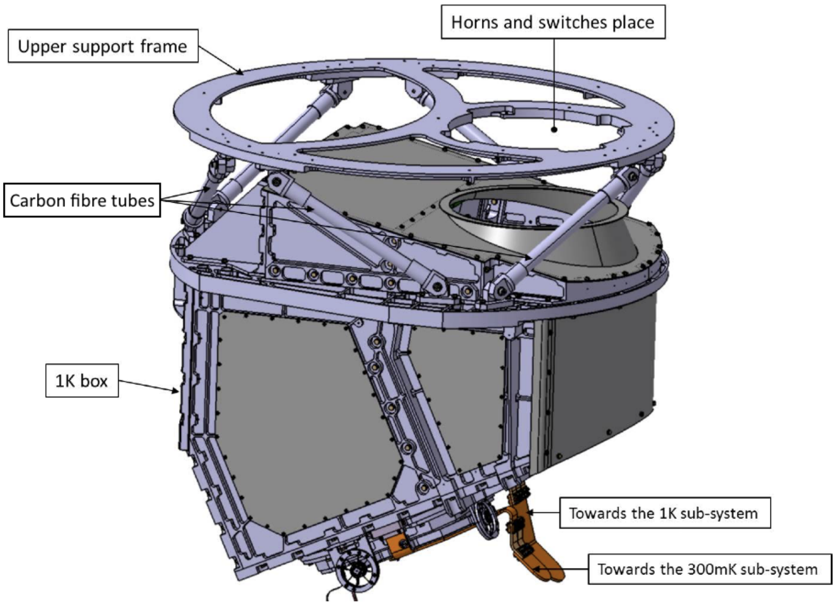

Figure 3.8: 1 K optics box CAD. Image courtesy: L. Grandsire

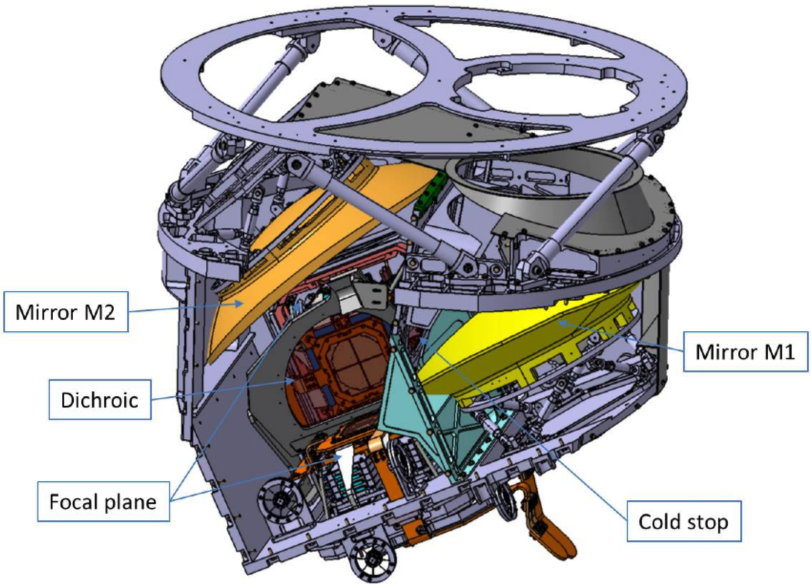

Figure 3.9: 1 K optics box CAD (section view). Image courtesy: L. Grandsire

to 1 K. The purpose of the optics box is to provide both the required thermal environment and mechanical support/alignment for the optics. Furthermore, it provides thermal shielding at 1 K for the 350 mK stage (see Section 3.7).

The 1 K box is mounted from the 4 K stage as shown in Figure 3.8. A hexapod of carbon fibre tie rods is used to meet the mechanical requirements whilst minimising parasitic conductive loading. An image of the assembled rods is shown in Figure 3.10. In order to validate the thermal and mechanical performance of the tie rods, a number of tests were carried out by the APC group at CEA Saclay. The measured properties are given in Table 3.1. These measurements were used to calculate the loading through the hexapod and are reported along with additional sources of parasitic loading in Table 3.2. This loading gives the steady state loading requirement for the 1 K cooler described in Section 3.5.

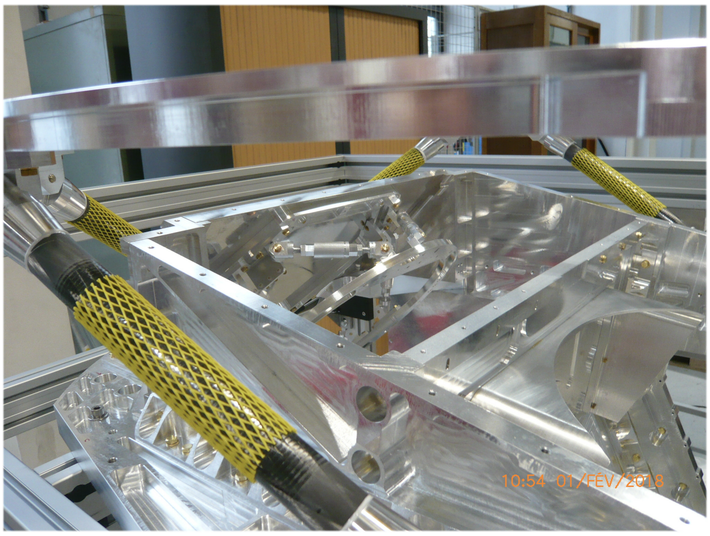

Figure 3.10: Carbon fibre tie rod 1 K box hexapod assembly. Image courtesy: L. Grandsire

The box contains 140 kg of aluminium 6061, 11 kg of stainless steel 304, 10 kg of copper and 4 kg of brass, giving a total mass of ∼165 kg. Given these masses and the specific heats of these materials [80], ∼20 MJ needs to be removed to cool the box from 300 K to 1 K.

As such, significant efforts have been devoted to optimising the cooldown of this stage (see Section 3.4). The solution that has been chosen is to use heat

Table 3.1: Measured carbon fibre tie rod properties for 1 K box hexapod assembly. Data from Reference [125].

Parameter	Value
Fibre content by volume	60 %
DP406 resin content by volume	40 %
External diameter	32 mm
Internal diameter	30 mm
Young's modulus (at 300 K)	120 GPa
Young's modulus (at 4.2 K)	80 GPa
Conductance integral 5 K to 1 K	12.7 mW·m^{-1}
Axial expansion 80 K to 280 K	-0.014 %
Radial expansion 80 K to 280 K	0.12 %

Table 3.2: 1 K box steady-state thermal loading contributions. Data from Reference [112].

Source	Value
6 tie rods (epoxy/carbon-fibre)	0.32 mW
2 precooling switches (see Section 3.4)	0.33 mW
Instrumentation wires	15 μW
Thermal radiation through window	1 μW
Thermal radiation (ε=0.1) 4.2 K to 1 K	6 μW
Total	0.7 mW

switches between the 1 K box and 4 K stage to utilise the high cooling power of the PTCs (see Section 3.2) in order to precool the box to 4 K; these switches are then opened before the box is cooled further to 1 K by the ^{4}He sorption cooler described in Section 3.5. In order to reduce thermal impedances between components within the 1 K box (and hence reduce the cooldown time), a thin layer of Apiezon N grease[5] is applied between all of the bolted interfaces.

3.4 Precooling Heat Switches

Given the thermal isolation of the 1 K box that is required to meet the steady-state heat load requirements (see Section 3.3), first-order transient thermal sim-

---

[5] `http://www.apiezon.com`

ulations have shown cooldown times on the order of a week [126]. For both development testing and operation after deployment, it is highly desirable to reduce the cooldown time significantly.

A number of other low temperature experiments have achieved faster cooldown of mechanically well isolated sub-4 K stages through the use of a low pressure exchange gas in the vacuum space to couple the isolated stage to a 4 K stage for precooling [127]. The sub-4 K stage can then be isolated by removing the exchange gas before cooling to its base temperature. This strategy is unsuitable for QUBIC however, due to both the potential damage to optical components due to differential thermal contraction and the well-documented affinity of helium to accumulate in the interstitial space of MLI [122]. As MLI will be used on both the 40 K and 4 K stages of the receiver, the use of exchange gas in this case would accordingly require significant pumping time to remove after precooling and would therefore be expected to increase the total cooldown time significantly.

An alternative (and far more attractive) strategy is the use of heat switches to couple the 1 K box to the 4 K stage. In order to support this, switches must be used that are reliable and have high switching ratios (i.e., the ratio between closed and open conductance) such that the precooling time to 4 K is minimised whilst at the same time not significantly increasing the steady-state heat leak at 1 K.

Based on open and closed conductance measurements of several types of heat switch (see Chapter 5), it has been decided to employ a combination of a mechanical switch (conductance on the order of 0.5 $W{\cdot}K^{-1}$ above ∼60 K but falls off sharply below this temperature) and two convective heat switches (higher conductance than the mechanical switch below ∼40 K, relatively constant with temperature down to 4 K).

Mechanical heat switches generally operate by actuating some mechanism in order to make or break a physical connection. In this way, zero open conductance is possible and very high closed conductances may be achieved as long as the required pressure may be developed at the interface (see Section 2.4.3). A mechanical switch (available commercially from Entropy[6]) will be used; the switch is shown under test in a cryostat at APC in Figure 3.11.

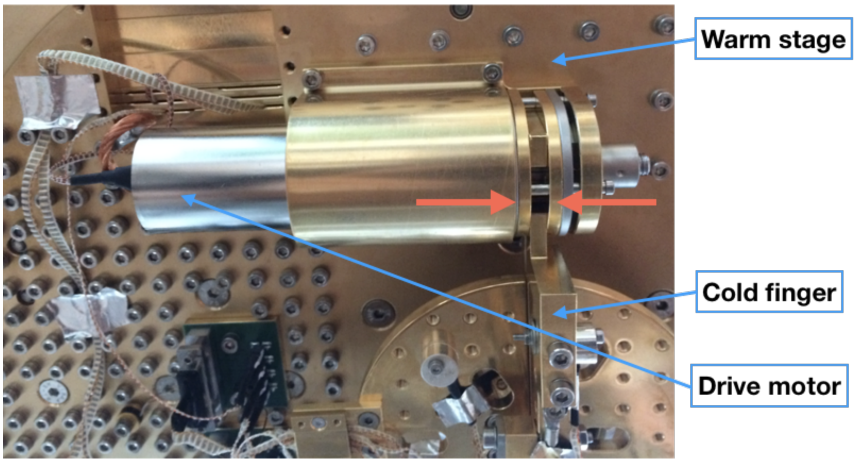

Figure 3.11: Entropy mechanical heat switch under test at APC. The red arrows indicate how the switch (mounted on the 4 K stage) operates to clamp with high pressure to the cold finger (1 K). The length of the switch is 131 mm. Image courtesy: M. Piat.

To provide a high conductance connection below 60 K, two convective heat switches [94, 128] are used in parallel with the mechanical switch. Each convective switch essentially consists of a circuit comprising two stainless steel tubes and a copper heat exchanger at either end connected to the warm and cold stages (as shown in Figure 3.12). A charcoal cryopump (see Section 2.2) is used to evacuate or fill the circuit with ^{4}He gas, opening and closing the switch respectively.

When the switch is evacuated, the only mechanism by which heat may pass through the switch is conduction through the thin-walled stainless steel tubes. Owing to the relatively low thermal conductivity of stainless steel at cryogenic temperatures and the small cross-sectional area of the tubes, the heat flow in this condition is minimal; this is the switch open state. When the cryopump is heated, the circuit is filled with gas and a convection current is established as long as the cold end is positioned higher with respect to gravity than the hot end

---

[6] `http://www.entropy-cryogenics.com`

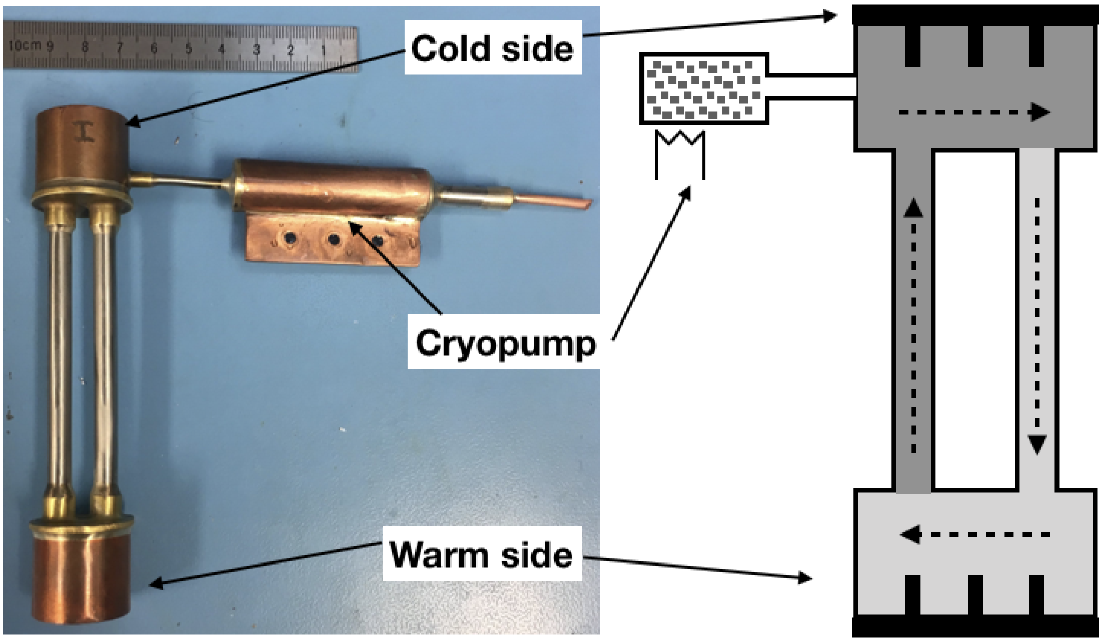

Figure 3.12: Photograph and schematic of convective switch. The direction of gas flow is shown by the dashed lines. The dark grey region denotes hot gas and the lighter grey region denotes cold gas.

(this may be achieved with copper heat straps). This provides a very effective mechanism for heat transfer and hence a high conductance through the switch in the closed position. The time required to fill and evacuate the tube (i.e., close or open the switch) is on the order of a few minutes.

Experimental measurements of the power through the switch in the open and closed states when the cold end is held at 4 K are shown in Figure 3.13, along with the modelled conductances [128].

The open conductance of the switch is calculated simply from the geometry of the stainless steel tubes and conductivity data as described in Section 2.3.1.

The closed conductance resulting from single-phase convection is calculated using a model that extends the work reported in Reference [129]. Taking the continuity equation [96] and considering that the flow is steady, it may be seen that the quantity $\rho U A$ is constant for any "cut" through the circuit, where ρ is density, U is mean velocity and A is the cross-sectional area. The fluid may

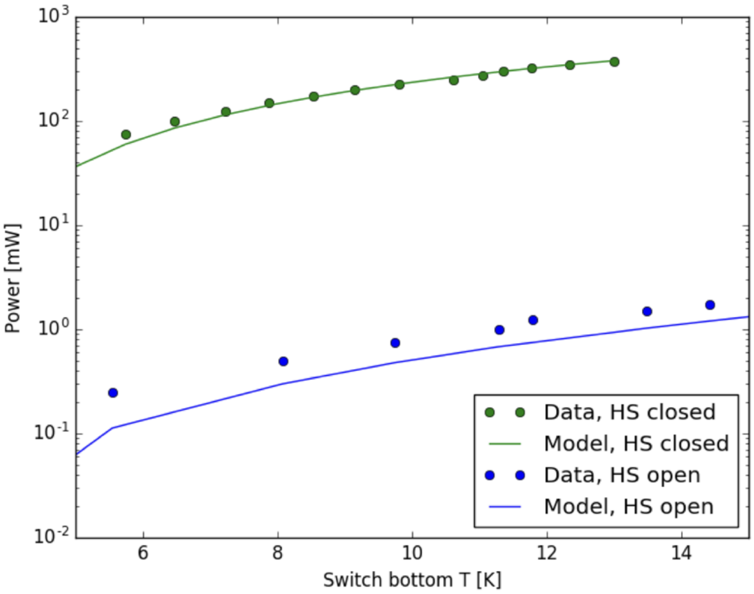

Figure 3.13: Open and closed conductance of convective switch. The top of the switch is sunk to a thermal reservoir at 4 K. For a description of the testing methodology, see Chapter 5.

be modelled as existing in two discrete regimes resulting from an instantaneous temperature change at the outlet of each heat exchanger. It may also be seen that, in the equilibrium condition, the sum of potentials around the loop is zero, i.e., the total pressure gain from buoyancy forces around the circuit is equal to the total viscous pressure loss (from the Darcy-Weisbach equation for laminar flow [96]). This can be written as

$$\Delta P_1 + \Delta P_2 = \left(\frac{128}{\pi} \cdot \frac{\mu Q L}{D^4}\right)_1 + \left(\frac{128}{\pi} \cdot \frac{\mu Q L}{D^4}\right)_2 = \frac{8\dot{M}L}{\pi r^4} \cdot \left(\frac{\mu_1}{\rho_1} + \frac{\mu_2}{\rho_2}\right) \tag{3.1}$$

given that

$$Q = \dot{M}/\rho,\ L_1 = L_2 \text{ and } L = L_1 + L_2 \tag{3.2}$$

It may also be considered that head gain from the buoyancy forces is

$$\Delta P = \Delta\rho g z = (\rho_1 - \rho_2)\, g z \tag{3.3}$$

and therefore

$$(\rho_1 - \rho_2)\, g z = \frac{4\dot{M}L}{\pi r^4} \cdot \left(\frac{\mu_1}{\rho_1} + \frac{\mu_2}{\rho_2}\right) \tag{3.4}$$

Rearranging now for the mass flow rate gives

$$\dot{M} = \frac{\pi r^4}{4L} \cdot \frac{(\rho_1 - \rho_2)\, g z}{\frac{\mu_1}{\rho_1} + \frac{\mu_2}{\rho_2}} \tag{3.5}$$

and hence the power through the switch as a function of temperatures becomes

$$\dot{Q}\,(T_H, T_C) = \frac{\pi r^4}{4L} \cdot \frac{(\rho_1\,(T_H) - \rho_2\,(T_C))\, g z}{\frac{\mu_H(T_H)}{\rho_H(T_H)} + \frac{\mu_C(T_C)}{\rho_C(T_C)}} \cdot (h_C\,(T_C) - h_H\,(T_H)) \tag{3.6}$$

Neglecting pressure loss through the heat exchangers gives

$$\delta h = c_v \delta T \tag{3.7}$$

all in agreement with the model reported in Reference [129]. This model may be then extended to include an experimentally determined efficiency factor to account for the imperfection of the heat exchangers. Given their identical geometries and the conservation of mass flow, it can be assumed that the exit temperatures are

$$T_1 = T_C + \left(\frac{f}{2} \cdot (T_H - T_C)\right) \tag{3.8}$$

$$T_2 = T_C + \left(\left(\frac{1-f}{2}\right) \cdot (T_H - T_C)\right) \tag{3.9}$$

and hence Equation 3.6 becomes

$$\dot{Q}\left(T_1, T_2\right) = \frac{\pi r^4}{4L} \cdot \frac{\left(\rho_1\left(T_1\right) - \rho_2\left(T_2\right)\right) g z}{\frac{\mu_1(T_1)}{\rho_1(T_1)} + \frac{\mu_2(T_2)}{\rho_2(T_2)}} \cdot \left(h_2\left(T_2\right) - h_1\left(T_1\right)\right) \tag{3.10}$$

This model may then be fit to the data as shown in Figure 3.13, considering that the switches provided for QUBIC were filled to their approximate cryopump saturation charges of 15 bara. A heat exchanger efficiency factor $f = 0.28$ gives good agreement with the data as shown.

3.5 1 K Cooler

As shown in Table 3.2, 0.7 mW of cooling at 1 K is required for operation of the optics box. As such, a high-power 1 K sorption cooler has been developed to meet this requirement. As a single-shot cooler (see below), the hold time required is set by the observation strategy as 22 hours, with 2 hours for recycling.

The initial design work for the cooler was the subject of the author's MSc thesis [130]. The interested reader is therefore directed there for an extensive report on the design, which is not given here. A brief overview is given however, along with the key developments in the design to meet the requirements for QUBIC. These primarily are the design, implementation, and theoretical description of a superfluid film breaker (see Section 3.5.2) which significantly improved the hold time performance, along with modelling of the condensation efficiency and integration with the QUBIC receiver cryostat at APC.

3.5.1 Cooler Design and Operation

A closed-cycle single-shot helium sorption cooler was first reported in 1985 by Torre and Chanin [131]. Since this initial design for a single-stage ^{3}He cooler, a number of developments have been variously reported; these include coolers using ^{4}He to cool to ~1 K and tandem coolers using a ^{4}He stage to precool a single or even multiple ^{3}He stages to improve the hold time and minimum temperature attainable [111, 132, 133, 134, 135, 136]. Given that the required cooling power and hold time performance for QUBIC is far higher than any previously reported system, a new design has been developed, as shown in Figure 3.14, featuring a novel superfluid film breaker (see Section 3.5.2).

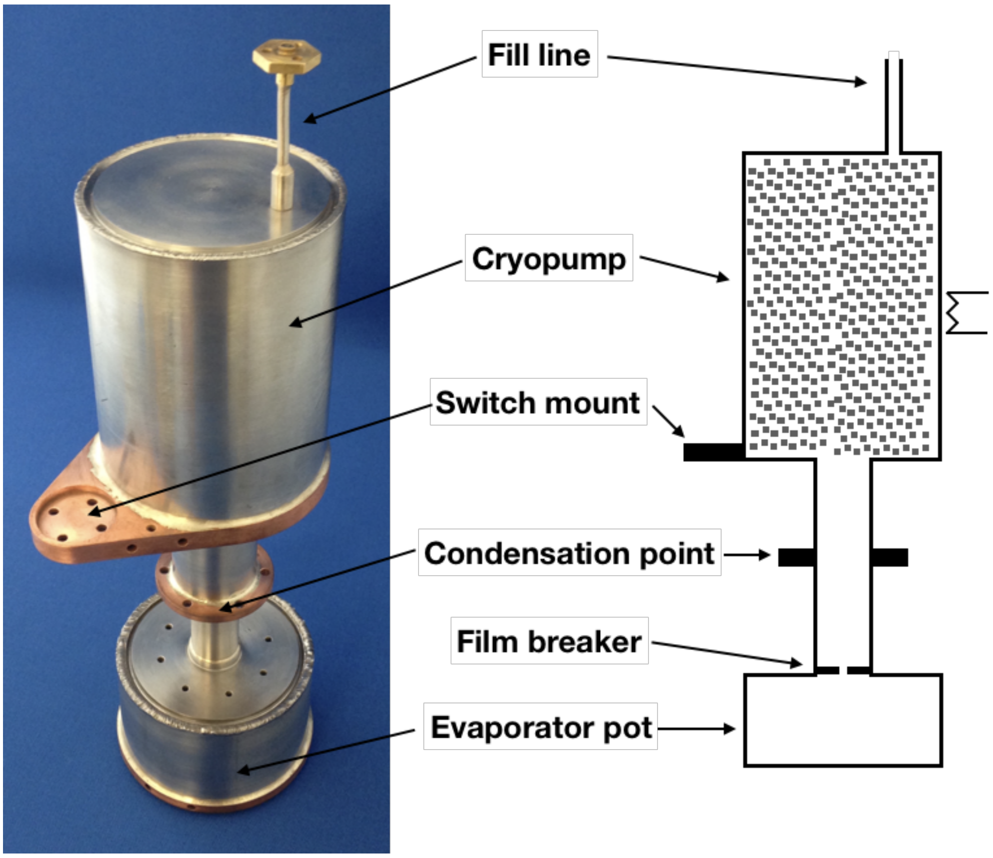

Figure 3.14: ^{4}He 1 K cooler; the total height of the cooler is 300 mm

The cryopump chamber, condenser flange and evaporator pot are connected by thin-walled stainless steel tubing such that they are only weakly thermally coupled at cryogenic temperatures.

The cooler is charged to high pressure (75 bara) with ^{4}He gas at room temperature; this is done from an external gas handling system through a fill line which is then permanently sealed before the cryostat is cooled.

The condenser flange is cooled by sinking to the 4 K stage.

In order to either strongly or weakly couple the cryopump to the 4 K stage, an active convective switch of the type described in Section 3.4 is used. The switch is mounted in parallel with the tubing connecting the condenser flange to the cryopump.

When the cryostat is cooled, the 4 K stage cools the condenser flange directly, as well as cooling the cryopump through the (at this point, closed) heat switch. By bringing the pump to ~4 K, the helium in the cooler is strongly adsorbed upon the large internal surface area of the charcoal and is therefore sequestered in the pump (See Section 2.2).

In order to regenerate the cooler, the switch is opened and the cryopump heated to ~40 K causing the gas to strongly desorb, condense in the condenser at ~4 K and collect as liquid in the evaporator under the action of gravity.

To run the cooler once the liquid is condensed, the switch is closed to cool the cryopump back to ~4 K which causes it to pump on the liquid, reducing the vapour pressure and cooling the evaporator to ~1 K under typical loading. The cooler will continue to run until the liquid has completely evaporated and is adsorbed onto the cryopump, at which point the cycle may be repeated.

The cooling power provided by the sorption cooler at a given temperature (in equilibrium) may be found by equating the total heat load $\dot{Q}_0$ to the rate of energy removal from pumping on the condensed liquid, i.e.,

$$\dot{Q}_0 = \Delta H \dot{n} = L \dot{n} \tag{3.11}$$

where ΔH is the difference in enthalpy between the liquid and vapour phases (i.e. the latent heat of evaporation L) and $\dot{n}$ is the molar flow rate of the boil-off.

The vapour is driven through the pumping line to the cryopump as shown in Figure 3.14. In the general case, the mass flow rate $\dot{m}$ through a tube in the molecular flow regime [137] is

$$\dot{m} = \frac{4}{3}\sqrt{\frac{2\pi M}{RT}}\frac{r^3}{l}\left(P_p - P_z\right) \tag{3.12}$$

where M is the molar mass, R is the gas constant, T is the gas temperature, r is the tube radius, l is the tube length, P_p is the pressure at the tube inlet and P_z is the pressure at the tube outlet.

It may be considered that in the case of the pumping line in Figure 3.14, P_p is the vapour pressure of the liquid in the pot (a function of temperature T) and P_z, the pressure developed by the cryopump, may be approximated to zero (assuming the pump has sufficient surface area so as to not saturate).

In order to find the mass flow rate as a function of temperature, this may be equated to the boil-off rate

$$\dot{m} = \frac{\dot{Q}_0 M}{L\left(T\right)} \tag{3.13}$$

where L is the (temperature-dependent) molar latent heat of evaporation. The total load curve is then given by

$$\dot{Q}_0 = \frac{4}{3}\sqrt{\frac{2\pi}{RT}}\frac{1}{\sqrt{M}}\frac{r^3}{l}P_{vap}\left(T\right)L\left(T\right) \tag{3.14}$$

The total heat load on the evaporator is simply the sum of the loading from the component(s) being cooled and the sum of the parasitic loads $\dot{Q}_{para}$. It may therefore be seen that the useful cooling power $\dot{Q}_{load}$ is given by

$$\dot{Q}_{load} = \dot{Q}_0 - \dot{Q}_{para} \tag{3.15}$$

Furthermore, it may be considered that the hold time t_{hold} (for a constant heat load) is given by

$$t_{hold} = \frac{n}{\left(\left(\dot{Q}_{load} + \dot{Q}_{para}\right)/L\right) + \dot{n}_{other}} \tag{3.16}$$

where n is the initial number of moles of liquid condensed in the pot and cooled to the base temperature, and $\dot{n}_{other}$ is the molar flow rate of helium out of the pot via mechanisms other than boil-off.

Parasitic loading is therefore be minimised to maximise both the useful cooling power and hold time as shown by Equations 3.15 and 3.16 respectively. Furthermore, in order to maximise the hold time, $\dot{n}_{other}$ should also be minimised.

3.5.2 Superfluid Film Breaker

As described in Section 2.1.1, the "fountain" term $s\nabla T$ in Equation 2.2 expresses the fact that the superfluid component in the two-fluid model will tend to move in the direction of positive temperature gradient.

The practical effect of this is that the superfluid film that forms on the inside surface of the evaporator pot below the λ-point will tend to flow up into the pumping tube and towards the condensation flange. It will flow upwards in this tube until it is warmed sufficiently either to evaporate or transition back to a normal fluid and return as droplets to the evaporator.

This in turn has several effects that degrade the performance of the cooler. Firstly, the superfluid film in the tube provides a high conductance path for heat to be transferred to the pot, constituting an increase in parasitic loading and hence a reduction in useful cooling power (see Equation 3.15). Secondly, any normal fluid helium droplets that return under the action of gravity to the pot will constitute a further parasitic heat load. Thirdly, the evaporation of helium inside the pumping tube raises the vapour pressure over the liquid in the pot which limits the minimum temperature that can be reached by the cooler. Finally, and perhaps most critically, the mass transport of helium out of the evaporator constitutes a significant $\dot{n}_{other}$ term in Equation 3.16 which significantly reduces the hold time performance of the cooler.

Several techniques currently exist for limiting superfluid film flow in various systems. The first is to mount a heater to the outside of the tube where the film should be broken [138]; by doing so, the tube can be heated at this point to "burn" the film and prevent it from moving further up the tube. However, this would be entirely unsuitable for application to a sorption cooler as the film is already being "burned" as it reaches the higher temperature part of the pumping tube; adding a heater would simply move the point where the film is "burned" lower down the tube and increase the parasitic loading through the tube to the evaporator, degrading the performance further.

As the mass transport rate of the film $\dot{m}_{film}$ may be found as

$$\dot{m}_{film} = \rho_s C d v_c \tag{3.17}$$

where ρ_s is the superfluid density, C is the smallest circumference of the flow line, d is the film thickness at the point of smallest circumference, and v_c is the critical flow velocity, the film flow may alternatively be restricted by minimising one or more of these terms.

The superfluid density is a function only of temperature. The critical superfluid velocity of a ^{4}He film is $\sim$30 cm·s^{-1} and varies only very weakly with material surface finish [80]. It may be considered however that a second type of technique for limiting the film flow is to minimise C and d. Shirron and DiPirro [139] showed that the film thickness wetted to a particular surface is given by

$$d = \left(\frac{\Gamma}{k_B T \ln\left(P_{vap}/P\right) - \left(m\sigma/\rho r_s\right)} \right)^{1/3} \tag{3.18}$$

where Γ is the van der Waals constant, k_B is the Boltzmann constant, m is the mass of the helium atom, σ is the surface tension, ρ is the superfluid density, and, crucially, r_s is the radius of curvature of the surface. As such, introducing an extremely sharp edge into the film flow path (having a small, negative radius of curvature) will significantly reduce the film thickness and, from Equation 3.17, the mass transport rate via the film.

This type of approach has been applied to the suppression of superfluid film in a sorption cooler by Lau et al. [140], who implemented a knife-edge orifice in the pumping line. However, the design and manufacture of this type of film breaker is, in the author's experience, exceptionally challenging, as any defect in the knife-edge will provide a low impedance path for the film to pass through and render the technique ineffective.

Furthermore, the model of Lau et al. to describe the performance of their film breaker relies on fitting several parameters, including the critical film speed, to experimental data, and is therefore not predictive. Indeed, the critical superfluid velocity required in order to fit reasonably to their data is unphysically large [80]. Their model also solves four simultaneous equations numerically, and has been found by the author to be unable to converge to a solution at higher heat lifts. It is therefore found not to be suitable for the development of this system; hence, a new model has been developed.

An alternative to the knife-edge type film breaker has been designed, modelled and implemented based on a capillary channel drilled perpendicularly through a stainless steel disk soldered into the pumping tube at the top of the evaporator pot. The disk used was of thickness 3 mm and the outside diameter of the disk to match the inside diameter of the pumping tube, as shown in Figure 3.15.

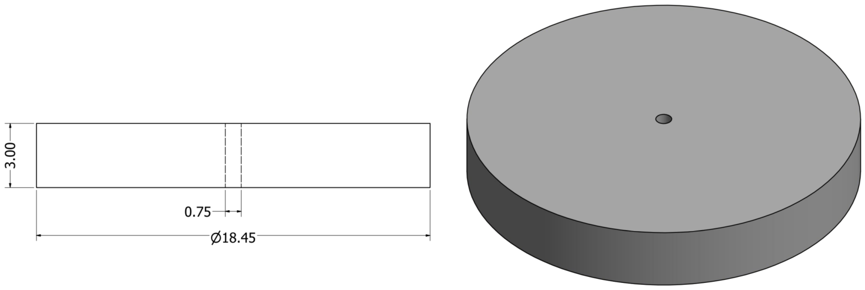

Figure 3.15: CAD drawing of film breaker disk

As determined from the theoretical analysis described below, the capillary channel was drilled with 750 μm drill bit to meet the heat lift requirement for QUBIC; subsequent optical microscopy of the capillary showed the diameter of the channel to be 767 ± 15 μm. The micrograph taken of the channel is shown in Figure 3.16.

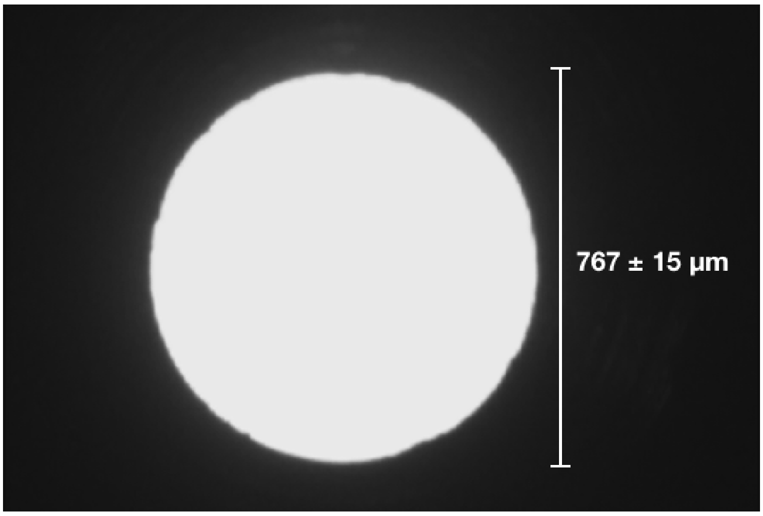

Figure 3.16: Micrograph of film breaker capillary taken in optical transmission

This type of film breaker was simple to manufacture with exceptionally clean edges at the top and bottom of the channel as shown in Figure 3.16. Drilling rendered the edges of the channel far less prone to defects of the type that would provide low impedance paths to the superfluid, whilst still providing sharp 90° corners at the top and bottom of the channel.

In order to break the film most effectively without restricting the gas flow, and hence cooling power, the capillary design borrows from supersonic aerodynamic theory. Considering the case of a convergent-divergent rocket nozzle as shown in Figure 3.17, it may be seen that the capillary may be designed to choke the flow of helium gas, such as to reach the sonic condition and maximise mass transport through the restriction (throat).

Sonic flow through the throat of this type of nozzle is induced by lowering the back pressure P_{back} below the upstream pressure P_{res}, which is taken to be constant. For $P_{back} > P*$, where $P*$ is the so-called critical pressure, flow is subsonic throughout the nozzle and the jet pressure after the throat is equal to P_{back}. The mass flow is then found from subsonic isentropic theory [96] and is

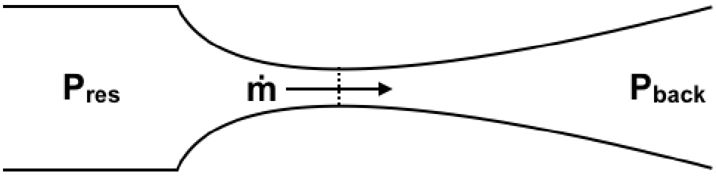

Figure 3.17: Convergent-divergent rocket nozzle with reservoir pressure P_{res}, mass flow $\dot{m}$, back pressure P_{back}; the throat of the nozzle is marked with a dotted line

less than the critical mass flow $\dot{m}*$.

If P_{back} is lowered to reach $P*$, flow through the throat becomes sonic and the mass flow reaches its maximum value of $\dot{m}*$.

If P_{back} is lowered further, the mass flow cannot increase further. Flow through the throat remains sonic and the jet downstream expands supersonically so that the jet pressure can reduce from $P*$ down to P_{back}.

By considering this model in analogy to the capillary-type film breaker, it may be seen that, in equilibrium, the vapour pressure over the liquid in the evaporator provides a reservoir at $P_{res} = P_{vap}(T)$, the capillary forms the throat of the nozzle, the mass flow rate through the nozzle equals the boil-off rate and the back pressure is that established at the base of the tube downstream of the restriction (see Equation 3.12).

Given a capillary of radius r, the mass transport of gas if molecular flow dynamics is assumed is

$$\dot{m} = \left(\frac{1}{2\pi}\right)^{1/2} \pi r^2 P_{res} \left(\frac{M}{RT}\right)^{1/2} \tag{3.19}$$

If continuum flow dynamics are assumed, then the mass flow instead is given by

$$\dot{m} = \gamma^{1/2} \left(\frac{2}{\gamma+1}\right)^{\frac{(1/2)(\gamma+1)}{\gamma-1}} \pi r^2 P_{res} \left(\frac{M}{RT}\right)^{1/2} \tag{3.20}$$

where γ is the ratio of specific heat capacities [96].

Given a required mass flow rate, it is possible (assuming the flow regime is also known) to calculate the appropriate radius of the capillary for the film breaker. In this way, the gas flow is not overly impeded and the cooling power not degraded below what is required. Note that it is necessary for the pumping tube radius and length to be designed sufficiently (see Equation 3.12) for the pressure at the tube inlet to be at or below the critical pressure, i.e. $P_P \leq P*$.

The flow regime, and hence flow mechanics that apply, may be characterised by the Knudsen number Kn as

$$Kn = \frac{\lambda}{L} \tag{3.21}$$

where λ is the mean free path and L is a characteristic length scale [96]. The mean free path in the reservoir may be found directly from the vapour pressure which is itself a function of temperature. Taking the characteristic length to be the diameter of the capillary, then for a 767 μm capillary Kn may be calculated as a function of evaporator temperature as shown in Figure 3.18; the interstitial region between the lower limit for molecular flow mechanics and the upper limit for continuum flow is a transition regime where the flow mechanics are exceptionally challenging to model.

It is clear from Figure 3.18 that below ~1 K, the flow is in a transition regime. Above 1 K however, the flow is clearly in the continuum regime and hence should be well-described by continuum flow mechanics.

Calculating the mass flow through the 767 ± 15 μm manufactured film breaker provides a theoretical load curve for both continuum and molecular flow. The code written for this is given in Appendix A.2. The load curve for the cooler was measured experimentally in a testbed cryostat in Manchester; these data are shown alongside both theoretical curves in Figure 3.19.

It may seen from Figure 3.19 that below 1 K, the data lie between the two curves (i.e. in the transition regime) and as the load and hence temperature increases, the data tend toward the curve for continuum flow. As such, these

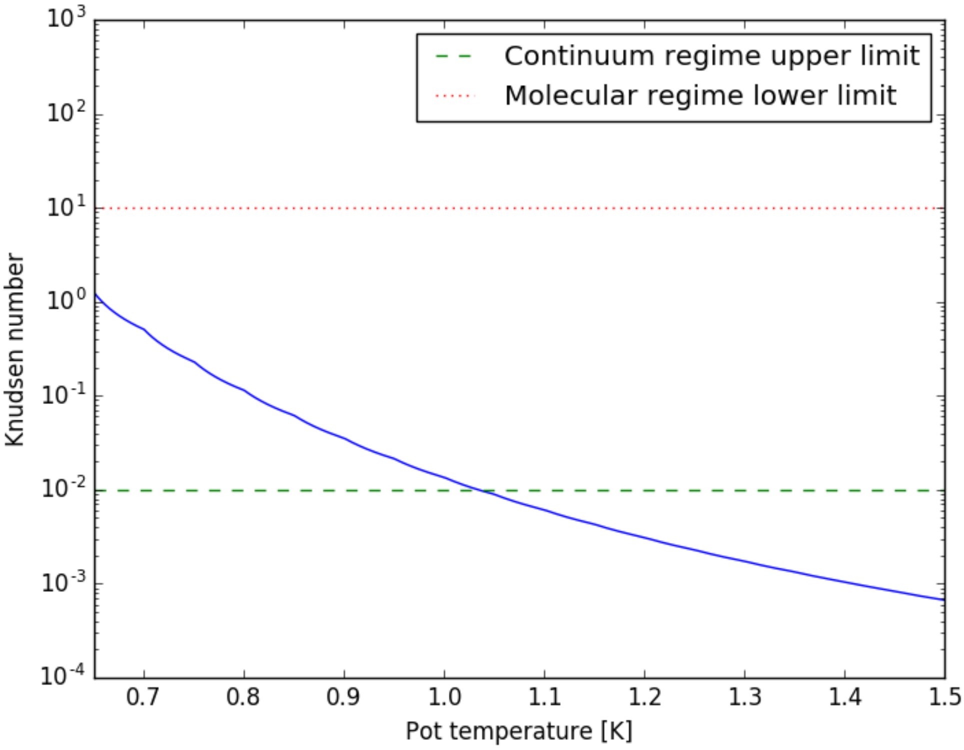

Figure 3.18: Knudsen number for an evaporator pot with capillary film breaker of diameter 767 μm.

data are in good agreement with the constraints of the theoretical model.

The measured data in Figure 3.19 also shows that under the expected loading from the 1 K optics box, the coldhead reaches a temperature of 871 mK, easily meeting the specification.

The hold time of the cooler was also measured in the testbed cryostat, as described in Section 3.5.3. Considering the helium charge and condensation efficiency, the testing showed that the film flow was negligible within the bounds of experimental uncertainty, and hence that the film breaker worked optimally as far as could be measured.

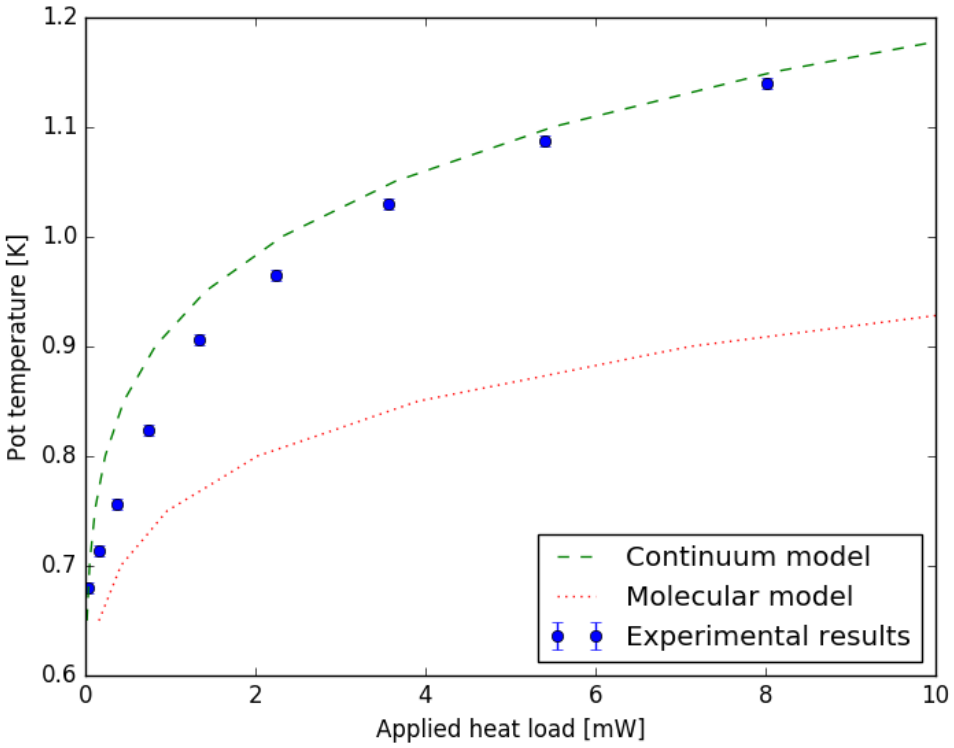

Figure 3.19: Measured and theoretical load curves (for both molecular and continuum flow models)

3.5.3 Hold Time and Condensation Efficiency

Under the expected loading from the 1 K optics box, applied artificially by a heater mounted directly onto the coldhead, the measured hold time of the cooler was 26.5 hours at a temperature of 871 mK[7]. The temperature time series data for the cold head during one of these tests is shown in Figure 3.20.

The specification for the receiver [112] was therefore met. The same data set was also used to find the total capacity of the cooler to be 66.8 J. In order to initially cool the 1 K box from 4 K to 1 K, ∼60 J must be removed, and hence this specification is also met.

By using an isolating switch between the evaporator and the box, it is possible

---

[7] The small temperature step observed is attributed to the interaction of the liquid with the sinter in the evaporator pot, although study of this phenonomon is ongoing. It does not affect the performance in the context of the requirements for QUBIC.

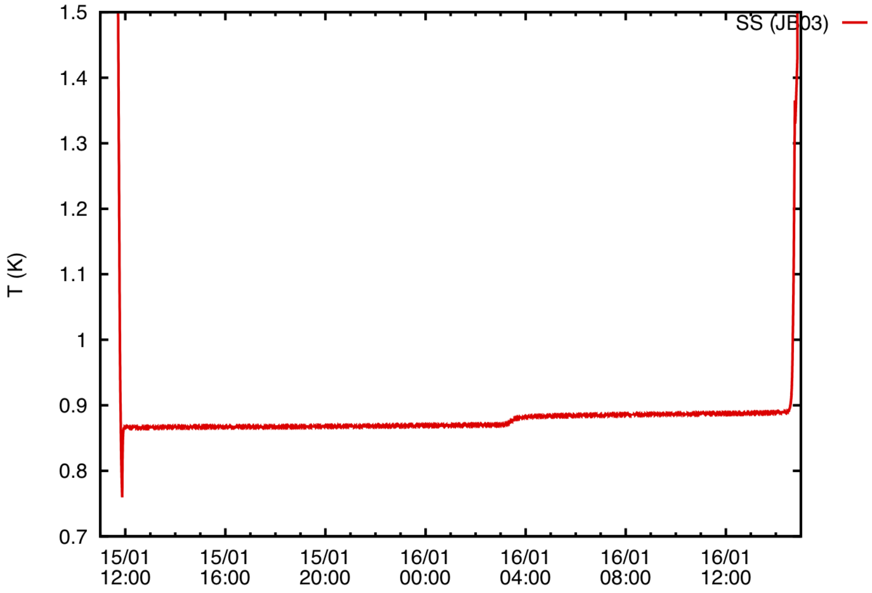

Figure 3.20: 1 K cooler hold time for 0.7 mW applied load

to cool the box to 1 K, recycle the cooler without significantly warming the box and then run the cooler again to maintain temperature during observations. When the cooler expires at the end of this observing period, the isolation switch is used again to avoid loading the box whilst the cooler is recycled. The switch design is described in detail in Section 3.6.

In the test shown shown in Figure 3.20, the condenser was cooled to 2.9 K. As reported by Cheng et al. [133], it is possible to model the condensation efficiency, which is shown below to vary with condensation temperature. Firstly, it may be considered that when the liquid is condensed, there will be pressure equilibrium in the cooler, with the different sections at their respective temperatures. The number of moles of liquid initially condensed n_l is then

$$n_l = \frac{n_0 - n_t - \frac{P}{R}\left(\frac{V_p}{T_p} + \frac{V_c}{T_c}\right)}{1 - \frac{\widetilde{V}P}{RT_p}} \tag{3.22}$$

where n_t is the number of moles in the tubes, n_0 is the initial number of moles of charge, the subscripts p and c indicate the properties of the ^{4}He in the evaporator pot and cryopump respectively, and $\widetilde{V}$ is the molar volume of the liquid ^{4}He. There is then an additional efficiency loss from the self-cooling of the liquid from its liquefaction temperature to its base temperature, so that the number of moles of liquid when the cooler reaches ∼1 K n is

$$n = n_l \cdot \exp \int_{T_{hi}}^{T_{low}} \frac{C(T)}{L(T)} dT \tag{3.23}$$

There is hence a strong dependence of the total condensation efficiency n/n_0, and hence the hold time t_{hold} (see Equation 3.16), on the temperature of the condensation point T_p. This is calculated for the QUBIC 1 K cooler in Figure 3.21. This also gives the hold time performance that will be expected in the QUBIC cryostat. The cooler, having been validated in Manchester, was then shipped to APC for integration with the receiver cryostat (see Section 3.8).

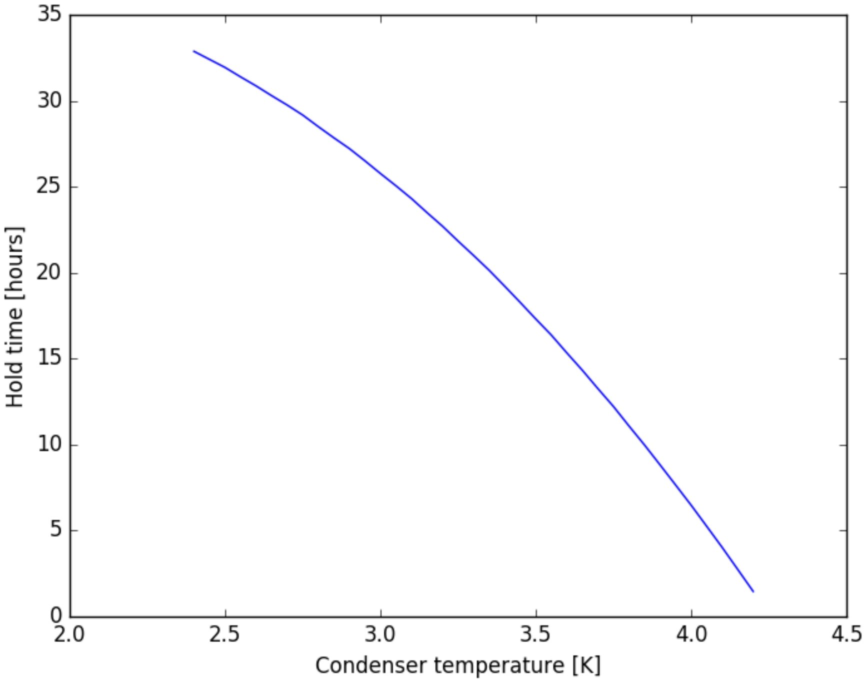

Figure 3.21: 1 K cooler condensation efficiency

3.6 1 K Box Isolation Heat Switch

As described in the previous section, an isolation switch is required between the 1 K cooler cold head and the 1 K box. For this purpose, a ^{4}He convective switch similar to that described in Section 3.4 is used. However, in order to avoid the thermal loading associated with a 40 K cryopump when the switch is closed, a passive design (i.e., one with no cryopump) has instead been used.

The switch should be closed when the 1 K cooler is at base temperature (i.e., colder than the 1 K box) and open when the cooler is recycling (i.e., warmer than the 1 K box). As such, a switch of similar construction to the precooling switch (Figure 3.12) is used with the 1 K cooler attached to the top of the switch. In this way, when the cooler is at base temperature the top of the switch will be colder than the bottom (attached to the 1 K box) and the switch couples the two stages strongly. Recycling the cooler will bring the top of the switch to a higher temperature than the bottom, stopping the convection and opening the switch to isolate the box. In this way, no cryopump is required to actively control the switch which instead simply operates passively in analogy to a diode. In the receiver cryostat, copper support pieces are used to achieve the desired orientation with respect to gravity. The switch is shown under test in Figure 3.22.

As there is a small temperature step across the switch in the closed position, the use of the switch gives an “effective” load curve, as shown in Figure 3.23. Under design load conditions, the temperature at the bottom of the switch is 910 mK, still meeting the design specification.

During testing, some residual conductance in the open state was observed below 2.2 K as a result of superfluid film behaviour inside the tubes. Whilst the ^{4}He switch will be used as is for the TD, a ^{3}He passive switch is currently being developed for use with the FI to improve cycling efficiency.

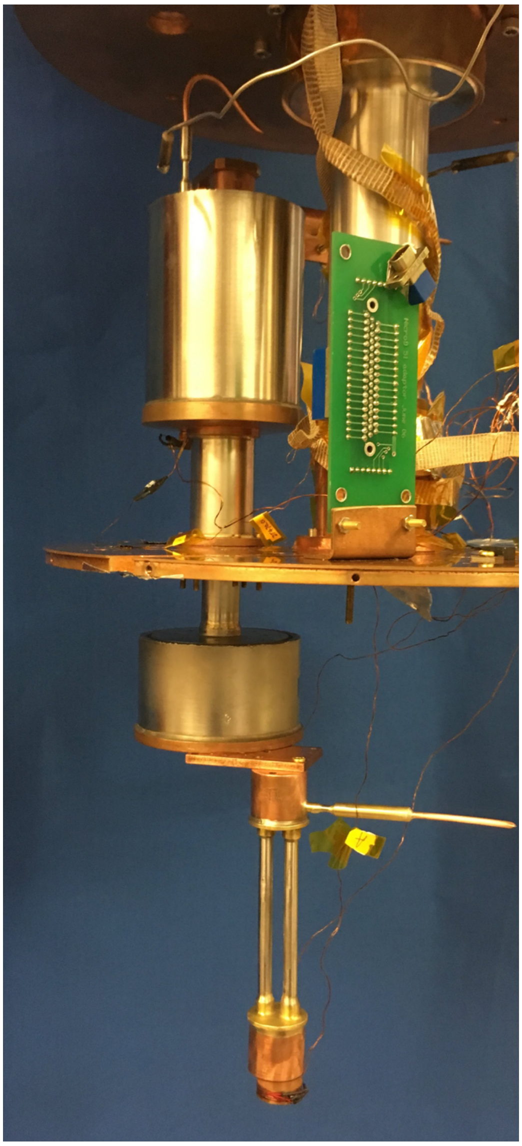

Figure 3.22: 1 K cooler with passive isolation switch under test; the total height of the assembly is 430 mm

3.7 350 mK Stage

After the beam combiner mirrors, a dichroic filter (also at 1 K) selects the two frequency bands, centered at 150 GHz and 220 GHz, which are focused onto two orthogonal focal planes cooled at 350 mK (see Figures 3.1 and 3.2). The focal planes are each tiled with 1024 NbSi Transition-Edge Sensors (TES) with

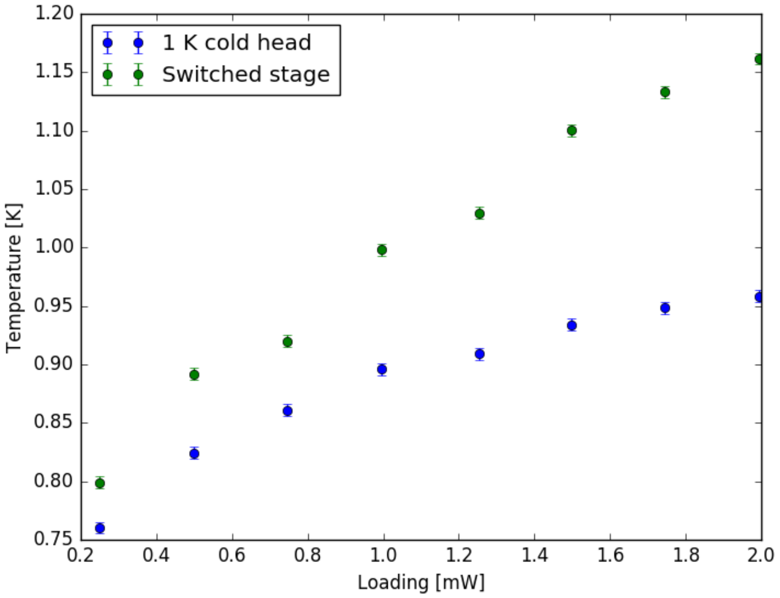

Figure 3.23: Effective load curve of 1 K cooler with isolation switch

a critical temperature close to 500 mK. A quarter-section of one of the detector arrays is shown in Figure 3.24.

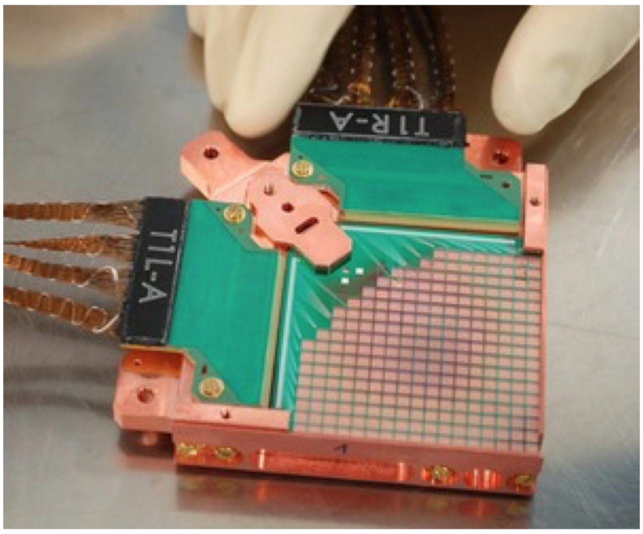

Figure 3.24: 256 TES array being integrated for the test [112]

The TESs are then read out by a time domain multiplexing (TDM) scheme

[141] based on superconducting quantum interference devices (SQUIDs) operating on the 1 K stage. The signals from the SQUIDs are then amplified by SiGe low noise amplifier (LNA) based application-specific integrated circuits (ASICs) at 40 K and read out by warm electronics at 300 K.

The contributions to the thermal loading on the 350 mK stage are given in Table 3.3.

Table 3.3: 350 mK stage steady-state thermal loading contributions

Source	Value
16 tie rods (epoxy/carbon-fibre)	17 μW
Instrumentation wires	6 μW
Thermal radiation through window	1 μW
Thermal radiation (ε=0.1) 1 K to 350 mK	$\ll 1$ μW
Total	25 μW

A double-stage ^{3}He/^{4}He sorption cooler, commercially available from Chase Research Cryogenics[8] is used to cool this stage. The cooler is mounted from the 4 K stage and operates in a similar manner to the 1 K cooler described in Section 3.5. In this case however, the ^{4}He stage is used only to condense ^{3}He in the second stage (sharing a common cold head), which cools to a lower temperature as a result of its different vapour pressure curve (see Section 2.1.4). Figure 3.25 shows a schematic of the cooler. The cryopumps in this case are operated by gas-gap heat switches[9].

In order to cycle the cooler, both cryopumps are heated to ∼40 K to desorb the gas, which condenses at the 4 K plate and collects as liquid in a pair of concentric chambers in the coldhead (one for the ^{3}He side and one for the ^{4}He). Keeping the ^{3}He pump at ∼40 K, the ^{4}He cryopump heater is switched off and the heat switch to the 4 K stage is closed. This cools the cryopump in order to pump the liquid ^{4}He in the coldhead down to ∼1 K, significantly improving the condensation efficiency of the ^{3}He. When the ^{4}He expires, the temperature of the

---

[8] `http://www.chasecryogenics.com`

[9] See Section 5.2.1

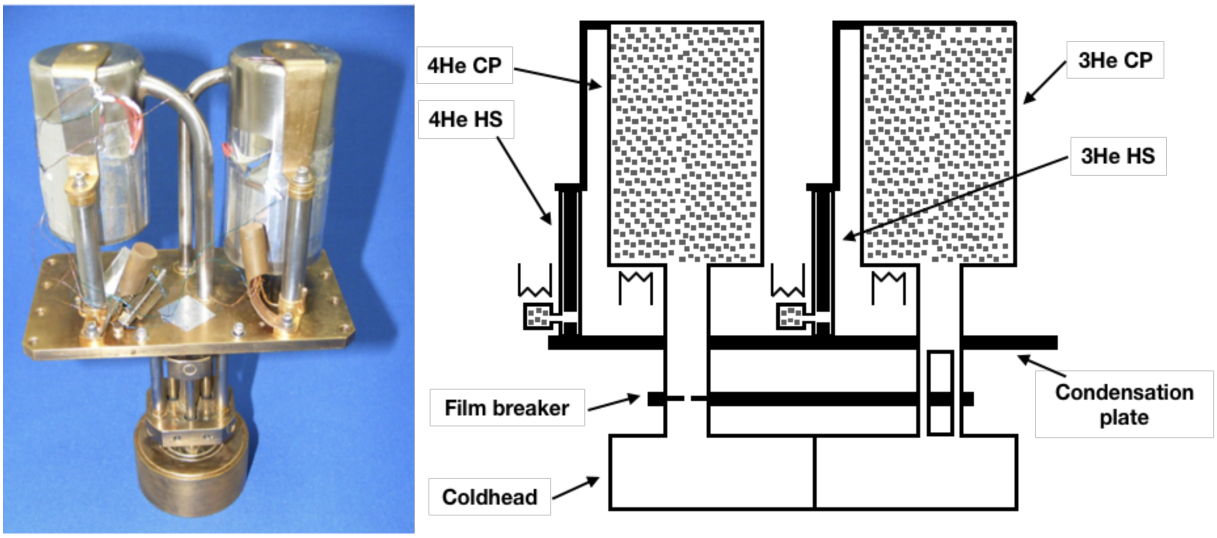

Figure 3.25: Photograph and schematic of double-stage ^{3}He/^{4}He 350 mK cooler. The height of the cooler is 240 mm. Photograph courtesy: S. Melhuish.

film breaker (see Figure 3.25) sharply increases as it is no longer cooled by the vapour moving through the pumping line, with the coldhead remaining at ~1 K due to its far higher heat capacity and lower thermal loading. The ^{3}He cryopump heater is then switched off and the heat switch closed, pumping the ^{3}He down to its base temperature ~320 mK. The equations govering the hold time and cooling power are the same as those given in Section 3.5. When the ^{3}He expires, both heat switches may be opened, both cryopumps heated to ~40 K, and the cycle repeated.

Having previously been used in another low temperature experiment in Manchester [142], the cooler was modified for QUBIC. The electronics were refitted and the cooler redressed, before being tested for load curve and hold time performance, as well as temperature stability.

Under the design load, this system showed a hold time of 90 hours and a base temperature of 339 mK in the Manchester test cryostat. A full load curve is shown in Figure 3.26. Calculation of the power spectral density, as shown in Figure 3.27, showed excellent temperature stability, with negligible long term drift observed. Having met the specifications [112], the cooler was shipped to APC along with the 1 K cooler for integration with the receiver.

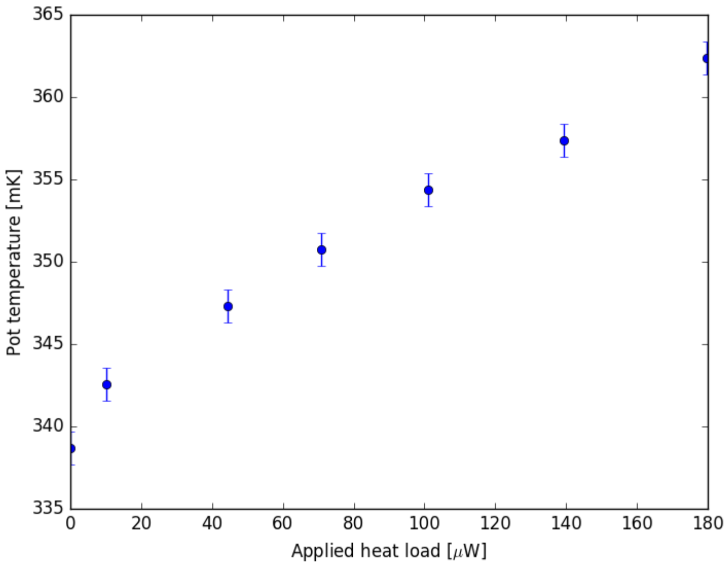

Figure 3.26: 350 mK cooler load curve measurements

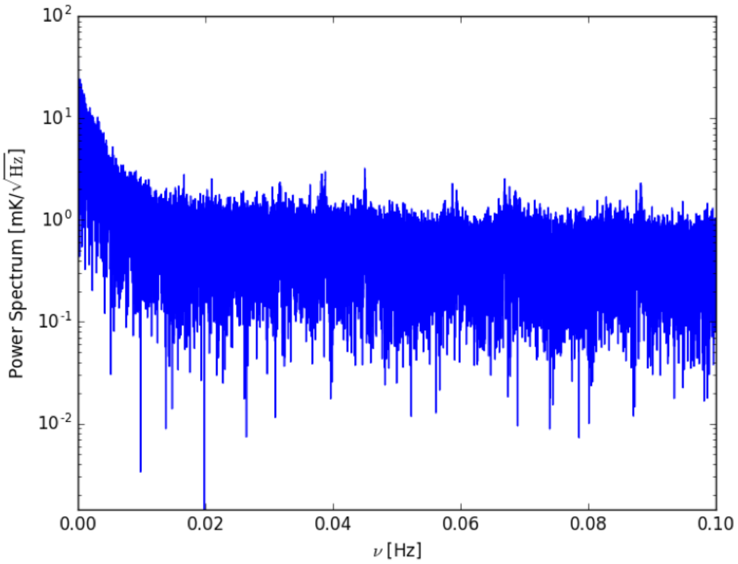

Figure 3.27: Power spectral density for 350 mK cooler under design loading

3.8 Cryostat Assembly and Integration

Having validated the performance of the 1 K cooler, 350 mK cooler, and convective heat switches, these subsystems were shipped to APC in June 2018.

In July 2018, both the 1 K and 350 mK coolers were installed on the 4 K stage of the receiver, and the cryostat cooled without installing the 1 K box for initial validation. The coolers were cycled and successfully reached base temperatures of 936 mK and 365 mK respectively. It should be noted that this test was carried out without optimisation of the thermal mounting or cycling, or addition of MLI.

Following these initial tests, the 1 K box was installed and the coolers remounted as shown in Figures 3.28 and 3.29. With the 1 K box installed and the receiver in a “blind” configuration (i.e., the optical path blanked off), the cryostat was cooled again in December 2018.

Figure 3.28: Installation of both sorption coolers with the 1 K box. Image courtesy: S. Torchinsky.

In this configuration, the TES array was cooled by the double-stage cooler to 350mK to allow preliminary dark testing, with the cold head reaching 323 mK.

The 1 K cooler in this configuration was not coupled to the 1 K box. Instead,

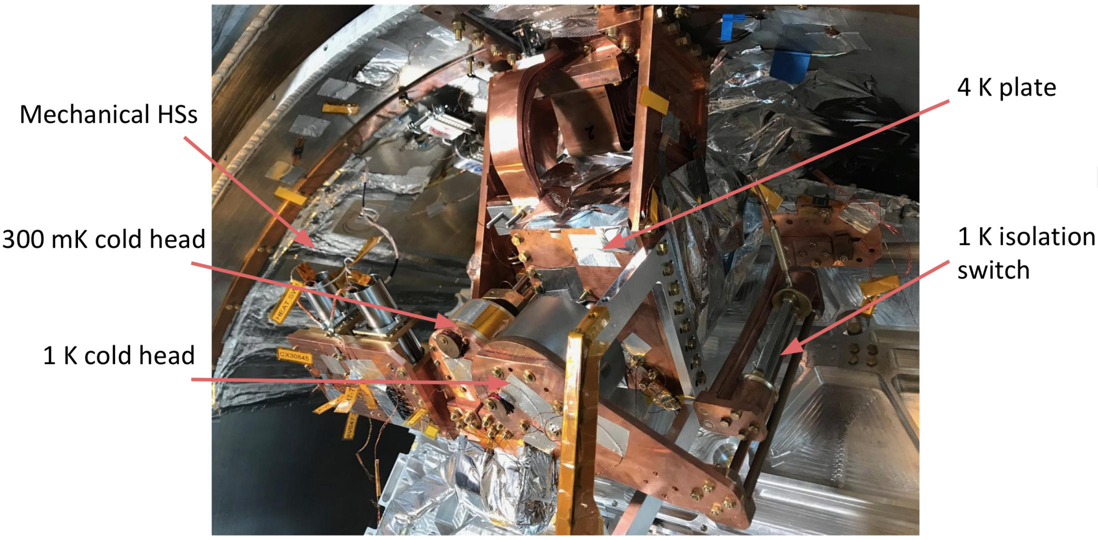

Figure 3.29: Installation of both sorption coolers with the 1 K box, showing mounting plate assembly and mechanical precooling switches. Image courtesy: S. Torchinsky.

a heater was mounted on the loading side of the isolation switch and the cooler capacity measured to be 28 J at 1 K, where the cycling is shown in Figure 3.30.

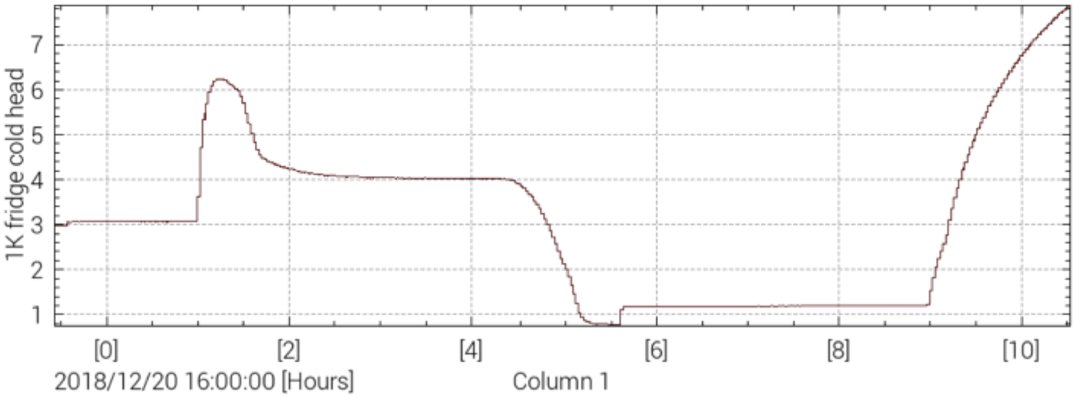

Figure 3.30: 1 K cooler cycling at APC with an artificially high loading to measure capacity. Figure courtesy: M. Piat.

This capacity is significantly less than was measured in the test cryostat in Manchester, and is consistent with a higher condensation temperature as shown in Figure 3.21. Whilst the isolation switch will still allow operation of the 1 K box with this performance, this would reduce the observation time upon deployment.

As such, the cooler assembly mount is currently being redesigned in order to reduce the thermal impedence between the PTC second-stage cold head and the condensation point. Testing of this is expected in Summer 2019.

Chapter 4

The POLARBEAR-2 Cryogenic Receivers for the Simons Array

An extension of the successful POLARBEAR experimental program [143], the Simons Array[1] [76, 144, 145] will consist of three independent telescopes, each equipped with upgraded cryogenic receivers to directly image the CMB from an altitude of 5200 m in the Atacama Desert in Northern Chile. The site is shown in Figure 4.1.

Each of the three receivers, namely POLARBEAR-2A, -2B, and -2C, will house the cold optics through to kilo-pixel TES arrays. As with the QUBIC receiver described in Chapter 3, the POLARBEAR-2 receivers will cool radiation interception and optical stages to 50 K and 4 K using two PTCs. The three receivers then use different configurations of multi-stage sorption fridges to cool various lower temperature stages down to a final temperature stage at 270 mK for the focal plane.

As well as contributing to the development, installation, and commissioning of the fridges used in POLARBEAR-2B and -2C (see Reference [147]), the author has been responsible for the development of a code to characterise the thermal

---

[1] The full collaboration list and details of supporting funding bodies are available at `https://cosmology.ucsd.edu/simonsarray.php`

Figure 4.1: The Simons Array site in the Atacama Desert, Chile, in 2016 [145]. The three telescopes, at the time under construction, are visible in in the foreground. The Atacama Cosmology Telescope [146] is visible in the background.

stability and identify noise sources in the temperature of the focal plane stage, as described in this chapter. The code will be used to analyse these as a function of telescope elevation and other instrument parameters, and hence feed back into developing a ground template to aid in optimising the scan strategy for the Simons Array.

4.1 Science Goals and Instrument Architecture

POLARBEAR was a direct-imaging CMB polarization experiment that began observation from the offset Gregorian-Dragone [148] Huan Tran Telescope (HTT) in the Atacama Desert in 2012 [143]. The telescope is shown in Figure 4.2. The 3.5 m primary aperture (denoted (a) in Figure 4.2) consists of a monolithic 2.5 m high-precision reflector. This is surrounded by a guard ring to prevent spillover of the beam. Sidelobe response is reduced by the inner shield (b) which provides baffling. The primary focus is reimaged by the secondary mirror (c) inside the cryogenic receiver (d) [149].

As discussed in Section 1.1.2, POLARBEAR reported the first direct mea-

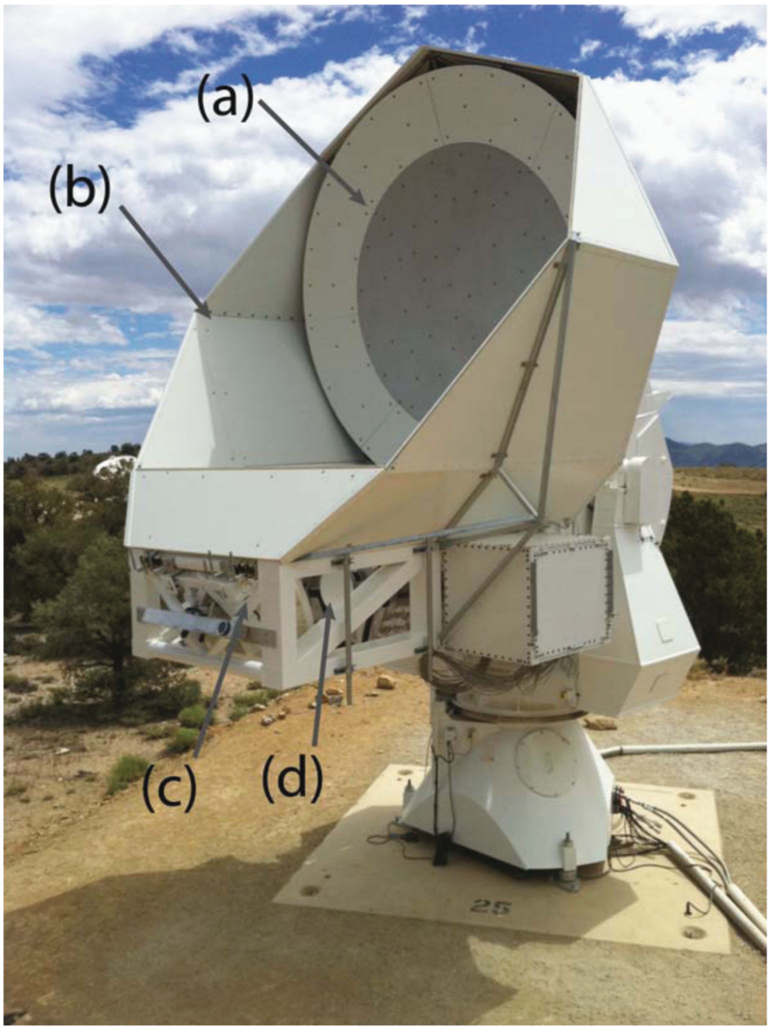

Figure 4.2: The Huan Tran Telescope in 2010 during testing before deployment to Chile [149]. A description is given in the text.

surement of the gravitational lensing B-mode signal in 2014 [40], with improved measurements from the two-year dataset reported in 2017 [150].

The Simons Array will consist of three POLARBEAR-type telescopes with upgraded cryogenic receivers, namely POLARBEAR-2A, -2B, and -2C. POLARBEAR-2A and -2B will observe the CMB with bands centred at 95 and 150 GHz, while POLARBEAR-2C will observe at 220 and 270 GHz to enable enhanced foreground separation and delensing [145]. These receivers will provide a factor of 18 increase in mapping speed by featuring an increased field-of-view, multichroic pixels, and an increased number of detectors compared with POLARBEAR [144, 151].

The receivers will be deployed in stages; the first to observe will be POLARBEAR-2A which was deployed in late 2018, with science observations expected to begin in mid-2019. POLARBEAR-2B will be an identical receiver to POLARBEAR-2A and will deploy on a second telescope later in 2019. Finally, POLARBEAR-2C will utilize a 220 GHz and 270 GHz array on a third telescope in mid-2020. The three telescopes will operate independently over a nominal observation campaign of three years.

With beam sizes of 3.5 arcmin and 5.2 arcmin (at 150 GHz and 95 GHz respectively) and the full array projected to achieve 2.5 $\mu\mathrm{K}_{CMB}\sqrt{s}$ noise equivalent temperature, the Simons Array will be able to probe a wide range of angular scales. As such, it will target both further measurements of the lensed B-mode signal (at high ℓ) and detection of the primordial GWB B-mode signal (at low ℓ).

Forecasting studies show that, after cross-correlations with Planck data, the Simons Array will be able to constrain $\sigma\left(r = 0.1\right) = 6{\times}10^{-3}$. Furthermore, as the lensed B-mode signal can be used to construct maps of the gravitational potential at high redshift [152], the Simons Array will also be able to constrain the sum of the neutrino masses $\sigma\left(\Sigma m_\nu\right) = 40$ meV when combined with baryon acoustic oscillation data [145].

4.2 Receiver Backend Cryostats

Each POLARBEAR-2 receiver consists of two cryostats [153], one each for the optics tube and the backend. These are able to operate independently during laboratory testing before being combined to form a single common cryostat during integration as shown in Figure 4.3. Both cryostats comprise a 300 K vacuum chamber, a ∼50 K radiation interception stage, and a ∼4 K stage. Cooling of the

50 K and 4 K stages in each cryostat is provided by a Cryomech[2] PT415 pulse tube cryocooler.

The optics tube cryostat houses the cold reimaging lenses, Lyot stop, infrared-blocking filters, and cryogenic half-wave plate. The backend cryostat, shown on the left, provides the housing for the focal plane detector modules, focal plane tower (FPT), cold readout components, SQUID preamplifiers, and a sorption cooler to provide several sub-Kelvin stages [153]. The three receivers each use a different sorption cooler configuration, as detailed below.

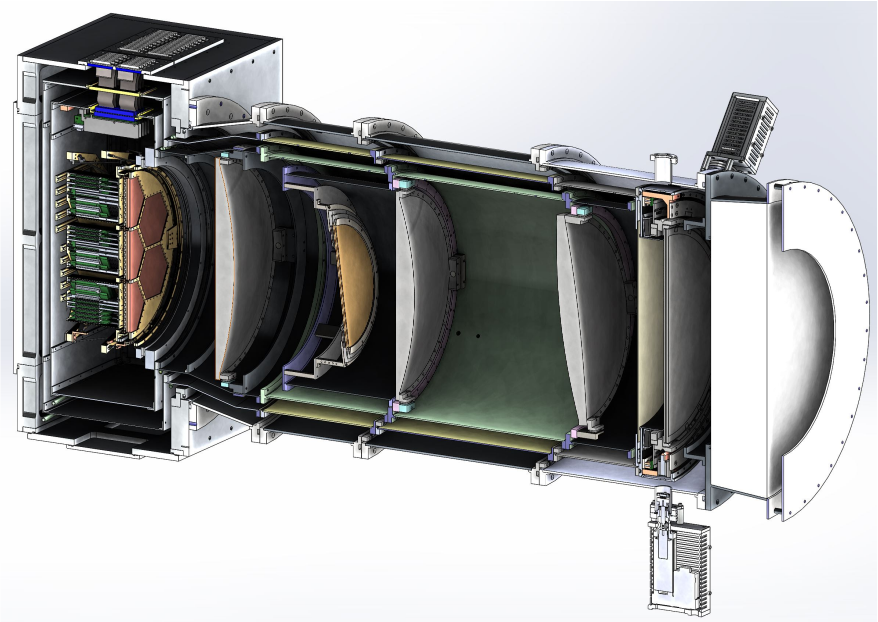

Figure 4.3: Section view of the POLARBEAR-2B receiver CAD model [153]. The length of receiver is 1.9 m. A description is given in the text.

The optics tube cryostat is located on the right of Figure 4.3. It consists of a vacuum window (the solid white structure on the far right), a cryogenic HWP (located between the vacuum window and the first lens), three reimaging lenses (the grey, convex circular structures), and a cold aperture (the yellow circular structure).

The focal plane and detector arrays are located on the far left of the figure,

---

[2] `https://www.cryomech.com`

inside the rectangular backend cryostat. The SQUID cards and wiring harnesses to readout the detector arrays are located directly above the focal plane assembly. The PTCs are not shown in the figure. An exploded view of the backend cryostat is shown in Figure 4.4.

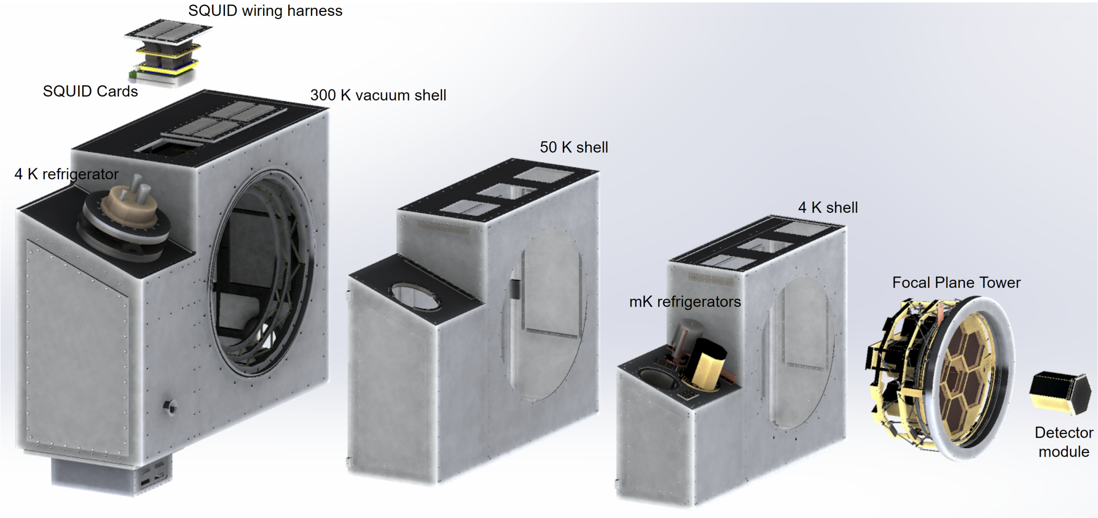

Figure 4.4: Exploded view of the of the POLARBEAR-2B receiver CAD model [153]. A description is given in the text.

The sorption fridges are, in the case of each receiver, mounted on the left hand side of the 4 K shell, as shown in Figure 4.4. The fridges then cool several thermal interception stages on the FPT, which is 360 mm in diameter. As well as providing thermal anchoring for the detector wiring, the FPT provides the required thermal environment and mechanical support and alignment for the detector modules. The detector stage is the circular plate with the hexagonal cutouts, which houses 7588 lenslet-antenna-coupled polarization sensitive TES bolometer pixels at 270 mK.

The sorption cooler used in the -2A cryostat is a standard Chase Research Cryogenics[3] CRC10 ("Berkeley-style") system, as shown in Figure 4.5. This fridge is similar to the one described in Section 3.7, with the addition of an extra ^{3}He stage in a separate coldhead.

---

[3] `http://www.chasecryogenics.com`

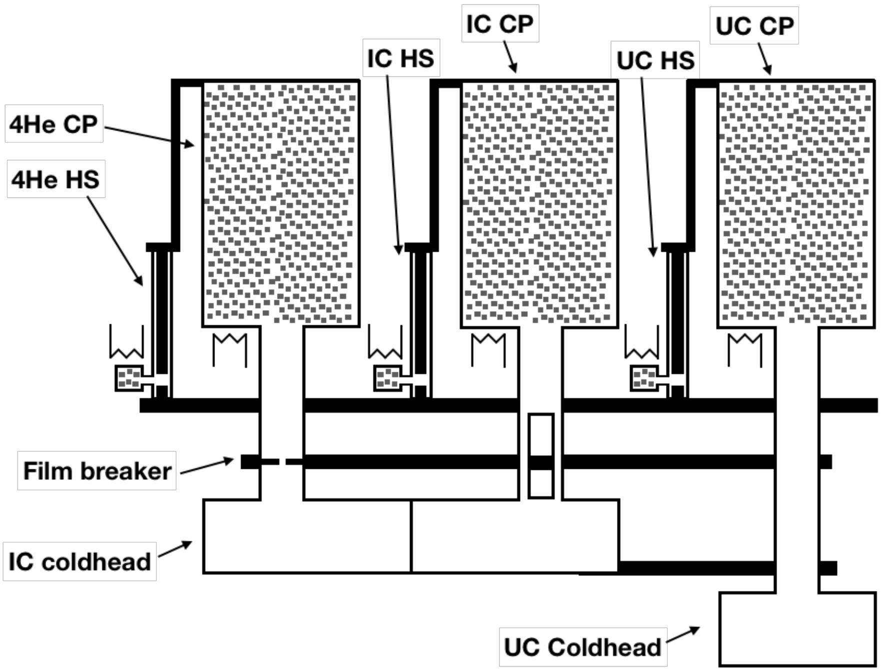

Figure 4.5: Schematic of CRC10 sorption cooler

The cycle is begun with all three pumps at 40 K in order to completely desorb all of the gas. The ^{4}He in the first stage (left in Figure 4.5) is condensed by the 4 K plate and liquid collected in the IC coldhead under the action of gravity.

The ^{4}He pump is then cooled (i.e., the heater switched off and the heat switch to the 4 K plate closed) in order to pump the condensed liquid down to 1 K[4] in the intercooler (IC) coldhead. The film breaker assembly[5] provides a vapour-cooled 2 K stage. The first ^{3}He stage shares the IC coldhead and therefore has liquid condensed at 1 K. The IC head is also coupled to the pumping tube of the ultracold (UC) stage and so the ^{3}He here is also condensed at 1 K. When the ^{4}He charge expires, the film breaker temperature is seen to sharply increase due to the absence of vapour cooling, whilst the IC coldhead will remain at 1 K due to its large heat capacity. The IC pump is then cooled to pump the condensed ^{3}He down to 350 mK which further precools and intercepts thermal loading to

---

[4] The temperatures of the stages quoted here are the nominal temperatures; the actual temperatures are of course loading dependent, as discussed later.

[5] CRC does not publish details of the mechanism of action of their film breakers, although they provide a similar function to the design described in Section 3.5.2

the UC stage. When the IC stage reaches its base temperature of 350 mK, the UC pump is then cooled which provides cooling for the detector stage at 270 mK. When cold, the fridge therefore can be seen to provide stages at 2 K, 350 mK, and 270 mK.

During testing of the POLARBEAR-2A receiver at the High Energy Accelerator Research Organization (KEK) in Japan, the 270 mK stage gave a measured cooling power of 10 μW at 270 mK [154]. However, it was also measured to have a hold time of only 20 hours, limited by the IC stage. This was traced to poor condensation efficiency of the ^{4}He, where it is completely used to precool the focal plane, requiring ^{3}He in the IC stage to be spent to cool to operational temperature. An example cycle is shown in Figure 4.6.

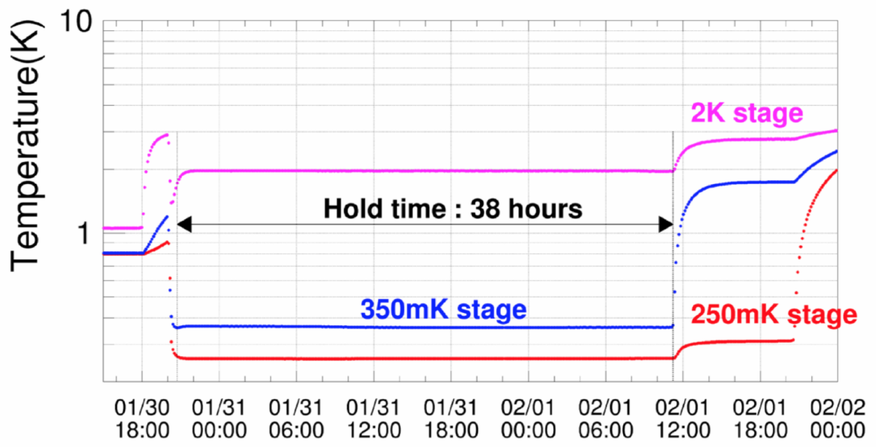

Figure 4.6: Cycling of CRC10 in POLARBEAR-2A cryostat at KEK [154]

In order to improve the observational efficiency for the -2B and -2C cryostats, with a goal of 72 hours to allow a 3 sidereal day schedule, different fridge configurations have been used. POLARBEAR-2B uses a so-called “gas-light” CRC system (GL10), which differs from the CRC10 in that the ^{4}He stage operates from a separate third coldhead, hence allowing it to be used as a thermal buffer for the IC and UC stages. A schematic is shown in Figure 4.7.

Whilst this did provide an improvement over the performance measured in -2A, in order to meet the goal of 72 hours hold time, an independently operated

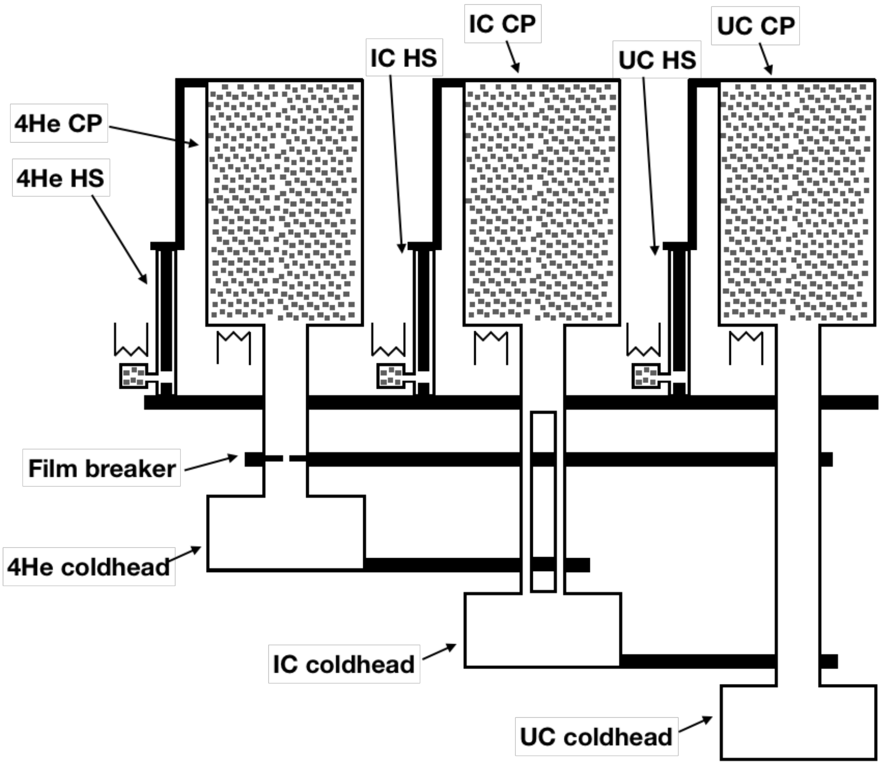

Figure 4.7: Schematic of GL10 sorption cooler

^{4}He "booster" fridge was designed in Manchester [147] and installed on -2B in order to increase the capacity of the 1 K stage further [153]. POLARBEAR-2C used a third type of CRC system, the so-called "super gas-light" which uses the same architecture as the gas-light shown in Figure 4.7, except with a much larger ^{4}He stage to negate the need for a booster fridge. Testing of these systems is reported in References [147, 153].

4.3 Temperature Stability Analysis

It has been observed during testing and characterisation of all three receivers, as well as by the author generally, that the temperature stability of sub-Kelvin sorption coolers is sensitive to a number of parameters, including the orientation of the system with respect to gravity. As the temperature stability affects the performance of the detector arrays, significant efforts have been devoted to characterising this stability in order to understand how it varies as a function of the telescope elevation and other parameters, and ultimately to help optimise the scan strategy of the Simons Array.

4.3.1 Allan Deviation

The standard approach for understanding noise in time series data, such as thermometry, is to calculate the power spectral density (PSD) of the signal. However, whilst this allows the clear identification of periodic signals which appear as spikes in the PSD plot at a given frequency, it is not possible to identify other noise contributions and instabilities in this way.

In order to both quantify the level of stability and identify different types of noise present in the bolometer stage temperature time-series data, it has been possible to use an approach based on Allan deviations. The Allan variance is a two-sample variance formed by the average of the squared differences between successive values of a given regularly measured quantity, and was originally developed to measure the system performance of atomic clocks. The difference from standard variance is therefore that the Allan variance is based on measurement-to-measurement variation rather than measurement-to-mean variation [155, 156].

For N measurements of some variable y at measurement interval τ_0, the Allan variance σ_y^2 is

$$\sigma_y^2\left(\tau_0\right) = \frac{1}{2\left(N-1\right)} \sum_{k=1}^{N-1} \left(y_{k+1} - y_k\right)^2 \tag{4.1}$$

The Allan variance may then be calculated for a range of sampling periods τ by averaging n adjacent values of y so that $\tau = n\tau_0$ up to half the maximum measurement time. The Allan variance as a function of τ is then

$$\sigma_y^2\left(\tau\right) = \frac{1}{2\left(N-2n+1\right)} \sum_{k=1}^{N-2n+1} \left(\frac{1}{n} \sum_{j=k+n}^{k+2n-1} y_j - \frac{1}{n} \sum_{j=k}^{k+n-1} y_j \right)^2 \tag{4.2}$$

It may be seen then that the Allan deviation σ_y may then be calculated for a given time-series data set as a function of τ. Log-log plotting of σ_y against τ may then be done, where the slope of these data give information about the spectral density and the noise type. Furthermore, these data can be approximated by a series of straight-line segments if it is approximated that only a single noise type dominates in a given averaging-time regime; this has been well-justified in practice [156, 157]. Several types of noise have characteristic slopes, as given in Table 4.1.

Table 4.1: Characteristic slopes of different noise types in Allan deviation plots [156]

Slope	Noise type
$\tau^{-0.5}$	White noise (Gaussian)
τ^{0}	1/f type noise (flicker)
$\tau^{0.5}$	Random walk type noise
τ^{1}	Steady drift

By identifying these different features in a log-log Allan deviation plot, it is possible to both distinguish different types of noise or variation and find their relative magnitudes. Neither of these have been shown to be possible when they are overlaid in a PSD plot.

4.3.2 Code Development

In order to develop such a method applied to temperature time-series data, it was important to first identify whether the noise parameters could be backed out for a given artificially generated signal.

First, three dummy signals were produced, each with a single different noise type as shown in Figure 4.8.

The PSD plots were then calculated as normal, as shown in Figure 4.9. It is clear from this figure that, for example, it would not be possible to distinguish between a signal containing only random walk noise and a signal containing both Gaussian noise and linear drift.

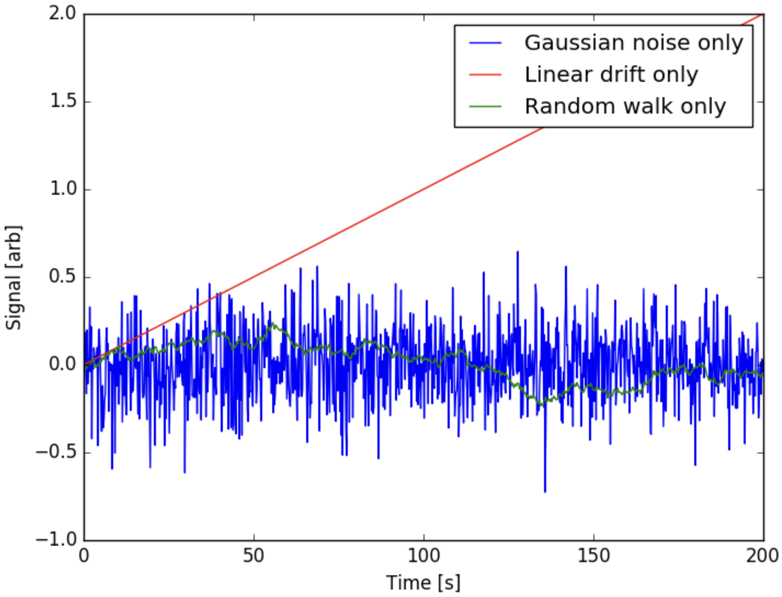

Figure 4.8: Dummy signals generated with different noise types

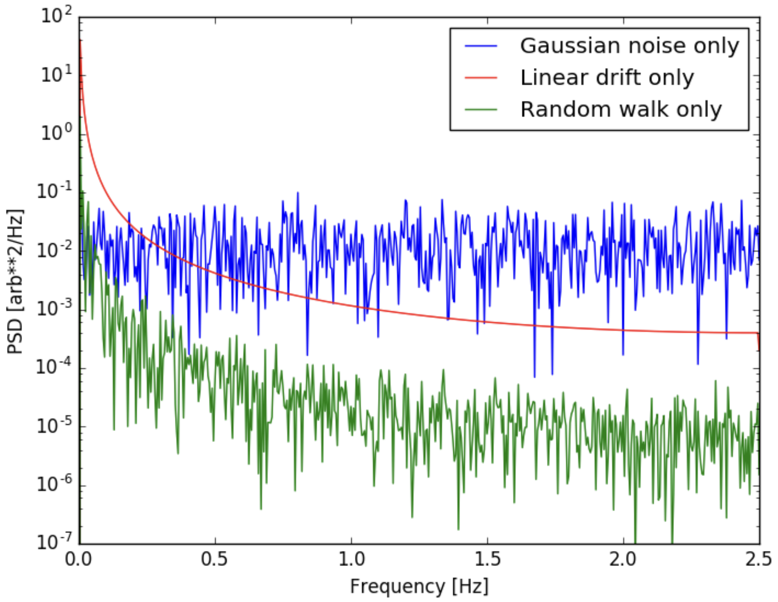

Figure 4.9: PSD plot for dummy signals with different noise types

The Allan deviation was then calculated and plotted for a range of sampling times as described in Section 4.3.1. The log-log plot in Figure 4.10 clearly shows the characteristic slopes in agreement with the theoretical values in Table 4.1.

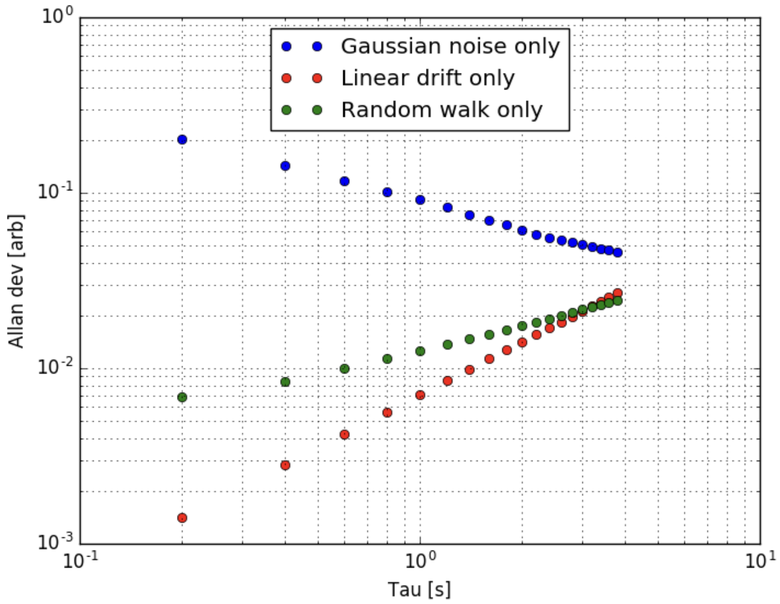

Figure 4.10: Allan deviation plot for dummy signals with different noise types

A dummy signal was then generated containing a combination of noise types, as shown in Figure 4.11.

Calculating the PSD, as shown in Figure 4.12, again demonstrates the difficulty in extracting information regarding the types, let alone relative magnitudes, of the noise components.

Calculating the Allan deviation however, clearly shows not only that the regime in which the different noise contributions dominate, but also that these regimes can be identified computationally by fitting straight-line segments to the data set, as in Figure 4.13. These fits show Gaussian noise dominating on timescales below ∼2 s and linear drift dominating on time scales above ∼10 s. The random walk component is sub-dominant at all time scales. The code written for this is given in Appendix A.3.

Given the loops required in the code, a brief study was also conducted to investigate the dependency of run time on the number of data points in the time-

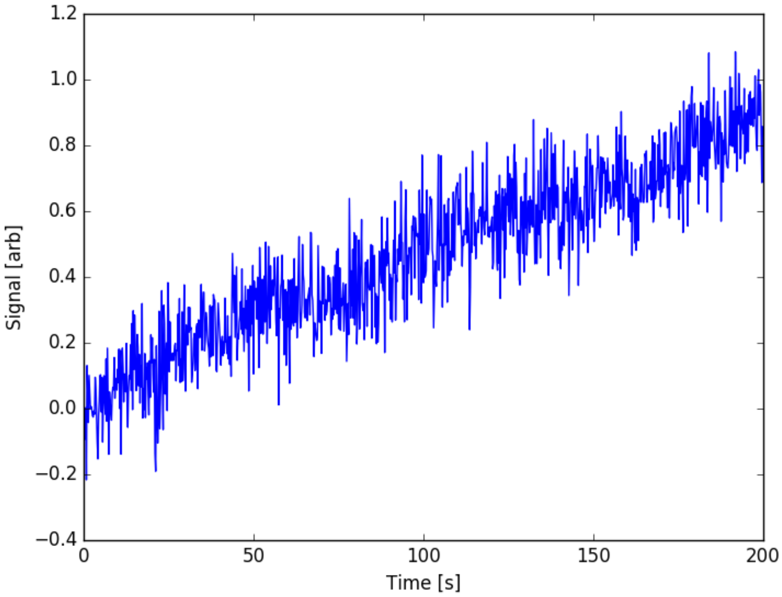

Figure 4.11: Dummy signal containing a combination of Gaussian and random walk noise with linear drift

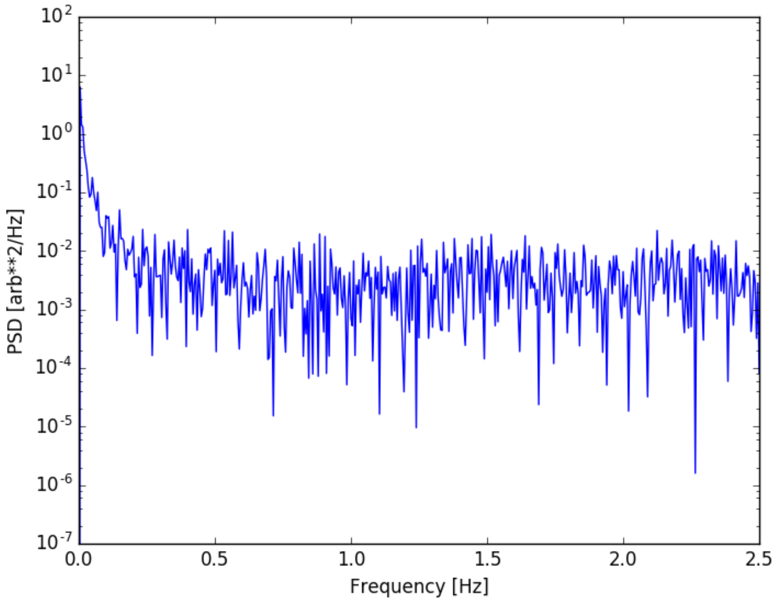

Figure 4.12: PSD for dummy signal with combination of noise components

series data N. As shown in Figure 4.14, the run time is proportional to $N^{5/3}$.

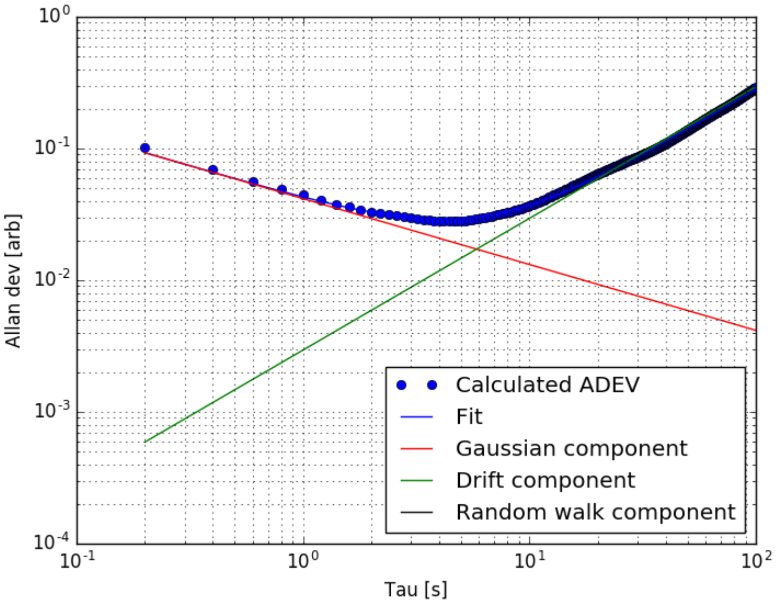

Figure 4.13: Allan deviation plot for dummy signal with combination of noise components

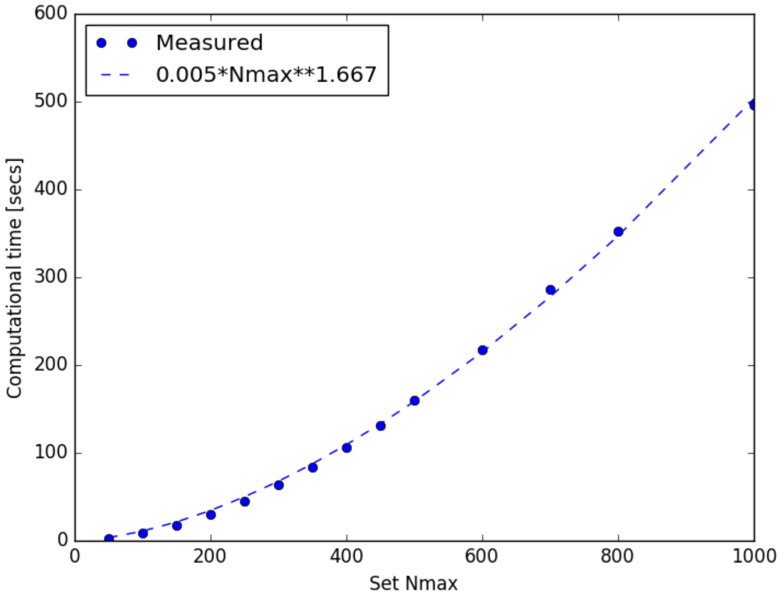

Figure 4.14: Computational time for Allan deviation plots as a function of number of data points

4.3.3 Stability Analysis of POLARBEAR-2A Detector Stage

Having validated the code with the dummy data, the same analysis was applied to actual data from POLARBEAR-2A. Figure 4.15 shows a sample data set for the CRC10 fridge showing multiple cycles under nominal conditions taken during the run39 experimental testing run at KEK in May 2018. All sub-2 K thermometers were Lake Shore RuO_2 RTDs.

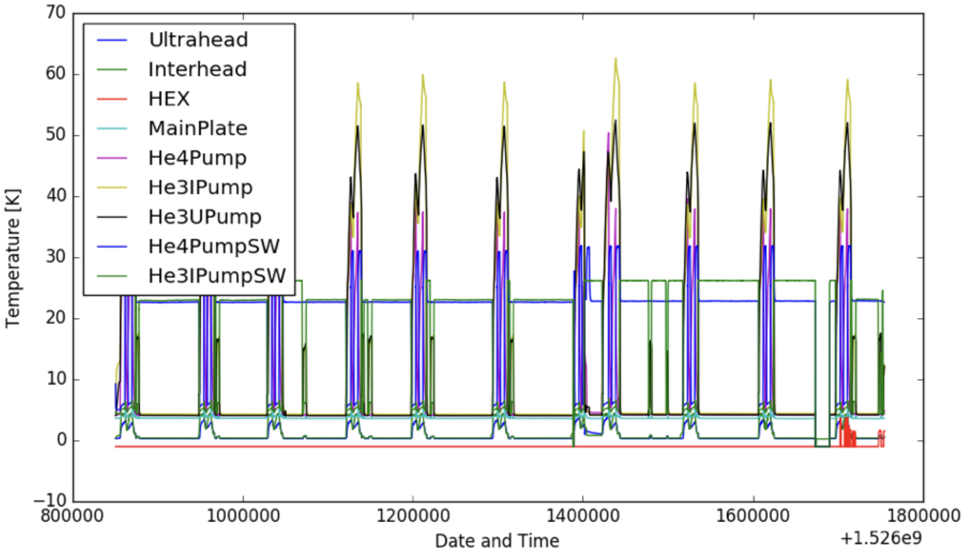

Figure 4.15: Temperature time-series data for multiple fridge cycles at KEK. Data courtesy of D. Tanabe.

The data were sampled at a rate of 0.2 Hz, giving $\tau_0 = 5$ s. A sample of temperature data for the UC head in the middle of a cycle was selected and is shown in Figure 4.16.

The Allan deviation was then calculated and is shown in Figure 4.17, along with the calculated noise fits. Excellent agreement with the data is shown by a noise profile containing four noise sources. Gaussian noise can be seen to dominate on time scales < 20 s. Flicker noise then appears to dominate on intermediate time scales. On time scales > 300 s, long term drift is dominant. A random walk component appears to be sub-dominant at all timescales.

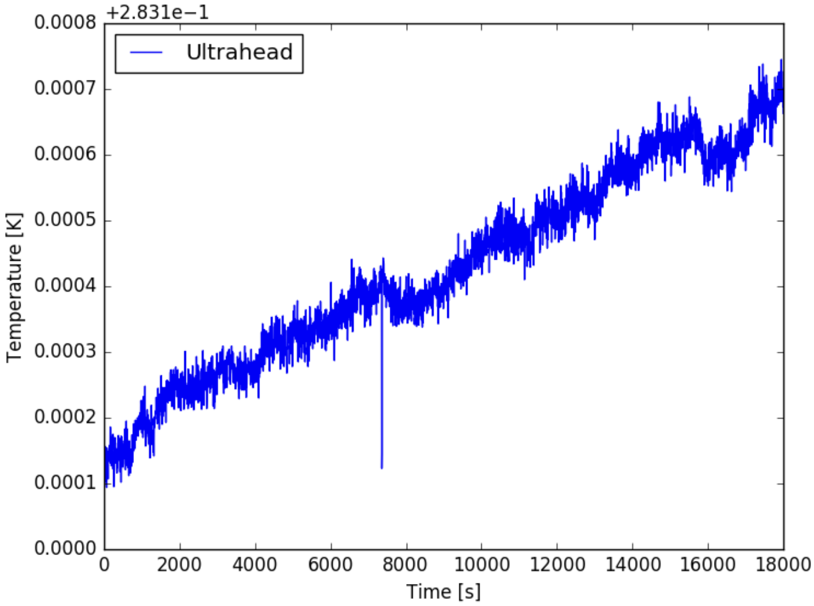

Figure 4.16: Selection of UC data mid-cycle

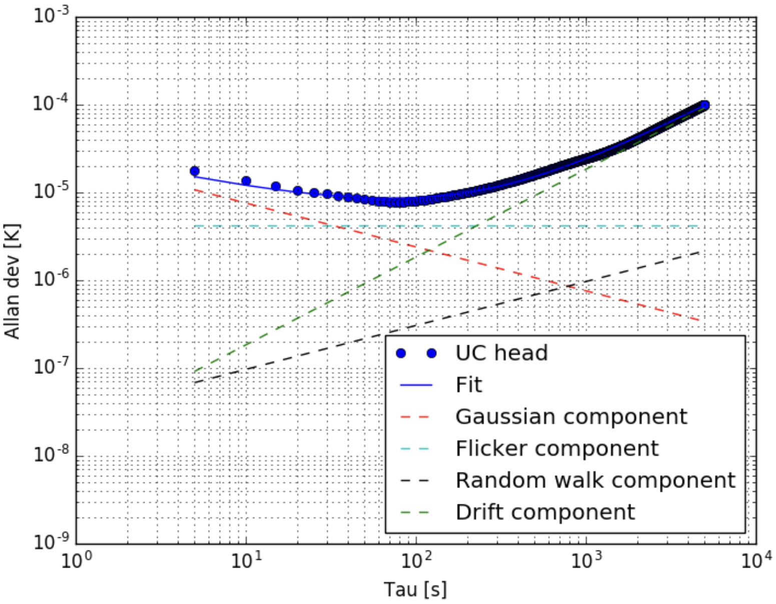

Figure 4.17: Allan deviation plot for selection of UC data mid-cycle

The POLARBEAR-2A receiver was deployed to the Atacama in December

2018. On site, the RTDs are read out by a Lakeshore[6] 370 and the temperature data from the site computer then packed in slowdaq files. Having been validated with this data format, the code will now be implemented as part of the housekeeping data analysis pipeline. For each fridge cycle, a report can be generated giving the Allan deviation plot along with other run parameters and added to a database. Investigations can then be carried out regarding the correlation of the stability with receiver elevation, as well as ambient air temperature, RF box temperature and other parameters. Ultimately, the aim will be to feed this information into the development of a ground template in order to further optimise the scan strategy.

It has also been suggested to apply the Allan deviation analysis developed here to bolometer time-stream data [158]. Whilst in principle this would allow the same characterisation of noise sources and drift as shown for the temperature data, this has not yet been explored in detail although is suggested for future work.

---

[6] `https://www.lakeshore.com/`

Chapter 5

Cryogenic Systems Development for the Simons Observatory

The Simons Observatory[1] [77, 159] is a forthcoming experiment that will bring together and build on the successes of the Simons Array[2] [145] and ACTPol [146] collaborations to develop a next generation CMB polarization observatory, increasing the detector count by approximately an order of magnitude.

The observatory will field both a 6 m telescope coupled to a cryogenic receiver and an array of 42 cm aperture cryogenic cameras, with a combined total of over 60,000 TES detectors at 100 mK targeting a broad range of angular scales.

The author has been responsible for the testing of a range of heat switch technologies in order to significantly improve the cooldown time of the large aperture telescope receiver, as well as the development of a fast-cooldown 100 mK detector test cryostat based around a novel miniature dilution refrigerator architecture.

---

[1] The full collaboration list and details of supporting funding bodies are available at `https://simonsobservatory.org`

[2] See Chapter 4

5.1 Project Overview, Science Goals and Overview of Instruments

The Simons Observatory (SO) [77, 159] will field a next-generation CMB polarization experiment from a site adjacent to the Simons Array [145] and ACTPol [146] observatories in the Atacama. Still in the design phase, SO is currently planned to begin observations in the early 2020s. SO will measure the CMB temperature and polarization anisotropy in six frequency bands centred at 27, 39, 93, 145, 225 and 280 GHz. The initial SO configuration will comprise three small-aperture 42 cm refractive telescopes and a single large-aperture 6 m telescope fielding a total of ∼60,000 TES bolometers. This will allow SO to target angular scales between 1 arcmin and tens of degrees, supporting a range of science goals; these include measurement of the tensor-to-scalar ratio r and placing tighter constraints on cosmological parameters (see Section 1.1.1), finding high-z galaxy clusters via the Sunyaev-Zel'dovich effect [160, 161, 162], and constraining the sum of the neutrino masses by measuring lensing by large-scale structure [152].

The small-aperture telescopes (SATs) will map ∼10% of the sky to a white noise level of ∼2 μK·arcmin [159]. They will observe at degree angular scales, to constrain $\sigma(r) = 0.003$. The conceptual design for the SAT array is shown in Figure 5.1, each mounted in an independent pointing platform and surrounded by a screen to shield from ground emission. The receiver, inset in Figure 5.1, is shown in detail in Figure 5.2.

A detailed CAD model of the SAT cryogenic receiver is shown in Figure 5.2, and is composed of a primary cylindrical volume surrounding the optics tube and focal plane combined with a secondary volume to accommodate the cryogenic systems. A Cryomech[3] PT420 pulse tube cryocooler is used to provide 40 K

---

[3] `https://www.cryomech.com`

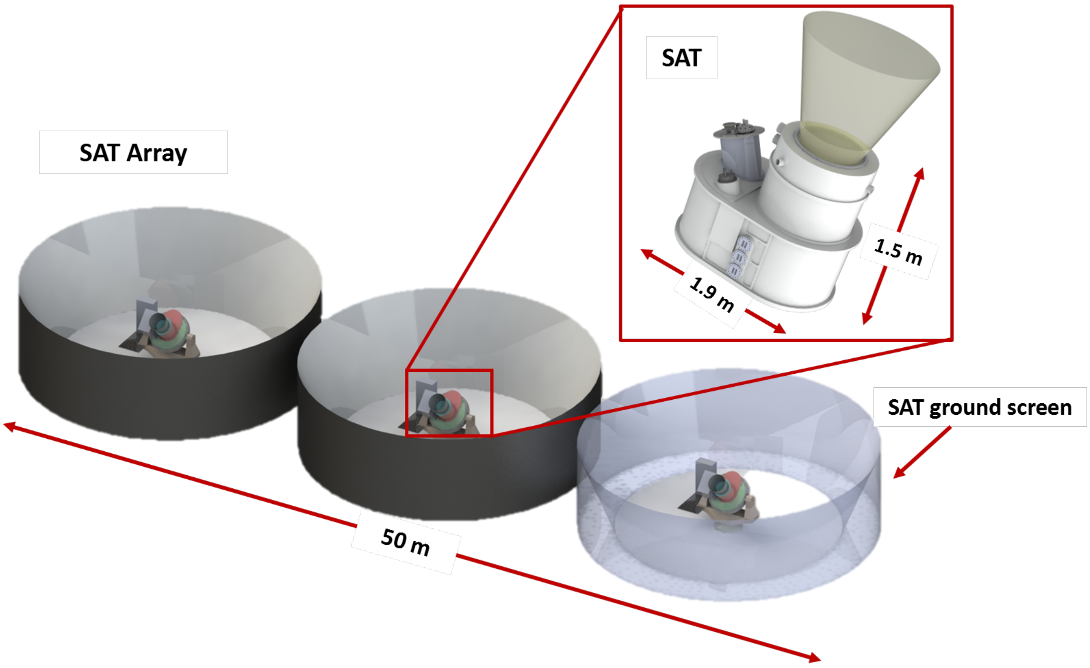

Figure 5.1: Conceptual design for the SAT array showing three telescopes on pointing platforms with surrounding ground shields [77]. The inset image shows a single SAT receiver cryostat with the 35° FOV as a shaded cone.

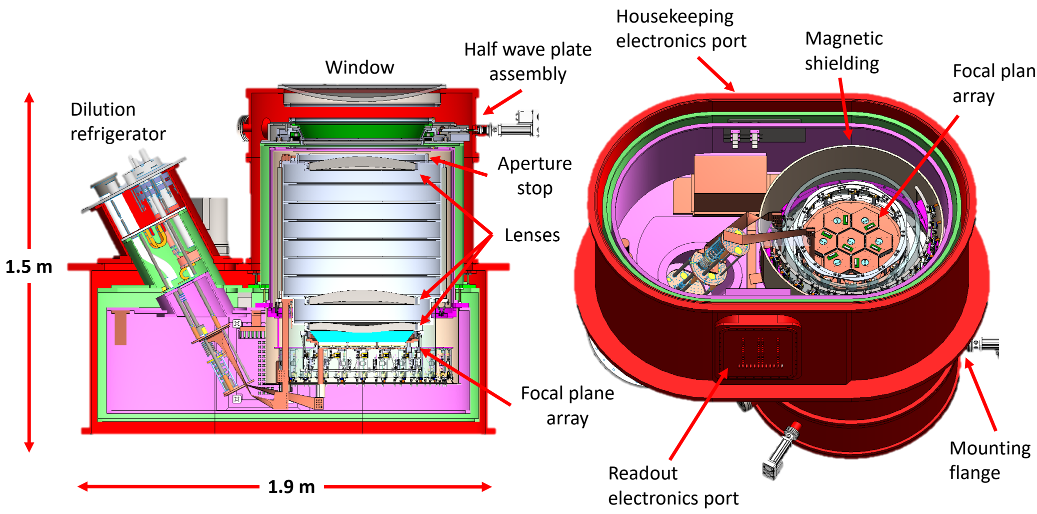

Figure 5.2: Design of SAT cryogenic receiver [77]. The image on the left shown a section view of the cryostat with the optics tube and focal plane array clearly visible, along with the angled dilution refrigerator. The PTC used to provide the 40 K and 4 K stages is not shown.

and 4 K stages, with 1 K and 100 mK stages provided by a Bluefors[4] SD400 dilution refrigerator (DR). The 40 K stage supports radiation shielding, as well as a continuously-rotating cold half-wave plate between the receiver window and the first lens to modulate polarization for improved control of systematics. Further shielding is cooled by the 4 K stage, with the aperture stop and lenses cooled to 1 K. The focal plane is operated at 100 mK, housing seven 150 mm detector wafers.

The 6 m Large Aperture Telescope (LAT), shown in Figure 5.3, is a crossed-Dragone [148] design, nearly identical to that of the Cerro Chajnantor Atacama Telescope prime (CCAT-prime) [163]. The LAT couples to the LAT Receiver (LATR) [164, 165] which houses the cold optics. The LAT optical design and optimisation are reported in Reference [166].

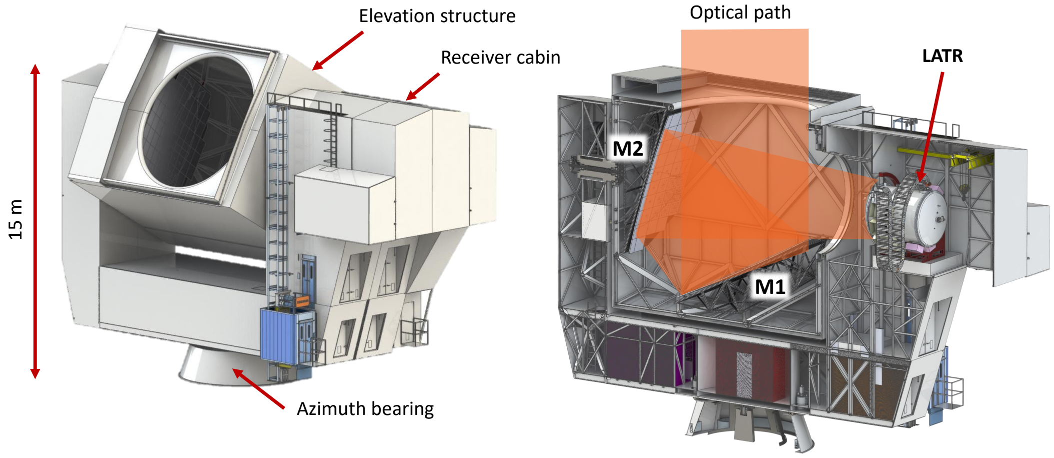

Figure 5.3: A cross-section of the LAT showing coupling to the LATR [77]. In the orientation shown in the image on the right, light enters the telescope structure from the top. It is then reflected by the 6 m primary (M1) and 6 m secondary (M2) before being directed to the receiver. The LATR is not directly coupled to the telescope elevation structure and will always be operated in the horizontal orientation shown; it may be rotated about its optical axis independently.

The LATR cryostat is designed to house 13 tightly-spaced optics tubes, as shown in Figure 5.4. For the planned initial deployment of seven optics tubes

---

[4] `https://bluefors.com`

(see Figure 5.5), the LATR will support ∼35,000 TES bolometers.

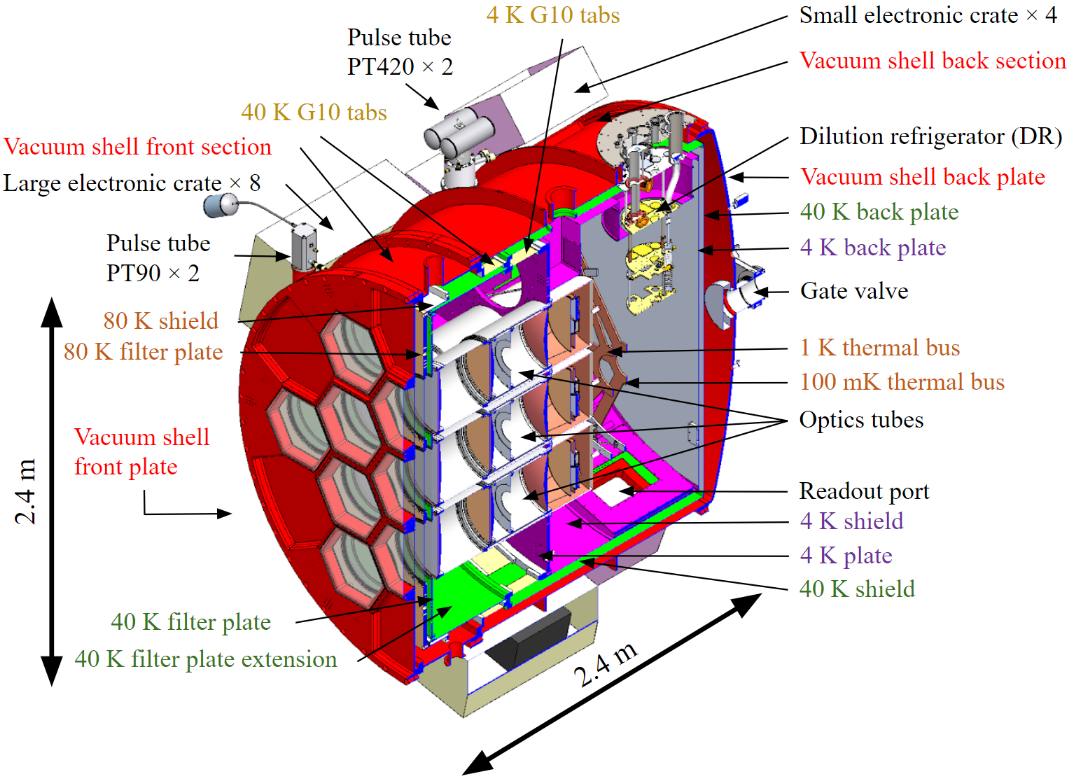

Figure 5.4: LATR cross-section [164]

Cooling stages at 80 K, 40 K, and 4 K are provided by two Cryomech PT90s and two PT420s respectively, with 1 K and 100 mK stages provided by a Bluefors LD400 DR (backed by an additional PT420). A detailed discussion of the theory and operation of DRs is given in Section 5.3.2. The optics tubes are designed modularly such that they can be installed as a single unit into the cryostat. The 80 K stage of the LATR supports a series of metal mesh and alumina filters to block infrared radiation from entering the optics tubes, as well as a short radiation shield. The 40 K stage supports a radiation shield completely surrounding the optics tubes, along with further IR blocking filters. The 4 K stage supports a further radiation shield and provides the primary mechanical and thermal mounting for the optics tubes, a cross-section of which is shown in Figure 5.5. The first lens is cooled by the 4 K stage, with the second lens, Lyot stop, and third lens

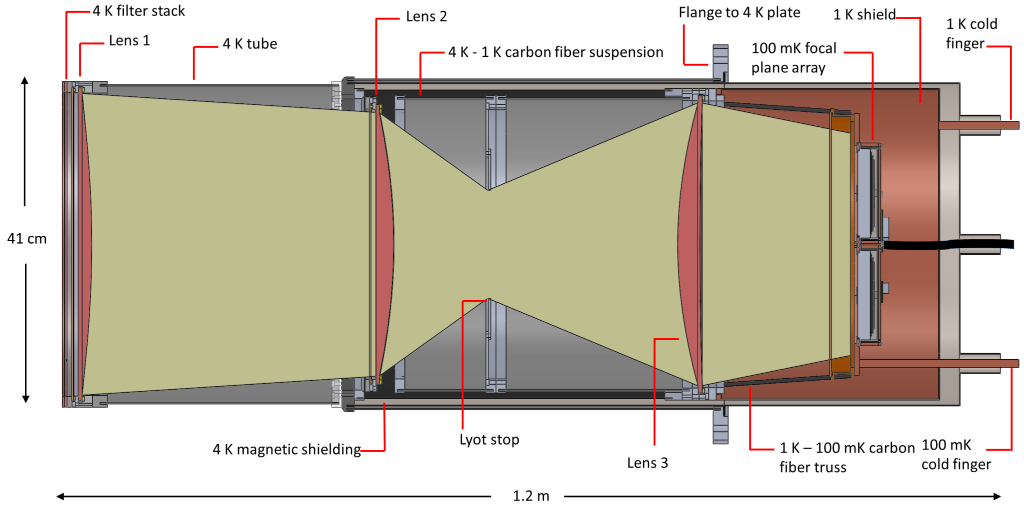

Figure 5.5: LATR optics tube cross-section, with the projected light path to the focal plane array shown in light green [164]

cooled by the 1 K stage.

The focal plane of each optics tube is cooled by the DR 100 mK stage via the 100 mK OFHC thermal bus shown in Figures 5.4 and 5.6. In order to minimise the thermal loadings from the 4 K stage to the 1 K stage and from 1 K to 100 mK, carbon fibre rods are used in truss assemblies as shown in Figure 5.6.

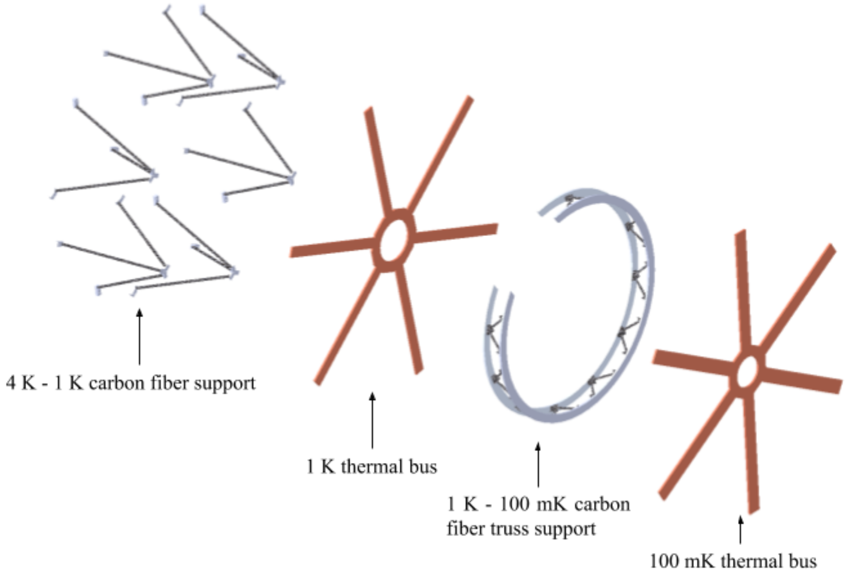

Figure 5.6: Exploded view of the LATR thermal bus [164]

Each focal plane will house three 150 mm detector wafers. Reference [167] details the universal focal plane module (UFM) architecture that has been developed, within which the detector wafer and readout components are stacked. As shown in Figure 5.7, the UFM has been designed so as to be compatible with both the ACTPol-style platelet horn-OMT coupled architecture developed at NIST [168] and the POLARBEAR-2 style lenselet-sinuous antenna coupled architecture developed at UC Berkeley [65].

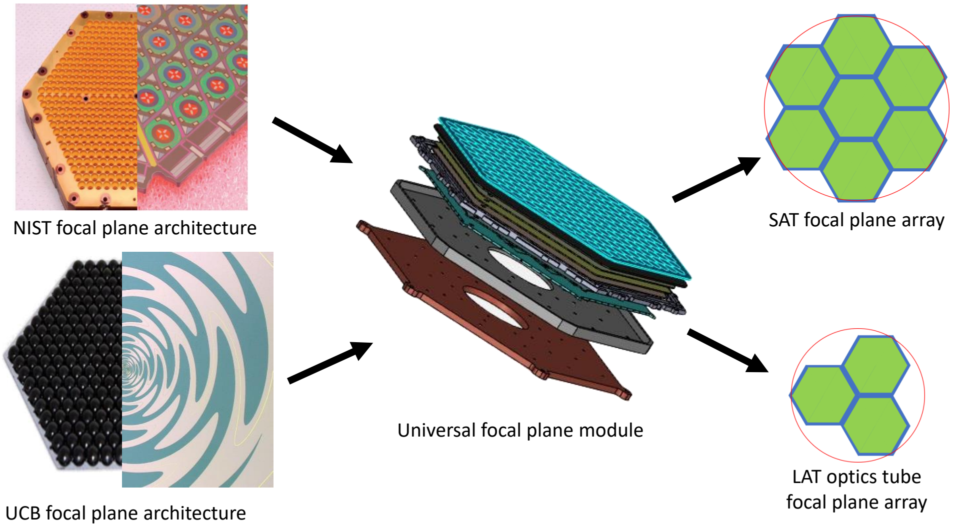

Figure 5.7: The SO universal focal plane module [77]. The upper left panel shows the NIST-ACTPol architecture which comprises a feedhorn array platelet coupled to an array of OMTs. The lower left panel shows the UCB-POLARBEAR-2 architecture which comprises a silicon lenslet array coupled to an array of sinuous antennas. Each type will be assembled into common UFM units which couple the detector arrays to cold readout wafers, magnetic shielding and mechanical/thermal mounting, as shown in the central panel. The UFMs are then assembled into the focal plane configurations shown in the upper and lower right panels for both the SATs and LATR optics tubes.

Each detector pixel will have four AlMn TES bolometers to measure orthogonal polarizations in two bands bands, with $T_c \sim 160$ mK. The TESs will be read out using microwave SQUID multiplexing (μmux) [169, 170]; this will allow thousands of detectors to be read out by a single pair of RF lines.

5.2 Precooling Heat Switches for the LATR

The complexity and optimisation of the LATR design have required significant efforts in static thermal and mechanical modelling, as detailed in Reference [165]. Furthermore, given the thermal isolation of the 1 K and 100 mK stages that has been required to meet the steady-state heat load requirements, significant efforts have been dedicated to modelling the transient thermal behaviour in order to estimate the cooldown time of the receiver [147, 171]. The thermal schematic used for the LATR is shown in Figure 5.8.

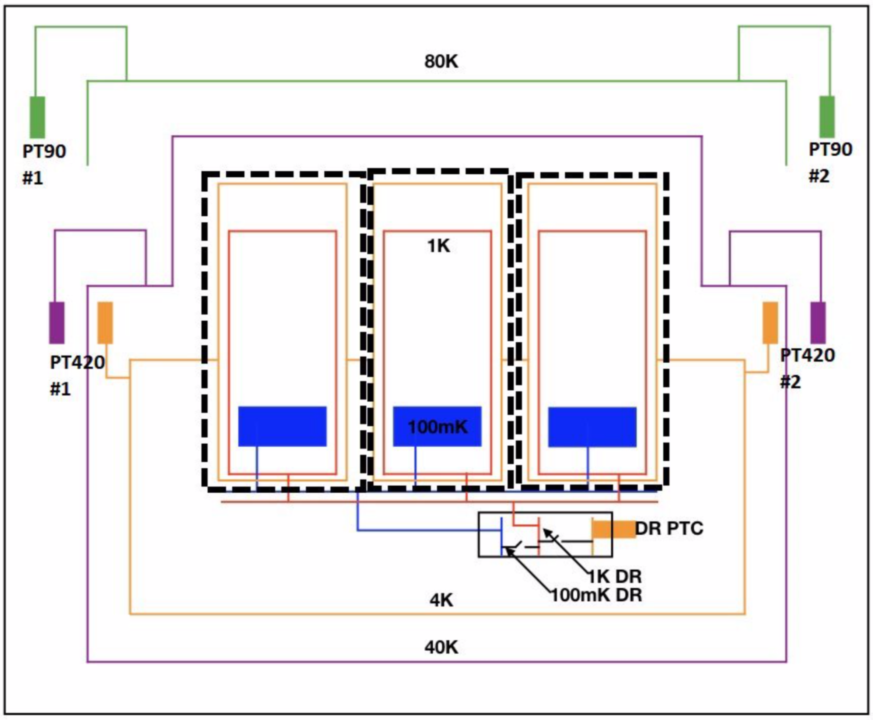

Figure 5.8: LATR thermal model [171]. Temperature stages are color coded (80 K in green, 40 K in purple, 4 K in orange, 1 K in red, and 100 mK in blue), with the heat lifts applied from the coolers as indicated. The dashed lines denote the optics tubes. The focal plane arrays are denoted by the blue boxes.

As opposed to the finite element modelling approach described in Section 2.6, the model here instead solves the heat transfer equations using an implicit finite difference method to improve the stability of the solutions. The model, discretisation scheme, and parameters are reported in References [147, 171].

In absence of any explicit precooling scheme, the results of the simulations for the LATR design as presented in Section 5.1 show that the 4 K, 1 K and 100 mK stages will reach their base temperatures in ∼35 days, with the 40 K and 80 K stages cooling in ∼15 and ∼10 days respectively [171]. The cooldown profiles of each stage are shown in Figure 5.9. For both receiver development testing and operation after deployment, it is highly desirable to reduce these cooling times. Several approaches have been considered to significantly improve the cooldown time for the LATR.

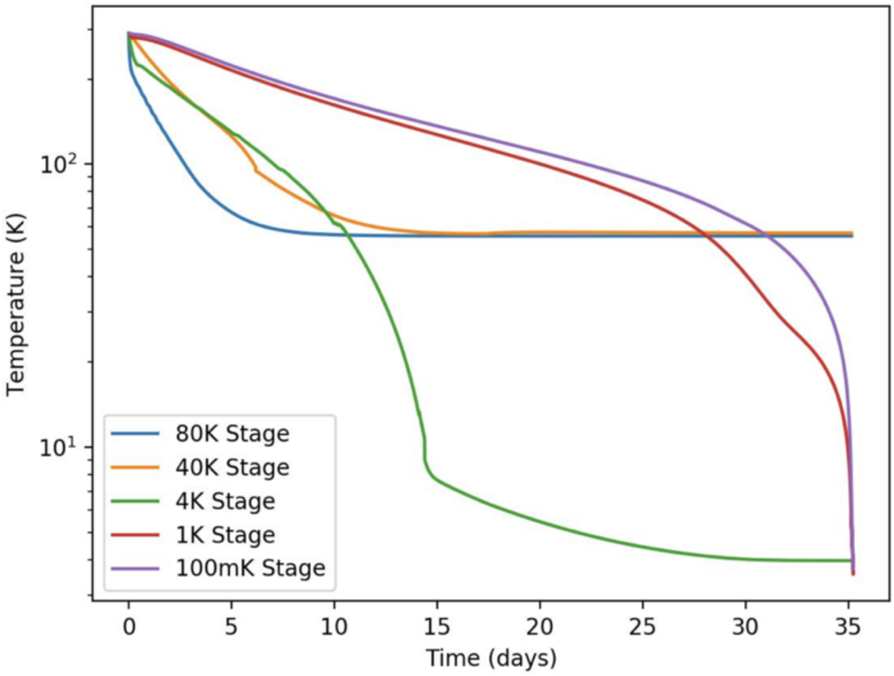

Figure 5.9: LATR modelled cooldown, without precooling scheme [171]

As described in Chapter 2, precooling of sub-80 K stages with LN_2 is common practice for many laboratory cryostat systems. Unfortunately however, given the remote deployment location for SO, along with the relative absence of laboratory infrastructure, LN_2 precooling has been considered impractical.

Other experiments have improved cooldown times for well-isolated cold stages through the use of a low pressure helium exchange gas in the vacuum space; this couples the low temperature stages to intermediate temperature stages [127, 172] to precool, before being pumped out and the cold stages cooled further to their base temperatures. This approach would also be challenging however, due to the affinity of helium to accumulate in the interstitial space of MLI [122], which in the case of the LATR will be used to minimise the emissivity of the 40 K stage. The use of helium exchange gas would therefore require significant pumping time to remove to a level where it does not induce additional loading (especially on the 100 mK stage).

A third and by far the most attractive strategy is the use of heat switches. By strongly coupling the 1 K stage to the 4 K stage, and the 100 mK stage to the 1 K stage, the lower temperature stages may be precooled and then decoupled for cooling to their base temperatures. In order to support this, switches must be used that are operationally reliable and have high switching ratios (i.e., the ratio between closed and open conductance), such that the precooling time is minimised whilst at the same time not appreciably increasing the steady-state heat leak to these stages. They must be operated in the closed position from room temperature down to ∼4 K, and then be opened below 4 K. In order to speed up the cryostat warmup phase, the switches would be required to transfer heat in the reverse direction; i.e., when the 4 K stage warms following cryocooler shut-off, the switch should strongly couple the lower temperature stages to 4 K. The switch must therefore not operate as a diode, as with the convective switches described in Chapter 3. Furthermore, the switch must operate without the use of magnetic fields, which could interfere with the detector readout. In principle, either passive or active switches could be used, presuming that the transition for the passive switches is tuned to ∼10 K.

These operating conditions preclude the use of superconducting, magnetoresistive, and liquid-gap switches [173, 174, 175, 176]. However, both gas-gap (either active or passive) and mechanical heat switches were considered to be candidate technologies. Several switches of each type were tested in Manchester and UC San Diego, with their open and closed conductances measured across a broad range of temperatures. The results are reported in the following sections, with comparison of the measurements and simulation results showing the improvement in cooldown time in Section 5.2.3.

5.2.1 Gas-Gap Heat Switches

Gas-gap switches typically operate through the use of a small gas adsorption pump which is able to actively fill or evacuate a small cavity between two copper rods inside a thin-walled stainless steel tube. This type of switch may be run using low current wiring (hence minimal thermal input to the cold side) and is notably very reliable [136]. On/off times on the order of 10 minutes are typical [177]. An illustrative schematic of such a switch is shown in Figure 5.10.

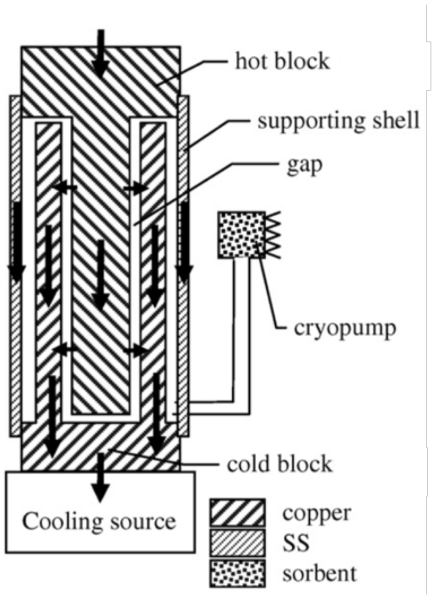

Figure 5.10: Gas-gap heat switch schematic, adapted from Reference [178]

One of several gas species may be used, including ^{4}He, H_2, and ^{3}He. Generally, ^{4}He may suffer from superfluid creep which can degrade the switch performance, and H_2 can suffer from the generation of heat via ortho-para conversion. ^{3}He on the other hand benefits from the absence of film creep and exothermic reactions, as well as high vapour pressure allowing operation down to lower temperatures than ^{4}He. Several low temperature groups have reported designs for switches of this type [177, 179, 180, 181, 182, 183].

In this way, the open conductance is reduced to the minimal conduction through the small cross-sectional area of the stainless steel and the closed conductance is several orders of magnitude larger due to the conduction through a small distance of helium gas and the copper rods inside the tube [94]. Both mechanisms of heat transfer are indicated by the arrows in Figure 5.10 (note that as the mechanism of heat transfer through the gas is conduction rather than convection, there is no dependence on gravity and hence the switch will work in any orientation).

Bluefors active gas-gap switches

The LD range of DRs available from Bluefors use active gas-gap switches in order to precool the still (1 K) and mixing chamber (100 mK) stages, which are then opened once the stages reach 4 K. These stages are shown for the LD250 model in Figures 5.11 and 5.12, which uses four switches between the 4 K and still stages and two switches between the still and mixing chamber stages.

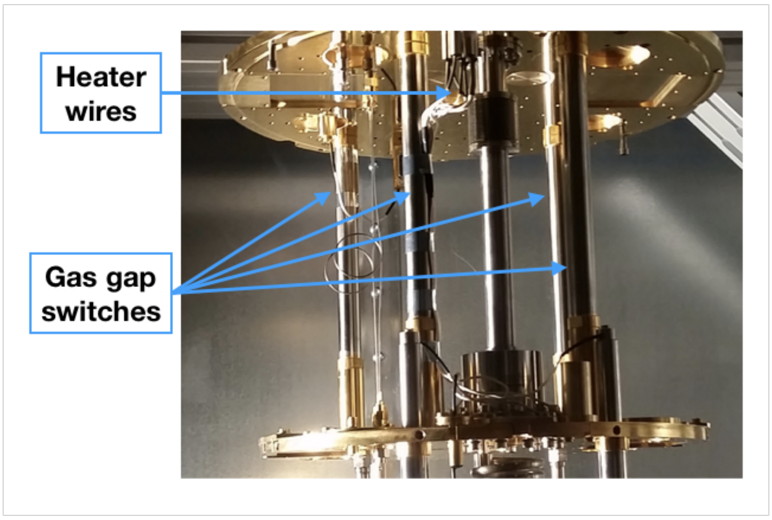

Figure 5.11: Photograph of LD250 gas-gap switches between the 4 K stage (upper plate) and still stage (lower plate), courtesy of N. Galitzki

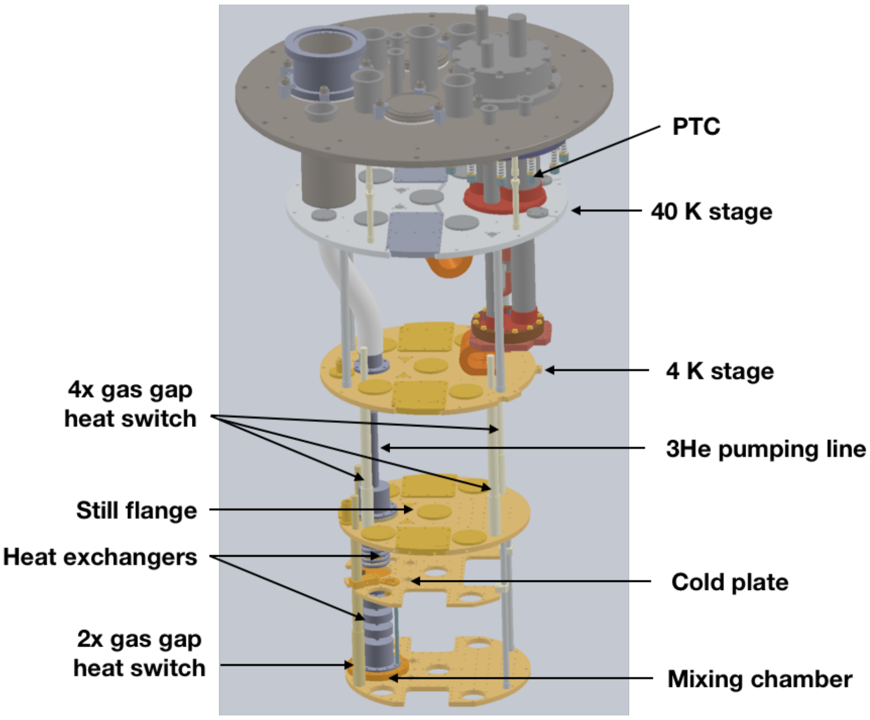

Figure 5.12: LD250 cryostat CAD model with vacuum chamber and radiation shields removed, courtesy of Bluefors

An LD250 has been purchased by the group at UC San Diego for a variety of 100 mK tests. Whilst the switches are a candidate technology, they are reasonably integrated with the cryostat structure as shown in Figure 5.11, and therefore could not be easily removed for conductance measurements. Instead, conductance values were backed out from cooldown data, where, to first order, the conductance can be modelled as function of mean switch temperature. The cooldown profile for each stage on the DR is shown in Figure 5.13, where the data was recorded at 60 sec intervals.

Two data sets were extracted, as indicated in Figure 5.13. The still, mixing chamber (MC), and cold plate (CP) stages are all well coupled above ∼100 K and were therefore approximated to be isothermal with each other for data set 1. In the cooldown data denoted data set 2, the MC and CP remain well coupled and were therefore approximated to be isothermal, whereas the still stage was treated separately. Data set 1 was hence used to find the conductance of the switches

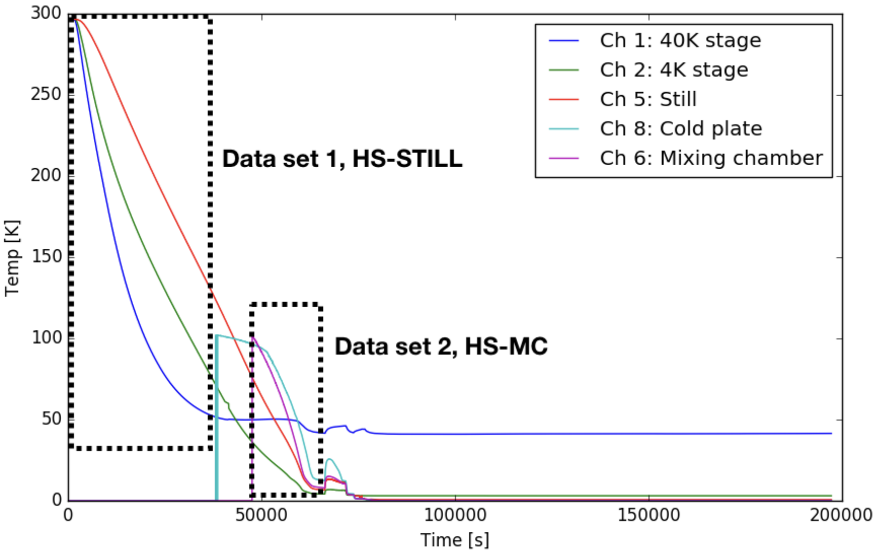

Figure 5.13: Bluefors LD250 cooldown, data courtesy of J. Seibert

above 100 K and data set 2 below 70 K. High order polynomials were fitted to the temperature data in order to smooth out thermometry noise.

As the masses and materials of each stage were known, lumped element models of both the still and MC+CP stages could be constructed for data sets 1 and 2, as shown in Figures 5.14 and 5.15. This model assumes that, firstly, the heat flow through the switches is the dominant source of heat transfer out of the cold stages (i.e., radiative cooling is neglected, given the high emissivity of the plate surface finish as shown in Figure 5.11) and, secondly, that the heat flow across the boundary of the elements was much greater than the heat flow internally (given the high conductivity of OFHC).

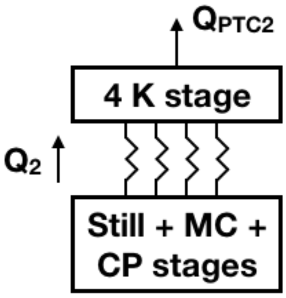

Figure 5.14: Lumped model for data set 1

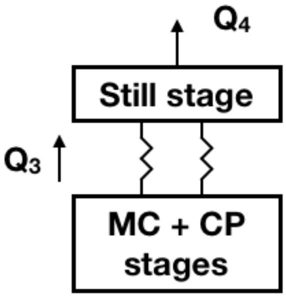

Figure 5.15: Lumped model for data set 2

The still was considered to be a single element of 9.1 kg of OFHC copper, and the MC+CP stage a single element of 5.0 kg of OFHC copper. Data for the specific heat capacity of copper was taken from Reference [100] (see Section 2.4.1).

The temperature step across the switches ΔT_{switch} and mean temperature could be found for the switches and, using the mass m and heat capacity c_p of the cold stages, the rate of heat transfer through the switches was calculated; the conductance κ of the switches was then found, from each data set, as a function of mean switch temperature T as

$$n\kappa\left(T\right) \simeq \frac{1}{\Delta T_{switch}}\frac{\Delta Q}{\Delta t} \simeq \frac{1}{\Delta T_{switch}}\frac{mc_p\left(T_{cold}\right)}{\Delta t} \simeq \frac{1}{\Delta T_{switch}}mc_p\left(T_{cold}\right)\frac{dT_{cold}}{dt} \tag{5.1}$$

where n is the number of switches in parallel. The calculated values for κ from each data set are shown in Figure 5.16.

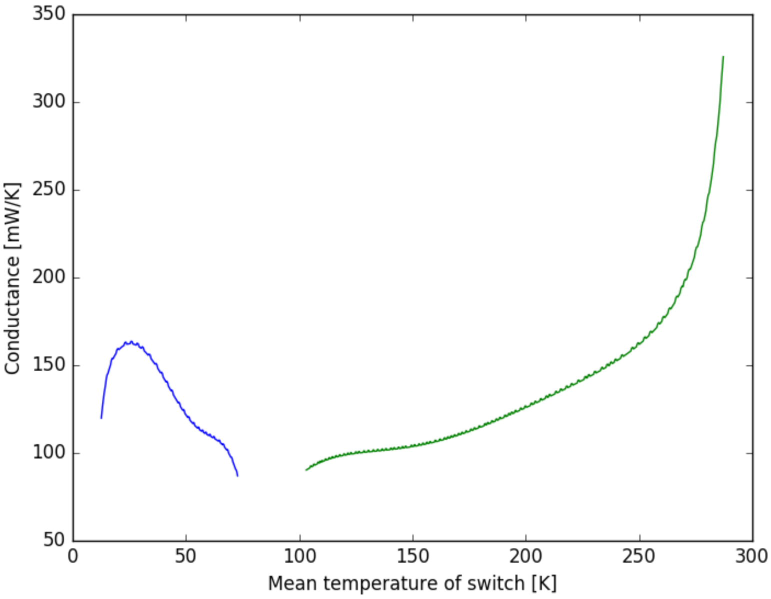

Figure 5.16: Calculated conductance of Bluefors gas-gap switches (per switch). The green curve denotes values calculated from data set 1 and the blue curve from set 2.

CRC passive gas-gap switches

A second type of gas-gap switch, in this case a passive switch manufactured by Chase Research Cryogenics[5], was tested in a 4 K test cryostat in Manchester, as shown in Figure 5.17.

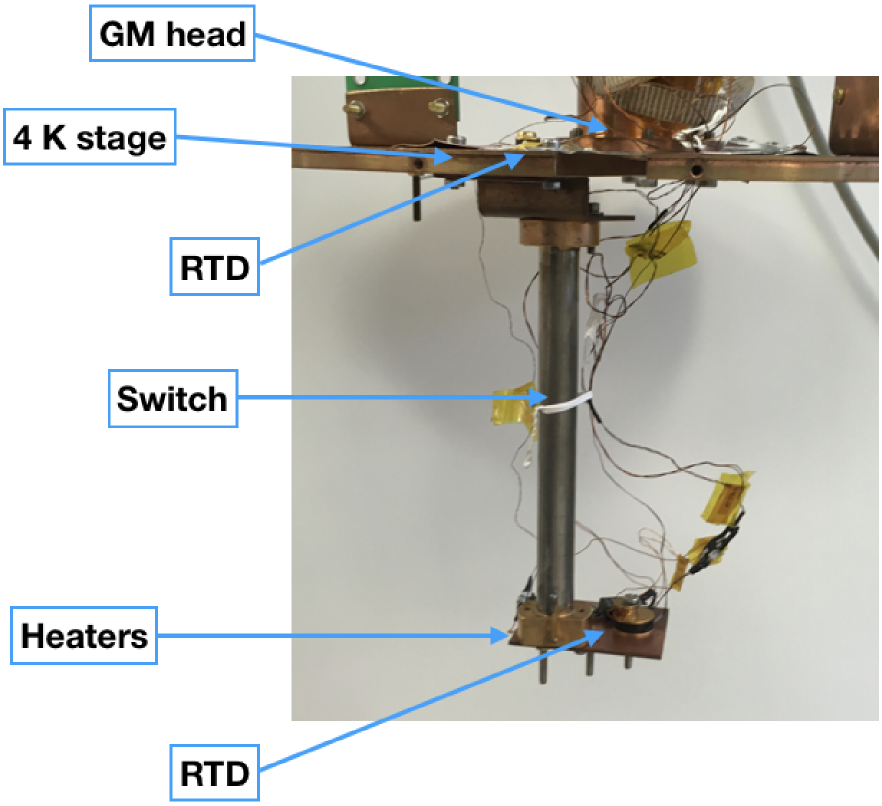

Figure 5.17: CRC passive gas-gap switch under test in Manchester 4 K cryostat

Here, the top of the switch was sunk to the 4 K stage as shown, with a heater and RTD mounted to the floating-temperature bottom end. The conductance was then measured for the switch by incrementally increasing the power applied through the heater and recording the steady state temperature of the floating end. The measured conductance data is shown for this switch in Figure 5.18, where the (passive) open/close transition is clear ∼10 K.

---

[5] `http://www.chasecryogenics.com`

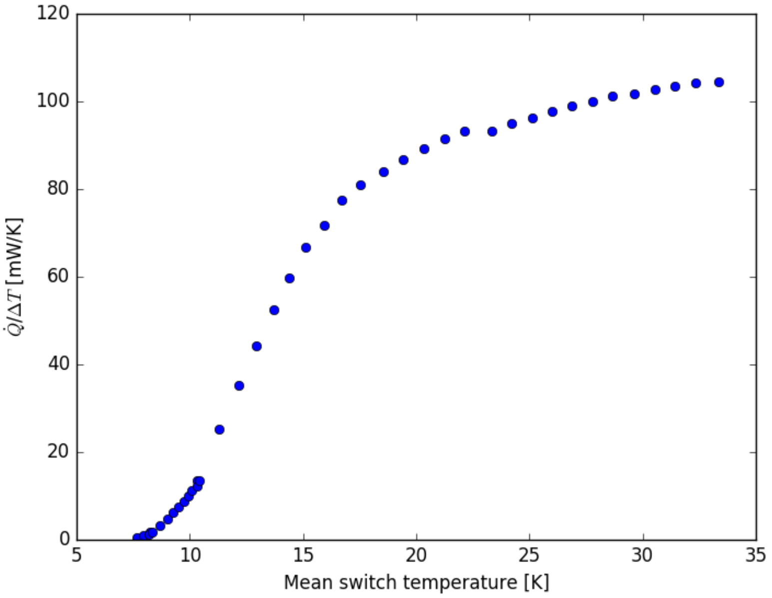

Figure 5.18: Measured conductance of CRC passive gas-gap switch as a function of mean switch temperature

5.2.2 Mechanical Heat Switches

Mechanical heat switches operate by actuating such as to make and break a physical connection. In this way, essentially zero open conductance is achieved, and very high closed conductances may be achieved as long as the required pressure may be developed at the interface (typically forces on the order of 100 N are required). As discussed in Section 2.4.3, thermal boundary resistance is an increasingly significant issue at lower temperatures and, as such, the surface finish of the mating components is also critical to the effective performance of these types of switches.

Operation of these switches also differs from gas-gap switches in that power is only required to change the state of the switch. However, these devices tend to be bulky and require high current leads to drive the motor, as well as requiring individual control units, complicating their integration with the LATR cryostat.

Two different mechanical switch architectures have been tested as with the

]

gas-gap switches in the previous section.

HPD mechanical switch

A mechanical switch available commercially from HPD[6] was purchased by the group at UC Berkeley and tested in Manchester using the same 4 K test cryostat as described in the previous section. The switch is shown mounted in this cryostat in Figure 5.19. The switch consists of a 12 V brushed DC motor which rotates a drive shaft to open or close the vice assembly as shown by the red arrows in Figure 5.19. The motor may be thermally decoupled from the vice by using a long, low conductance extension piece for the drive shaft if required. The motor in this case is thermally sunk at 4 K. The vice works so as to clamp or unclamp a pair of flexible gold-coated OFHC thermal shorts (in this case sunk at the top to the 4 K stage) to a cold finger which can then be coupled to the isolated stage.

The conductance of the switch was measured using both of the methods described in Section 5.2.1. Firstly, a cooldown run was carried out with an OFHC copper mass mounted to the cold finger such that heat transfer would occur through the switch to the 4 K plate as the cryostat cooled. A carbon fibre truss was used to support the cold finger from the 4 K stage in parallel with the switch in case of a switch failure, however as the thermal conductance of the truss was several orders of magnitude lower than the switch [80], this did not affect the analysis. The conductance of the switch as a function of mean temperature was then found as described for the Bluefors gas-gap switches in the previous section.

Several further cooldown runs were then carried out with several different heaters mounted to the cold finger as shown in Figure 5.19 to apply a range of heat loads. Again, a carbon fibre assembly was used to secure the cold finger. The heater powers were stepped and the steady-state temperatures recorded as for the CRC passive switch described in the previous section. The measurements from both methods are given in Figure 5.20, and give results that appear broadly

---

[6] `http://www.hpd-online.com`

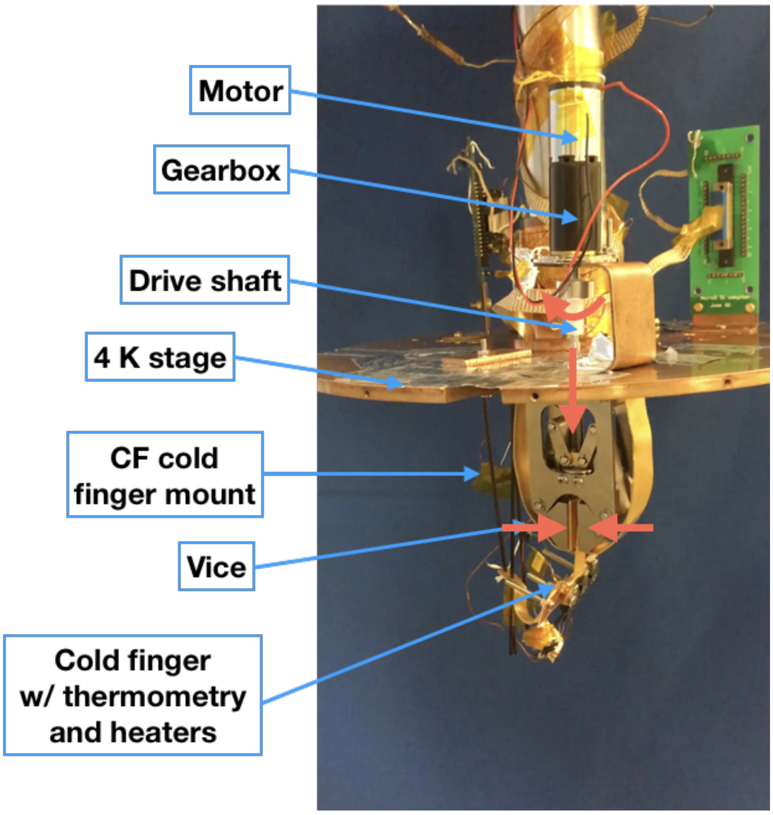

Figure 5.19: HPD switch under test in Manchester cryostat

consistent with each other.

Entropy mechanical switch

The Entropy[7] mechanical switch described briefly in Section 3.4 used for QUBIC was analysed using the backing out method.

As shown in Figure 5.21, the switch operates in a broadly similar fashion to the HPD switch. A motor, mounted on the warm stage, actuates so as as to clamp or unclamp the switch assembly to a gold-plated OFHC copper cold finger, bolted to the cold stage. Actuating the motor to open or close the switch dissipates ∼1 W on the warm stage for ∼30 secs. Both the thickness of the cold finger and the area of the clamp contact for the Entropy switch are significantly larger than for the HPD switch.

---

[7] `http://www.entropy-cryogenics.com`

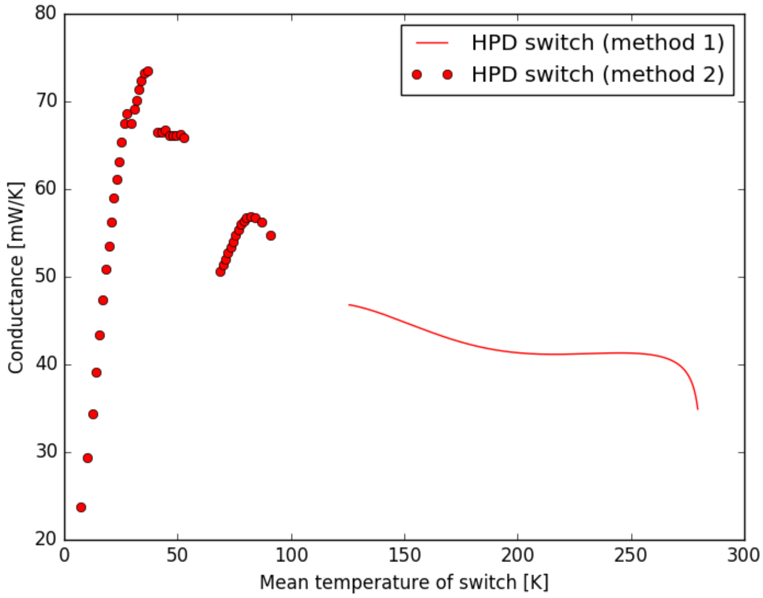

Figure 5.20: Measured and calculated conductance of HPD mechanical switch as a function of mean switch temperature. The red line show the values calculated using the backing out method and the red dots show the values measured from stepped heater loads.

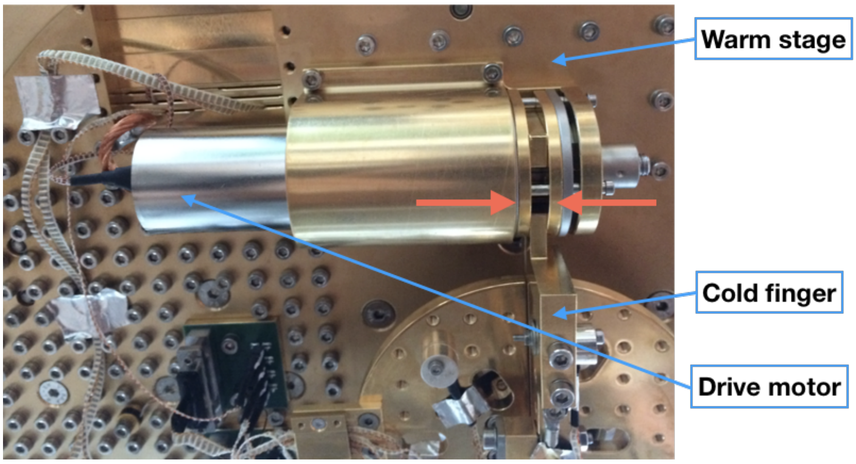

Figure 5.21: Entropy mechanical heat switch under test at APC. The length of the switch is 131 mm. Image courtesy: M. Piat.

Using cooldown data from a DR cryostat provided by Entropy, along with mass and material data for the cold stage, the conductance was calculated as described previously. The calculated values are shown in Figure 5.22.

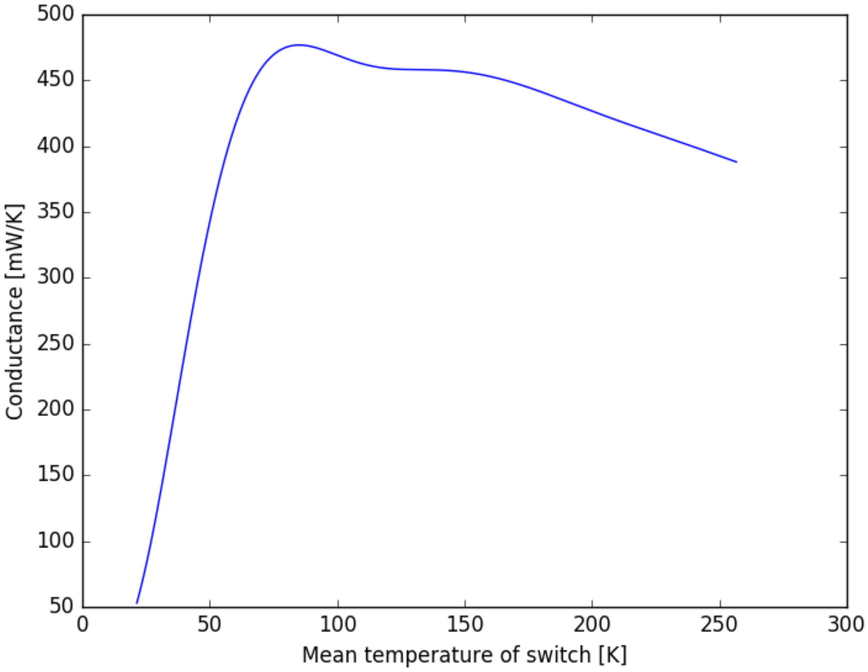

Figure 5.22: Calculated conductance of Entropy mechanical switch

5.2.3 Switch Comparison and LATR Cooldown Modelling

Having measured the temperature-dependent conductance of a range of candidate switch technologies, the data were compared as shown in Figure 5.23. This shows that the Entropy mechanical switch had a significantly higher conductance than the rest of the switches above ∼30 K.

On this basis, along with its characteristic of zero open conductance, it has been decided by the SO Cryogenics and Cryostat Working Group to proceed with the use of this type of heat switch for the LATR precooling. In order to characterise the reduction in cooling time for the 1 K and 100 mK stages, the simulation reported at the start of Section 5.2 has been rerun with several different configurations of the Entropy switch between the different stages as described in Table 5.1 [184]. The resultant cooldown times are given in Figure 5.24. Note that Sim C is the same model as that reported at the start of Section 5.2, i.e., with

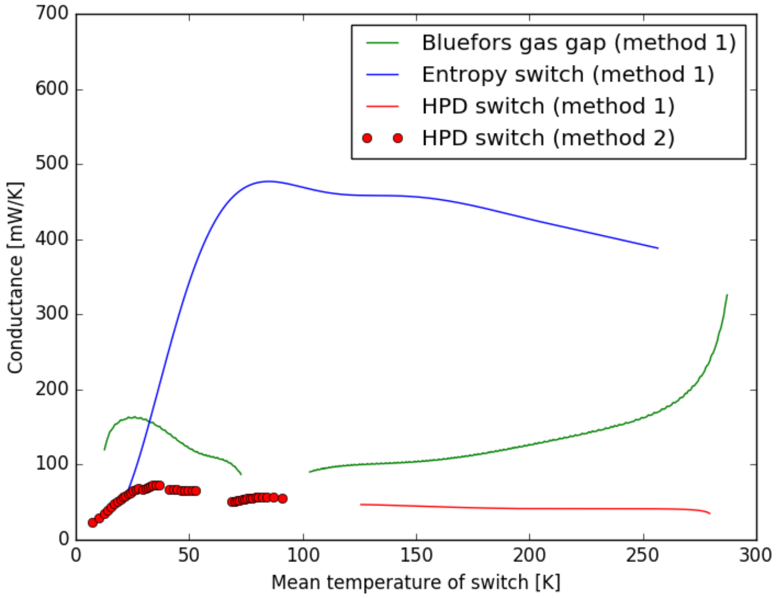

Figure 5.23: Comparison of heat switch conductances with temperature

no precooling scheme, for comparison.

Table 5.1: Mechanical heat switch configurations for the second set of LATR cooldown simulations [184]

Simulation	HSs 4 K to 1 K	HSs 4 K to 100 mK	HSs 1 K to 100 mK
A	1	1	0
B	4	0	4
C	0	0	0
E	8	0	4

It is clear from the simulation results that the cooldown time reduces with increased number of heat switches. However, there are diminishing returns in that a single switch between 4 K and 1 K and a second between 4 K and 100 mK reduces the cooldown time by ∼10 days (Sim A), whereas four switches between 4 K and 1 K and another four between 1 K and 100 mK reduce the cooldown only by an extra ∼2 days (Sim B). Adding further switches does not appear to improve the cooldown time any further (Sim E). Given the cost of the switches, it has been decided to purchase a pair of switches to be used as in Sim A.

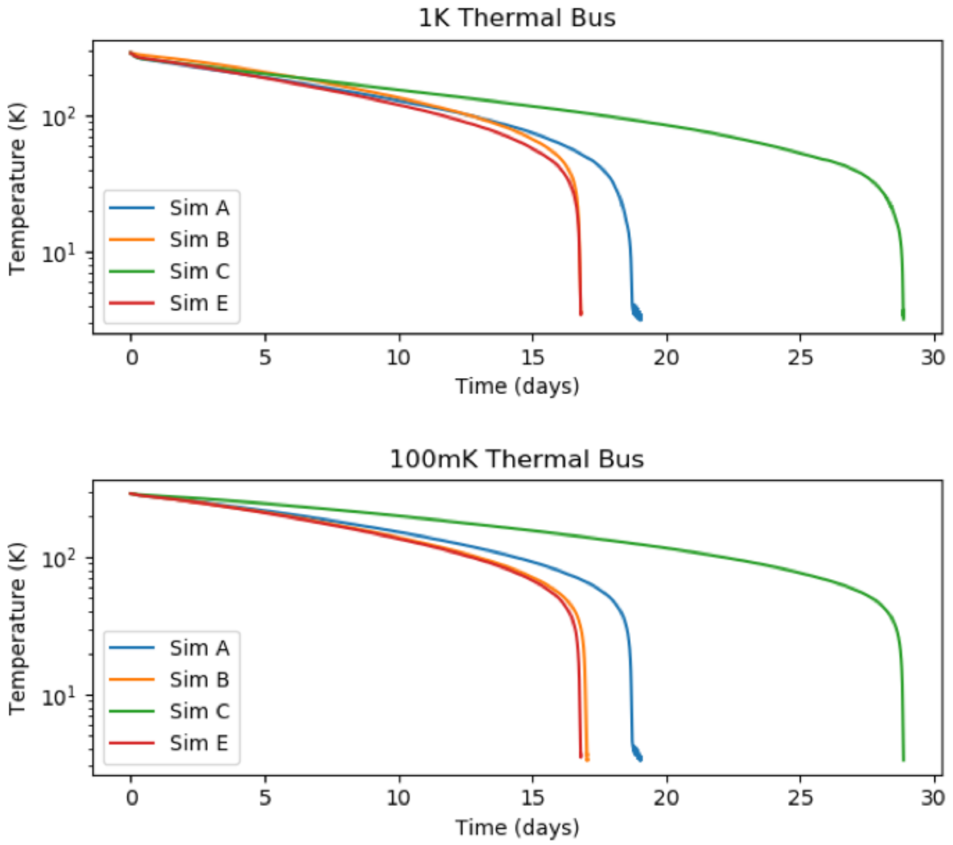

Figure 5.24: Comparison of LATR 1 K and 100 mK stage cooldown times with different precooling Entropy mechanical heat switch configurations [184]

5.3 Detector Test Cryostat Development

Given the volume of detector wafers that will need to be produced for SO (see Section 5.1), along with the challenges associated with fabrication [65, 185, 186], there is a clear need within the collaboration for rapid feedback testing capability at 100 mK. Given the complexities, as well as cost, associated with conventional, commercially available DR cryostats, it has been proposed to develop a rapid-cooldown 100 mK detector wafer test cryostat based around a miniature dilution refrigerator (MDR) architecture. In order to reduce the development time and costs associated with such a project, it was decided to modify the existing APEX test cryostat at UC Berkeley which is currently being used for POLARBEAR-2 detector testing.

5.3.1 Existing APEX Test Cryostat

The APEX test cryostat at UC Berkeley is shown in Figure 5.25. Concentric 40 K and 4 K stages are cooled by a PTC. A CRC10 fridge (see Section 4.2, especially Figure 4.5) provides several cold stages down to 250 mK, where the detector wafer under test is located.

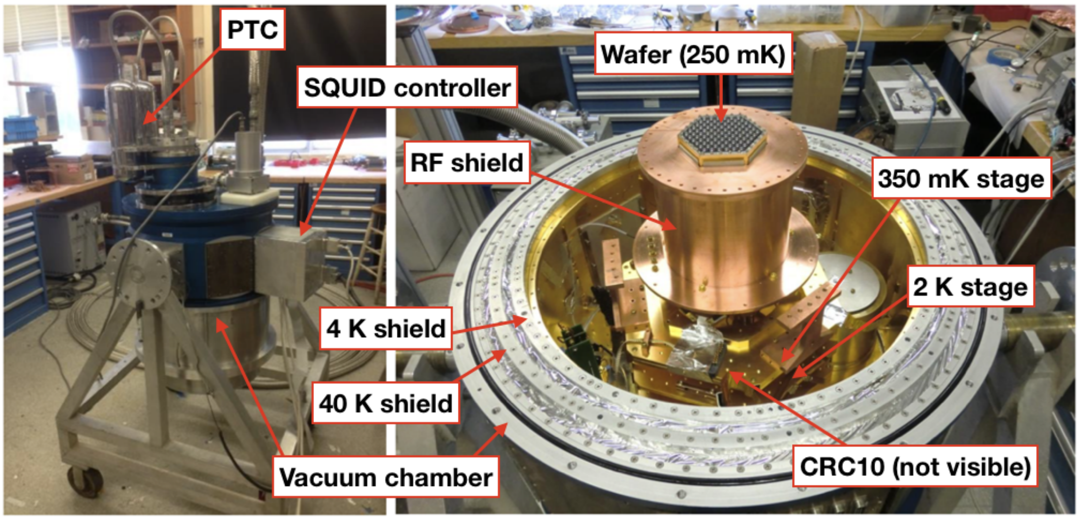

Figure 5.25: APEX test cryostat at UC Berkeley. The cryostat is shown during cooldown in the left panel. In the right panel, the cryostat has been rotated upside down and the 40 K and 4 K radiation shields removed. Photographs courtesy of A. Suzuki.

As described in Section 4.2, the CRC10 uses a ^{4}He stage to precool the IC coldhead to 1 K, with a 2 K stage provided by the film breaker (see Figure 5.25). Once the ^{4}He charge has expired, the IC (^{3}He) pump is cooled, pumping the condensed ^{3}He in the IC coldhead down to 350 mK (stage also shown in Figure 5.25). This stage also provides further precooling and thermal inception for the UC (^{3}He) stage which is then pumped down to 250 mK, cooling the detector wafer.

In order to modify this and similar cryostats to provide a 100 mK stage for SO detector testing, a design has been developed to retrofit the CRC10. The UC stage is removed entirely and an MDR stage installed which uses the IC stage to precool and operate a condensation pump as described in Section 5.3.3.

5.3.2 Dilution Refrigeration and Conventional Design

Having been described theoretically in 1962 [187], dilution refrigeration using ^{3}He in ^{4}He was first demonstrated in 1965 [188] and used to cool below 100 mK in 1966 [189]. Conventional DR systems today are available commercially from a number of manufacturers including Bluefors (see Section 5.1), Oxford Instruments[8], ICE Oxford[9], and Janis[10], and are widely used in a range of laboratory applications to reach temperatures on the order of 50 mK.

The dilution cooling process relies on the unique properties of ^{3}He/^{4}He mixtures. A review is given of the properties of the pure isotopes in Section 2.1. For ^{3}He/^{4}He mixtures, the phase diagram is shown in Figure 5.26, where

$$x = x_3 = \frac{n_3}{n_3 + n_4}, x_4 = \frac{n_4}{n_3 + n_4} \tag{5.2}$$

The λ-line denotes the temperature at which the superfluid transition takes place for a given x. In the region above the λ-line, the mixture behaves as a low density classical fluid. For $x = 0$, the superfluid phase transition takes place at 2.177 K [194] (see Figure 2.1). For $x > 0$, T_λ decreases with increased ^{3}He concentration [195] as

$$T_\lambda \propto (1 - x)^{2/3} \tag{5.3}$$

down to the tricritical point ($x = 0.67$ and $T = 870$ mK) [196] shown in Figure 5.26. As a fermion, pure ^{3}He does not undergo a superfluid transition in this

---

[8] `https://www.oxinst.com/`

[9] `https://www.iceoxford.com/`

[10] `https://www.janis.com/`

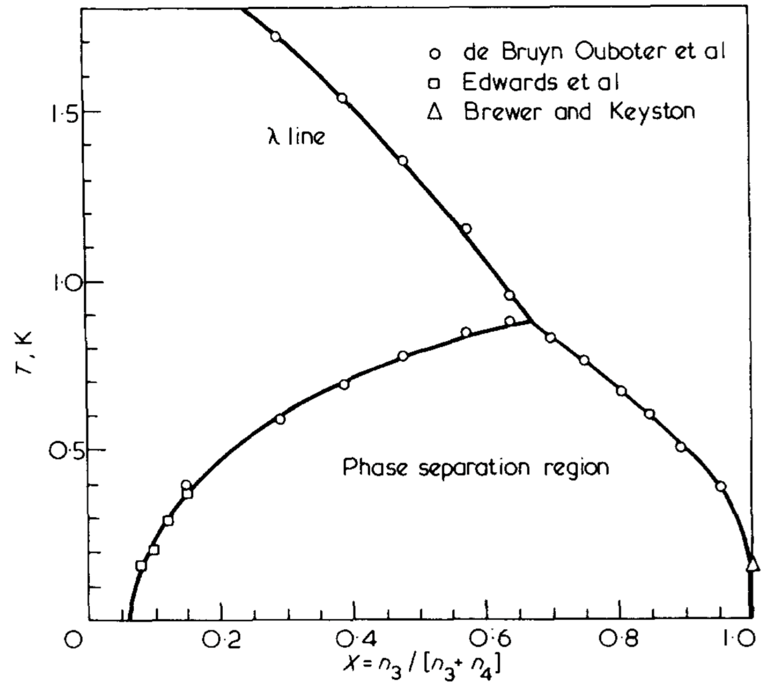

Figure 5.26: ^{3}He-^{4}He phase diagram from Radebaugh [190]; data from References [191, 192, 193]

way. However, at 0.94 mK (at saturated vapour pressure), the weak attraction between a pair of ^{3}He molecules does allow them to form a bosonic particle which undergoes a superfluid transition [84]; this is far below the normal operating regime of DRs however.

Considering the external cooling of a mixture $x = 0.5$, it may be seen from Figure 5.26 that the mixture will cross the λ-line, undergoing the transition to superfluidity at ~1.25 K. It then reaches the boundary of the phase separation region at ~750 mK. It is not possible for mixtures to exist in this regime and hence a phase separation occurs if the mixture is cooled further: the mixture separates into two phases at a higher and lower ^{3}He concentration known as the concentrate and dilute phases respectively.

By considering a pot of mixture cooled in this way, it may be seen that, as ^{3}He is less dense than ^{4}He, the concentrated phase floats on top of the dilute phase if operating under gravity. Furthermore, the dilute phase here is superfluid (i.e.

below the λ-line) but the concentrated phase is not.

As a strongly interacting Fermi liquid, it is not possible with current theory to calculate the specific heat for pure ^{3}He, although this has been measured experimentally [197]. It is possible however to calculate the specific heat for ^{3}He in the dilute phase, which is weakly interacting.

The heat capacity of electrons in a metal where $T \ll T_F$ is

$$c = \frac{\pi}{2}\frac{T}{T_F}R \tag{5.4}$$

which assumes no interaction. In the dilute phase the interaction with the superfluid ^{4}He atoms has been shown experimentally to approximate that of heavy particles in a vacuum; hence the effective mass $m*$ is introduced [198]. Taking $m* = 2.5m_3$ (for $x = 0.066$, see below) and $T_F = 1$ K, it may be found that $c_3 = 94T$.

In equilibrium, the chemical potentials of the ^{3}He in each phase will be equal, i.e., $\mu_{3D} = \mu_{3C}$. L_{03} is the amount of energy required to remove an atom of ^{3}He from the concentrated phase and place it at infinity at rest. Considering an atom of ^{3}He with energy E_{03}, as $E_{03} > L_{03}$ (i.e., the ^{3}He is more strongly bound in the ^{4}He) then the ^{3}He will dissolve across the boundary. However, this will only occur up to the point that $-L_{03} = -E_{03} + kT_F\,(x)$ where kT_F is the Fermi energy of an ideal gas of fermions with mass $m*$; the Pauli Exclusion Principle means that only two atoms are able to occupy each translational state [199].

At temperatures below 100 mK, the highest concentration possible in the dilute phase is $x = 0.066$. As a result, if the mixture at the start of the process has a higher concentration than this and is cooled to this temperature, then it will always end up with a dilute phase ($x = 0.066$) and a concentrated phase of pure ^{3}He ($x = 1$). It is important to note that even as T approaches 0 K, the solubility limit is still 0.066; this is integral to the operation of DRs.

If the above situation is considered, it may be seen that by decreasing the

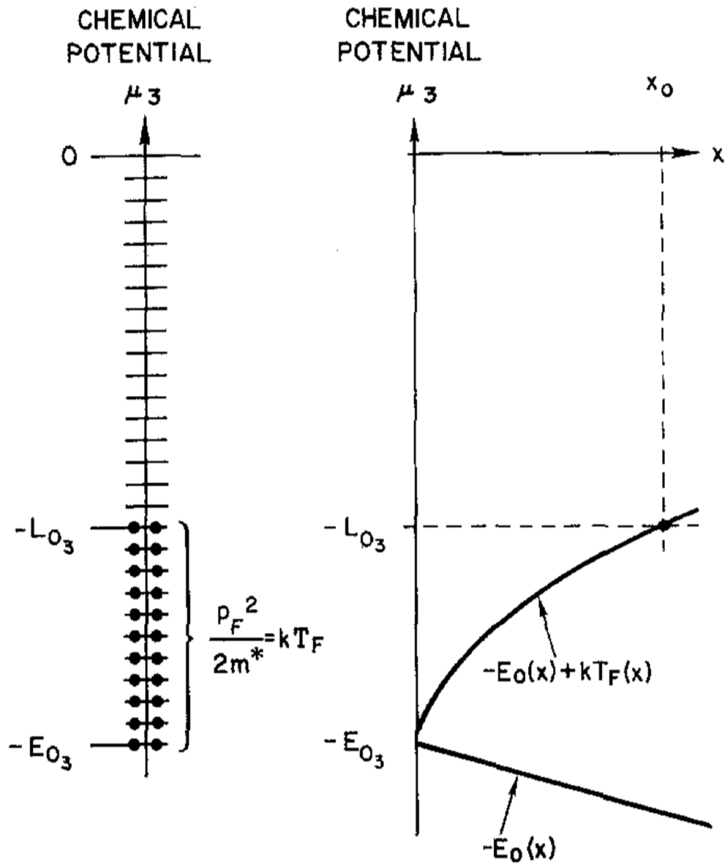

Figure 5.27: Energy diagrams describing the equilibrium of pure ^{3}He with a dilute solution at $T = 0$ K [199]

concentration of ^{3}He in the dilute phase, the two phases are moved away from equilibrium and ^{3}He atoms will migrate across the phase boundary into the dilute phase up to the solubility limit. This dilution is an endothermic process as the enthalpy of dilute ^{3}He is higher than that of concentrated ^{3}He [200], and hence this may be used to produce a useful heat lift at the mixing chamber.

In order to produce a continuous cooling, ^{3}He must be continually removed from the dilute phase. To find the cooling power of this process, a mixing chamber may be considered containing the two phases, as shown in Figure 5.28, for which ^{3}He is continuously removed from the dilute phase and injected into the concentrate.

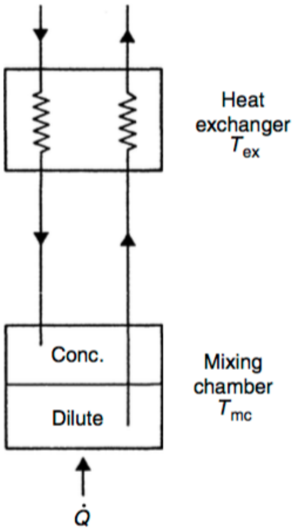

Figure 5.28: Diagram of mixing chamber and heat exchanger [80]

Since no external work is done in this process, the first law of thermodynamics shows that the cooling power at the mixing chamber is given simply by the difference in enthalpy entering and leaving the chamber as

$$\dot{Q} = \Delta H \dot{n}_3 \tag{5.5}$$

In this temperature regime, the molar enthalpy of the incoming pure ^{3}He and of the dilute solution have been found experimentally to approximate to 12T^2 and 94T^2 J/mol respectively [197] and hence the cooling power of the diluter is

$$\dot{Q} = \dot{n}\left(94T_m^2 - 12T_i^2\right) \tag{5.6}$$

where T_m is the temperature of the mixing chamber and T_i is the temperature of the incoming ^{3}He. Hence the minimum temperature that may be reached is limited only by the heat load, circulation rate and heat exchanger design. A further limitation to the minimum temperature that may be communicated from the helium in the mixing chamber to the cold stage is the Kapitza resistance between the liquid the copper used to construct the mixing chamber (see Section

2.4.3). Considering that $T_i > T_m$, it may be seen that the limit exists where cooling power goes to zero at

$$\frac{T_i}{T_m} = 2.8 \tag{5.7}$$

$T_i - T_m$ is minimised by careful design of the heat exchanger which precools the incoming ^{3}He using the enthalpy of the returning ^{3}He returning to the still. Approximating for a suitably well designed heat exchanger (HEX) $T_m = T_i$,

$$\dot{Q} \propto T^2 \tag{5.8}$$

In the general case, it may be considered how a conventional DR may be constructed based on the principals described, as shown in Figure 5.29.

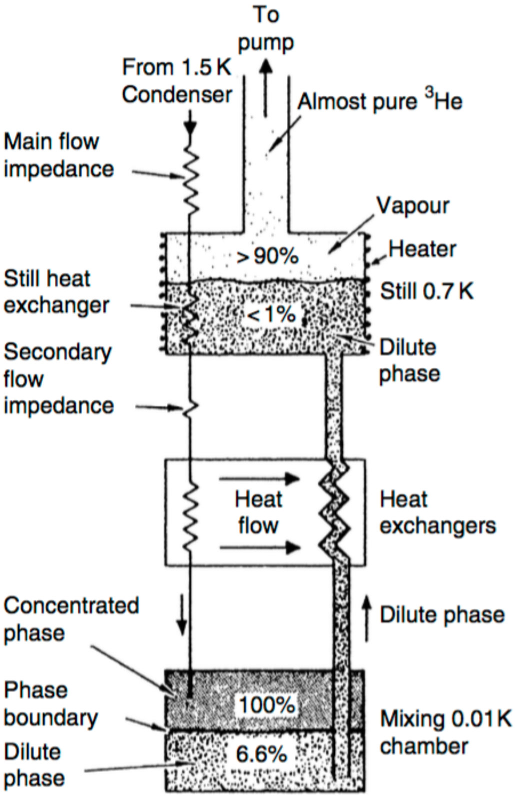

Figure 5.29: Diagram of typical dilution refrigerator [80]

Concentrated ^{3}He is injected at the top precooled to 1.5 K. It then flows (due to gravity) down a capillary (acting as an impedance) which provides adequate pressure drop for condensation to occur. The ^{3}He is then cooled further as it passes through the still heat exchanger and additional HEX before entering the concentrated phase of the MC (of the same form as that in Figure 5.28).

As described above, the ^{3}He in the dilute phase behaves as an ideal gas. The Van 't Hoff equation [80] gives the osmotic pressure Π as

$$\Pi \simeq \frac{xRT}{V_{m,4}} \tag{5.9}$$

where $V_{m,4}$ is the molar volume of ^{4}He. For two vessels containing this phase at different temperatures, it can then be seen that

$$\Pi_2 - \Pi_1 \simeq \frac{(x_2T_2 - x_1T_1)\,R}{V_{m,4}} \tag{5.10}$$

By coupling the mixing chamber to a chamber at higher temperature (the still) through a superleak, an osmotic pressure gradient will exist between the two. By means of pumping on the still, ^{3}He atoms leave the diluted phase in the MC and migrate along the osmotic pressure gradient. By continuously pumping on the still, subsequent ^{3}He atoms are forced to cross the boundary in the MC. As the still contains two isotopes, Raoult's law is exact and the partial pressure of each component is given by its vapour pressure multiplied by its molar fraction. Given the difference in the vapour pressures of ^{3}He and ^{4}He (shown in Figure 2.5), the pumped vapour is almost entirely ^{3}He. It should be noted here that as the still is kept artificially at a suitable temperature to support the cycling of ^{3}He, some significant cooling power can be made available here ~700 mK through suitable design. The boil-off rate (and hence rate of circulation) is given by

$$\dot{n} = \frac{P_s}{L_{3D}\left(T_s, x_s\right)} \tag{5.11}$$

where P_s is the power applied to the still. Reference [197] gives $L_{3D} \simeq 24$ J/mol at $T_s = 700$ mK.

By recycling the pumped ^{3}He and reinjecting, it may be seen how continuous cooling may be provided at the mixing chamber. It may further be considered that it is possible to run a diluter in single-shot mode (e.g., Reference [201]), where ^{3}He is not recirculated to the mixing chamber. In this case, the cooling power is increased to

$$\dot{Q} = 94\dot{n}T_m^2 \tag{5.12}$$

As mechanical cryocooler technology has developed over the last several decades, DRs have been designed which use GM [202] and subsequently PTCs [203] rather than wet dewars as in Figure 5.29.

In all types of conventional DRs however, room temperature pumps and compressors are required for gas circulation and hence both the cost and complexity of operation is high. Therefore, for the purposes of quick turnaround detector testing as required in SO, it is highly desirable to design a self-contained system where the ^{3}He is circulated within the cold stage. In this way, a so-called "miniature dilution refrigerator" (MDR) could be run in a similar fashion to the sorption coolers described throughout this thesis whilst providing cooling of several μW at 100 mK.

5.3.3 Miniature Dilution Refrigerator

It has been decided to develop the APEX dewar described in Section 5.3.1 to provide a 100 mK stage retrofitted to the CRC10. Wiring to the detector stage can be thermally sunk at the 4 K, 2 K, and 350 mK stages. It has been calculated that cooling at 100 mK of ∼5 μW for ∼8 hours would be more than suitable for initial wafer tests [204]. From Equation 5.6, this corresponds to a flow rate $\dot{n} >6$ μmol/s.

Two options were considered for the architecture of the MDR. It has previously been demonstrated that ^{3}He can be circulated within the cold stage of a diluter by using a sorption pump to pump on the still [205]. This type of cooler, an example of which is shown in Figure 5.30, uses a double-stage ^{3}He/^{4}He sorption cooler to provide precooling to 500 mK. This stage is also used to condense and phase separate mixture in the MDR stage. A passive convective switch (see Section 3.6) is used to precool the mixing chamber directly. With the mixture precooled, the mixture pump is then cooled and the still heated to 800 mK in order to drive off ^{3}He, which then drives ^{3}He from the mixing chamber along an osmotic pressure gradient and induces dilution cooling. No film breaker is required above the still, as the 500 mK stage intercepts the pumping line above the still and hence there is no thermomechanical effect driving ^{4}He film out of the still (see Section 3.5.2). This type of architecture is clearly single-shot; once the ^{3}He charge in the mixing chamber expires, the system must be recycled.

A fridge of this architecture was previously provided by the Manchester group for OLIMPO detector testing by the group at Università di Roma La Sapienza [206], which provided a heat lift of 5 μW at 100 mK. Whilst an attractive option insofar as a similar MDR stage could be retrofitted to the APEX CRC10 in place of the UC stage, scaling values from Reference [205] showed that >2.4 mol of ^{3}He would be needed to give the hold time required for the wafer test dewar; this would both incur great expense and present significant challenges in terms of a mechanical design to cope with the required charging pressure.

An alternative method of circulating ^{3}He is to use condensation pumps, whereby a suitably cooled surface is placed above the free surface in the still. The condensation pump works on the principle that as it operates at a lower temperature than the still, vapour evaporating from the still will recondense and may be recirculated using a suitable geometry. The lower vapour pressure ensures the circulation of ^{3}He from the still.

A design is reported in Reference [201] for such a method applied to a large DR. In this design, a pumped bath was used to cool a single pumping surface.

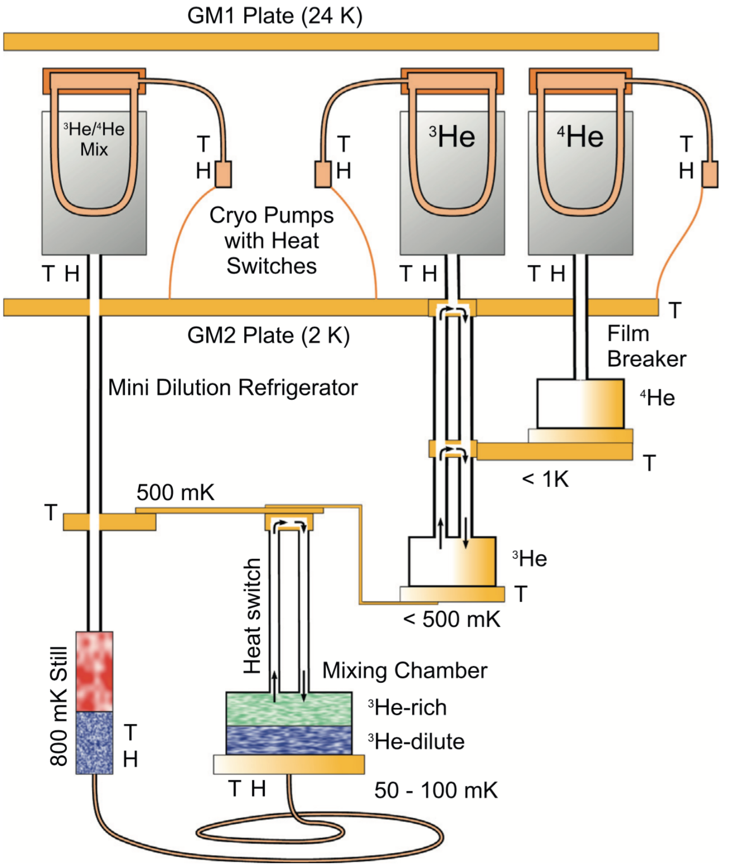

Figure 5.30: Schematic of single-shot sorption-pumped MDR [205].

Whilst this allowed recirculation of ^{3}He, the hold time was limited by the lifetime of the bath. A further design is reported in Reference [207] which used two alternating condensation pumps cooled by a pair of ^{3}He sorption coolers. Whilst both of these architectures successfully demonstrated cooling in the range of the requirement for the test dewar, neither were suitably compact or fast to cool down.

References [208] and [209] have both reported compact closed-cycle diluters using condensation pumps cooled by sorption coolers. However, the cooling power provided in both cases was below what is required for the APEX dewar and so a design has been developed that is compatible with the CRC10 in place of the UC stage which is expected to meet the cooling power and hold time requirements. A schematic of the cooler is shown in Figure 5.31. Note that the precooling stages are identical to the CRC10 used in POLARBEAR-2A (see Section 4.2 and Figure 4.5), with the UC stage removed. Geometrical specifications for the MDR are given in Table 5.2

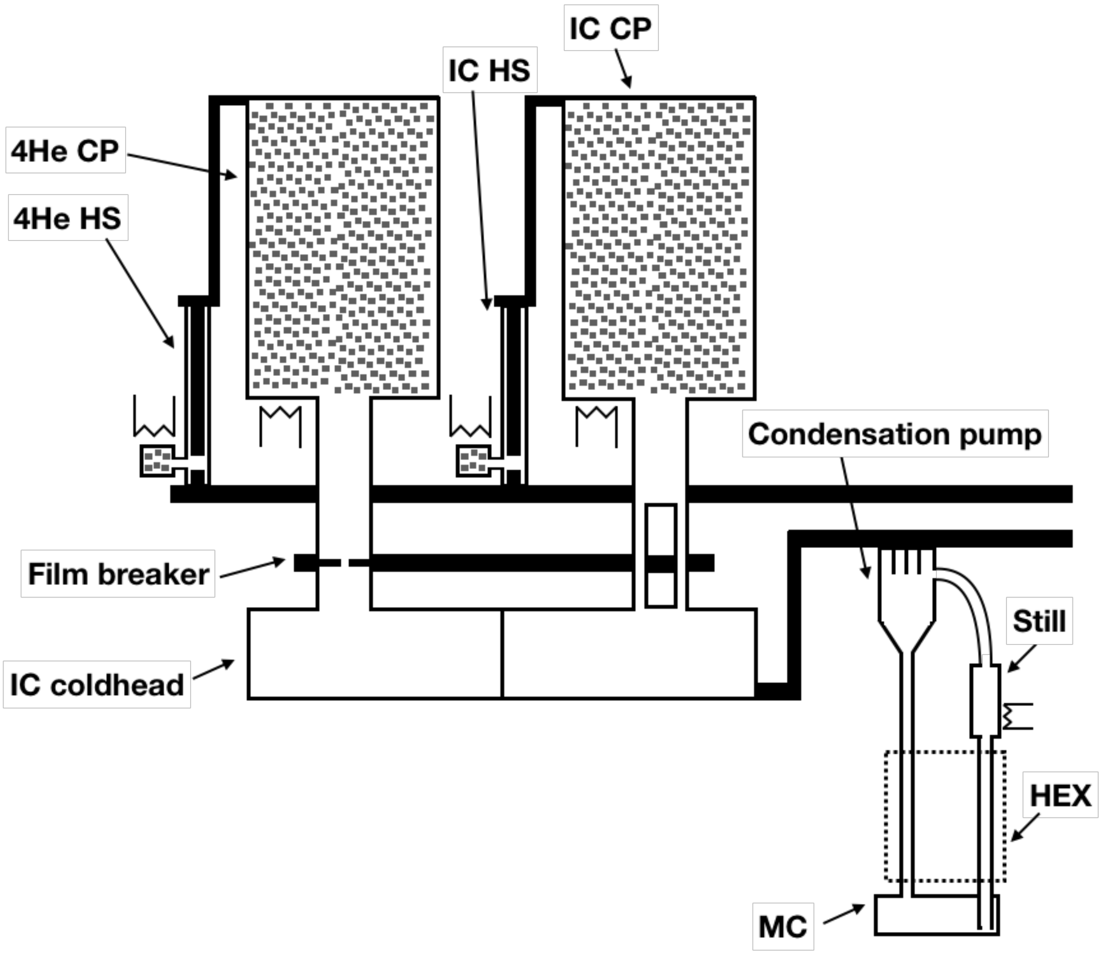

Figure 5.31: Schematic of MDR for APEX dewar

The MDR consists of a condensation pump chamber at the top which is mounted to the IC stage via a thermal link. A return line connects the bottom of this chamber with the mixing chamber. A second tube runs from the bottom of the mixing chamber up to the still through a heat exchanger assembly (represented by the dashed box, see below). Another tube then runs from the top of the still back to the condensation pump to allow pumping of the ^{3}He gas.

The MDR is charged with ^{3}He/^{4}He mix which is precooled and condensed by the IC coldhead to 350 mK. At this point, the liquid in the still and the return line from the condensation pump has been condensed, undergone its superfluid transition and phase separated.

The condensation pump, the CAD for which is shown in Figure 5.32, is composed of an OFHC copper piece which is mounted to the 350 mK thermal link with eight flat protruding fins to maximise the cold surface area available to the incoming gas. A stainless steel chamber was silver soldered into a mounting groove in the copper piece. A copper capillary charging line was silver soldered into one side of the stainless steel piece, a stainless steel tube from the still into the other, and a second stainless steel tube for the return line to the HEX soldered to the through hole in the bottom of the piece. The chamber was designed with a conical profile to aid in collecting the condensed ^{3}He.

The mixing chamber, CAD for which is shown in Figure 5.33, is comprised of an OFHC base piece which forms the 100 mK cold head, a surrounding piece for the chamber in stainless steel which was silver soldered into a mounting groove in the OFHC piece, and a stainless steel disk which formed the top of the pot, also silver soldered in place. The heat exchanger outer tube (see below) was soldered into the top stainless piece.

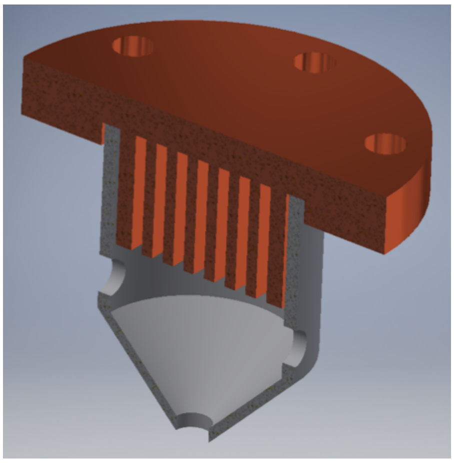

Figure 5.32: Condensation pump CAD

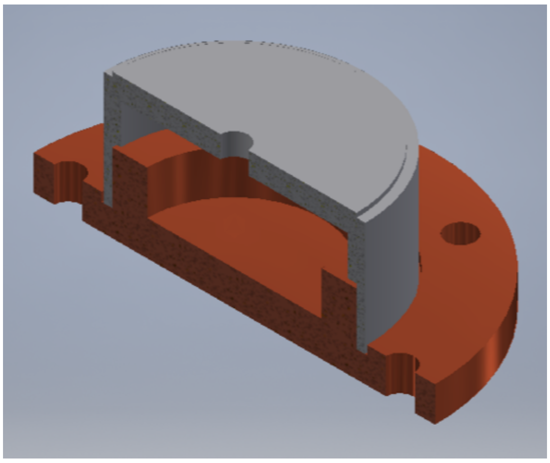

Figure 5.33: Mixing chamber CAD

As described in Section 5.3.2, the design of the heat exchanger is critical to the performance of the MDR. Tube-in-tube counterflow heat exchangers have been shown to be well suited to DRs with flow rates on the order of a few μmol/s with 100 mK base temperatures [208]. A model for modelling the performance of tube-in-tube heat exchangers was first reported by Reference [210] and later improved in Reference [211], which gives

$$\frac{\dot{Q}}{\dot{n}} = \frac{(\gamma_D - \gamma_C)\left[\gamma_D (f-1) - \gamma_C\right]}{\gamma_D (f-1) - \gamma_C (f+1)} T_M^2 \tag{5.13}$$

where the enthalpy coefficient $\gamma_D = 23$ JK^{-2}mol^{-1} and $\gamma_C = 107$ JK^{-2}mol^{-1}. The dimensionless factor f is

$$f = \exp\left(\frac{A/a_K}{\dot{n}\gamma_D\gamma_C}\left[(\gamma_D - \gamma_C) T_M^2 - 2\dot{Q}/\dot{n}\right]\right) \tag{5.14}$$

where, crucially, A is the total surface area of the inner tube of the heat exchanger (i.e., the heat exchanger area), and the Kapitza resistivity $a_K = 0.01$ m^{2}K^{4}W^{-1}. As described in Reference [208], it is difficult to solve the heat exchanger equations numerically. However, by using the logarithmic versions of Equations 5.13 and 5.14, it is possible to show that for a CuNi tube-in-tube heat exchanger, an area of 40 cm^2 is reasonable for the cooling power requirements here.

All of the parts shown in Figure 5.34 for the MDR were fabricated in the School of Physics Machine Shop in Manchester. The tube-in-tube heat exchanger is shown in the centre of the image, where it is possible to see that the inner tube protrudes further down than the outer; in this way it was possible during assembly to ensure that the outer tube mated with the top piece of the mixing chamber and the inner tube reached nearly flush with the bottom of the chamber.

During operation, the phase separation will be such that the still side of the circuit will contain dilute mixture and the condenser side with contain concentrate. As a result of the difference in density of ^{3}He and ^{4}He (see Section 2.1), there will be a difference in the column height in the equilbrium condition. In

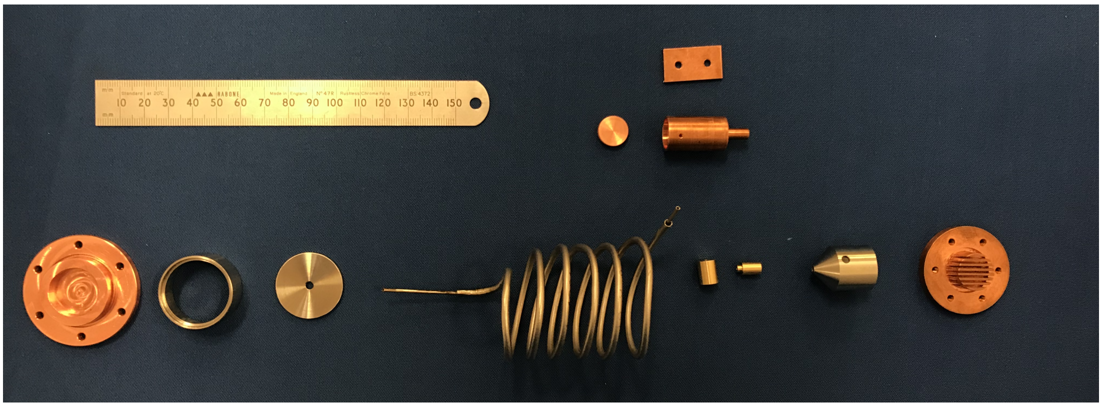

Figure 5.34: MDR parts before assembly

order that the free surfaces remain in the still and at the bottom of the condenser, the still has been positioned according the dimensions in Table 5.2.

In order to minimise the Kapitza resistance between the liquid in the mixing chamber and the copper base piece shown in Figure 5.33, a copper sinter was used. The central pocket of the base piece was filled with copper powder with a maximum grain size of 63 μm from ECKA Granules[11] which was then pressed in a Specac[12] hydraulic laboratory pellet press. Several prototypes were made and it was found that a load of 10 tons was needed to produce a robust sinter. The packing factor achieved was $\sim$65%, similar to the value suggested in Reference [212]. The base piece with the finished sinter is shown in Figure 5.35.

The geometrical specifications of the MDR design are given in Table 5.2.

5.3.4 MDR Testing in Manchester Cryostat

An uncharged CRC10 fridge was provided by CRC, including gas-gap switches, with the UC stage removed. The fridge was installed in the Manchester 4 K test cryostat as shown in Figure 5.36.

Given the size of the CRC10 condenser plate, five OFHC struts were used to mount the fridge directly underneath the 4 K plate. Charging lines, heat sunk

---

[11] `https://www.kymerainternational.com`

[12] `https://www.specac.com/en`

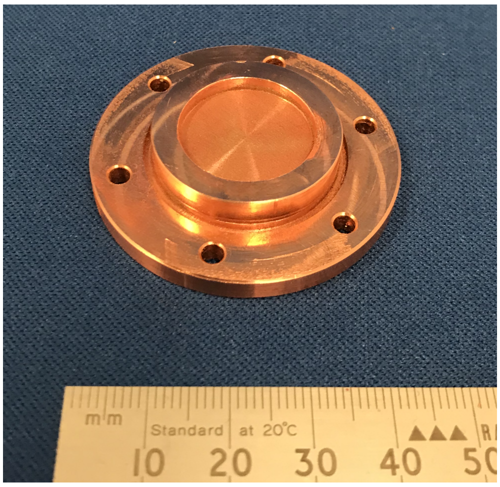

Figure 5.35: Mixing chamber base piece with sinter

Table 5.2: Geometrical specifications of the MDR design

Dimension	Value
Height of MDR unit	180 mm
Distance from base to shoulder of condenser	170 mm
Area of condenser fins	21 cm^2
Internal volume of condenser chamber	3.4 cm^3
Distance from base to midpoint of still	99.5 mm
Internal volume of still	2.7 cm^3
Length of heat exchanger	80 cm
Outer tube OD	3.18 mm
Outer tube wall thickness	0.25 mm
Inner tube OD	1.6 mm
Inner tube wall thickness	0.25 mm
Heat exchanger area	40.2 cm^2
Internal volume of mixing chamber	5.8 cm^3

at 40 K and 4 K, were then soft-soldered for each volume in order to be able to control the level of charge during commissioning. Heaters came preinstalled from CRC on both pumps and heat switches. An additional heater was mounted to the IC coldhead in order to be able to measure a load curve (see below). Diode thermometers were mounted on both pumps and were preinstalled on both heat switch pumps by CRC. Cernox thermometers were installed on the condensation plate and IC head, with an Oxford Instruments RuO_2 thermometer on the film

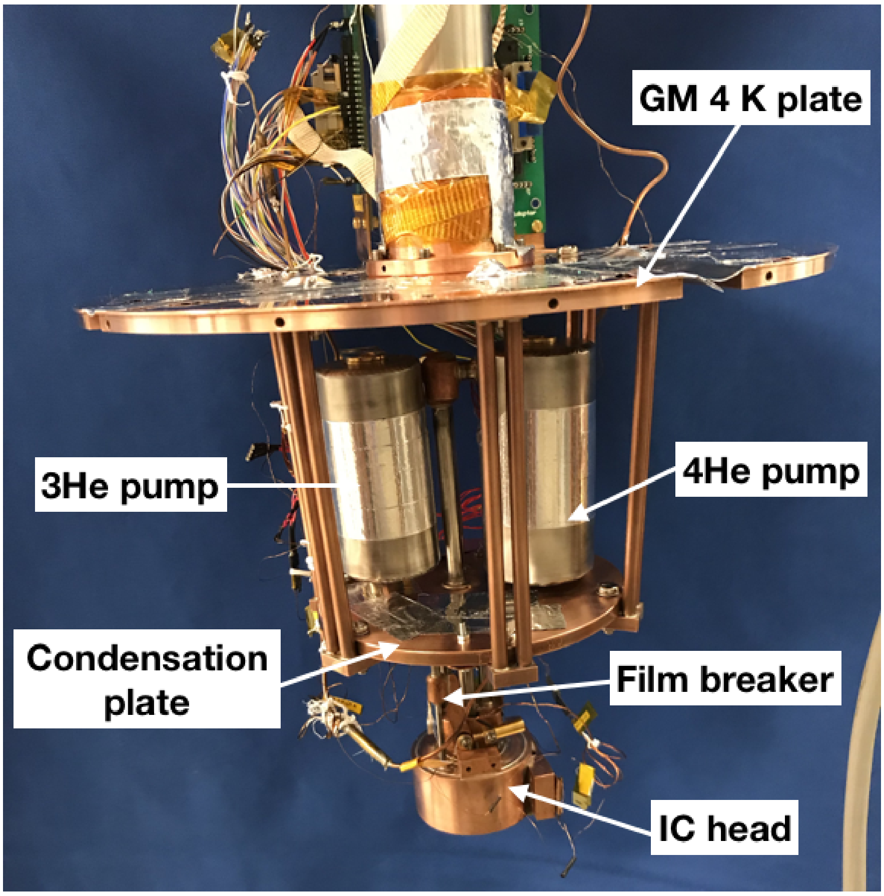

Figure 5.36: CRC10 installed in Manchester test cryostat

breaker stage.

Both stages were then pressure tested and vacuum tested to confirm their integrity after shipping. Both cryopumps were baked out overnight and the cryostat cooled to 4 K. As per instructions from CRC, the ^{4}He side was charged with 16 LSTP and the ^{3}He side with 8 LSTP. This was done by opening an external volume for each gas species to the evacuated charging line with the pumps cold.

Having allowed the system to return to thermal equilibrium after the gas charging, the cycle was started with both pumps cold and both switches closed (pumps hot). The ^{4}He pump switch (4HS) was then opened and the cryopump (4CP) heated using a PID controller to thermostat at 40 K. This desorbed all of the ^{4}He charge which was then condensed by the 4 K plate and collected as liquid in the cold head. The IC cryopump switch (3HS) was then opened and the IC cryopump (3CP) heated with a second PID controller to 40 K to desorb and cool the gas to 4 K in the IC head. After cooling all of the ^{3}He to 4 K, the heater on 4CP was switched off and 4HS closed. This pumped the ^{4}He down to 1 K, condensing the ^{3}He charge. When the ^{4}He charge expired (in the case of some runs, this was done artificially by loading the IC head), the film breaker was observed to sharply increase in temperature due to the absence of vapour cooling. The IC head was not observed to change significantly in temperature due to the large heat capacity of the ^{3}He. The 3CP heater was then switched off and 3HS closed. This pumped the ^{3}He down to a base temperature of 308 mK. The cycle was repeated several times and a load curve was taken as described for the QUBIC 1 K fridge in Section 3.5 by stepping the voltage applied across the heater on the IC head. The measured data are shown in Figure 5.37.

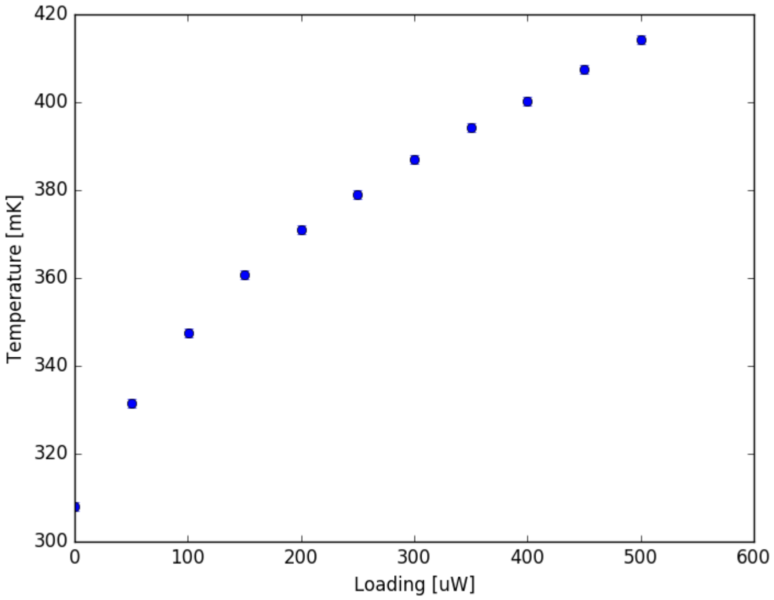

Figure 5.37: Load curve measured for IC stage of CRC10

The hold time measured under a representative load of 300 μW was 420 mins. Given the ^{3}He charge and its latent heat at 380 mK, this gave a total condensation efficiency (see Section 3.5.3) of ∼90%. It may be that it is possible to increase this by optimising the cycling further.

In order to provide the required flow rate of 6 μmol/s (assuming a perfect heat exchanger), Equation 5.11 gives a required still power of 144 μW. It may be considered either by applying the first law to the entire MDR, or by considering that the latent heat to condense the ^{3}He entering the condenser dominates the load to this stage, that the loading on the IC will be ∼144 μW. From the measured load curve shown in Figure 5.37, this can be seen to correspond to a condenser temperature of ∼360 mK.

Increasing the power to the still further would increase the boil-off rate, which in principle increases the cooling power available at the mixing chamber. However, increasing the boil-off rate also increases the loading on the condensation pump. Given the geometry of the condensation surface and the cooling power of the IC head, increasing the molar flow rate up to a certain point would increase the temperature of the returning ^{3}He and, past that point (dependent on the pressure in the condenser), condensation would not be possible. Therefore, there exists an optimum still temperature (given a required heat lift or MC temperature) which should be found experimentally.

The hold time of the MDR t is limited by the hold time of the IC stage as

$$t = \left(Q_0 - Q_{precool}\right)/\dot{Q} \tag{5.15}$$

where Q_0 is the total heat capacity of the condensed ^{3}He, $Q_{precool}$ is the heat removed to precool the MDR from 1 K to 300 mK, and $\dot{Q}$ is the total load on this stage (dominated by the cooling power to condense the recirculating ^{3}He in the MDR).

The MDR was assembled from the parts shown in Figure 5.34 in the School of Physics Machine Shop and mounted from the IC stage in the cryostat as shown in Figure 5.38. Given the thermal isolation of the mixing chamber, a CRC passive gas-gap switch was also installed between the IC head and the mixing chamber to reduce the cooldown time. The switch used here was the same unit as described in Section 5.2.1.

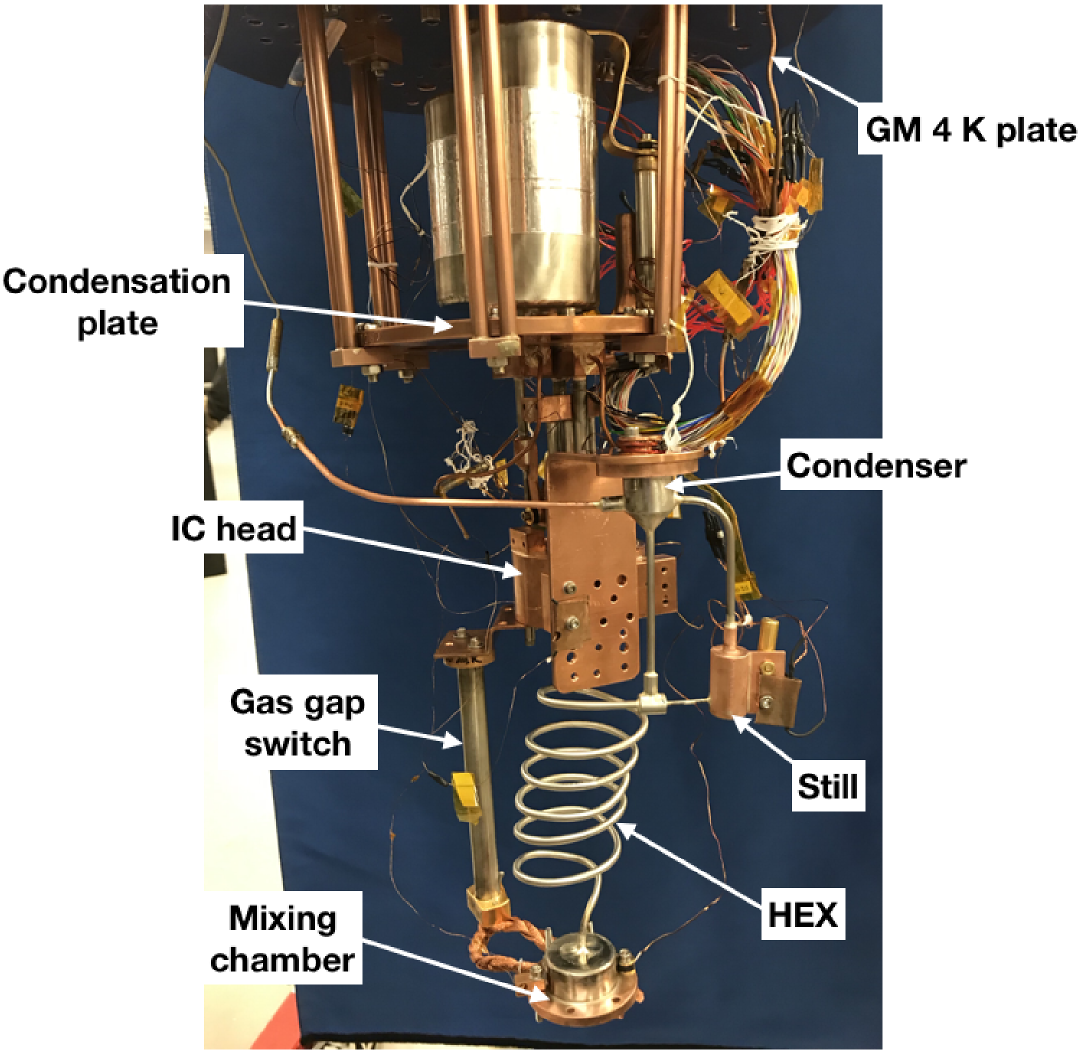

Figure 5.38: MDR installed in Manchester test cryostat

In order to reduce thermal impedances between components below 4 K, all surfaces were cleaned with isopropyl alcohol and a thin layer of Apiezon N grease[13] was applied between all of the bolted interfaces. The charging line was soldered into the gas handling system to allow evacuating and charging of the MDR. Leak and pressure testing was then carried out to confirm the integrity of the MDR.

---

[13] `http://www.apiezon.com`

In addition to the thermometry already installed on the CRC10, a Cernox was mounted to the mixing chamber and an Oxford Instruments RuO_2 was mounted to the still. Heaters were also added to both the mixing chamber and still. As the precooling switch was passive, no thermometry or heaters were required for its operation.

The MDR was evacuated and the cryostat closed. The system was then cooled to 4 K and the MDR charged with the ^{3}He/^{4}He mixture from an external low pressure volume. Before charging, a residual gas analysis was carried out to measure the mixture ratio using a Spectra[14] Microvision Plus. The raw counts are shown in Figure 5.39, with peaks clearly visible for the two isotopes. In order to determine the ratio, two Gaussians and a constant baseline (as the RGA was operating close to the noise floor) were fitted to the data, with the ratio of the magnitudes giving the concentration. This showed $x = 0.39$.

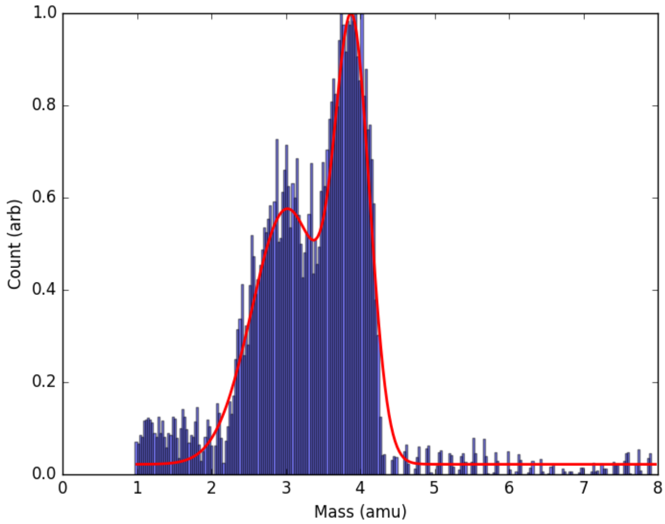

Figure 5.39: Residual gas analysis data for the ^{3}He/^{4}He mixture. The raw data has been scaled and is shown in blue, with the fitted Gaussians in red.

Although the transfer line was evacuated and leak tested, the gas line into the cryostat was routed through an LN_2 trap to reduce further the risk of contami-

---

[14] `https://www.mksinst.com`

nation of the mixture during transfer. In order to draw the full charge into the MDR from the low pressure expansion volume outside the cryostat, the CRC10 was cycled down to 350 mK in order to begin condensing mixture in the MDR. Once the full charge was transferred, the gas line was closed and the CRC10 recycled in order to precool the entire MDR unit.

Unfortunately however, despite multiple attempts with different rates of cycling, it was not possible to completely precool the MDR unit. The base temperatures reached for the condenser, still, and mixing chamber were 360 mK, 420 mK, and 799 mK respectively. Whilst this showed that the condenser and still were suitably precooled and well-coupled in this condition, the mixing chamber was much less strongly coupled and was not precooled suitably far to induce phase separation. As a result, it was not possible to drive dilution in this case by heating the still.

The mixing chamber should have been precooled to ∼500 mK by conduction through both the superfluid in the heat exchanger to the still, as well as the passive gas-gap switch to the IC stage. It is theorised that as the inner tube of the heat exchanger is significantly smaller in diameter (see Table 5.2) than other DR systems discussed above, and the conductance of superfluid is strongly dependent on the diameter of the tube containing it due to phonon scattering with the tube walls (see Section 2.3.1), that the superfluid does not provide a suitably high conductance path to precool the MC. Furthermore, the conductance measurements of the switch in Figure 5.18 show that the transition temperature is ∼10 K. This is in agreement with the observed cooldown of the system where the mixing chamber was well-coupled to the IC head above this temperature. The residual open conductance of the switch below 1 K was clearly also too low to provide adequate precooling.

In order to address this issue, two options are clearly possible: either to replace the heat exchanger with a similar design of larger diameter tubes, or replace the heat switch with either a passive design tuned to open at ∼500 mK or an active design (provided it does not load the cold stages of the system). An active ^{3}He gas-gap switch is being prepared for this purpose.

A second experimental run is planned with the alternative precooling switch in May 2019. The author hopes to report full results in due course.

5.3.5 Test Cryostat Integration

After suitable characterisation in Manchester is completed, the plan is to design a second version of this MDR with the same mechanical footprint as the UC stage of the CRC10 as a self-contained unit. After testing, this second MDR will then be directly shipped to UC Berkeley and swapped out for the UC stage on the APEX dewar CRC10 as planned.

In order to modify the geometry to meet this requirement, the main change will be vertical compression of the HEX design. Whilst the length and cross-section should remain unchanged in order not to change the performance from the system described above, the pitch of the helix will need to be reduced. As described in Section 5.3.3, this will also require the lengths of the tubes from the condenser to the top of the HEX and the top of the still to be shortened in order to keep the free surfaces in the correct positions. A shorter precooling switch will also be required.

In the testing of the system in Manchester, an external low pressure expansion volume was used such that the pressure in the MDR during warm up of the cryostat never exceeded 400 mbar. In the second version of the MDR, the unit should be self-contained. Therefore, in order to minimise the room-temperature pressure inside the sealed unit, it is proposed to use an internal expansion volume above the 4 K plate next to the ^{4}He and IC pumps. This could be designed such as to fit within the footprint of the existing UC pump.

Furthermore, in order to improve the mechanical robustness of the unit without significantly increasing the parasitic loading to the mixing chamber during operation, it is proposed to use a carbon fibre hexapod assembly to between the condenser flange and the mixing chamber flange. Care should be taken in its design such that it does not interfere geometrically with the HEX.

In order to minimise the turnaround time for detector wafer testing, it is proposed to automate the precooler and MDR cycling down to 100 mK. Automatic cycling of this type has been demonstrated in Manchester for a number of systems using XML scripts defining state machines. Using this, or a functionally equivalent approach, could allow a wafer to be mounted in the cryostat, the cryostat closed up and vacuumed down, the PTC switched on and the system to then automate down to 100 mK overnight for wafer testing the following morning. Such a facility would be a significant asset to the collaboration. Furthermore, several other similar 250 mK cryostats are operated by the collaboration at other universities and laboratories which could be retrofitted in the same way.

Chapter 6

Conclusions and Future Developments

As described in Chapter 1, the forthcoming generation of CMB polarization observatories will target an ambitious set of science goals requiring unprecedented sensitivities. In order to support this, significant developments in a range of cryogenic systems have been and continue to be required, with the necessary background given in Chapter 2.

This thesis has described the development of a number of key subsystems for several of these forthcoming experiments, QUBIC, Simons Array, and the Simons Observatory, in Chapters 3, 4, and 5 respectively.

6.1 QUBIC

The science goals and instrument architecture for QUBIC have been reported, along with the cryogenic systems that have been provided.

A high-capacity 1 K ^{4}He sorption cooler has been developed and demonstrated a load curve suitable for the cooling requirements of the 1 K optics box. A novel superfluid film breaker has been designed to maximise the hold time of the system, and has been well described theoretically in good agreement with the data. The cooler has been installed on the QUBIC receiver at APC and successfully cycled. However, due to the thermal gradient between the PTC second stage cold heads and the condensation point of the cooler, the hold time achieved was less than is required for observations. As such, a new fridge assembly mount with far lower thermal impedance is presently being designed in order to improve the condensation efficiency.

Novel active and passive convective heat switches have been developed to pre-cool the 1 K stage and provide isolation during the cooler recycling. A theoretical model of the heat transfer has been developed and is in good agreement with the data.

A dual ^{3}He/^{4}He cooler has been provided to operate the detector stage at 350 mK. This has also been installed on the QUBIC receiver and preliminary TES testing carried out.

Full perfomance of the receiver is expected by Summer 2019, with deployment to Argentina tentatively scheduled for the end of 2019.

6.2 Simons Array

The science goals and instrument architecture for the Simons Array have been described. The thermal architecture of the POLARBEAR-2 receivers has been detailed, along with the operation of the three CRC 270 mK sorption coolers used to provide cooling of the detector stages.

A temperature stability analysis code has been developed and applied to the focal plane stage of POLARBEAR-2A. The code has been shown to allow recovery and characterisation of the individual noise components for Gaussian, 1/f, and random walk noise, along with steady drift. Having deployed the receiver in January 2019, these data will be fed into the analysis pipeline and will aid in creating a ground template to optimise the scan strategy for the observatory.

The possibility will also be explored of applying this analysis to bolometer time stream data.

6.3 Simons Observatory

The observatory configuration, instrument architectures, and science goals of the Simons Observatory have been described, along with the thermal designs of the large aperture telescope receiver and small aperture telescopes.

A range of heat switches, including gas-gap and mechanical designs, have been tested to significantly improve the cooldown time of the LATR cryostat. The highest closed conductance measured was for a mechanical switch $\sim$0.5 W·K^{-1}. These data have then been included into a transient thermal model of the receiver to develop the precooling scheme, showing an improvement in cooldown time from $\sim$28 to $\sim$18 days for the lowest temperature stages.

Furthermore, as both the large and small aperture telescopes will operate focal planes at 100 mK, development has been reported of a novel miniature dilution refrigerator for fast-turnaround operation of a detector wafer test cryostat. The precooling CRC fridge has been demonstrated down to a base temperarture of 308 mK, and an MDR designed and manufactured. The lack of an available precooling heat switch has not allowed demonstration of the MDR down to 100 mK; however, such a switch is currently being prepared and the author hopes to report full results of the MDR test in due course.

Appendix A

Python Codes

Throughout this thesis, reference has been made to a number of Python codes that have be written for a range of applications. Several of these are included here for completeness.

A.1 Cryostat Cooldown Simulation Code

The following code uses a finite element approach to model the cooldown of a medium-sized pulse-tube cooled cryostat. Commenting throughout describes the code in detail.

```
###################

# Cryostat cooldown thermal simulation - Andy May, Oct 2017
# andrew.may-3@postgrad.manchester.ac.uk

###################

# The following code models the cooldown of a medium-sized 2 stage cryostat by a PT415 pulse tube cryostat

# The capacity map of the mechanical coolers are used from Green et al. (2015)
# http://iopscience.iop.org/article/10.1088/1757-899X/101/1/012002/pdf

# Radiative loads are accounted for using typical shield sizings with emissivity consistent with MLI
```

```

# The thermal masses on the 1st and 2nd stages are modeled as lumped elements (i
    .e. isothermal)
# These stages are treated as copper with temperature dependent heat capacity
    from Marquardt, Le, and Radebaugh
# Cryogenic Material Properties Database, National Institute of Standards and
    Technology Boulder, CO 80303

###################

# Import packages

import numpy as np
import scipy as sp
import matplotlib
from matplotlib import pyplot as plt
from scipy import interpolate

###################

# Model time

endtime = 5 # hours
endtime = endtime * 3600 # secs
timestep = 0.1 # secs
globaltime = np.array([0.00]) # secs # initialise, will increase by "timestep"
    until reaches "endtime"

###################

# Define physical constants

stefboltz = 5.67E-8 # W/m2.K4

###################

# Define initial conditions and parameters for thermal elements

# Element 0 # Outer vacuum chamber, model as thermal reservoir at 300 K

T_0 = np.array([300.0]) # K # Initialise temperature array

# Element 1 # 1st stage, thermal mass

```

```
A_1 = 0.5 # m2 # Surface area
eps1 = 0.01 # Surface emissivity
m_1 = 12 # kg # Mass
T_1 = np.array([300.0]) # K # Initialise temperature array

# Element 2 # 2nd stage, thermal mass

A_2 = 0.5 # m2 # Surface area
eps2 = 0.01 # Surface emissivity
m_2 = 15 # kg # Mass
T_2 = np.array([300.0]) # K # Initialise temperature array

###################

# Initialise heat flow arrays

Qdot1_record = np.array([0.00]) # W # PTC 1st stage heat lift
Qdot2_record = np.array([0.00]) # W # PTC 2nd stage heat lift

QRdot1_record = np.array([0.00]) # W # Radiative load on 1st stage
QRdot2_record = np.array([0.00]) # W # Radiative load on 2nd stage

###################

# PTC heat lift data

T_PTC1 = np.array([31.42, 42.26, 41.72, 41.72, 41.72, 42.26, 49.85, 57.43,
     59.06, 59.06, 60.68, 62.31, 75.31, 85.06, 89.40, 100.23, 115.94, 122.99,
     114.32,141.41, 153.33, 154.95, 163.08, 175.54, 216.18, 218.89, 236.76,
     246.52, 250.85, 286.61, 295.82, 303.95, 308.28]) # K # PTC 1st stage
     temperature
T_PTC2 = np.array([2.51, 33.52, 76.26, 144.97, 248.04, 292.46, 2.52, 36.03,
     78.77, 144.97, 224.58, 310.06, 3.35, 40.22, 79.61, 134.08, 201.12, 282.40,
     5.03, 51.12, 97.21, 151.68, 222.07, 315.08, 41.07, 82.96, 150.00, 232.122,
     320.11, 70.39, 130.72, 204.47, 284.92]) # K # PTC 2nd stage temperature
Q_PTC1 = np.array([0.0, 0.0, 0.0, 0.0, 0.0, 0.0, 50.0, 50.0, 50.0, 50.0, 50.0,
     50.0, 100.0, 100.0, 100.0, 100.0, 100.0, 100.0, 150.0, 150.0, 150.0, 150.0,
      150.0, 150.0, 200.0, 200.0, 200.0, 200.0, 200.0, 250.0, 250.0, 250.0,
     250.0]) # W # PTC 1st stage heat lift
Q_PTC2 = np.array([0.0, 25.0, 50.0, 75.0, 100.0, 125.0, 0.0, 25.0, 50.0, 75.0,
     100.0, 125.0, 0.0, 25.0, 50.0, 75.0, 100.0, 125.0, 0.0, 25.0, 50.0, 75.0,
     100.0, 125.0, 0.0, 25.0, 50.0, 75.0, 100.0, 0.0, 25.0, 50.0, 75.0]) # W #
     PTC 2nd stage heat lift

```

```
# Interpolated values as f(T_1,T_2)

Q_PTC1_interp_func = interpolate.interp2d(T_PTC1, T_PTC2, Q_PTC1, kind='linear')
      # W # PTC 1st stage heat lift
Q_PTC2_interp_func = interpolate.interp2d(T_PTC1, T_PTC2, Q_PTC2, kind='linear')
      # W # PTC 2nd stage heat lift

###################

# Solver

while globaltime[-1] < endtime : # Loop until simulation reaches endtime

    ###################

    # Calculate temperature dependent properties

    # Element 0

    #

    # Element 1

    cp_1 = 10**((-1.91844) + (-0.15973*np.log10(T_1[-1])) + (8.61013*(np.log10(
         T_1[-1])**2)) + (-18.99640*(np.log10(T_1[-1])**3)) + (21.96610*(np.
         log10(T_1[-1])**4)) + (-12.73280*(np.log10(T_1[-1])**5) + (3.54322*(np.
         log10(T_1[-1])**6))) + (-0.37970*(np.log10(T_1[-1])**7)))
    Cp_1 = cp_1 * m_1 # J/K

    # Element 2

    cp_2 = 10**((-1.91844) + (-0.15973*np.log10(T_2[-1])) + (8.61013*(np.log10(
         T_2[-1])**2)) + (-18.99640*(np.log10(T_2[-1])**3)) + (21.96610*(np.
         log10(T_2[-1])**4)) + (-12.73280*(np.log10(T_2[-1])**5) + (3.54322*(np.
         log10(T_2[-1])**6))) + (-0.37970*(np.log10(T_2[-1])**7)))
    Cp_2 = cp_2 * m_2 # J/K

    ###################

    # Calculate heat transfer

    # Element 0

    #
```

```

    # Element 1

    # PTC heat lift

    Qdot1 = Q_PTC1_interp_func(T_1[-1], T_2[-1]) # W # 1st stage heat lift as function of 1st and 2nd stage temperatures
    Q1 = Qdot1 * timestep # J # Heat removed in timestep
    Qdot1_record = np.append(Qdot1_record,Qdot1) # W # Record for plotting

    # Radiative load

    QRdot1 = A_1 * eps1 * stefboltz * ((T_0[-1] **4) - (T_1[-1] **4)) # W # Rad load on 1st stage
    QR1 = QRdot1 * timestep # J # Radiative heat added in timestep
    QRdot1_record = np.append(QRdot1_record,QRdot1) # W # Record for plotting

    # Element 2

    # PTC heat lift

    Qdot2 = Q_PTC2_interp_func(T_1[-1], T_2[-1]) # W # 2nd stage heat lift as function of 1st and 2nd stage temperatures
    Q2 = Qdot2 * timestep # J # Heat removed in timestep
    Qdot2_record = np.append(Qdot2_record,Qdot2) # W # Record for plotting

    # Radiative load

    QRdot2 = A_2 * eps2 * stefboltz * ((T_1[-1] **4) - (T_2[-1] **4)) # W # Rad load on 2nd stage
    QR2 = QRdot2 * timestep # J # Radiative heat added in timestep
    QRdot2_record = np.append(QRdot2_record,QRdot2) # W # Record for plotting

    ###################

    # Calculate temperatures at end of timestep

    # Element 0

    T_0_new = T_0[-1] # K # Thermal reservoir, hence temperature unchanged
    T_0 = np.append(T_0,T_0_new) # Add new temperature to array


    # Element 1
```

```

    T_1_new = ( T_1[-1] ) + ( ( -Q1 + QR1 -QR2 ) / Cp_1) # K # Temperature change from net heat transfer divided by total heat capacity
    T_1 = np.append(T_1,T_1_new) # K # Add new temperature to array

    # Element 2

    T_2_new = ( T_2[-1] ) + ((-Q2+QR1) / Cp_2) # K # Temperature change from net heat transfer divided by total heat capacity
    T_2 = np.append(T_2,T_2_new) # K # Add new temperature to array

    ###################

    # Timekeeping

    time_new = globaltime[-1] + timestep # Move time on by one timestep
    globaltime = np.append(globaltime,time_new) # Add new time to array

    ###################

###################

# Plotting

# Plot temperatures over time

plt.figure() # Initialise figure

globaltime = globaltime / 3600 # hours

plt.plot(globaltime, T_0, label='Vacuum chamber') # Plot vacuum chamber temperature
plt.plot(globaltime, T_1, label='1st stage') # Plot 1st stage temperature
plt.plot(globaltime, T_2, label='2nd stage') # Plot 2nd stage temperature

plt.xlabel('Time [hours]') # x-axis label
plt.ylabel('Temperature [K]') # y-axis label
plt.title('Thermal simulation of Manchester cryostat cooldown') # Title
plt.legend(loc=1) # Legend position

x1,x2,y1,y2 = plt.axis() # Define axis ranges
plt.axis((x1,x2,y1,310)) # Define axis ranges

# Plot heat transfer rates
```

```

plt.figure() # Initialise figure

plt.plot(globaltime, Qdot1_record, label='PTC1 heat lift') # Plot PTC 1st stage heat lift
plt.plot(globaltime, Qdot2_record, label='PTC2 heat lift') # Plot PTC 2nd stage heat lift
plt.plot(globaltime, QRdot1_record, label='Radiative load on 1st stage') # Plot 1st stage radiative heat load
plt.plot(globaltime, QRdot2_record, label='Radiative load on 2nd stage') # Plot 2nd stage radiative heat load

plt.xlabel('Time [hours]') # x-axis label
plt.ylabel('Qdot [W]') # y-axis label
plt.title('Thermal simulation of Manchester cryostat cooldown') # Title
plt.legend(loc=1) # Legend position

x1,x2,y1,y2 = plt.axis() # Define axis ranges
plt.axis((0,x2,0,y2)) # Define axis ranges

plt.show() # Display plots

###################

# End

###################
```

A.2 Film Breaker Design Code

This code generates the plots in Section 3.5.2. The user may enter an orifice diameter and the code will calculate the load curves given in the case of both molecular and continuum flow. As was discussed in Section 3.5.2, the actual physical load curve will tend towards the continuum model at higher pressures. As such, the author recommends using the load curve from the continuum model as a conservative guide in designing the film breaker.

```
###################

```

```python
# Film breaker design code - Andy May, Jan 2017
# andrew.may-3@postgrad.manchester.ac.uk

###################

# Import packages

import numpy as np
import scipy as sp
import matplotlib
from matplotlib import pyplot as plt

###################

# Helium properties

# Helium data from Donnelly, Russell J., and Carlo F. Barenghi.
# "The observed properties of liquid helium at the saturated vapor pressure."
# Journal of Physical and Chemical Reference Data 27.6 (1998): 1217-1274.

# Vapour pressure (T in K, P in Pa)

T_DONNELLY_P = np.array([0.65, 0.7, 0.75, 0.8, 0.85, 0.9, 0.95, 1, 1.05, 1.1, 1.15, 1.2, 1.25, 1.3, 1.35, 1.4, 1.45, 1.5, 1.55, 1.6, 1.65, 1.7, 1.75, 1.8, 1.85, 1.9, 1.95, 2, 2.05, 2.1, 2.15, 2.2, 2.25, 2.3, 2.35, 2.4, 2.45, 2.5, 2.55, 2.6, 2.65, 2.7, 2.75, 2.8, 2.85, 2.9, 2.95, 3, 3.05, 3.1, 3.15, 3.2, 3.25, 3.3, 3.35, 3.4, 3.45, 3.5, 3.55, 3.6, 3.65, 3.7, 3.75, 3.8, 3.85, 3.9, 3.95, 4, 4.05, 4.1, 4.15, 4.2, 4.25, 4.3, 4.35, 4.4, 4.45, 4.5, 4.55, 4.6, 4.65, 4.7, 4.75, 4.8, 4.85, 4.9, 4.95, 5, 5.05, 5.1])

P_DONNELLY_P = np.array([1.10E-01, 2.92E-01, 6.89E-01, 1.48E+00, 2.91E+00, 5.38E+00, 9.38E+00, 1.56E+01, 2.48E+01, 3.80E+01, 5.65E+01, 8.15E+01, 1.15E+02, 1.58E+02, 2.13E+02, 2.82E+02, 3.67E+02, 4.72E+02, 5.97E+02, 7.47E+02, 9.23E+02, 1.13E+03, 1.37E+03, 1.64E+03, 1.95E+03, 2.30E+03, 2.69E+03, 3.13E+03, 3.61E+03, 4.14E+03, 4.72E+03, 5.34E+03, 6.01E+03, 6.73E+03, 7.51E+03, 8.35E+03, 9.26E+03, 1.02E+04, 1.13E+04, 1.24E+04, 1.36E+04, 1.48E+04, 1.61E+04, 1.76E+04, 1.91E+04, 2.06E+04, 2.23E+04, 2.41E+04, 2.59E+04, 2.78E+04, 2.99E+04, 3.20E+04, 3.43E+04, 3.66E+04, 3.90E+04, 4.16E+04, 4.43E+04, 4.71E+04, 4.99E+04, 5.30E+04, 5.61E+04, 5.94E+04, 6.27E+04, 6.63E+04, 6.99E+04, 7.37E+04, 7.76E+04, 8.16E+04, 8.58E+04, 9.01E+04, 9.46E+04, 9.92E+04, 1.04E+05, 1.09E+05, 1.14E+05, 1.19E+05, 1.25E+05, 1.30E+05, 1.36E+05, 1.42E+05, 1.48E+05, 1.54E+05, 1.61E+05, 1.67E+05, 1.74E+05, 1.81E+05, 1.89E+05, 1.96E+05, 2.04E+05, 2.12E+05])

```

```
# Latent heat (T in K, L in J/mol)

T_DONNELLY_L = np.array([0, 0.05, 0.1, 0.15, 0.2, 0.25, 0.3, 0.35, 0.4, 0.45,
     0.5, 0.55, 0.6, 0.65, 0.7, 0.75, 0.8, 0.85, 0.9, 0.95, 1, 1.05, 1.1, 1.15,
     1.2, 1.25, 1.3, 1.35, 1.4, 1.45, 1.5, 1.55, 1.6, 1.65, 1.7, 1.75, 1.8,
     1.85, 1.9, 1.95, 2, 2.05, 2.1, 2.18, 2.2, 2.25, 2.3, 2.35, 2.4, 2.45, 2.5,
     2.55, 2.6, 2.65, 2.7, 2.75, 2.8, 2.85, 2.9, 2.95, 3, 3.05, 3.1, 3.15, 3.2,
     3.25, 3.3, 3.35, 3.4, 3.45, 3.5, 3.55, 3.6, 3.65, 3.7, 3.75, 3.8, 3.85,
     3.9, 3.95, 4, 4.05, 4.1, 4.15, 4.2, 4.25, 4.3, 4.35, 4.4, 4.45, 4.5, 4.55,
     4.6, 4.65, 4.7, 4.75, 4.8, 4.85, 4.9, 4.95, 5, 5.05, 5.1, 5.15])

L_DONNELLY_L = np.array([59.83, 60.87, 61.91, 62.95, 64, 65.04, 66.08, 67.13,
     68.17, 69.21, 70.24, 71.28, 72.31, 73.33, 74.35, 75.37, 76.38, 77.38,
     78.37, 79.35, 80.33, 81.3, 82.26, 83.21, 84.14, 85.06, 85.97, 86.87, 87.73,
      88.56, 89.35, 90.09, 90.77, 91.38, 91.91, 92.36, 92.72, 92.98, 93.13,
     93.16, 93.07, 92.8, 92.27, 90.75, 90.87, 91.15, 91.43, 91.71, 91.98, 92.24,
      92.5, 92.74, 92.97, 93.18, 93.38, 93.56, 93.71, 93.85, 93.96, 94.05,
     94.11, 94.14, 94.14, 94.11, 94.05, 93.94, 93.8, 93.63, 93.41, 93.14, 92.84,
      92.48, 92.08, 91.63, 91.13, 90.58, 89.97, 89.31, 88.59, 87.82, 87, 86.13,
     85.2, 84.22, 83.19, 82.11, 80.98, 79.8, 78.57, 77.27, 75.86, 74.32, 72.59,
     70.64, 68.44, 65.94, 63.11, 59.9, 56.28, 52.22, 47.67, 42.59, 36.95,
     29.34])

# Define temperature range for model

T_model = np.arange(0.65, 1., 0.0001)

# Define latent heat and vapour pressure as function of temperature

L_model_fT = np.interp(T_model, T_DONNELLY_L, L_DONNELLY_L)
P_model_fT = np.interp(T_model, T_DONNELLY_P, P_DONNELLY_P)

# Additional physical properties

M = 4.E-3 # Molar mass
k = 5./3. # Ratio of specific heat capacities
R = 2077. # Specific gas constant

###################

# Geometrical properties of system

r = 500.E-6 / 2. # Orifice radius in m

```

```
###################

# Models

# Model A: Continuum flow

# Mass flow, kg/s

mA = np.pi * (r**2) * ((P_model_fT)/(T_model * R)) * ((2/(k-1))**0.5) * ((2/(k
     +1))**(1/(k-1))) * ((1-(2/(k+1)))**0.5) * (((k*T_model*R))**0.5)

# Heat lift, W

QA = ( mA * L_model_fT ) / M

# Model B: Molecular flow

# Mass flow, kg/s

mB = np.pi * (r**2) * ((P_model_fT)/(T_model * R)) * (((k*T_model*R)/M)**0.5) *
     ((1/(2*np.pi*k))**0.5)

# Heat lift, W

QB = ( mB * L_model_fT ) / M

###################

# Plotting

# Plot model A

plt.plot(QA, T_model, label='Continuum')

# Plot model B

plt.plot(QB, T_model, label='Molecular')

# Plot labels

plt.xlabel('Applied heat load [W]')
plt.ylabel('Pot temperature [K]')
plt.title('Load curve bounds in presence of restriction-type film breaker')
plt.legend(loc=4)
```

```

# Define data range to plot

x1,x2,y1,y2 = plt.axis()
plt.axis((x1,0.004,y1,y2))

# Print

plt.show()

# End
```

A.3 Allan Deviation Thermal Stability Analysis Demonstration Code

This version of the Allan deviation code described in Section 4.3.1 generates dummy signals and shows that the parameters can be recovered.

```
################################

# Demonstration script for Allan deviation as function of averaging time (tau) -
      Andrew May, Nov 2018
# andrew.may-3@postgrad.manchester.ac.uk

################################

# Import packages

import numpy as np
import scipy as sp
from scipy import optimize
from scipy.optimize import fmin
from scipy import interpolate
from scipy.optimize import curve_fit
from scipy import signal as sg
import pandas as pd
import matplotlib
from matplotlib import pyplot as plt
from matplotlib import dates as mdates
import matplotlib.mlab as mlab
```

```
from datetime import datetime
import time
import random

################################

# PREAMBLE

start_time = time.time() # set start time for script run time

################################

# Dummy signal generator

# First, generate blank signal of desired shape

dataN0 = 1000 # number of data points to be generated for signal, i.e. we have dataN0 measurements
datafs0 = 5 # sampling frequency for signal, Hz
datatime0 = np.arange(float(dataN0)) / datafs0 # time stamps for data points (as length of time sampled over * sampling freq = number of data points, we calculate this backwards)

dataTi0 = np.zeros(dataN0) # measured Ti data starts as array of zeros same length as time data array

# Next add noise components (NB: any noise component can be switched off by commenting out the line where it is added, i.e. # dataTi0 += ...

# Add Gaussian noise

dataTi0 += np.random.normal(loc=0.0,scale=0.1,size=dataN0) # adds Gaussian noise to data array, scale argument sets std dev

# Add linear drift

dataTi0 += 0.005 * (datatime0) # add linear drift

# Generate and add random walk noise

randwalk_ns = dataN0 - 1 # number of steps for walk
randwalk_noise = np.array([0]) # 'position' for walk starts at zero

for step in range(randwalk_ns): # loop over range of time data
```

```
    move = np.random.normal(loc=0.0,scale=0.01) # scaled random walk noise
    newposition = randwalk_noise[-1] + move
    randwalk_noise = np.append(randwalk_noise,newposition) # new position is
         added to array of positions

dataTi0 += (0.5 * randwalk_noise) # add scaled random walk noise

################################

# Process data

# Calculate PSD

f0, Pxx_den0 = sg.periodogram(dataTi0, datafs0) # get data for PSD vs frequency

# Calculate ADEV

# Calculate sigma_y of tau_0

tau0sumofsummationterms = 0.0 # initialise to zero

for i in range(0,dataN0-1): # indexing starts from 0 remember! goes to last
     number before N-1 in index, which means N-1 in equation
    summationterm = (dataTi0[i+1] - dataTi0[i]) ** 2.
    tau0sumofsummationterms += summationterm
    # returns sum of summationterms

sigmayoftau0 = np.sqrt(tau0sumofsummationterms/(2.*(dataN0-1.)))

sigmayoftau0 = np.sqrt((np.sum(((dataTi0[1:] - dataTi0[:-1])**2)))/((2.*(dataN0
     -1.))))

# Calculate sigma_y ...

tau0 = (datatime0[1]-datatime0[0])
tauarray = np.array([]) # initialise
sigmayoftauarray = np.array([]) # initialise
Nmax = dataN0 / 2

for n in range(1,Nmax):
    tau = n * tau0
    tauarray = np.append(tauarray, tau)
    bigsummationterm = 0.
```

```
    for k in range(0,dataN0-(2*n)+1): # indexing starts from 0, goes to last
         number before N-1 in index, which means N-1 in equation
        firsttermforsummation = 0. # initialise
        for j in range(k+n,k+(2*n)):
            firsttermforsummation += dataTi0[j]
        secondtermforsummation = 0. # initialise
        for j in range(k,k+n):
            secondtermforsummation += dataTi0[j]
        bigsummationterm += (((1./n)*(firsttermforsummation))-((1./n)*(
             secondtermforsummation)))**2
    sigmayoftau = np.sqrt((1./(2*(dataN0-(2*n)+1))*bigsummationterm))
    sigmayoftauarray = np.append(sigmayoftauarray, sigmayoftau)

# Calculate Gaussian fit parameters

def goodness (func, *x):
    ax=x[0]
    ay=x[1]
    sigma=x[2]
    # define initial guesses
    gaussianpara = func[0]
    driftpara = func[1]
    randwalkpara = func[2]
    # fit is sum of scaled noise components
    fit = (gaussianpara * (tauarray ** -0.5)) + (driftpara * (tauarray ** 1.0))
         + (randwalkpara * (tauarray ** 0.5))
    # goodness (to be minimised) is fit function
    good = (fit - ay)**2 / (sigma**2) # define the 'good' parameter (chi squared
         ), as expected value from fit minus value from data squared divided by
         sigma squared
    return good.sum() # good.sum is total chi squared

# Define parameters for goodness function

gaussianpara = 1.0
driftpara = 1.0
randwalkpara = 1.0
fit_sigma = sigmayoftauarray
func = np.array([gaussianpara,driftpara,randwalkpara])

# Run optimisation

xopt = fmin(goodness, func, args=(tauarray, sigmayoftauarray,fit_sigma))

```

```
# Get outputs

gaussianpara = xopt[0]
driftpara = xopt[1]
randwalkpara = xopt[2]

# Contributions to fit

gaussianfit = gaussianpara * (tauarray ** -0.5)
driftfit = driftpara * (tauarray ** 1.0)
randwalkfit = randwalkpara * (tauarray ** 0.5)

adevfit = gaussianfit + driftfit + randwalkfit


################################

# Plot figures

# Plot time series data for signal

plt.figure(1)
plt.plot(datatime0,dataTi0)
plt.legend()
plt.xlabel('Time [s]')
plt.ylabel('Signal [arb]')
plt.show()

# Plot PSD

plt.figure(2)
plt.semilogy(f0, Pxx_den0)
plt.legend()
plt.ylim([1e-7, 1e2])
plt.xlabel('Frequency [Hz]')
plt.ylabel('PSD [arb**2/Hz]')
plt.show()

# Plot ADEV

plt.figure(3)
plt.loglog(tauarray, sigmayoftauarray,'bo', label='Calculated ADEV')
plt.loglog(tauarray, adevfit, 'b-', label='Fit')
plt.loglog(tauarray, gaussianfit, 'r-', label='Gaussian component')
```

```
plt.loglog(tauarray, driftfit, 'g-', label='Drift component')
plt.loglog(tauarray, randwalkfit, 'k-', label='Random walk component')
plt.legend(loc=4)
plt.grid(which='both')
plt.xlabel('Tau [s]')
plt.ylabel('Allan dev [arb]')
plt.show()

################################

# End matter

print("End - %s seconds" % (time.time() - start_time))

################################
```

Bibliography

[1] S. Dodelson, *Modern Cosmology.* Academic Press, 2003.

[2] A. A. Penzias and R. W. Wilson, "A measurement of excess antenna temperature at 4080 Mc/s.," *Astrophysical Journal*, vol. 142, pp. 419–421, July 1965.

[3] W. Hu and S. Dodelson, "Cosmic microwave background anisotropies," *Annual Review of Astron and Astrophys*, vol. 40, pp. 171–216, 2002.

[4] E. Hubble, "A relation between distance and radial velocity among extragalactic nebulae," *Proceedings of the National Academy of Sciences*, vol. 15, no. 3, pp. 168–173, 1929.

[5] W. L. Freedman, B. F. Madore, B. K. Gibson, L. Ferrarese, D. D. Kelson, S. Sakai, J. R. Mould, R. C. Kennicutt Jr, H. C. Ford, J. A. Graham, *et al.*, "Final results from the Hubble Space Telescope Key Project to measure the Hubble constant based on observations with the NASA/ESA Hubble Space Telescope, obtained at the Space Telescope Science Institute, which is operated by AURA, Inc., under NASA contract NAS5-26555.," *The Astrophysical Journal*, vol. 553, no. 1, p. 47, 2001.

[6] R. V. Wagoner, W. A. Fowler, and F. Hoyle, "On the synthesis of elements at very high temperatures," *The Astrophysical Journal*, vol. 148, p. 3, 1967.

[7] F. Iocco, G. Mangano, G. Miele, O. Pisanti, and P. D. Serpico, "Primordial nucleosynthesis: from precision cosmology to fundamental physics," *Physics Reports*, vol. 472, no. 1, pp. 1–76, 2009.

[8] NASA/WMAP Science Team, "Timeline of the universe." `http://map.gsfc.nasa.gov/media/060915/`, 2012.

[9] G. B. Rybicki and A. P. Lightman, *Radiative Processes in Astrophysics.* John Wiley & Sons, 2008.

[10] R. C. Tolman, *Relativity, Thermodynamics, and Cosmology.* Oxford: Clarendon Press, 1934.

[11] R. H. Dicke, P. J. E. Peebles, P. G. Roll, and D. T. Wilkinson, "Cosmic black-body radiation," *The Astrophysical Journal*, vol. 142, pp. 414–419, 1965.

[12] M. Bucher, "Physics of the cosmic microwave background anisotropy," *International Journal of Modern Physics D*, vol. 24, no. 02, p. 1530004, 2015.

[13] J. C. Mather, "The Cosmic Background Explorer (COBE)," *Optical Engineering*, vol. 21, no. 4, pp. 214769–214769, 1982.

[14] J. C. Mather, E. Cheng, R. Eplee Jr, R. Isaacman, S. Meyer, R. Shafer, R. Weiss, E. Wright, C. Bennett, N. Boggess, *et al.*, "A preliminary measurement of the cosmic microwave background spectrum by the Cosmic Background Explorer (COBE) satellite," *The Astrophysical Journal*, vol. 354, pp. L37–L40, 1990.

[15] J. C. Mather, E. Cheng, D. Cottingham, R. Eplee Jr, D. Fixsen, T. Hewagama, R. Isaacman, K. Jensen, S. Meyer, P. Noerdlinger, *et al.*, "Measurement of the cosmic microwave background spectrum by the COBE FIRAS instrument," *The Astrophysical Journal*, vol. 420, pp. 439–444, 1994.

[16] G. F. Smoot, C. Bennett, A. Kogut, E. Wright, J. Aymon, N. Boggess, E. Cheng, G. De Amici, S. Gulkis, M. Hauser, *et al.*, "Structure in the COBE differential microwave radiometer first-year maps," *The Astrophysical Journal*, vol. 396, pp. L1–L5, 1992.

[17] G. Hinshaw, D. Larson, E. Komatsu, D. Spergel, C. Bennett, J. Dunkley, M. Nolta, M. Halpern, R. Hill, N. Odegard, *et al.*, "Nine-year Wilkinson Microwave Anisotropy Probe (WMAP) observations: cosmological parameter results," *The Astrophysical Journal Supplement Series*, vol. 208, no. 2, p. 19, 2013.

[18] R. Adam, P. Ade, N. Aghanim, Y. Akrami, M. Alves, F. Argüeso, M. Arnaud, F. Arroja, M. Ashdown, J. Aumont, *et al.*, "Planck 2015 results - I. Overview of products and scientific results," *Astronomy & Astrophysics*, vol. 594, p. A1, 2016.

[19] C. Haslam, C. Salter, H. Stoffel, and W. Wilson, "A 408 MHz all-sky continuum survey. II-The atlas of contour maps," *Astronomy and Astrophysics Supplement Series*, vol. 47, p. 1, 1982.

[20] J. Bock, S. Church, M. Devlin, G. Hinshaw, A. Lange, A. Lee, L. Page, B. Partridge, J. Ruhl, M. Tegmark, *et al.*, "Task force on cosmic microwave background research," *arXiv preprint astro-ph/0604101*, 2006.

[21] J. R. Bond, R. Crittenden, R. L. Davis, G. Efstathiou, and P. J. Steinhardt, "Measuring cosmological parameters with cosmic microwave background experiments," *Physical Review Letters*, vol. 72, no. 1, p. 13, 1994.

[22] R. Durrer, *The Cosmic Microwave Background.* Cambridge University Press, 2008.

[23] P. de Bernardis, P. A. Ade, J. Bock, J. Bond, J. Borrill, A. Boscaleri, K. Coble, B. Crill, G. De Gasperis, P. Farese, *et al.*, "A flat universe from

high-resolution maps of the cosmic microwave background radiation," *Nature*, vol. 404, no. 6781, pp. 955–959, 2000.

[24] S. Hanany, P. Ade, A. Balbi, J. Bock, J. Borrill, A. Boscaleri, P. De Bernardis, P. Ferreira, V. Hristov, A. Jaffe, *et al.*, "MAXIMA-1: a measurement of the cosmic microwave background anisotropy on angular scales of 10'-5," *The Astrophysical Journal Letters*, vol. 545, no. 1, p. L5, 2000.

[25] P. A. Ade, N. Aghanim, M. Arnaud, M. Ashdown, J. Aumont, C. Baccigalupi, A. Banday, R. Barreiro, J. Bartlett, N. Bartolo, *et al.*, "Planck 2015 results - XIII. cosmological parameters," *Astronomy & Astrophysics*, vol. 594, p. A13, 2016.

[26] A. Kosowsky, M. Milosavljevic, and R. Jimenez, "Efficient cosmological parameter estimation from microwave background anisotropies," *Physical Review D*, vol. 66, no. 6, p. 063007, 2002.

[27] N. Aghanim, M. Arnaud, M. Ashdown, J. Aumont, C. Baccigalupi, A. Banday, R. Barreiro, J. Bartlett, N. Bartolo, E. Battaner, *et al.*, "Planck 2015 results - XI. CMB power spectra, likelihoods, and robustness of parameters," *Astronomy & Astrophysics*, vol. 594, p. A11, 2016.

[28] G. De Zotti, "Prospects for next generation cosmic microwave background experiments," *ArXiv e-prints*, Feb. 2018.

[29] A. H. Guth, "Inflationary universe: A possible solution to the horizon and flatness problems," *Physical Review D*, vol. 23, no. 2, p. 347, 1981.

[30] A. D. Linde, "A new inflationary universe scenario: a possible solution of the horizon, flatness, homogeneity, isotropy and primordial monopole problems," *Physics Letters B*, vol. 108, no. 6, pp. 389–393, 1982.

[31] A. H. Guth, "Inflation and the new era of high precision cosmology," *Physics@ MIT*, pp. 28–39, 2002.

[32] V. F. Mukhanov and G. Chibisov, "Quantum fluctuations and a nonsingular universe," *JETP Lett.*, vol. 33, pp. 532–535, 1981.

[33] A. A. Starobinsky, "Relict gravitation radiation spectrum and initial state of the universe," *JETP lett*, vol. 30, no. 682-685, pp. 131–132, 1979.

[34] W. Hu and N. Sugiyama, "Toward understanding CMB anisotropies and their implications," *Physical Review D*, vol. 51, no. 6, p. 2599, 1995.

[35] W. Hu and M. White, "A CMB polarization primer," *New Astronomy*, vol. 2, no. 4, pp. 323–344, 1997.

[36] B. F. Burke and F. Graham-Smith, *An Introduction to Radio Astronomy.* Cambridge University Press, third ed., 2010.

[37] M. Zaldarriaga and U. Seljak, "All-sky analysis of polarization in the microwave background," *Physical Review D*, vol. 55, no. 4, p. 1830, 1997.

[38] J. M. Kovac, E. Leitch, C. Pryke, J. Carlstrom, N. Halverson, and W. Holzapfel, "Detection of polarization in the cosmic microwave background using DASI," *Nature*, vol. 420, no. 6917, pp. 772–787, 2002.

[39] M. Zaldarriaga and U. Seljak, "Reconstructing projected matter density power spectrum from cosmic microwave background," *Physical Review D*, vol. 59, no. 12, p. 123507, 1999.

[40] P. Ade, Y. Akiba, A. Anthony, K. Arnold, M. Atlas, D. Barron, D. Boettger, J. Borrill, S. Chapman, Y. Chinone, *et al.*, "A measurement of the cosmic microwave background B-mode polarization power spectrum at sub-degree scales with POLARBEAR," *The Astrophysical Journal*, vol. 794, no. 2, p. 171, 2014.

[41] R. Keisler, S. Hoover, N. Harrington, J. Henning, P. Ade, K. Aird, J. Austermann, J. Beall, A. Bender, B. Benson, *et al.*, "Measurements of sub-degree B-mode polarization in the cosmic microwave background from 100 square degrees of SPTpol data," *The Astrophysical Journal*, vol. 807, no. 2, p. 151, 2015.

[42] S. Naess, M. Hasselfield, J. McMahon, M. D. Niemack, G. E. Addison, P. A. Ade, R. Allison, M. Amiri, N. Battaglia, J. A. Beall, *et al.*, "The Atacama Cosmology Telescope: CMB Polarization at $200< \ell <9000$," *Journal of Cosmology and Astroparticle Physics*, vol. 2014, no. 10, p. 007, 2014.

[43] U. Seljak and M. Zaldarriaga, "Signature of gravity waves in the polarization of the microwave background," *Physical Review Letters*, vol. 78, no. 11, p. 2054, 1997.

[44] M. Kamionkowski, A. Kosowsky, and A. Stebbins, "A probe of primordial gravity waves and vorticity," *Physical Review Letters*, vol. 78, no. 11, p. 2058, 1997.

[45] P. Ade, Z. Ahmed, R. Aikin, K. Alexander, D. Barkats, S. Benton, C. Bischoff, J. Bock, H. Boenish, *et al.*, "Measurements of degree-scale B-mode polarization with the BICEP/Keck experiments at South Pole," *arXiv preprint arXiv:1807.02199*, 2018.

[46] K. Abazajian, K. Arnold, J. Austermann, B. Benson, C. Bischoff, J. Bock, J. Bond, J. Borrill, I. Buder, D. Burke, *et al.*, "Inflation physics from the cosmic microwave background and large scale structure," *Astroparticle Physics*, vol. 63, pp. 55–65, 2015.

[47] The BICEP Collaboration, "Detection of B-mode polarization at degree angular scales by BICEP2," *Phys. Rev. Lett*, vol. 112, p. 241101, 2014.

[48] R. Flauger, J. C. Hill, and D. N. Spergel, “Toward an understanding of foreground emission in the BICEP2 region,” *Journal of Cosmology and Astroparticle Physics*, vol. 2014, no. 08, p. 039, 2014.

[49] P. A. Ade, N. Aghanim, Z. Ahmed, R. Aikin, K. Alexander, M. Arnaud, J. Aumont, C. Baccigalupi, A. J. Banday, D. Barkats, *et al.*, “Joint analysis of BICEP2/Keck Array and Planck data,” *Physical Review Letters*, vol. 114, no. 10, pp. 101–301, 2015.

[50] N. Aghanim, Y. Akrami, M. Ashdown, J. Aumont, C. Baccigalupi, M. Ballardini, A. Banday, R. Barreiro, N. Bartolo, S. Basak, *et al.*, “Planck 2018 results. VI. Cosmological parameters,” *arXiv preprint arXiv:1807.06209*, 2018.

[51] K. N. Abazajian, P. Adshead, Z. Ahmed, S. W. Allen, D. Alonso, K. S. Arnold, C. Baccigalupi, J. G. Bartlett, N. Battaglia, B. A. Benson, *et al.*, “CMB-S4 science book,” *arXiv preprint arXiv:1610.02743*, 2016.

[52] W. Wu, J. Errard, C. Dvorkin, C. Kuo, A. Lee, P. McDonald, A. Slosar, and O. Zahn, “A guide to designing future ground-based cosmic microwave background experiments,” *The Astrophysical Journal*, vol. 788, no. 2, p. 138, 2014.

[53] N. Mandolesi, G. Morgante, and F. Villa, “Low frequency instrument of Planck,” in *Astronomical Telescopes and Instrumentation*, pp. 722–729, International Society for Optics and Photonics, 2003.

[54] J.-M. Lamarre, J. Puget, F. Bouchet, P. A. Ade, A. Benoit, J. Bernard, J. Bock, P. De Bernardis, J. Charra, F. Couchot, *et al.*, “The Planck High Frequency Instrument, a third generation CMB experiment, and a full sky submillimeter survey,” *New Astronomy Reviews*, vol. 47, no. 11-12, pp. 1017–1024, 2003.

[55] C. Kuo, J. Bock, J. Bonetti, J. Brevik, G. Chattopadhyay, P. Day, S. Golwala, M. Kenyon, A. Lange, H. LeDuc, *et al.*, “Antenna-coupled TES bolometer arrays for CMB polarimetry,” in *SPIE Astronomical Telescopes+ Instrumentation*, pp. 70201I–70201I, International Society for Optics and Photonics, 2008.

[56] A. Paiella, A. Coppolecchia, M. Castellano, I. Colantoni, A. Cruciani, A. DAddabbo, P. de Bernardis, S. Masi, and G. Presta, “Development of lumped element kinetic inductance detectors for the W-band,” *Journal of Low Temperature Physics*, pp. 1–6, 2016.

[57] P. Richards, “Bolometers for infrared and millimeter waves,” *Journal of Applied Physics*, vol. 76, no. 1, pp. 1–24, 1994.

[58] C. Enss and D. McCammon, “Physical principles of low temperature detectors: ultimate performance limits and current detector capabilities,” *Journal of Low Temperature Physics*, vol. 151, no. 1-2, pp. 5–24, 2008.

[59] K. Morgan, “Hot science with cool sensors,” *Physics Today*, vol. 71, no. 8, 2018.

[60] K. Irwin, “An application of electrothermal feedback for high resolution cryogenic particle detection,” *Applied Physics Letters*, vol. 66, no. 15, pp. 1998–2000, 1995.

[61] K. D. Irwin and G. C. Hilton, “Transition-edge sensors,” in *Cryogenic particle detection*, pp. 63–150, Springer, 2005.

[62] S.-F. Lee, J. M. Gildemeister, W. Holmes, A. T. Lee, and P. L. Richards, “Voltage-biased superconducting transition-edge bolometer with strong electrothermal feedback operated at 370 mK,” *Applied Optics*, vol. 37, no. 16, pp. 3391–3397, 1998.

[63] K. D. Irwin, "SQUID multiplexers for transition-edge sensors," *Physica C: Superconductivity*, vol. 368, no. 1-4, pp. 203–210, 2002.

[64] S. W. Henderson, J. Stevens, M. Amiri, J. Austermann, J. A. Beall, S. Chaudhuri, H.-M. Cho, S. K. Choi, N. F. Cothard, K. T. Crowley, *et al.*, "Readout of two-kilopixel transition-edge sensor arrays for Advanced ACT-Pol," in *SPIE Astronomical Telescopes+ Instrumentation*, pp. 99141G–99141G, International Society for Optics and Photonics, 2016.

[65] A. Suzuki, K. Arnold, J. Edwards, G. Engargiola, A. Ghribi, W. Holzapfel, A. T. Lee, X. F. Meng, M. J. Myers, R. O'Brient, *et al.*, "Multichroic dual-polarization bolometric detectors for studies of the cosmic microwave background," in *SPIE Astronomical Telescopes+ Instrumentation*, pp. 84523H–84523H, International Society for Optics and Photonics, 2012.

[66] J. Bock, D. Chen, P. D. Mauskopf, and A. Lange, "A novel bolometer for infrared and millimeter-wave astrophysics," *Space Science Reviews*, vol. 74, no. 1-2, pp. 229–235, 1995.

[67] M. D. Audley, R. W. Barker, M. Crane, R. Dace, D. Glowacka, D. J. Goldie, A. N. Lasenby, H. M. Stevenson, V. Tsaneva, S. Withington, *et al.*, "TES imaging array technology for ClOVER," in *Millimeter and Submillimeter Detectors and Instrumentation for Astronomy III*, vol. 6275, p. 627524, International Society for Optics and Photonics, 2006.

[68] M. D. Niemack, "Designs for a large-aperture telescope to map the CMB 10x faster," *Appl. Opt.*, vol. 55, pp. 1688–1696, Mar 2016.

[69] M. H. Abitbol, Z. Ahmed, D. Barron, R. B. Thakur, A. N. Bender, B. A. Benson, C. A. Bischoff, S. A. Bryan, J. E. Carlstrom, C. L. Chang, *et al.*, "CMB-S4 technology book," *arXiv preprint arXiv:1706.02464*, 2017.

[70] J. Pardo, J. Cernicharo, and E. Serabyn, "Modeling the atmospheric long-wave spectrum: State of the art in the horizon of ALMA," in *Astronomical Site Evaluation in the Visible and Radio Range*, vol. 266, p. 188, 2002.

[71] S. Henderson, R. Allison, J. Austermann, T. Baildon, N. Battaglia, J. Beall, D. Becker, F. De Bernardis, J. Bond, E. Calabrese, *et al.*, "Advanced ACT-Pol cryogenic detector arrays and readout," *Journal of Low Temperature Physics*, pp. 1–8, 2016.

[72] Z. Ahmed, M. Amiri, S. Benton, J. Bock, R. Bowens-Rubin, I. Buder, E. Bullock, J. Connors, J. Filippini, J. Grayson, *et al.*, "BICEP3: a 95GHz refracting telescope for degree-scale CMB polarization," in *SPIE Astronomical Telescopes+ Instrumentation*, pp. 91531N–91531N, International Society for Optics and Photonics, 2014.

[73] T. Essinger-Hileman, A. Ali, M. Amiri, J. W. Appel, D. Araujo, C. L. Bennett, F. Boone, M. Chan, H.-M. Cho, D. T. Chuss, *et al.*, "CLASS: the Cosmology Large Angular Scale Surveyor," in *SPIE Astronomical Telescopes+ Instrumentation*, pp. 91531I–91531I, International Society for Optics and Photonics, 2014.

[74] R. Gualtieri, E. S. Battistelli, A. Cruciani, P. de Bernardis, M. Biasotti, D. Corsini, F. Gatti, L. Lamagna, and S. Masi, "Multi-mode TES bolometer optimization for the LSPE-SWIPE instrument," *Journal of Low Temperature Physics*, pp. 1–7, 2016.

[75] A. Tartari, J. Aumont, S. Banfi, P. Battaglia, E. Battistelli, A. Baù, B. Bélier, D. Bennett, L. Bergé, J. P. Bernard, *et al.*, "QUBIC: a Fizeau interferometer targeting primordial B-modes," *Journal of Low Temperature Physics*, vol. 184, no. 3-4, pp. 739–745, 2016.

[76] K. Arnold, N. Stebor, P. Ade, Y. Akiba, A. Anthony, M. Atlas, D. Barron, A. Bender, D. Boettger, J. Borrill, *et al.*, "The Simons Array: expand-

ing POLARBEAR to three multi-chroic telescopes," in *SPIE Astronomical Telescopes+ Instrumentation*, pp. 91531F–91531F, International Society for Optics and Photonics, 2014.

[77] N. Galitzki, A. Ali, K. Arnold, P. Ashton, J. Austermann, J. Beall, S. Bryan, P. Calisse, Y. Chinone, G. Coppi, *et al.*, "The Simons Observatory cryogenic cameras," in *Proc. SPIE*, pp. 10708–3, 2018.

[78] J. Filippini, P. A. Ade, M. Amiri, S. Benton, R. Bihary, J. Bock, J. Bond, J. Bonetti, S. Bryan, B. Burger, *et al.*, "SPIDER: a balloon-borne CMB polarimeter for large angular scales," in *SPIE Astronomical Telescopes+ Instrumentation*, pp. 77411N–77411N, International Society for Optics and Photonics, 2010.

[79] B. Benson, P. Ade, Z. Ahmed, S. Allen, K. Arnold, J. Austermann, A. Bender, L. Bleem, J. Carlstrom, C. Chang, *et al.*, "SPT-3G: a next-generation cosmic microwave background polarization experiment on the South Pole telescope," in *SPIE Astronomical Telescopes+ Instrumentation*, pp. 91531P–91531P, International Society for Optics and Photonics, 2014.

[80] F. Pobell, *Matter and Methods at Low Temperatures.* Springer Science & Business Media, 2007.

[81] J. G. Weisend, *Handbook of Cryogenic Engineering.* Taylor & Francis, Philadelphia, PA, 1998.

[82] R. F. Barron, *Cryogenic Heat Transfer*, vol. 1. Taylor & Francis Philadelphia, PA, 1999.

[83] S. W. Van Sciver, *Helium Cryogenics.* Springer Science & Business Media, 2012.

[84] G. Ventura and L. Risegari, *The Art of Cryogenics: Low-Temperature Experimental Techniques.* Elsevier, 2010.

[85] J. Wilks and D. S. Betts, *An Introduction to Liquid Helium.* Clarendon Press, 1987.

[86] D. R. Tilley and J. Tilley, *Superfluidity and Superconductivity.* CRC Press, 1990.

[87] L. Landau, "On the theory of superfluidity," *Physical Review*, vol. 75, no. 5, p. 884, 1949.

[88] L. Landau, "Theory of the superfluidity of helium II," *Physical Review*, vol. 60, no. 4, p. 356, 1941.

[89] L. Tisza, "Transport phenomena in helium II," *Nature*, vol. 141, no. 3577, p. 913, 1938.

[90] L. Duband, L. Clerc, E. Ercolani, L. Guillemet, and R. Vallcorba, "Herschel flight models sorption coolers," *Cryogenics*, vol. 48, no. 3, pp. 95–105, 2008.

[91] D. Sedgley, A. Tobin, T. Batzer, and W. Call, "Characterization of charcoals for helium cryopumping in fusion devices," *Journal of Vacuum Science & Technology A*, vol. 5, no. 4, pp. 2572–2576, 1987.

[92] J. E. Lennard-Jones, "Cohesion," *Proceedings of the Physical Society*, vol. 43, no. 5, p. 461, 1931.

[93] S. Brunauer, P. H. Emmett, and E. Teller, "Adsorption of gases in multimolecular layers," *Journal of the American chemical society*, vol. 60, no. 2, pp. 309–319, 1938.

[94] L. Piccirillo, G. Coppi, and A. May, *Miniature Sorption Coolers: Theory and Applications.* CRC Press, 2018.

[95] B. Baudouy, "Heat transfer and cooling techniques at low temperature," *arXiv preprint arXiv:1501.07153*, 2015.

[96] F. M. White, *Fluid Mechanics.* McGraw-Hill, 5th ed., 2003.

[97] J. Ekin, *Experimental Techniques for Low-Temperature Measurements: Cryostat design, material properties and superconductor critical-current testing.* Oxford university press, 2006.

[98] W. Obert, "Emissivity measurements of metallic surfaces used in cryogenic applications," *Advances in Cryogenic Engineering*, vol. 27, p. 293, 1982.

[99] V. Parma, "Cryostat design," *arXiv preprint arXiv:1501.07154*, 2015.

[100] E. Marquardt, J. Le, and R. Radebaugh, "Cryogenic material properties database," in *Cryocoolers 11*, pp. 681–687, Springer, 2002.

[101] P. Duthil, "Material properties at low temperature," *arXiv preprint arXiv:1501.07100*, 2015.

[102] E. Swartz and R. O. Pohl, "Thermal boundary resistance," *Review of Modern Physics*, vol. 61, no. 3, p. 605, 1989.

[103] P. Kapitza, "The study of heat transfer in helium II," *J. Phys.(USSR)*, vol. 4, no. 1-6, pp. 181–210, 1941.

[104] I. Khalatnikov, "Teploobmen mezhdu tverdym telom i geliem-II," *Zhurnal Eksperimentalnoi I Teoreticheskoi Fiziki*, vol. 22, no. 6, pp. 687–704, 1952.

[105] R. Mazo, *Theoretical studies on low temperature phenomena.* PhD thesis, Yale University, New Haven, 1955.

[106] R. Radebaugh, "Cryocoolers: the state of the art and recent developments," *Journal of Physics: Condensed Matter*, vol. 21, no. 16, p. 164219, 2009.

[107] L. Trevisani, T. Kuriyama, F. Negrini, T. Okamura, Y. Ohtani, M. Okamura, and M. Fabbri, "Performance improvement of a two-stage GM cryocooler by use of Er (Ni0. 075Co0. 925) 2 magnetic regenerator material," *Cryogenics*, vol. 42, no. 10, pp. 653–657, 2002.

[108] R. Radebaugh, “A review of pulse tube refrigeration,” in *Advances in cryogenic engineering*, pp. 1191–1205, Springer, 1990.

[109] R. Radebaugh, *Handbook of Measurement in Science and Engineering*, vol. 3, ch. 61. John Wiley & Sons, 2016.

[110] N. Luchier, J. Duval, L. Duband, P. Camus, G. Donnier-Valentin, and M. Linder, “50mK cooling solution with an ADR precooled by a sorption cooler,” *Cryogenics*, vol. 50, no. 9, pp. 591–596, 2010.

[111] G. Dall’Oglio, L. Pizzo, L. Piccirillo, and L. Martinis, “New 3He/4He refrigerator,” *Cryogenics*, vol. 31, no. 1, pp. 61–63, 1991.

[112] J. Aumont, S. Banfi, P. Battaglia, E. S. Battistelli, A. Baù, B. Bélier, D. Bennett, L. Bergé, J. P. Bernard, M. Bersanelli, M. A. Bigot-Sazy, N. Bleurvacq, G. Bordier, J. Brossard, E. F. Bunn, D. Buzi, A. Buzzelli, D. Cammilleri, F. Cavaliere, P. Chanial, C. Chapron, G. Coppi, A. Coppolecchia, F. Couchot, R. D’Agostino, G. D’Alessandro, P. de Bernardis, G. De Gasperis, M. De Petris, T. Decourcelle, F. Del Torto, L. Dumoulin, A. Etchegoyen, C. Franceschet, B. Garcia, A. Gault, D. Gayer, M. Gervasi, A. Ghribi, M. Giard, Y. Giraud-Héraud, M. Gradziel, L. Grandsire, J. C. Hamilton, D. Harari, V. Haynes, S. Henrot-Versillé, N. Holtzer, J. Kaplan, A. Korotkov, L. Lamagna, J. Lande, S. Loucatos, A. Lowitz, V. Lukovic, B. Maffei, S. Marnieros, J. Martino, S. Masi, A. May, M. McCulloch, M. C. Medina, S. Melhuish, A. Mennella, L. Montier, A. Murphy, D. Néel, M. W. Ng, C. O’Sullivan, A. Paiella, F. Pajot, A. Passerini, A. Pelosi, C. Perbost, O. Perdereau, F. Piacentini, M. Piat, L. Piccirillo, G. Pisano, D. Prêle, R. Puddu, D. Rambaud, O. Rigaut, G. E. Romero, M. Salatino, A. Schillaci, S. Scully, M. Stolpovskiy, F. Suarez, A. Tartari, P. Timbie, M. Tristram, G. Tucker, D. Viganò, N. Vittori, F. Voisin, B. Watson, M. Zannoni, and A. Zullo, “QUBIC Technical Design Report,” *ArXiv e-prints*, Sept. 2016.

[113] C. O'Sullivan, P. Ade, G. Amico, D. Auguste, J. Aumont, S. Banfi, G. Barbarán, P. Battaglia, E. Battistelli, A. Baù, *et al.*, "QUBIC: the Q and U Bolometric Interferometer for Cosmology," in *Millimeter, Submillimeter, and Far-Infrared Detectors and Instrumentation for Astronomy IX*, vol. 10708, p. 107082B, International Society for Optics and Photonics, 2018.

[114] S. Ali, P. Rossinot, L. Piccirillo, W. K. Gear, P. Mauskopf, P. Ade, V. Haynes, and P. Timbie, "MBI: Millimetre-wave Bolometric Interferometer," in *AIP Conference Proceedings*, vol. 616, pp. 126–128, AIP, 2002.

[115] C. J. Koester, "Achromatic combinations of half-wave plates," *JOSA*, vol. 49, no. 4, pp. 405–409, 1959.

[116] B. R. Johnson, J. Collins, M. Abroe, P. A. Ade, J. Bock, J. Borrill, A. Boscaleri, P. De Bernardis, S. Hanany, A. Jaffe, *et al.*, "Maxipol: cosmic microwave background polarimetry using a rotating half-wave plate," *The Astrophysical Journal*, vol. 665, no. 1, p. 42, 2007.

[117] C. A. Hill, A. Kusaka, P. Barton, B. Bixler, A. G. Droster, M. Flament, S. Ganjam, A. Jadbabaie, O. Jeong, A. T. Lee, *et al.*, "A large-diameter cryogenic rotation stage for half-wave plate polarization modulation on the POLARBEAR-2 experiment," *Journal of Low Temperature Physics*, vol. 193, no. 5-6, pp. 851–859, 2018.

[118] S. Scully, D. Burke, C. O'Sullivan, D. Gayer, M. Gradziel, J. Murphy, M. De Petris, D. Buzi, M. Zannoni, A. Mennella, *et al.*, "Optical design and modelling of the QUBIC instrument, a next-generation quasi-optical bolometric interferometer for cosmology," in *Millimeter, Submillimeter, and Far-Infrared Detectors and Instrumentation for Astronomy VIII*, vol. 9914, p. 99142S, International Society for Optics and Photonics, 2016.

[119] M.-A. Bigot-Sazy, R. Charlassier, J.-C. Hamilton, J. Kaplan, and G. Zahariade, "Self-calibration: an efficient method to control systematic effects in bolometric interferometry," *Astronomy & Astrophysics*, vol. 550, p. A59, 2013.

[120] A. Mennella, P. Ade, G. Amico, D. Auguste, J. Aumont, S. Banfi, G. Baràn, P. Battaglia, E. Battistelli, A. Baù, *et al.*, "QUBIC: Exploring the primordial universe with the Q&U Bolometric Interferometer," *Universe*, vol. 5, no. 2, p. 42, 2019.

[121] G. D'Alessandro, A. Paiella, A. Coppolecchia, M. Castellano, I. Colantoni, P. de Bernardis, L. Lamagna, and S. Masi, "Ultra high molecular weight polyethylene: optical features at millimeter wavelengths," *Infrared Physics & Technology*, vol. 90, pp. 59–65, 2018.

[122] S. Bapat, K. Narayankhedkar, and T. Lukose, "Performance prediction of multilayer insulation," *Cryogenics*, vol. 30, no. 8, pp. 700–710, 1990.

[123] G. Pisano, M. W. Ng, V. Haynes, and B. Maffei, "A broadband metal-mesh half-wave plate for millimetre wave linear polarisation rotation," *Progress In Electromagnetics Research*, vol. 25, pp. 101–114, 2012.

[124] M. Salatino, P. de Bernardis, and S. Masi, "A cryogenic waveplate rotator for polarimetry at mm and submm wavelengths," *Astronomy & Astrophysics*, vol. 528, p. A138, 2011.

[125] J.-P. Thermeau. Private communication.

[126] J.-P. Thermeau. Private communication.

[127] O. V. Lounasmaa, *Experimental Principles and Methods Below 1 K*, vol. 8. academic Press London, 1974.

[128] A. May, G. Coppi, L. Martinis, S. Melhuish, and L. Piccirillo, "A closed-cycle convective ^{4}He heat switch," *In Preparation*, 2019.

[129] R. H. Torii and H. J. Maris, "Low-temperature heat switch using unforced convection," *Review of scientific instruments*, vol. 57, no. 4, pp. 655–657, 1986.

[130] A. May, "Closed-cycle sorption coolers and tiltable miniature dilution refrigerators for astrophysics," Master's thesis, University of Manchester, 2017.

[131] J. Torre and G. Chanin, "Miniature liquid-3He refrigerator," *Review of scientific instruments*, vol. 56, no. 2, pp. 318–320, 1985.

[132] J. Bock, L. Duband, M. Kawada, H. Matsuhara, T. Matsumoto, and A. Lange, "4He refrigerator for space," *Cryogenics*, vol. 34, no. 8, pp. 635–640, 1994.

[133] E. Cheng, S. Meyer, and L. Page, "A high capacity 0.23 K 3He refrigerator for balloon-borne payloads," *Review of scientific instruments*, vol. 67, no. 11, pp. 4008–4016, 1996.

[134] L. Duband and B. Collaudin, "Sorption coolers development at CEA-SBT," *Cryogenics*, vol. 39, no. 8, pp. 659–663, 1999.

[135] R. Bhatia, S. Chase, S. Edgington, J. Glenn, W. Jones, A. Lange, B. Maffei, A. Mainzer, P. Mauskopf, B. Philhour, *et al.*, "A three-stage helium sorption refrigerator for cooling of infrared detectors to 280 mK," *Cryogenics*, vol. 40, no. 11, pp. 685–691, 2000.

[136] M. Devlin, S. Dicker, J. Klein, and M. Supanich, "A high capacity completely closed-cycle 250 mK 3He refrigeration system based on a pulse tube cooler," *Cryogenics*, vol. 44, no. 9, pp. 611–616, 2004.

[137] S. Dushman and J. Lafferty, *Scientific Foundations of Vacuum Technology.* Wiley, New York, 1962.

[138] P. Nacher and J. Dupont-Roc, "Experimental evidence for nonwetting with superfluid helium," *Physical review letters*, vol. 67, no. 21, p. 2966, 1991.

[139] P. Shirron and M. DiPirro, "Suppression of superfluid film flow in the XRS helium dewar," in *Advances in cryogenic engineering*, pp. 949–956, Springer, 1998.

[140] J. Lau, M. Benna, M. Devlin, S. Dicker, and L. Page, "Experimental tests and modeling of the optimal orifice size for a closed cycle 4 He sorption refrigerator," *Cryogenics*, vol. 46, no. 11, pp. 809–814, 2006.

[141] M. Salatino, B. Bélier, C. Chapron, D. Hoang, S. Maestre, S. Marnieros, W. Marty, L. Montier, M. Piat, D. Prêle, *et al.*, "Performance of NbSi transition-edge sensors readout with a 128 MUX factor for the QUBIC experiment," in *Millimeter, Submillimeter, and Far-Infrared Detectors and Instrumentation for Astronomy IX*, vol. 10708, p. 1070845, International Society for Optics and Photonics, 2018.

[142] C. Stott, *Optically Detected Magnetic Resonance and Sub-Kelvin EPR at Q Band.* PhD thesis, The University of Manchester (United Kingdom), 2016.

[143] Z. D. Kermish, P. Ade, A. Anthony, K. Arnold, D. Barron, D. Boettger, J. Borrill, S. Chapman, Y. Chinone, M. A. Dobbs, *et al.*, "The POLARBEAR experiment," in *Millimeter, Submillimeter, and Far-Infrared Detectors and Instrumentation for Astronomy VI*, vol. 8452, p. 84521C, International Society for Optics and Photonics, 2012.

[144] A. Suzuki, P. Ade, Y. Akiba, C. Aleman, K. Arnold, C. Baccigalupi, B. Barch, D. Barron, A. Bender, D. Boettger, *et al.*, "The Polarbear-2

and the Simons Array Experiments," *Journal of Low Temperature Physics*, pp. 1–6, 2015.

[145] N. Stebor, P. Ade, Y. Akiba, C. Aleman, K. Arnold, C. Baccigalupi, B. Barch, D. Barron, S. Beckman, A. Bender, *et al.*, "The Simons Array CMB polarization experiment," in *SPIE Astronomical Telescopes+ Instrumentation*, pp. 99141H–99141H, International Society for Optics and Photonics, 2016.

[146] R. Thornton, P. Ade, S. Aiola, F. Angile, M. Amiri, J. Beall, D. Becker, H. Cho, S. Choi, P. Corlies, *et al.*, "The Atacama Cosmology Telescope: The polarization-sensitive ACTPol instrument," *The Astrophysical Journal Supplement Series*, vol. 227, no. 2, p. 21, 2016.

[147] G. Coppi, *Cryogenic Design and Instrumentation for CMB Experiments.* PhD thesis, University of Manchester, 2018.

[148] C. Dragone, "Offset multireflector antennas with perfect pattern symmetry and polarization discrimination," *Bell System Technical Journal*, vol. 57, no. 7, pp. 2663–2684, 1978.

[149] K. Arnold, P. A. Ade, A. Anthony, F. Aubin, D. Boettger, J. Borrill, C. Cantalupo, M. Dobbs, J. Errard, D. Flanigan, *et al.*, "The POLARBEAR CMB polarization experiment," in *Millimeter, Submillimeter, and Far-Infrared Detectors and Instrumentation for Astronomy V*, vol. 7741, p. 77411E, International Society for Optics and Photonics, 2010.

[150] P. Ade, M. Aguilar, Y. Akiba, K. Arnold, C. Baccigalupi, D. Barron, D. Beck, F. Bianchini, D. Boettger, J. Borrill, *et al.*, "A measurement of the cosmic microwave background B-mode polarization power spectrum at subdegree scales from two years of Polarbear data," *The Astrophysical Journal*, vol. 848, no. 2, p. 121, 2017.

[151] T. Matsumura, P. Ade, K. Arnold, D. Barron, J. Borrill, S. Chapman, Y. Chinone, M. Dobbs, J. Errard, G. Fabbian, *et al.*, "Polarbear-2 optical and polarimeter designs," in *Millimeter, Submillimeter, and Far-Infrared Detectors and Instrumentation for Astronomy VI*, vol. 8452, p. 84523E, International Society for Optics and Photonics, 2012.

[152] W. Hu and T. Okamoto, "Mass reconstruction with cosmic microwave background polarization," *The Astrophysical Journal*, vol. 574, no. 2, p. 566, 2002.

[153] L. Howe, C. Tsai, L. Lowry, K. Arnold, G. Coppi, J. Groh, X. Guo, B. Keating, A. Lee, A. J. May, *et al.*, "Design and characterization of the POLARBEAR-2b and POLARBEAR-2c cosmic microwave background cryogenic receivers," in *Millimeter, Submillimeter, and Far-Infrared Detectors and Instrumentation for Astronomy IX*, vol. 10708, p. 107083W, International Society for Optics and Photonics, 2018.

[154] Y. Inoue, *Development of POLARBEAR-2 receiver system for cosmic microwave background polarization experiment.* PhD thesis, SOKENDAI - The Graduate University for Advanced Studies, 2016.

[155] D. W. Allan, "Statistics of atomic frequency standards," *Proceedings of the IEEE*, vol. 54, no. 2, pp. 221–230, 1966.

[156] D. W. Allan, "Should the classical variance be used as a basic measure in standards metrology?," *IEEE Transactions on instrumentation and measurement*, no. 2, pp. 646–654, 1987.

[157] D. Land, A. Levick, and J. Hand, "The use of the Allan deviation for the measurement of the noise and drift performance of microwave radiometers," *Measurement science and technology*, vol. 18, no. 7, p. 1917, 2007.

[158] A. Lee. Private Communication.

[159] P. Ade, J. Aguirre, Z. Ahmed, S. Aiola, A. Ali, D. Alonso, M. A. Alvarez, K. Arnold, P. Ashton, J. Austermann, *et al.*, "The Simons Observatory: science goals and forecasts," *Journal of Cosmology and Astroparticle Physics*, vol. 2019, no. 02, p. 056, 2019.

[160] R. Sunyaev and Y. B. Zeldovich, "The observations of relic radiation as a test of the nature of x-ray radiation from the clusters of galaxies," *Comments on Astrophysics and Space Physics*, vol. 4, p. 173, 1972.

[161] R. Sunyaev and I. B. Zeldovich, "The velocity of clusters of galaxies relative to the microwave background-the possibility of its measurement," *Monthly Notices of the Royal Astronomical Society*, vol. 190, pp. 413–420, 1980.

[162] J. E. Carlstrom, G. P. Holder, and E. D. Reese, "Cosmology with the Sunyaev-Zel'dovich effect," *Annual Review of Astronomy and Astrophysics*, vol. 40, no. 1, pp. 643–680, 2002.

[163] S. C. Parshley, J. Kronshage, J. Blair, T. Herter, M. Nolta, G. J. Stacey, A. Bazarko, F. Bertoldi, R. Bustos, D. B. Campbell, *et al.*, "CCAT-prime: a novel telescope for sub-millimeter astronomy," in *Ground-based and Airborne Telescopes VII*, vol. 10700, p. 107005X, International Society for Optics and Photonics, 2018.

[164] N. Zhu, J. L. Orlowski-Scherer, Z. Xu, A. Ali, K. S. Arnold, P. C. Ashton, G. Coppi, M. J. Devlin, S. R. Dicker, N. Galitzki, *et al.*, "Simons Observatory large aperture telescope receiver design overview," in *Millimeter, Submillimeter, and Far-Infrared Detectors and Instrumentation for Astronomy IX*, vol. 10708, p. 1070829, International Society for Optics and Photonics, 2018.

[165] J. L. Orlowski-Scherer, N. Zhu, Z. Xu, A. Ali, K. S. Arnold, P. C. Ashton, G. Coppi, M. Devlin, S. Dicker, N. Galitzki, *et al.*, "Simons Observatory

large aperture receiver simulation overview," in *Millimeter, Submillimeter, and Far-Infrared Detectors and Instrumentation for Astronomy IX*, vol. 10708, p. 107083X, International Society for Optics and Photonics, 2018.

[166] S. R. Dicker, P. A. Gallardo, J. Gundmudsson, P. D. Mauskopf, M. D. Niemack, A. Ali, P. C. Ashton, G. Coppi, M. J. Devlin, N. Galitzki, H. S. P., C. A. Hill, J. Hubmayr, B. Keating, A. T. Lee, M. Limon, F. Matsuda, J. McMahon, J. L. Orlowski-Scherer, L. Piccirillo, S. S. M., R. Thornton, J. N. Ullom, E. M. Vavagiakis, E. J. Wollack, Z. Xu, and N. Zhu, "Cold optical design for the Large Aperture Simons Observatory telescope," in *Ground-based and Airborne Telescopes VII*, Proc. SPIE, pp. 10700–122, 2018.

[167] S.-P. Ho *et al.*, "The universal focal plane module for the Simons Observatory," in *Millimeter, Submillimeter, and Far-Infrared Detectors and Instrumentation for Astronomy IX*, pp. 10708 – 126, 2018.

[168] R. Datta, J. Hubmayr, C. Munson, J. Austermann, J. Beall, D. Becker, H.-M. Cho, N. Halverson, G. Hilton, K. Irwin, *et al.*, "Horn coupled multichroic polarimeters for the Atacama Cosmology Telescope polarization experiment," *Journal of Low Temperature Physics*, vol. 176, no. 5-6, pp. 670–676, 2014.

[169] J. A. B. Mates, *The microwave SQUID multiplexer.* PhD thesis, The University of Colorado, Boulder, 2011.

[170] B. Dober, D. T. Becker, D. A. Bennett, S. A. Bryan, S. M. Duff, J. D. Gard, J. P. Hays-Wehle, G. Hilton, J. Hubmayr, J. Mates, *et al.*, "Microwave SQUID multiplexer demonstration for cosmic microwave background imagers," *Applied physics letters*, vol. 111, no. 24, p. 243510, 2017.

[171] G. Coppi, Z. Xu, A. Ali, N. Galitzki, P. A. Gallardo, A. J. May, J. L. Orlowski-Scherer, N. Zhu, M. J. Devlin, S. R. Dicker, *et al.*, "Cooldown strategies and transient thermal simulations for the Simons Observatory," in *Millimeter, Submillimeter, and Far-Infrared Detectors and Instrumentation for Astronomy IX*, vol. 10708, p. 1070827, International Society for Optics and Photonics, 2018.

[172] K. Guckelsberger, H. Hennecke, and R. Scherm, "An efficient cryopump for exchange gas in dilution refrigerators," *Cryogenics*, vol. 23, no. 12, p. 675, 1983.

[173] H. Wang, T. Wagner, and G. Eska, "An aluminium heat switch made from cold-pressed Cu–Al composite," *Physica B: Condensed Matter*, vol. 284, pp. 2024–2025, 2000.

[174] A. Kashani, B. Helvensteijn, F. McCormack, and A. Spivak, "Helium liquid- and gas-gap heat switches," in *Proceedings of the ICCC*, vol. 7, pp. 355–370, DTIC Document, 1993.

[175] W. Keller, H. Sommers Jr, and J. Dash, "Simple He II heat switch," *Review of Scientific Instruments*, vol. 29, no. 6, pp. 530–530, 1958.

[176] J. Bartlett, G. Hardy, I. Hepburn, C. Brockley-Blatt, P. Coker, E. Crofts, B. Winter, S. Milward, R. Stafford-Allen, M. Brownhill, J. Reed, M. Linder, and N. Rando, "Improved performance of an engineering model cryogen free double adiabatic demagnetization refrigerator," *Cryogenics*, vol. 50, no. 9, pp. 582 – 590, 2010. 2009 Space Cryogenic Workshop.

[177] A. Kashani, P. B. Helvensteijn, F. J. McCormack, and A. L. Spivak, "Helium liquid-and gas-gap heat switches for applications at 2 K," in *Advances in cryogenic engineering*, pp. 1657–1663, Springer, 1994.

[178] I. Catarino, G. Bonfait, and L. Duband, "Neon gas-gap heat switch," *Cryogenics*, vol. 48, no. 1-2, pp. 17–25, 2008.

[179] R. Bywaters and R. Griffin, "A gas-gap thermal switch for cryogenic applications," *Cryogenics*, vol. 13, no. 6, pp. 344–349, 1973.

[180] T. Nast, G. Bell, and C. Barnes, "Development of gas gap cryogenic thermal switch," in *Advances in Cryogenic Engineering*, vol. 27, pp. 1117–1124, 1982.

[181] L. Duband, L. Hui, and A. Lange, "Space-borne 3He refrigerator," *Cryogenics*, vol. 30, no. 3, pp. 263–270, 1990.

[182] P. Shirron, E. Canavan, M. DiPirro, M. Jackson, J. Panek, and J. Tuttle, "Passive gas-gap heat switches for use in adiabatic demagnetization refrigerators," in *AIP Conference Proceedings*, pp. 1175–1182, IOP Publishing Ltd, 2002.

[183] J. Franco, D. Martins, I. Catarino, and G. Bonfait, "Narrow gas gap in cryogenic heat switch," *Applied Thermal Engineering*, vol. 70, no. 1, pp. 115–121, 2014.

[184] G. Coppi. Private Communication.

[185] B. Westbrook, A. Cukierman, A. Lee, A. Suzuki, C. Raum, and W. Holzapfel, "Development of the next generation of multi-chroic antenna-coupled transition edge sensor detectors for CMB polarimetry," *Journal of Low Temperature Physics*, vol. 184, no. 1-2, pp. 74–81, 2016.

[186] A. Suzuki, C. Bebek, M. Garcia-Sciveres, S. Holland, A. Kusaka, A. T. Lee, N. Palaio, N. Roe, and L. Steinmetz, "Commercialization of micro-fabrication of antenna-coupled transition edge sensor bolometer detectors for studies of the cosmic microwave background," *Journal of Low Temperature Physics*, vol. 193, no. 5-6, pp. 744–751, 2018.

[187] H. London, G. Clarke, and E. Mendoza, "Osmotic pressure of He 3 in liquid He 4, with proposals for a refrigerator to work below 1 K," *Physical Review*, vol. 128, no. 5, p. 1992, 1962.

[188] P. Das, R. B. de Ouboter, and K. Taconis, "A realization of a London-Clarke-Mendoza type refrigerator," in *Low Temperature Physics LT9*, pp. 1253–1255, Springer, 1965.

[189] H. Hall, P. Ford, and K. Thompson, "A helium-3 dilution refrigerator," *Cryogenics*, vol. 6, no. 2, pp. 80–88, 1966.

[190] R. Radebaugh and J. Siegwarth, "Dilution refrigerator technology," *Cryogenics*, vol. 11, no. 5, pp. 368 – 384, 1971.

[191] D. Edwards, D. Brewer, P. Seligman, M. Skertic, and M. Yaqub, "Solubility of He 3 in liquid He 4 at 0 K," *Physical Review Letters*, vol. 15, no. 20, p. 773, 1965.

[192] R. de Bruyn Ouboter, K. Taconis, C. Le Pair, and J. Beenakker, "Thermodynamic properties of liquid 3He - 4He mixtures derived from specific heat measurements between 0.4 K and 2 K over the complete concentration range," *Physica*, vol. 26, no. 11, pp. 853–888, 1960.

[193] D. Brewer and J. Keyston, "Phase separation of dilute mixtures of He 4 in He 3," *Physics Letters*, vol. 1, no. 1, pp. 5–6, 1962.

[194] R. J. Donnelly and C. F. Barenghi, "The observed properties of liquid helium at the saturated vapor pressure," *Journal of Physical and Chemical Reference Data*, vol. 27, no. 6, pp. 1217–1274, 1998.

[195] C. Heer and J. Daunt, "A Contribution to the theory of Bose-Einstein liquids," *Physical Review*, vol. 81, no. 3, p. 447, 1951.

[196] D. S. Betts, *An Introduction to Millikelvin Technology*, vol. 1. Cambridge University Press, 1989.

[197] R. Radebaugh, "Thermodynamic properties of He3-He4 solutions with applications to the He3-He4 dilution refrigerator," *NBS Technical Note*, vol. 392, 1967.

[198] A. Anderson, W. Roach, R. Sarwinski, and J. Wheatley, "Heat capacity of dilute solutions of liquid He3 in He4 at low temperatures," *Physical Review Letters*, vol. 16, no. 7, p. 263, 1966.

[199] J. C. Wheatley, "Dilute solutions of 3He in 4He at low temperatures," *American Journal of Physics*, vol. 36, no. 3, pp. 181–210, 1968.

[200] F. London, *Superfluids*. Wiley, 1954.

[201] V. Edel'man, "A dilution refrigerator with condensation pump," *Cryogenics*, vol. 12, no. 5, pp. 385–387, 1972.

[202] K. Uhlig and W. Hehn, "3He 4He dilution refrigerator precooled by Gifford-McMahon refrigerator," *Cryogenics*, vol. 37, no. 5, pp. 279 – 282, 1997.

[203] K. Uhlig, "3He 4He dilution refrigerator with pulse-tube refrigerator precooling," *Cryogenics*, vol. 42, no. 2, pp. 73 – 77, 2002.

[204] A. Suzuki. Private Communication.

[205] S. J. Melhuish, L. Martinis, and L. Piccirillo, "A tiltable single-shot miniature dilution refrigerator for astrophysical applications," *Cryogenics*, vol. 55, pp. 63–67, 2013.

[206] A. Paiella, A. Coppolecchia, L. Lamagna, P. Ade, E. Battistelli, M. Castellano, I. Colantoni, F. Columbro, G. D'Alessandro, P. de Bernardis, *et al.*,

"Kinetic inductance detectors for the OLIMPO experiment: design and pre-flight characterization," *Journal of Cosmology and Astroparticle Physics*, vol. 2019, no. 01, p. 039, 2019.

[207] V. Sivokon, V. Dotsenko, L. Pogorelov, and V. Sobolev, "Dilution refrigerator with condensation pumping," *Cryogenics*, vol. 32, pp. 207–210, 1992.

[208] G. Teleberg, S. T. Chase, and L. Piccirillo, "A miniature dilution refrigerator for sub-Kelvin detector arrays," in *SPIE Astronomical Telescopes+ Instrumentation*, pp. 62750D–62750D, International Society for Optics and Photonics, 2006.

[209] T. Prouvé, N. Luchier, and L. Duband, "Pocket dilution cooler," in *Proceedings of the 15th International Cryocooler Conference, Long Beach, CA*, Citeseer, 2008.

[210] G. Frossati, "Experimental techniques: Methods for cooling below 300 mK," *Journal of Low Temperature Physics*, vol. 87, no. 3-4, pp. 595–633, 1992.

[211] Y. Takano, "Cooling power of the dilution refrigerator with a perfect continuous counterflow heat exchanger," *Review of scientific instruments*, vol. 65, no. 5, pp. 1667–1674, 1994.

[212] Y. Oda, G. Fujii, and H. Nagano, "Practical design of a heat exchanger for dilution refrigeration 1," *Cryogenics*, vol. 18, no. 2, pp. 73–78, 1978.

The End